Bangor University

DOCTOR OF PHILOSOPHY

The assay of nitroreductases with CB1954 and immobilisation onto Gold surfaces

Cude, Matt

Award date:
2014

Awarding institution:
University of Wales, Bangor

THE ASSAY OF NITROREDUCTASES WITH CB1954 AND IMMOBILISATION ONTO GOLD SURFACES

A thesis submitted for the degree of
Doctor of Philosophy

Prifysgol Cymru • University of Wales Bangor

by
Matt Cude

Contents

Abstract

Directed enzyme prodrug therapies (DEPT) are currently being clinically trialled, the aim being to localise cytotoxic compounds at cancer sites; enzymes are either expressed or delivered to solid tumours so that non-toxic prodrugs are activated to cytotoxic derivatives exclusively at cancer cells. Nitroreductases (NTRs) have been clinically trialled in DEPT with the prodrug CB1954 (5-[aziridin-1-yl]-2,4-dinitrobenzamide), however the rate of tumour transduction and subsequent over-expression of the NTR was relatively low for effective cancer treatment, as was the activity of the enzyme with the prodrug.

This research details the assay of a series of NTRs as yet untested with CB1954 to measure activity with the prodrug and evaluate their potential suitability for application in the therapy. The enzymes were assayed in a range of environmental conditions and their kinetic parameters with CB1954 determined and compared to other NTRs reported in the literature. The *nfrA2* NTR from *Bacillus licheniformis* was identified as having a higher catalytic efficiency (K_{cat}/K_m) to the much studied *nfnB* from *Escherichia coli* which has been used in phase I/II clinical trials and is currently the leading candidate for application in DEPT.

Magnetic nanoparticles were synthesised which behave superparamagnetically at room temperature and coated with gold using an aqueous, low cost, non-toxic synthesis. The gold coated magnetic nanoparticles were characterised by transmission electron microscopy (TEM), energy-dispersive X-ray spectroscopy (EDAX), x-ray diffraction (XRD) and ultraviolet-visible (UV-vis) spectrometry, indicating successful Au surface coating producing 38 nm ± 6 nm nanoparticles, which separated under exposure to an applied magnetic field of 1.28 T and readily redispersed upon agitation.

The genetically modified NTRs self-assembled onto Au surfaces and could do so *via* the introduced cysteine sequence, meaning the enzymes can be immobilised with controlled orientation.

Acknowledgments

I would like to thank the North West Cancer Research Fund Institute, Bangor University, the School of Chemistry, Bangor University and the School of Biological Sciences, Bangor University, for funding this research. I would also like to thank Professor M. Kalaji for giving me the opportunity to undertake this PhD as well as the other staff and students of Bangor University, who offered me support and guidance with my research.

I would also like to thank Dr. Erwan Rauwel (Department of Chemistry, University of Oslo, Kjemibygningen, Norway) Dr. Christopher J von Ruhland (School of Medicine, Cardiff University, Cardiff, UK) for their contributions to characterise some of the particles that were produced during this research.

Chapter 1

INTRODUCTION

1.1 Introduction to cancer

1.1.1 Background on cancer

Throughout recorded history humans have suffered with cancer, one of the earliest known records being in the Edwin Smith Papyrus dated to *circa* 1600 B.C, which describes surgical cauterisation of breast cancer and subsequent death of the patient, then comments "there is no treatment".[1, 2] According to the World Health Organisation (WHO) 7.6 million people died of cancer in 2008 worldwide, equating to 13% of all fatalities and makes the disease a leading cause of death globally.[3] Cancer mortality rates have been slowly declining in western countries since the late 1980's and are predicted to decrease further before stabilising at a fixed proportion of the population in the future.[4-6] This is credited to a better understanding of the disease and more advanced treatments attained through research, which now commands an estimated global spend of over £12Bn per year.[7] While there is a decline in mortality rates, global deaths are still expected to total 11 million by 2030[3] and cancer will likely remain a prevalent cause of death in the foreseeable future.[8, 9]

Cancer originates from alterations to deoxyribonucleic acid (DNA) sequences causing a cells' biological processes to change. The transformation of a normal functioning cell into a malignant tumour cell is a multi-stage process.[10-12] The causes and key features of cancer are perhaps best defined by Douglas Hanahan and Robert Weinberg in *"The hallmarks of cancer"*,[13] which describes fully developed cancer cells as being self-sufficient in growth signals, insensitive to anti-growth signals, able to sustain angiogenesis, evade apoptosis, have limitless replicative potential and invade other tissues and undergo metastasis.[13] A malignant growth with all these capabilities can cause severe harm and death if left untreated.

Mutations occur within DNA sequences by chemical reaction, either by direct contact to carcinogens or mutagens,[14] exposure to ionising radiations[15] or infection by harmful bacteria,[16] viruses[17, 18] or fungi.[19, 20] Inheritance of defective genes or certain gene variants is also linked to cancer as these oncogenes play roles in preventing or encouraging malignant traits to develop.[21-23] There are a variety of routes for a cell to acquire malignant traits and there are a range of mechanisms for a cell to promote or evade a particular biological pathway necessary to acquire malignant functionality,[13] we therefore need a variety of treatments to combat the vast array of diseases.

1.1.2 Cancer treatment

Cancer treatments are designed to remove all malignant cells from a patient as cells remaining post-treatment may proliferate and re-establish.[13] Conventional cancer therapies include surgery, chemotherapy, radiotherapy, hormonal therapy, antibody therapy, immunotherapy and angiogenesis inhibitor therapy.[24-26] the treatments administered to a patient depend on the type, grade and stage of the cancer, as well as individual circumstances.

Primum non nocere is a Latin phrase meaning "first, do no harm" and is a principle of medical ethics around the world.[27] For the treatment of complex diseases such as cancers however the objective is to physically destroy cells which were once a normal functioning part of the body, necessitating a compromise between the harm being caused by the cancer and the harm being caused by the treatment. For some treatments, such as surgery, scrupulous hygiene protocols and the use of modern technologies such as video cameras and advanced surgical tools can dramatically reduce the invasiveness of procedures making those which were once dangerous relatively routine.[28]

However treatments such as the administration of pharmaceuticals may interact with all bioavailable cell types indiscriminately, needing rational chemical design and a better understanding of their biological interactions to avoid unwanted side-effects. This has led to the development of specific tumour-targeting drugs which is now a burgeoning research topic.[29-31] Chemotherapies can be severely hampered by their dose limiting toxicity (DLT) which is the concentration above which severe side-effects prevent higher dosage, often due to damage caused to healthy cells rather than target cells. A consequence is that a treatment cannot necessarily be applied at sufficient frequency or concentrations to effectively combat disease, as the treatment itself causes significant harm to the patient.[32, 33] It is hoped that development of tumour-targeting therapies, where biologically active moieties are delivered exclusively to cancer sites, will minimise unwanted side-effects.

1.2 Directed enzyme prodrug therapies

Directed enzyme prodrug therapies (DEPT) utilise non-toxic prodrugs which are activated to cytotoxic compounds by specific enzymes.[34-36] Targeted tumour therapies require the enzyme to be uniquely present in cancer cells but absent in normally functioning cells, or for endogenous enzymes to be expressed only in specific target organs where a tumour is localised.[37] Achieving the former has led to the development of a range of strategies to deliver exogenous enzymes (enzymes not native to the host) exclusively to tumour cells. These strategies have in some cases shown promise, initiating significant research in the areas of antibody-DEPT (ADEPT), which employs antibody-enzyme conjugates to target tumour specific antigens.[38-43] While gene-DEPT (GDEPT) and virus-DEPT (VDEPT). rely on delivering the genes encoding the enzymes to the target cells and transducing them using genetically engineered viruses.[36, 44-50] The use of the nitroreductase (NTR) family of enzymes with nitro-aromatic substances such as 5-(1-aziridinyl)-2,4-dinitrobenzamide (CB1954) has attracted particular attention given the results of early investigations and subsequent clinical trials.[42, 44, 48, 51-58]

1.2.1 Introduction to nitroreductase based therapy

Nitroreductases (NTRs) are a group of enzymes which reduce nitro groups and have found application in DEPT following the administration of CB1954 to Walker carcinoma-cells by Knox *et al.* in 1988.[51] The nitro-reducing enzyme DT diaphorase was found to be responsible for generating an effective DNA cross-linking agent from the prodrug, however the equivalent DT diaphorase in humans has limited activity such that it is ineffective at producing the reduced, cytotoxic derivative at levels high enough to be useful for cancer therapy.[59, 60] The NTR *nfnB* from *Escherichia coli* was subsequently found to be substantially more active with the prodrug than the Walker rat DT diaphorase *in vitro*[54] with an experimental k_{cat} (CB1954) of 360 min^{-1} compared to 4 min^{-1}.[55] NTRs such as *nfnB* can therefore be introduced into hosts which do not contain native NTRs, transforming them from cells that are unreactive to the prodrug to cells that are very sensitive to it.

In mouse studies, incorporating the *nfnB* gene into a virus and transducing tumours has shown the median survival doubles with administration of CB1954.[61] In a separate study 80% of the population with NTR gene transduction showed long term remission, while none of the mice that weren't given *nfnB* VDEPT showed remission.[58] Significantly in both studies tumours which were cisplatin resistant showed an equal sensitivity to the treatment as non-cisplatin resistant tumours. Early phase clinical trials in humans have shown the virus and NTR are well tolerated by patients, as is systemic administration of CB1954 and while the treatment has shown promise, improvements are needed.[44, 62]

1.2.2 Prodrugs for nitroreductase based therapy

CB1954 is reduced by *nfnB* to form 2- and 4-hydroxylamine derivatives in equal proportions. In a physiological environment the latter becomes the N-acetoxy derivative shown as compound (6) in *Figure 1.2.1* which is a potent DNA crosslinking agent.[53] CB1954 can be reduced to four cytotoxic metabolites by NTRs prior to thioester reaction; the 2- and 4-hydroxylamines (compounds (2) and (4)) of which the latter is the most cytotoxic, and their corresponding amines (compounds (3) and (5)), of which the 2-amino derivative is the most cytotoxic and has a similar potency to the 4-hydroxylamine derivative.[63]

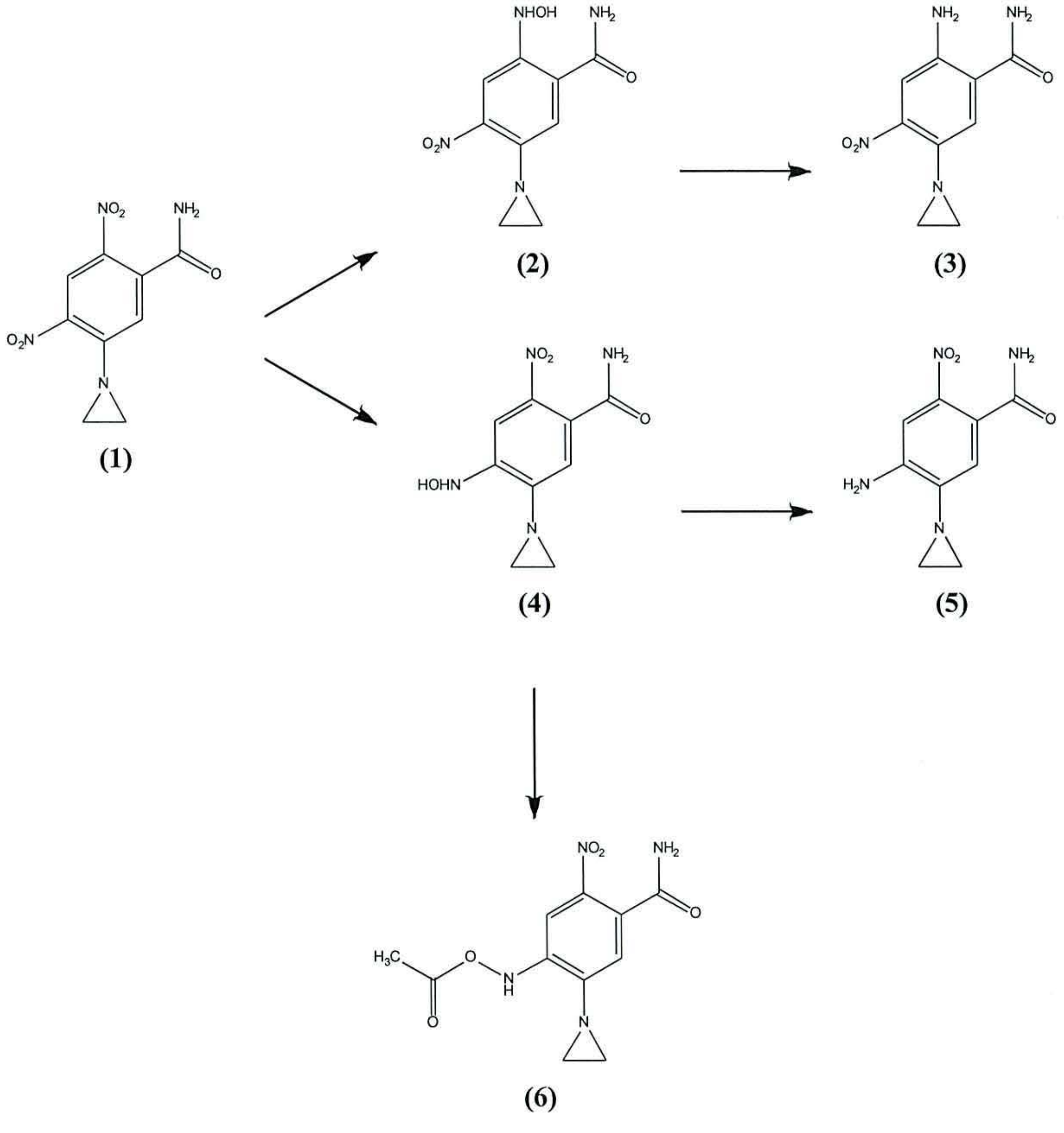

Figure 1.2.1 The reduction of 5-(1-aziridinyl)-2,4-dinitrobenzamide (CB1954) (1) *to 2 and 4 hydroxylamine derivaties* (2) *and* (4) *which may further reduce to amino derivatives* (3) *and* (5). *In a physiological environment* (4) *may react with thioesters such as acetyl coenzyme A to become* (6) *which is a potent DNA crosslinking agent.*[53, 63]

The "bystander effect", where diffusion of the cytotoxic metabolite kills neighbouring cells which are not expressing the enzyme is an important and well reported phenomenon exhibited by the therapy.[64-66] The ability of a transduced cell to produce cytotoxic compounds which can diffuse through a tumour and kill multiple cells makes the "bystander effect" a key therapeutic property and it is thought the 2-amino derivate over the 4-amino and both hydroxylamine derivatives is *in vitro* the dominant bystander species due to its superior diffusion.[63]

Development of prodrugs with increased potency has led to the creation of compounds such as SN23862, a chloromustard analogue of CB1954 which possesses a higher k_{cat} than CB1954 and a higher potency *in vitro*.[57, 63, 67, 68] Prodrugs designed for improved application in DEPT, which are better suited for cancer therapy, should be stable to endogenous enzymes, rapidly reduced by the NTR, have a large difference in cytotoxicity between the oxidised and reduced forms, be very soluble in physiological conditions and produce metabolites with high diffusion rates which effectively crosslink DNA. DNA crosslinking is thought to be *via* the amide group of the aromatic ring and derivatives generated *in vivo* of the aziridine ring, such as the N-acetoxy group following thioester reduction (e.g. from Acetyl coenzyme A).[53] Many analogues of CB1954 and SN23862 have been synthesised in attempt to improve these properties including addition of side chains at the amide group, halogenated mustards in place of aziridine and addition of mesyl groups.[69, 70] A single alteration and combinations of alterations can produce prodrugs with very different properties, for example dihydroxypropyl substitution of the carboxamide improves aqueous solubility but as the analogue is less cytotoxic the modification is not advantageous.[69]

(1) **(7)**

Figure 1.2.2. CB1954 (1) *and the chloromustard analogue SN23862* (7), *which has a higher k_{cat} with E. coli nfnB than CB1954 and a higher potency in vitro.*[57, 67]

The modification of prodrugs to improve the efficacy of DEPT is important and substituting functional groups and assessing the alterations to chemical activity and cytotoxicity should improve the treatment. While this is a key area of research it is not to the exclusion of the kinetic properties of the enzyme and the ability of the NTR to rapidly reduce the prodrug in a physiological environment for therapeutic application. An enzyme which operates at 'catalytic perfection' will have a k_{cat}/k_m of the order of 10^8 to 10^9 $M^{-1}s^{-1}$ which is approaching the diffusion controlled limit, the point at which the reaction rate is limited by the rate of substrate diffusion rather than reaction with the enzyme.[71] Several enzymes such as catalase, superoxide dismutase, fumarase and acetylcholinesterase have catalytic efficiencies of this magnitude[71] yet *nfnB* from *E. coli* has a catalytic efficiency with CB1954 of the order of 10^4.[72-74] There is therefore significant scope to improve the catalytic efficiency of the enzyme with the prodrug, an area investigated in this thesis by identifying and assaying enzymes as yet uncharacterised with CB1954. The aim is to identify enzymes which have a higher catalytic efficiency than those currently reported as they will be better suited for cancer therapy.

The structure of an enzyme is determined by the amino acid sequence which it is constructed from and this governs the catalytic efficiency. For superoxide dismutase the arrangement of charged groups and amino acids around the enzyme surface electrostatically guide the substrate to the active site, this funnelling effect means that almost every time the enzyme and substrate encounter a reaction occurs, hence the rate approaches the rate of diffusion.[71] The structure around the active site is also crucial so that reactions occur rapidly and the product vacates the active site to allow subsequent reactions to proceed, given CB1954 is not a natural substrate to *nfnB* there is substantial scope to improve the rate at which the prodrug is reduced by improving the enzyme rather than the prodrug.

1.3 Nitroreductases

1.3.1 Nitroreductases for directed enzyme prodrug therapy

Both Walker rats and humans possess DT diaphorase however CB1954 is not cytotoxic to humans as the human DT diaphorase does not effectively reduce the prodrug.[60] This initial observation has generated great interest in NTRs for DEPT as there is potential to isolate enzymes which reduce the prodrug effectively from other species and attempt to localise these at human sites of disease for targeted therapy.[52]

The NTR *nfnB* from *E. coli* has been the focus of NTR DEPT, however there are a variety of other NTRs across many bacterial strains which may have potential application for therapy. The precise physiological role of the enzymes for the bacteria is unclear, although the substrate versatility may suggest there is both a metabolic role as well as a role in breaking down environmental toxins.[75] NTRs are classified into two groups; type I, oxygen insensitive and type II, oxygen sensitive enzymes. Oxygen insensitive NTRs are flavoproteins which involve a two electron transfer (utilising NADH and/or NADPH as an electron source) to reduce nitro groups producing nitroso and then hydroxylamine derivatives which are of interest for DEPT.[76] Humans do not naturally produce enzymes capable of reducing prodrugs such as CB1954 to these derivatives, so by introducing NTRs that are able to, it is hoped therapies can be targeted to specific sites of disease.[44]

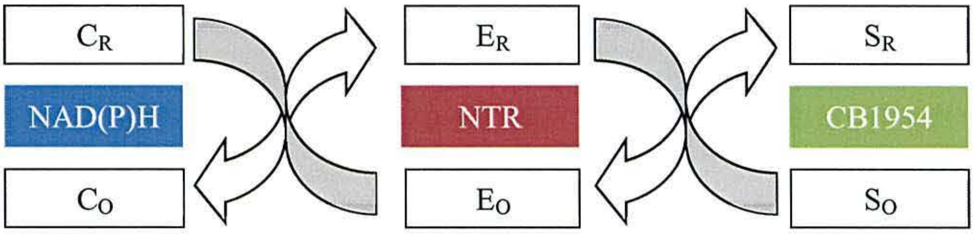

Figure 1.3.1. Schematic showing the redox cycle of an enzyme reducing a substrate via oxidation of a cofactor. C, E and S represent cofactor, enzyme and substrate respectively, the subscripts denote whether in reduced or oxidised form. The arrows show the movement of electrons.[77]

nfnB from *E. coli* is a homodimeric enzyme containing two active sites of tightly bound flavin mononucleotide (FMN). Each amino acid monomer contains 217 amino acids which come together to form a rigid structure around the two FMN sites, binding each unit at the dimer interface with residues from both monomers. Investigations into a homologous NTR from *Enterobacter cloaccae* (which is 88% identical to the NTR from *E. coli*) reveals the amino acids are not directly involved in substrate reduction and the key difference between the oxidised and reduced forms of the enzyme is the angle of the isoalloxazine ring within the FMN, which increases from 16° to 25°.[78, 79]

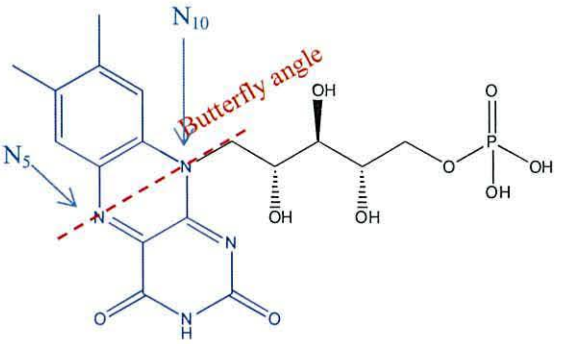

The butterfly angle of the isoalloxazine ring changes across the N_5 to N_{10} axis of FMN from 16° to 25° when the enzyme goes from an oxidised to a reduced state

Figure 1.3.2. The chemical structure of flavin mononucleotide (FMN).[79]

The reaction proceeds *via* a ping-pong Bi-Bi pathway which is where FMN is first reduced by NAD(P)H, releasing NAD(P)+ and the FMN subsequently donates two electrons to CB1954, reducing one of the nitro groups to a nitroso group.[78] The crystal structure of *nfnB* shows there is one accessible channel to the active site and that NAD(P)H and CB1954 cannot simultaneously occupy the pocket where FMN is bound.[80] This is why the reaction proceeds via a ping-pong Bi-Bi pathway. In solution the nitroso group is further reduced to the hydroxylamine derivatives after it has vacated the active site, so the reaction rate is limited by the reduction rate of the nitro group at the FMN. Molecular dynamics simulations show that this reaction proceeds by donation of two electrons from FMN to CB1954, which picks up two protons from water molecules, rather than there being a direct hydride transfer from FMN.[81] The following figures illustrate the oxidation of FMN and reduction of CB1954 *via* two 1 electron transfers from FMN to CB1954.

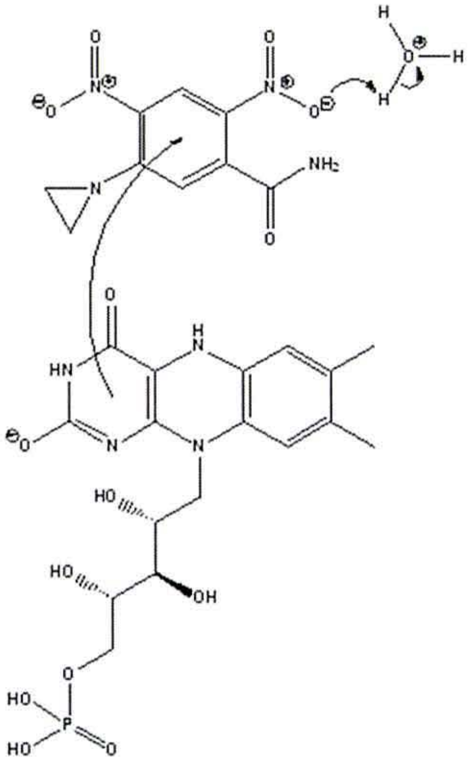

Figure 1.3.3. Reduced FMN donating an electron to CB1954 and reduction of the 2-nitro group.[81]

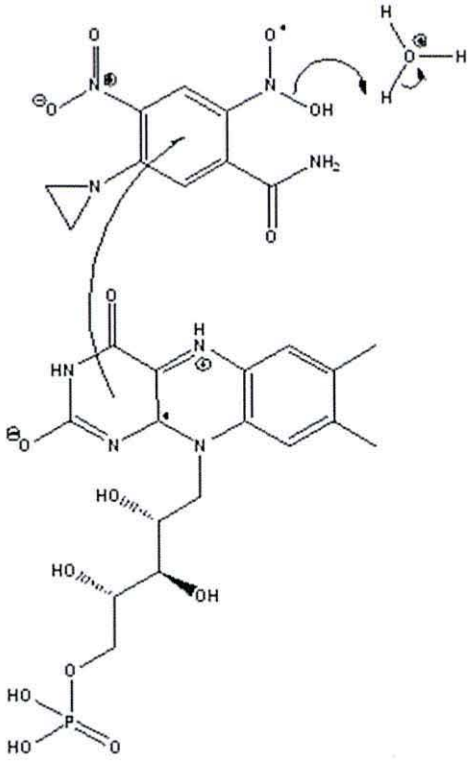

Figure 1.3.4. FMN radical donating a second electron to CB1954 and condensation of the CB1954 2-nitro group.[81]

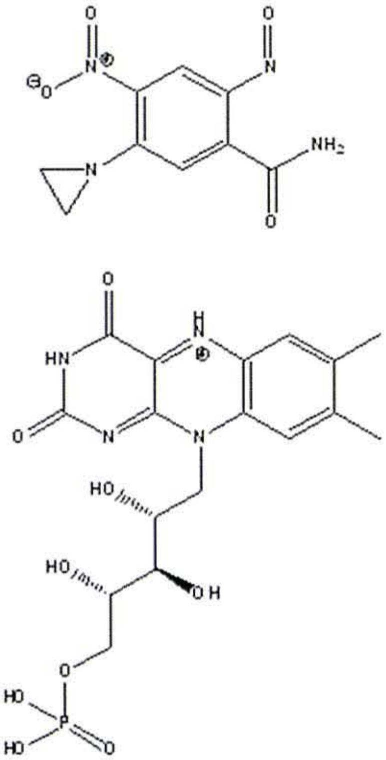

Figure 1.3.5. Oxidised FMN and the 2-nitroso derivative of CB1954.[81]

The reduction of the nitro groups of CB1954 by direct hydride transfer from N_5 of FMN is thermodynamically possible, however molecular dynamic simulations show the substrate is not able to orientate in such a way that the groups are in close enough proximity for this to occur.[81] Analysis of the enzyme crystal structure shows there are 230 water molecules associated with the 4453 protein atoms and 2 FMN molecules of *nfnB*[80] and that within the FMN pockets both the 2- and 4- nitro groups of CB1954 are in direct contact with solvent molecules, accounting for the equal proportions of the 2- and 4-hydroxylamine products.[81]

The nitroreductase from *E. coli* known as *nfnA* was recently found to be active with CB1954.[82] The NTR is NADPH dependant unlike *nfnB* which utilises both NADH and NADPH as an electron source for nitroreduction. The authors found *nfnA* possessed superior kinetic properties to *nfnB in vitro* with bacterial and human cell lines being 4 to 8 times more sensitive to CB1954 when *nfnA* was present compared to *nfnB*. *nfnA* also selectively reduced the 2-nitro group whereas *nfnB* reduced the 2- and 4-nitro groups in equal proportions and was more effective at sensitising cells to a range of alternative dinitrobenzamide mustard prodrugs.[82] The crystal structure of *nfnA* was elucidated almost a decade prior and specific amino acids were identified as being important in explaining the different activities observed between *nfnA* type NTRs from *Vibrio harveyi* and *Bacillus subtilis*.[83]

Attempts to improve the catalytic efficiency of *nfnB* by substituting amino acids within the structure have shown that mutant enzymes can be significantly more effective at reducing CB1954.[73, 74, 84] However it is difficult to predict which mutations will confer beneficial effects and how combinations of single, double and triple mutants will interact to effect the final enzyme structure and activity with the prodrug.[74] The crystal structure of enzymes can be very different to their structures in a physiological environment[85] and an enzyme's surface functionality as well as the sizes and charges of clefts and channels along with the specific amino acid conformation around the active site of the enzyme make the process of rational design complex.

Given the large number of NTRs that exist across a range of bacterial species the number which have been assayed with CB1954 is comparatively very small, this means the pool of knowledge from which structure-activity relationships is being derived from could become much larger by screening potential NTRs with the prodrug. Not only does this develop the understanding of CB1954 nitroreduction there is also potential to discover naturally occurring enzymes which already offer superior catalytic properties and would potentially be better candidates for cancer therapy as has been attempted in a few studies recently.[72, 86, 87]

1.3.2 Potential delivery strategies of nitroreductases

By design antibody DEPT (ADEPT) utilises enzyme-antibody conjugates to target antigens expressed by tumour cells. The conjugates are theoretically able to bind to tumour specific antigens localising the enzymes which are covalently bound to the antibodies to the cancer site.[43, 88] However clinical trials of ADEPT show that localisation is not adequate for treatment due to the low number of successful binding interactions between antibody and antigen *in vivo*.[41]

These issues have been addressed with virus DEPT (VDEPT) where tumour cells are transduced to contain the genetic material necessary to produce the enzyme.[89] However recent clinical trials have highlighted limitations to the treatment *in vivo* including the need to improve virus administration and NTR activity towards the prodrug.[44] It is common for gene therapies to suffer low tumour transduction rates as there is an auto-immune response against viral infection,[90] this means repeat treatments are necessary and adds importance to the need of a significant bystander effect to counter the low number of cells producing the enzyme.

1.4 Nanotechnology

Nanotechnology is a rapidly expanding research topic[91, 92] and has been of great interest during the last two decades for potential application in a large number of disciplines. A recent study surveying research outputs associated with nanotechnology identifies subjects within the biomedical sciences as being the most prolifically cited.[93] In its broadest sense nanotechnology relates to matter of dimensions between 1 nm and 100 nm, which often possess unique physical, chemical and biological properties compared to the same matter of larger dimensions.

1.4.1 Gold nanoparticles

Gold nanoparticles have been utilised since the 4th or 5th century B.C;[94] initially used as dyes and stains[95] and later medical treatments and diagnostic tools. The colloids were first scientifically studied by Faraday (1791-1876) in the 19th century.[96] Today extensive research is undertaken on gold nanoparticles in pursuit of improved catalysts,[97] electronics,[98] surface coatings,[99] sensors,[100] diagnostics,[101, 102] imaging agents,[103, 104] cancer therapies,[105-108] bio-conjugates,[109] hyperthermia treatments,[110-112] cell labelling, gene and drug delivery agents.[113, 114] The extensive research and application of gold nanoparticles shows the perceived potential for social, economic and academic impact. Underpinning these potential applications is the controlled synthesis of the particles, given that size, shape, charge and ligand conjugation dictate the physical and chemical properties exhibited by the colloids, determining their potential use.[115]

1.4.2 Surface plasmon resonance

The distinct deep ruby red colour of a gold sol is due to surface plasmon resonance (SPR), a property exhibited by many metal nanoparticles where electromagnetic radiation excites conduction electrons over the particle surface, in phase, at a specific wavelength, typically around 520 nm for spherical gold nanoparticles in aqueous solution.[116] This is an important property of gold nanoparticles which facilitates their application in many of the systems described in section 1.4.1.[117]

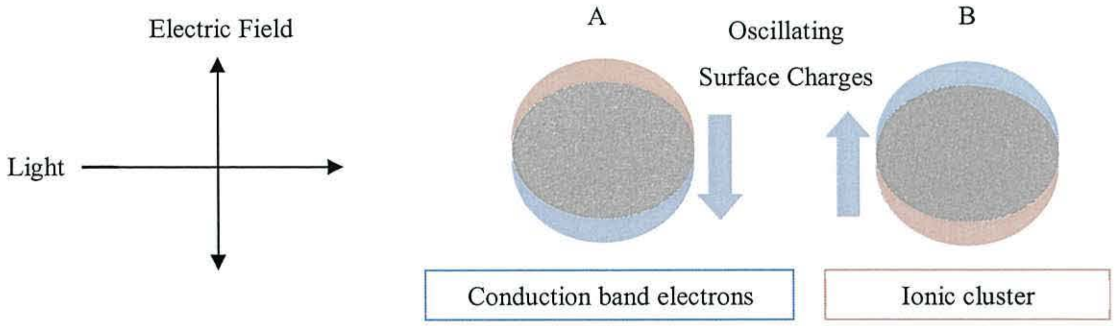

Figure 1.4.1. An illustration of electromagnetic radiation causing electric charge to oscillate in phase over a metal nanoparticle surface, inducing surface plasmon resonance (SPR).[116]

SPR is extremely sensitive to the electronic environment at the nanoparticle surface and is affected by ligand conjugation, solvent dielectric, surface charge, nanoparticle size and shape.[118-120] The sensitivity of SPR is a useful diagnostic tool and also has potential for therapeutic application using plasmonic heating to either apply thermal therapy or initiate controlled drug release.[121]

1.4.3 Gold nanoparticles in biology

Gold nanoparticles have generated a great deal of interest for application in biology and medicine given the ease with which they can be synthesised and functionalised with biologically active compounds.[122] As an inorganic delivery agent, imaging agent or photoactive agent, their cytotoxicity and biological fate are fundamental for effective application *in vivo*. Studies *in vitro* have generally found that gold nanoparticles are non-toxic[123] and can be taken up by cells *via* endocytosis.[124, 125] Previous research into nanoparticle toxicity and cellular fate, and the relationship to particle size and surface conjugation can be considered when designing a new potential biological application.

A study incubating gold nanoparticles with mammalian cells has shown that particles between 10 nm and 100 nm are included into the cells and those of 50 nm are taken up in higher concentration and at a faster rate (uptake half-life of 14, 50, and 74 nm nanoparticles is 2.10, 1.90, and 2.24 h, respectively).[126] Surface ligands also play a significant role in cellular inclusion, for example particles with proteins bound to the surface are generally taken up *via* endocytosis into vesicles.[127] However particles surface capped with anionic and hydrophobic ligands in controlled bands have been shown to pass through cell membranes directly and without membrane disruption.[128] Both positively charged and negatively charged particles will typically adsorb serum proteins which can bind to the particle surface facilitating endocytosis,[129] while charged particles without prior exposure to biological compounds or with immobilised cationic and anionic side chains will bind to, damage and disrupt cell membranes, causing cytotoxicity,[130, 131] suggesting surface chemistry plays a more dominant role than shape or size in cellular fate. Both surface chemistry and particle size must therefore be considered when designing a new bioconjugate for potential biological application.

In vivo experiments add a further dimension to observations from *in vitro* studies as they can produce unexpected results; a recent study of gold nanoparticles between 3 nm and 100 nm in mice showed that *in vivo*,[132] particles between 8 nm and 37 nm caused severe health problems and death for the majority of mice within 21 days, with abnormalities to the liver, lungs and spleen post mortem where the gold nanoparticles had accumulated, while particles of 3 nm, 5 nm, 50 nm and 100 nm did not cause death over 50 days. The mechanism of disease and death for the particles remains unclear and incubation of the same particles *in vitro* with HeLa cells showed no cytotoxicity for particles of any size.[132] There is growing evidence to suggest that gold particles are themselves not inherently cytotoxic, however interactions within a complex physiological environment can lead to toxicity.[133]

The toxicity of gold nanoparticles also depends on their shape and surface ligands and given the large number of studies using different assays, cell lines and animal models, in combination with the different sizes, shapes and capping agents of the gold nanoparticles used in each experiment, only a fragmented picture has so far been built as to how and why particular particles are or are not toxic, however controlled surface chemistry will play a crucial part ensuring particles are biocompatible.[134]

1.4.4 Magnetic nanoparticles

Background on magnetic nanoparticles in medicine

Following the discovery that metastasis occurs *via* the lymphatic system, an article from 1957 "*Selective Inductive Heating of Lymph Nodes*" details the administration of sub-micron magnetic iron oxide particles to lymph nodes, followed by application of an external magnetic field to induce heating.[135] A ground breaking piece of work at the time the article concludes:

"All of our findings indicate that we will be able to inject sufficient amounts of recently available magnetic metallic particles into nodes in man. The improved magnetic characteristics and the smaller size of these metallic particles plus an improved type of coil now under construction should give us sufficient heat differential to attain any thermal effect desired in the lymph nodes. When perfected, this system should make it possible to raise the temperature of any part of the body for either a few seconds or for prolonged periods. The possible application of such a tool in the investigation of numerous problems of growth or physiology requires little imagination."[135]

This early example of the use of iron oxide particles in cancer therapy highlights the exciting potential that surrounds this field of research. In the following decades substantial work has built on this foundation and today magnetic nanoparticles have FDA approval for use against certain solid tumours in human patients both in combination with radiotherapy and alone. Companies such as Sirtex Medical (delivering Selective Internal Radiation Therapy (SIRT) to the liver), Aspen MediSys (developing Magnetically Energized Thermotherapies for the treatment of cancer and other diseases) and MagForce (the first company in the world to receive European approval for a medical product using nanoparticles). Are all producing and developing magnetic particles for thermal cancer therapy, applying high-frequency magnetic field causing the magnetic nanoparticles to oscillate, generating heat directly within the tumour tissue to either kill the tumour or sensitise the area for chemotherapy.[136]

Principles of magnetism and magnetic nanoparticles

Magnetic nanoparticles have received significant attention for application in diagnostics, as MRI contrast agents (compounds which enhance MRI), drug delivery systems and as hyperthermia treatments[137-139] and these applications depend considerably on the magnetic properties of the particles and the applied magnetic fields. The attraction of iron to magnetite was first written about at least as long ago as 600 B.C., the idea of magnetic 'poles' came about in the 13th century and in the 18th century accurate quantitative experiments were done by Coulomb (1736-1806). A very brief outline of the principles of magnetism and magnetic materials is outlined in the following section.[140, 141]

Magnetic materials are classified based on their magnetic susceptibility χ which derives from the intrinsic magnetic moments generated by the electron environment within a material. The magnetic susceptibility represents the parallel or anti-parallel alignment of magnetic moments within a material and the degree of magnetisation when in an applied magnetic field, as defined in *Equation 1.4.1.*[141]

$$\chi = \frac{M}{H}$$

Equation 1.4.1. The relationship between magnetic susceptibility χ, magnetisation M and an H-field H.[141]

If the magnetic susceptibility of a material is less than zero it is termed diamagnetic and, when placed in an external magnetic field, the material will weaken the applied field as intrinsic magnetic moments oppose it. All materials possess some diamagnetism as paired core electrons of an atom contribute a diamagnetic response. Values of χ (unitless) range from around -10^{-5} to -10^{-6} for this common group of materials often described as non-magnetic. The second group of diamagnetic materials are the superconductors which have, below critical temperature, a magnetic susceptibility of -1 and are therefore perfectly diamagnetic and completely expel an external magnetic field.[140, 141]

If the magnetic susceptibility of a material is greater than zero it is termed paramagnetic and when placed in an external magnetic field the material will strengthen it, typical values of χ range from around 10^{-3} to 10^{-5} for weak paramagnets, whose group includes aluminium, platinum and manganese. Exposed to an external magnetic field at room temperature a paramagnets magnetisation aligns parallel with it, however when the applied field is removed thermal agitation disorders internal magnetic moments and there is no longer a net magnetic dipole moment. Where this is not the case and magnetic moments remain aligned after exposure to an applied field, the material is termed ferromagnetic.[141] Paramagnets are unsuitable to utilise as magnetic nanoparticles *in vivo* given the disordered magnetic dipoles, meaning they have a low magnetic saturation and weak response to an applied field. Ferromagnets have much greater order, however retain a permanent magnetic field, meaning they would induce magnetic flocculation rather than exist as a colloid.

Ferromagnets typically have magnetic susceptibilities in the range of 50 to 10,000 and are often the materials of common permanent magnets. In some cases a material exhibits permanent magnetism but contains magnetic moments which lie antiparallel to the net magnetic dipole moment. These materials are termed ferrimagnetic and in the particular instance where there are an equal number of magnetic moments aligned and anti-aligned they are termed antiferromagnetic, these materials have no net magnetic dipole moment.

Raising the temperature of these materials adds disorder to magnetic moment alignment. For ferromagnetic and antiferromagnetic materials, the Curie temperature for the former and Neel temperature for the latter are the critical points where thermal agitation and entropy exceeds the tendency for the magnetic moments to align, at these points the magnetic susceptibility decreases and the materials become paramagnetic.[141]

Characterising magnetic materials can be done by analysing the plot produced from the variation of the B-field with an applied H-field for a given material, an example B-H curve for a ferromagnetic material is shown in *Figure 1.4.2*. The magnetic saturation is the point at which all magnetic domains within a material are aligned and further increase in the H-field will no longer induce an increase in the B-field. The remanence shows the proportion of magnetic domains which remain aligned in the absence of an applied filed and the coercivity the strength of H-field required in the opposite direction to return the B-field to zero after induction.[141]

For magnetic nanoparticles to exist as a colloid there must be no remanence, as this would induce magnetic flocculation and aggregation of the particles. Figure 1.4.2 illustrates the theoretical response of a ferromagnetic and superparamagnetic material. The superparamagnetic material has a magnetic saturation equal to that of a ferromagnetic material, however when the H-field is removed the B-field returns to zero. Superparamagnetism in practice means superparamagnetic particles can be completely separated from a solution in the presence of an H-field, but return to a stable sol in its absence.

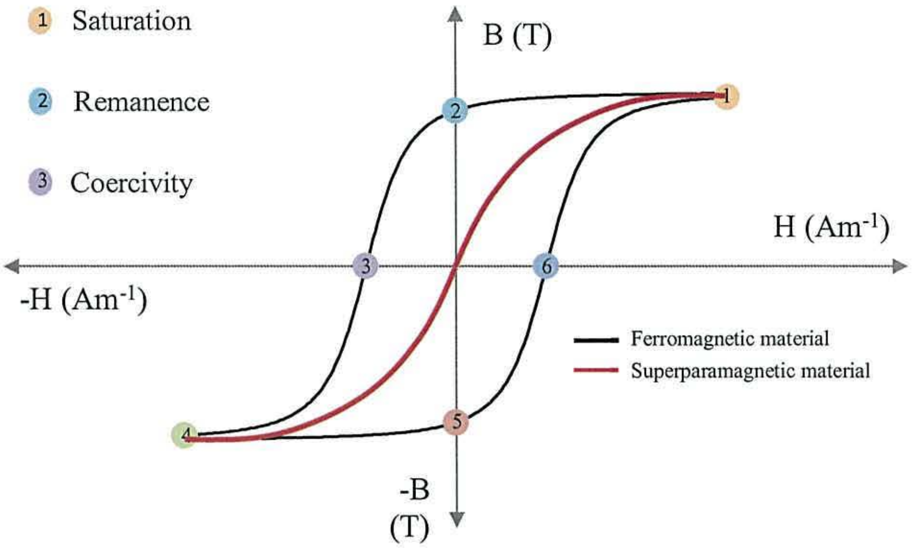

Figure 1.4.2. A model B-H plot showing magnetic hysteresis of a ferromagnetic material in black and superparamagnetic material in red. 1,2 & 3 show the magnetic saturation, remenance and coercivity while 4,5, & 6 show the same parameters in opposite fields.[141]

The response of magnetic nanoparticles to an applied field depends on the strength of the applied field and the magnetisation of the particles. MRI scanners can typically apply fields up to around 3 T, the National High Magnetic Field Laboratory in Florida has a magnet which can generate fields up to 45 T but commercially available magnets are around 1 T. The magnetisation of a material depends on the ratio of magnetic moments to volume, as defined in *Equation 1.4.2.*[140]

$$M = \frac{N}{V} m$$

Equation 1.4.2. M represents magnetisation, N the number of magnetic moments, m the magnetic moment (vector) and V the volume[140]

From *Equation 1.4.2* particles which possess a high number of aligned magnetic moments within a small volume will exhibit a greater response to an applied magnetic field. Paramagnetic and diamagnetic materials by definition do not contain a significant number of aligned magnetic moments, so as particles, would not show a significant response to an applied field. Ferromagnetic and ferrimagnetic materials however have more ordered arrangements of magnetic moments and therefore substantially larger magnetisation values.

Weiss (1865-1940) proposed in the early twentieth century the existence of magnetic domains in ferromagnets, containing 10^{12} to 10^{18} aligned atomic magnetic moments which within a domain remain almost completely aligned.[141] These domains can be randomly orientated throughout a material and produce a net magnetic dipole moment of zero, similar to paramagnets, however if an external field is applied these domains can align and remain aligned. This early domain theory explained the significant difference in magnetisation observed between ferromagnets and paramagnets.[141]

For magnetic nanoparticles to exhibit a substantial response to an applied magnetic field they must contain a significant number of aligned magnetic moments. However once ferromagnetic and ferrimagnetic materials have been exposed to an applied field a portion of the magnetic domains throughout the material remain aligned. This remanence would induce magnetic flocculation among the nanoparticles, producing a magnetic aggregate attracting all the nanoparticles together. To avoid this, magnetic nanoparticles must be of the order of single magnetic domains, so that once the applied field is removed inter-particle attraction does not exceed thermal disorder. *Figure 1.4.3* shows an illustration of different types of magnetic material.

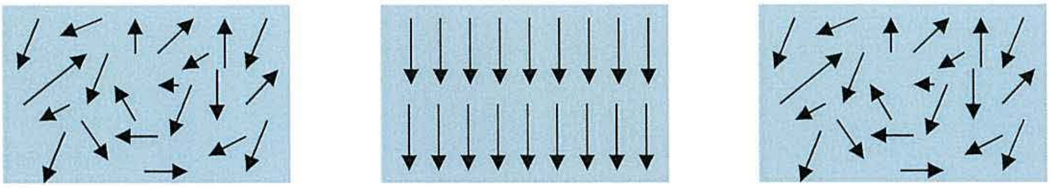

A diamagnetic material in the absence of an applied field

A diamagnetic material during exposure to applied field H↑

A diamagnetic material after exposure to applied field H↑

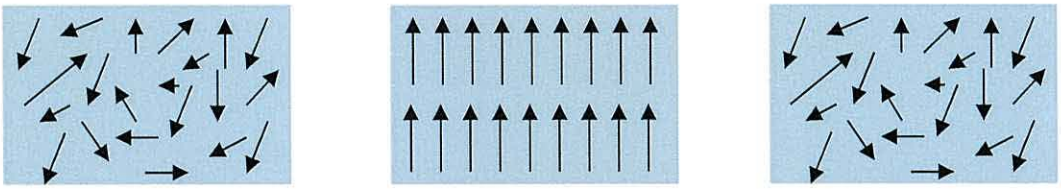

A paramagnetic material in the absence of an applied field

A paramagnetic material during exposure to applied field H↑

A paramagnetic material after exposure to applied field H↑

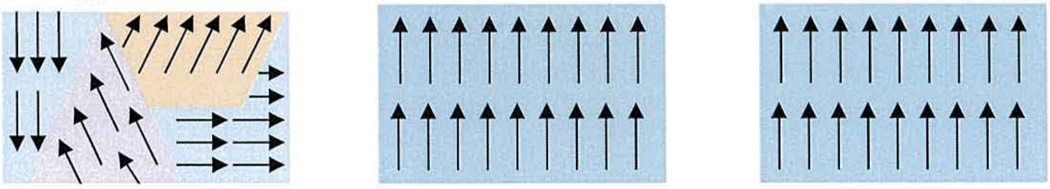

A ferromagnetic material in the absence of an applied field

A ferromagnetic material during exposure to applied field H↑

A ferromagnetic material after exposure to applied field H↑

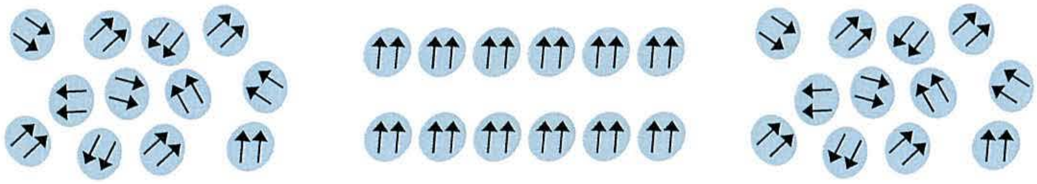

A superparamagnetic colloid in the absence of an applied field

A superparamagnetic colloid during exposure to applied field H↑

A superparamagnetic colloid after exposure to applied field H↑

Figure 1.4.3. Illustrations of the idealised responses of diamagnetic, paramagnetic, ferromagnetic and superparamagnetic materials before, during and after exposure to an applied magnetic field. The arrows represent magnetic moments.[140, 141]

Magnetic nanoparticles for DEPT

The application of magnetic nanoparticles for biological purposes has been very well studied, resulting in numerous review articles which discuss the subject and detail the physical properties needed by the particles. [142-145] Magnetic nanoparticles must possess a magnetic response significant enough for magnetic manipulation, be superparamagnetic, biocompatible and stable in a physiological environment.[142-145] Iron oxide nanoparticles are the fore-runner in current biomedical research given their high magnetic saturation, superparamagnetism and approval by both the FDA and European Medicine Agency for use in medicine.[146] Given the well-defined properties of iron oxide nanoparticles and existing approval for medicinal use, they are a suitable material to use in the preliminary stages of a new therapy.[147] Research into other magnetic materials which have higher magnetic saturation, and would have a greater magnetic response to an applied field is on-going.[148] However there are still concerns regarding biocompatibility of these new materials, typically containing cobalt, platinum, manganese, nickel or magnesium.[145, 148]

Chemical stability is important in a physiological environment as many metals will oxidise, changing their physical and chemical properties. It is also therefore advantageous to utilise a material which is already in a fully or partially oxidised state, is stable and biocompatible. As mentioned previously iron oxide particles have been applied therapeutically since the 1950's and have been well studied in both bulk and nano forms, the iron oxides of interest for nanomedicine are Fe_3O_4 and γ-Fe_2O_3, the properties of which are shown below in *Table 1.4.1.*[149]

Table 1.4.1. Physical properties of bulk magnetite, Fe_3O_4 and maghemite, γ-Fe_2O_3.[149]

Property	**Magnetite, Fe_3O_4**	**Maghemite, γ-Fe_2O_3**
Density (gcm^{-3})	5.18	4.87
Melting Point (°C)	1583-1597	Transforms to α-Fe_2O_3 at ~400°C
Magnetism	Ferromagnetic	Ferrimagnetic
Curie Temperature (K)	858	1020
Magnetic Saturation (Am^2kg^{-1})	92-100	60-80
Crystallographic System	Cubic	Cubic or tetrahedral
Structural Type	Inverse spinel	Defect spinel
Space Group	Fd3m	$P4_332$ (cubic); $P4_12_12$ (tetragonal)
Lattice Parameter (nm)	a = 0.8396	a = 0.83474 (cubic); a = 0.8347, c = 2.501 (tetragonal)

Oxidation of magnetite to maghemite occurs in the presence of oxygen, for magnetite nanoparticles this is a very rapid process given their small size and high surface to volume ratio. It is therefore more accurate to use the term iron oxide nanoparticles to describe nanoparticles that are stored in an aerobic environment rather than specifically maghemite or magnetite.

The point zero charge of iron oxide nanoparticles is around 7,[150] so to be stable as a sol in an aqueous solution of around pH 7, iron oxide nanoparticle must be functionalised. For application in a physiological environment this must be biocompatible and ligands such as organic acids, polymers and inorganic surface coatings have shown to be suitable.[151, 152] Dextran has been a popular surface coating given its stability and biocompatibility[153-155] as has polyethylene glycol (PEG).[156] PEG has been of particular interest as it prevents adsorption of other biological compounds and the nanoparticles do not initiate a response by the reticulo endothelial system (RES) giving PEGylated nanoparticles an enhanced permeation and retention (EPR) effect.[156] Similarly to results from investigations with gold nanoparticles *in vitro* and *in vivo*, the surface chemistry of the nanoparticles dominates the biocompatibility and physiological response, so must be carefully controlled to suit the intended biological application.[157] For application in DEPT the surface chemistry of the nanoparticles must be suitable for enzyme immobilisation which is discussed in the following section.

1.5 Nitroreductase immobilisation and magnetic nanobioconjugates

For nanoparticles to be utilised as magnetic delivery agents for NTRs, there are several properties which must be exhibited by the colloid; a significant response to an applied magnetic field, an NTR which reduces a prodrug such as CB1954 effectively in a physiological environment and an immobilisation strategy to bind the enzymes to the particles and produce a stable sol in biological media. Given magnetic nanoparticles and NTRs have been independently trialled in humans and have approval for medical studies,[44] the key area for developing a magnetically controlled DEPT is generating a method to bind the proteins to the nanocarriers.

Immobilising enzymes onto nanoparticles often shows improved enzyme characteristics with increased stabilities, retained and even improved activities in many examples[158-171] and there has been substantial research in the subject over the last decade producing a range of potential applications for these new biotechnologies.[164] Covering in detail the diverse strategies that have been employed given the wide range of materials that can be synthesised at nanoscale and the variety of biological moieties that are of interest is beyond the scope of this introduction and is very well reviewed elsewhere.[172]

The primary objective from a rational chemical design perspective is to ensure immobilisation is achieved such that the enzymes do not readily dissociate from the particle surface which means a covalent bond from enzyme to particle is a practical choice for bioconjugate generation.[122] A recently developed approach of incorporating bond-compatible chemical species into the biological moiety and nanoparticle is inspired from biomineralisation, a process in nature where crystalline materials are synthesised under strictly controlled conditions utilising specific recognition sequences in proteins to coordinate crystal growth.[173] This has been exploited to coordinate specific amino acid sequences to inorganic substrates based on recognition sequences, which are peptides of approximately half a dozen to two dozen amino acids which contain functional groups that specifically coordinate to the inorganic material of interest.[174-176]

1.5.1 Protein modification for conjugation to inorganic substrates

Using genetically engineered peptide sequences for nanoparticle coordination can be easily achieved using recombinant DNA techniques.[160, 177, 178] The amino acid structure around the active site of an enzyme is crucial in dictating its activity with a given substrate, so the addition of an amino acid sequence designed to bond to an inorganic surface is typically at the end of a polypeptide chain, to limit the impact of modification.

The most utilised example of this type of amino acid immobilisation sequence is the addition of a consecutive sequence of six Histidine units (His_6-tag) to a target gene, developed in the 1980's by Roche. The process involves the insertion of genetic code to the end of a gene sequence so that six consecutive histidine residues are added to the N-terminus or C-terminus of the resulting amino acid sequence.[179] The His_6-tag chelates to Ni^{2+} allowing the target sequence to be easily isolated from other proteins by passing them through a nickel purification column.[180] This system of genetic modification for protein purification has been widely adopted and commercial purification kits are readily available from suppliers such as QIAgen, Sigma Aldrich, GE Healthcare and Thermo Scientific among others.

The use of His_6-tagged proteins not only facilitates protein purification, but the modified proteins also readily bond to nickel and nickel oxide nanoparticle surfaces *via* self-assembly.[181, 182] However nickel is unsuitable for bio-application given its toxicity.[183,

[183]Other studies have shown that His_6-tagged proteins can be immobilised *via* the introduced histidine sequence onto gold surfaces[184] and gold nanoparticles.[185] As detailed in Section 1.4.3, gold has received substantial attention as a biomaterial at the nanoscale given its chemical stability, biocompatibility, resistance to corrosion and oxidation, as well as the ease with which gold nanoparticles can be synthesised and functionalised with predictable physical and chemical properties.[186]

Self-assembly of thiols at Au surfaces produces Au-S bond of approximately 170 – 210 $kJmol^{-1}$ and the ease with which Au can be functionalised with thioalkanes has made the combination very attractive for biological application.[187, 188] The use of cysteine alone or as a functional bonding component of peptides, proteins and enzymes to functionalise Au has been well studied[98, 189-194] and well reviewed for nanosystems.[188] Cysteine is non-toxic and both S-H and S-S groups (where proximal cysteines form di-sulphide bridges) bond to Au.[191] Examples of genetic modification to specifically introduce additional cysteine sequences into proteins to act as Au immobilisation sequences has also been investigated. For example, in the development of an antibody piezoimmunosensor, a cysteine residue was added to act as a linker for the antibody sequence, which immobilised onto Au with controlled orientation forming a dense monolayer at the Au surface. The dense array of available antigen-binding sites displayed a higher selectivity and sensitivity as an antigen sensor compared to the unmodified antibody.[195]

A piezoelectric quartz crystal biosensor has also been developed which utilises the glucose/galactose receptor of *Escherichia coli*. To immobilise the protein onto the Au surface, two genetically engineered versions of the receptor were created, each with a single cysteine addition into the amino acid sequence, resulting in different protein orientations upon immobilisation.[196] Controlling the orientation of proteins upon immobilisation is a powerful facet of the Au-cysteine immobilisation system.

Immobilising the protease subtilisin BPN' (a protein digesting enzyme from *Bacillus subtilis*) by introducing a cysteine residue to form tiol bonds to gold has also shown improved enzyme activity compared to the unmodified enzyme.[197] In this case the cysteine was introduced by mutation away from the active site of the enzyme so that upon immobilisation *via* the Au-S linkage an ordered two-dimensional array of enzymes formed. By design, the active site of the enzyme was positioned to allow easy substrate access once the Au-thiol bonds had formed. Compared to the unmodified enzymes which bound with random orientation at the surface, the site-specific cysteine modified enzymes displayed a significantly higher specificity constant ($42.9 \pm 2.8 \times 10^{-3}$ $M^{-1}s^{-1}$ c.f. $12.8 \pm 1.1 \times 10^{-3}$ $M^{-1}s^{-1}$).[197]

Protein G from *Streptococcus* is a cell surface protein which binds antibodies and is of interest for immunoassays. An investigation into its immobilisation onto Au for sensor development studied the use of a cysteine tag (Cys-tag) to bind the protein to an Au surface and onto Au nanoparticles.[198] Between one and five cysteine amino acids were added to the N-terminus of the sequence, away from the antibody binding site, to act as a preferential bonding sequence to Au. Expression of the proteins showed that when four and five consecutive cysteine residues were added to the sequence the protein could only be isolated in multimeric form, so only proteins with one, two and three additional cysteine amino acid residues were investigated. The Cys-tagged proteins formed ordered layers over gold surfaces and gold nanoparticles *via* the introduced cysteines at the N-terminus, with higher densities than the non-Cys-tagged proteins. The immobilised Cys-tagged proteins showed enhanced antibody binding activity, attributed to the controlled orientation of immobilisation, with activity retained after multiple antibody stripping.[198]

1.5.2 Incorporating a cysteine sequence into nitroreductases

The introduction of a cysteine sequence into a protein for immobilisation onto an Au substrate with controlled protein orientation appears to be a practical method of generating gold:protein bioconjugates.[195-198] However the self-assembly of proteins *via* the introduced cysteine after the addition of just a single cysteine residue suggests that if there are naturally occurring cysteine amino acids within a given protein sequence there is potential for immobilisation to occur *via* the natural cysteine as well as the artificially introduced residue. In addition, if the bioconjugate is exposed to other cysteine containing proteins, as would occur in a physiological environment, there is potential for surface exchange where other cysteine containing moieties with a preferential binding sequence displace the original protein.

To ensure the introduced Cys-tag becomes the preferential binding site for immobilisation a consecutive series of six cysteine sequences can be incorporated into an NTR sequence similar to His_6-tag immobilisation. In a previous study by Gwenin *et al.* this was shown to be an effective route to immobilise proteins onto Au in the development of an amperometric biosensor for the detection of explosives.[199] Following on from this study a similar approach could be utilised in the immobilisation of nitroreductases onto inorganic substrates for the application in a directed enzyme prodrug therapy.

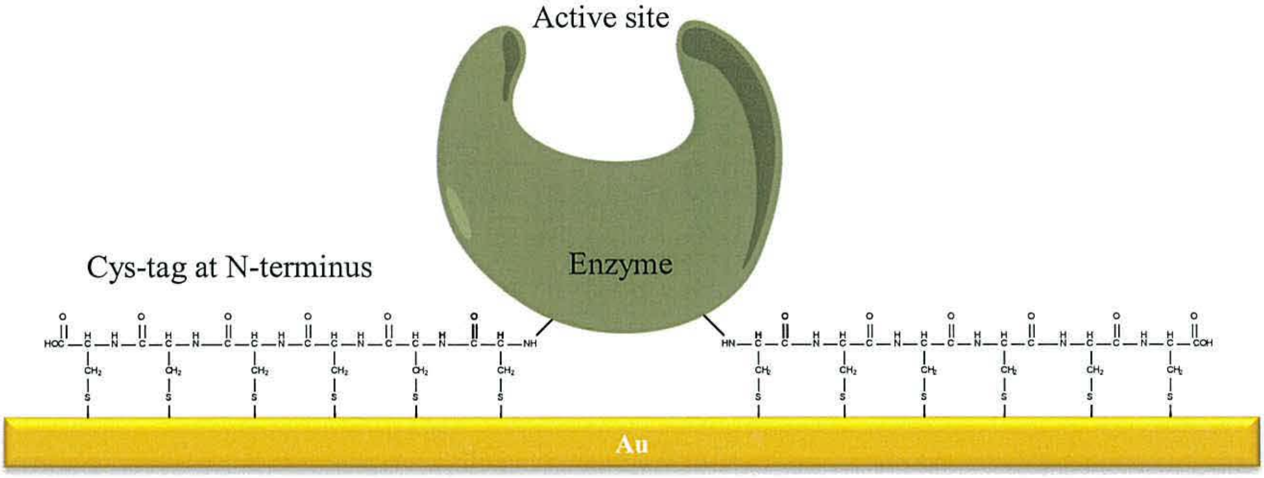

Figure 1.5.1. Illustration showing a consecutive sequence of six cysteine residues in each monomer unit of a homodimeric enzyme enabling immobilisation with controlled orientation onto a flat Au substrate via Au-S bonds.[199]

Figure 1.5.1 shows an illustration of a consecutive sequence of six cysteine residues in each monomer unit of a homodimeric enzyme enabling immobilisation with controlled orientation onto a flat Au substrate *via* Au-S bonds.[199] A similar approach could be used for NTRs to conjugate them onto the curved surfaces of nanoparticles. The illustration shows that adding the Cys-tag to the N-terminus allows the amino acids to access the Au surface, while theoretically not significantly altering the native enzyme structure.

NTRs may reduce a wide range of nitroaromatic compounds and are of interest for application in bioremediation, nitroaromatic detection, biocatalysis, and biomedicine.[200] The specificity constant of an NTR with CB1954 is an important kinetic parameter to consider in developing a magnetically controllable DEPT which has high efficacy in human patients. Currently there are a number of enzymes which have been identified as being active with some nitroaromatic compounds but have yet to be trialled with the prodrug.

An example of this is the recent identification of three novel NTRs from *Bacillus licheniformis* which have an amino acid structure around the FMN site of enzymes homologous to NTRs with known activity to nitroaromatics, but until recently had yet to be isolated and trialled with any substrates.[201] Not only did the previously uncharacterised enzymes show activity to a range of nitro-containing explosives, it was shown that the enzymes could retain activity to the explosives in free solution after addition of a His_6-tag or a Cys-tag, where six consecutive cysteine residues were added to the N-terminus of each monomer using recombinant DNA methods.[201]

Identifying putative enzymes from gene sequences allows proteins of similar and dissimilar structures from different bacterial species to be identified and assayed with substrates of interest. In this case the enzymes *yfkO*, *nfrA1* and *nfrA2* from *B. Licheniformis* are homologues of *E. coli K12 nfnB*, *Pseudomonas putida JLR11pnrA* and *Bacillus subtilis subsp. subtilis strain 168 ycnD,* respectively. Their activity in reducing nitro-groups of explosive compounds suggests they may also be of interest in DEPT and determining their activity with CB1954 and comparing this to other NTRs which have previously been assayed with the prodrug will allow NTRs with superior kinetic parameters (K_{cat}, K_m, V_{max}, specificity constants, thermal and pH stabilities) towards the prodrug to be identified. The crystal structure of the *E. coli* NTR *ydjA* was also recently elucidated[202] and it appears to have a very flexible and therefore accommodating structure around the active site.[202] As CB1954 is not a natural substrate to NTRs this is potentially advantageous for a high turnover as CB1954 should be able to enter and vacate the active site very rapidly.[202]

1.5.3 Gold coated iron oxide nanoparticles for nitroreductase immobilisation

Surface modification of iron oxide nanoparticles is necessary for biomedical application as the particles flocculate without suitable surface functionalisation. [152, 203-205] Gold is biocompatible, has low chemical reactivity and provides colloid stability as well as a compatible bonding surface for biological compounds.[204] This has made the coating of iron oxide nanoparticles with gold an area of interest and research has been undertaken to synthesise core/shell magnetic/gold nanoparticles.[206]

One such approach is the use of a reverse micelle process to generate nanoparticles potentially offers control over the size and morphology of the particles as the micelles act as a template. The particles synthesised from a micellar solution depend on solvent type, surfactant/co-surfactant type, concentration of the reagents, ionic additives and the ratios of solvent/surfactant.[207] A reverse micelle method has been developed to create Fe@Au nanoparticles which is also applicable for Au coated iron oxide particles[208-210] where a solution of $FeSO_4$, cetyltrimethylammonium bromide (CTAB) and 1-butanol in octane is mixed with the same micellar solution containing $NaBH_4$ which acts as a reducing agent to create iron/ iron oxide nanoparticles (< 20 nm) within the confines of the aqueous micelles. The micelle size is then expanded by mixing with a CTAB/1-butanol/octane solution altering the surfactant ratio, first containing $HAuCl_4$ and then a second reducing agent such as $NaBH_4$ which reduces the gold salt onto the Fe surface within the expanded confines of the micelle. The use of a micelle method controls the size and morphology of the resulting gold coated magnetic particles including the Au thickness. However the experimental procedure is not facile, involving organic solvents such as octane and surfactants such as 1-butanol and CTAB which need to be removed prior to enzyme adsorption and the particles must be transferred from an organic solvent to an aqueous solution.[211] The potential control offered by such a synthesis, and indicated in the literature, makes the procedure attractive for utilisation in this work. However the additional steps needed to transfer the particles from different solvents and ensure surfactants, co-surfactants and organic solvents are removed make an aqueous synthesis practically more convenient.

Many examples of syntheses which create iron oxide cores with an Au surface coating involve the use of capping agents, which rapidly bind to the particle surface after nucleation and growth to control the particle size and morphology.[212] Thioalkanes are commonly used capping agents for Au coated particles as they control particle growth and stabilise the resulting colloids.[213-215] For application in DEPT however, if the Au coated particles are already thiolated, immobilisation of cysteine modified NTRs *via* self-assembly may not be possible. This is because the Au surface would already contain a layer of bound cysteine residues, so the cysteine modified NTRs would not be able to access the Au to form a self-assembled monolayer.

It is also common to synthesise the particles in solvents or use toxic reagents, meaning extensive washing and phase transfers must be performed to ensure the final colloid is biocompatible,[216] stable in aqueous solution and that the Au surface is available for cysteine self-assembly.[188] Of the many syntheses which have been developed to create hybrid nanoparticles[217] the strategies which are of most interest for Au coated iron oxide nanoparticles for NTR immobilisation are those performed in aqueous solution, with no organic solvents, toxic reagents or strongly bound capping agents utilised at any stage.

Procedures such as the boiling citrate method to reduce $HAuCl_4$ onto pre-synthesised iron oxide cores in aqueous solution[218] or the iterative hydroxylamine seeding approach which uses hydroxylamine to do so are highly suited for application in DEPT.[219]

1.6 Concluding remarks and aims of this study

The efficacy of DEPT that are currently being trialled[44] is low and the treatment is in need of improvement,[44] one of the areas that are limiting the success of the therapy is the reduction of CB1954 by *nfnB*. The NTRs *yfkO*, *nfrA1* and *nfrA2* from *B. Licheniformis* along with *ydjA* from *S. typhimurium* have been identified as potential candidates for the therapy.[201, 202] The enzymes will be cloned, genetically modified, over-expressed, assayed with CB1954 and compared to NTRs that have previously been characterised with CB1954 in the literature, the aim being to identify an NTR with superior catalytic properties.

The currently employed strategy of transducing tumour cells with genetically modified viruses containing the material necessary for the cells to produce NTRs can also be improved. Genetic modification of the candidate NTRs will include the incorporation of a preferential binding sequence to Au utilising cysteine. Both the non-cysteine modified and cysteine modified NTRs will be assayed with CB1954 and the capability of the enzymes to immobilise onto Au determined. The viability of developing a system that allows the NTRs to be conjugated to magnetic nanoparticles will also be explored, the aim being to develop a magnetically controllable DEPT which allows the NTRs to be manipulated magnetically.

Chapter 2

EXPERIMENTAL METHODS

2.1 Cloning and nitroreductase generation

Introduction to cloning

Nucleotides are monomeric units which bond together to form nucleic acids, they are phosphate esters of pentoses containing nitrogenous heterocycles and bind to form both deoxyribonucleic acids (DNA) and ribonucleic acids (RNA). The bases are bound to C_1' of the ribose structures and are analogues of purine and pyrimidine. For DNA, these bases are adenine (A), cytosine (C), guanine (G) and thymine (T). For RNA, thymine is replaced by uracil (U) which is an unmethylated analogue of thymine. The bases are illustrated in *Figure 2.1.1* which shows a short nucleic acid sequence.[71]

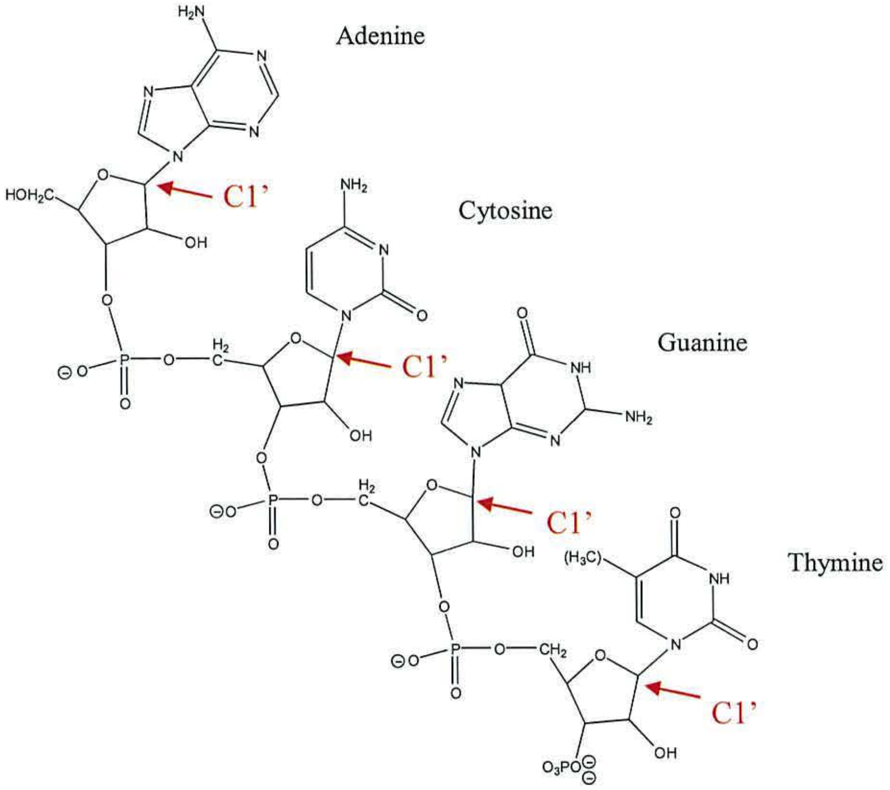

Figure 2.1.1. A short nucleic acid sequence showing the four DNA bases adenine, cytosine, guanine and thymine

Nucleic acids are polymers of nucleotides bound from 5' to 3' (C_5 to C_3 of the ribose) through a bridging phosphate group. DNA is double stranded meaning each polymer chain is linked to a second polymer chain through hydrogen bonding which occurs between the aromatic bases. This creates a helical structure, first proposed by Watson and Crick.[220] The conformation is such that G always binds to C and A to T creating a core of complimentary paired stacked bases and a periphery of coiled sugar-phosphate chains. This is illustrated in *Figure 2.1.2.*[71]

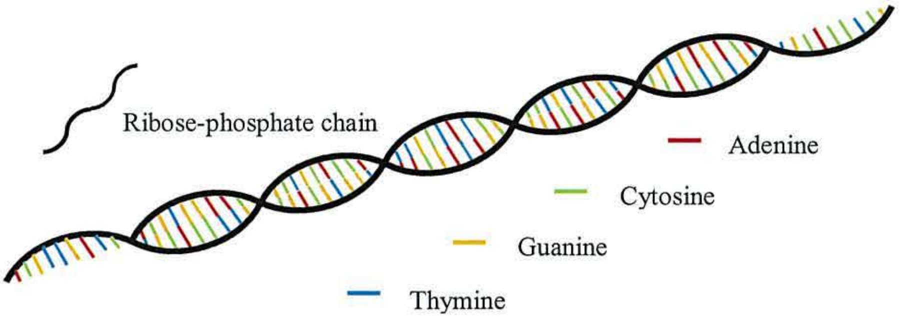

Figure 2.1.2. An illustration showing the helical structure of DNA and complimentary H-bonding between bases.[71]

The biosynthesis of proteins occurs through transcription of a protein coding gene in a DNA sequence, which creates a complimentary base pair sequence of messenger RNA (mRNA).[71] The template strand of DNA is transcribed from 3' → 5' enzymatically by RNA polymerase, creating a single mRNA strand identical to that of the coding DNA strand but with uracil in place of thymine and riboses in place of deoxyriboses. This is a highly complex process which is controlled in prokaryotes by activators and repressors and in eukaryotes by transcription factors; the rate of mRNA transcription controls the rate of protein biosynthesis. The process of transcription is illustrated in *Figure 2.1.3.*[71]

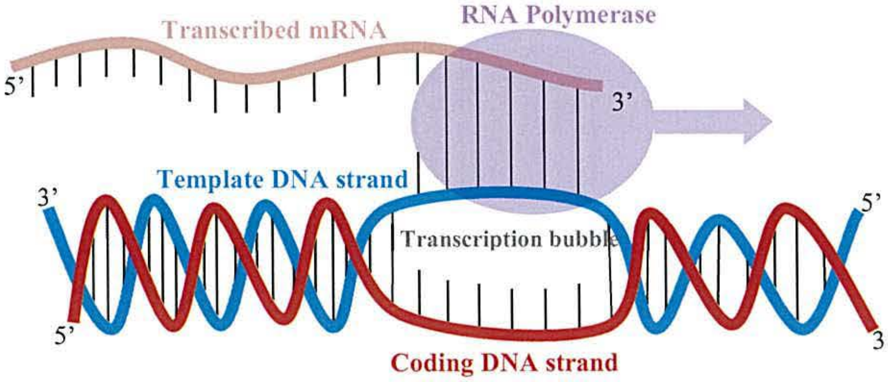

Figure 2.1.3. An illustration of the transcription process where RNA polymerase transcribes a DNA sequence.[71]

The synthesis of polypeptides occurs at ribosomes which are complexes made of ribosomal RNA and ribosomal proteins.[71] One unit of a ribosome binds to mRNA while the second facilitates the binding of transfer RNA (tRNA) molecules to the mRNA strand. Aminoacyl-tRNA contains a covalently bound α-amino acid at its 3' as well as a sequence of 3 complimentary bases to those coded for in mRNA.[71] Each triplet code in mRNA is known as a codon and its complimentary sequence in tRNA an anticodon. Translation occurs through incoming aminoacyl-tRNA molecules binding *via* an anticodon to a codon of mRNA, where the ribosome catalyses the nucleophilic substitution of the bound amino acid onto the synthesised polypeptide chain of the adjacent bound peptidyl-tRNA.[71] The peptidyl-tRNA essentially passes on the polypeptide to the adjacent tRNA in the ribosome and is released from the mRNA strand picking up a proton. The ribosome moves down the mRNA strand toward its 3' and the process repeats. A schematic illustration of translation is shown in *Figure 2.1.4.*

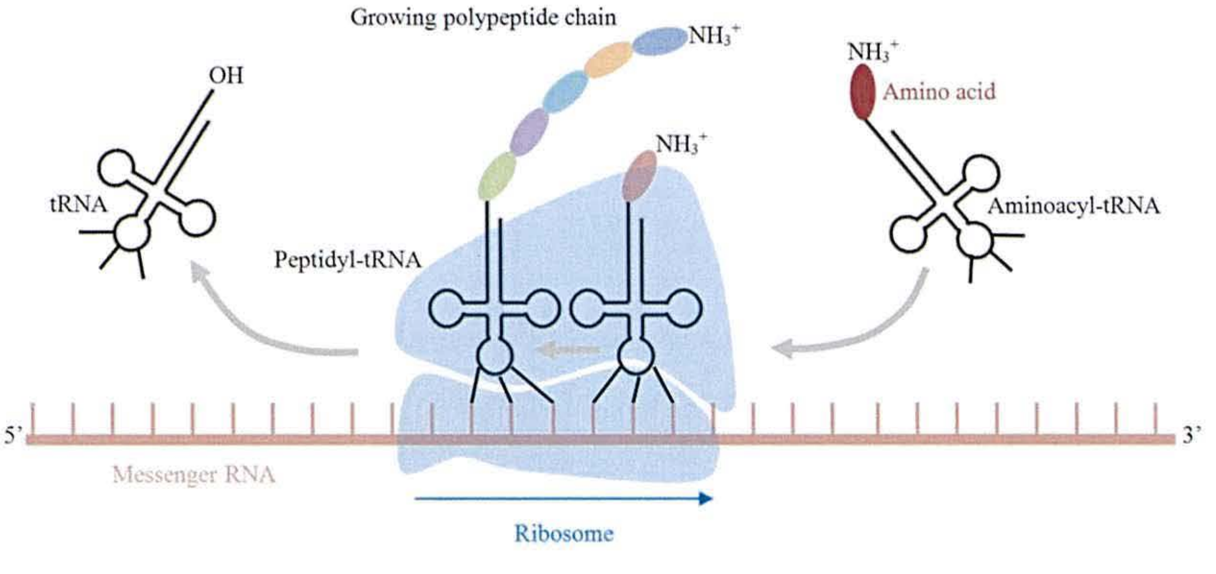

Figure 2.1.4. Illustration of mRNA translation via ribosome bonding amino acid monomers to form a polypeptide chain.[71]

There are 4 possible DNA base combinations, with each codon representing 1 unit of code, which means there are 64 possible combinations. 61 of these combinations code for the 20 amino acids shown in *Table 2.1.1* and the remaining 3 combinations cause the ribosome stop adding amino acid monomers and release the polypeptide chain.[71] A table of the codon combinations and the amino acids they code for is. The combination of bases in a sequence (and the corresponding RNA sequences and α-amino acids they represent) is known as the genetic code and is common to nearly all known life on earth. This also means genetic material from one organism can be transcribed and translated in another and is the foundation of molecular cloning and recombinant DNA techniques.[71]

Table 2.1.1. A table showing the combinations of RNA bases and the amino acids these are translated to via ribosome. The 1st 2nd and 3rd bases represent a triplet code for the twenty amino acids displayed, as well as a sequence which initiates translation (AUG) and three sequences which end translation (UAA, UGA and UAG).[71]

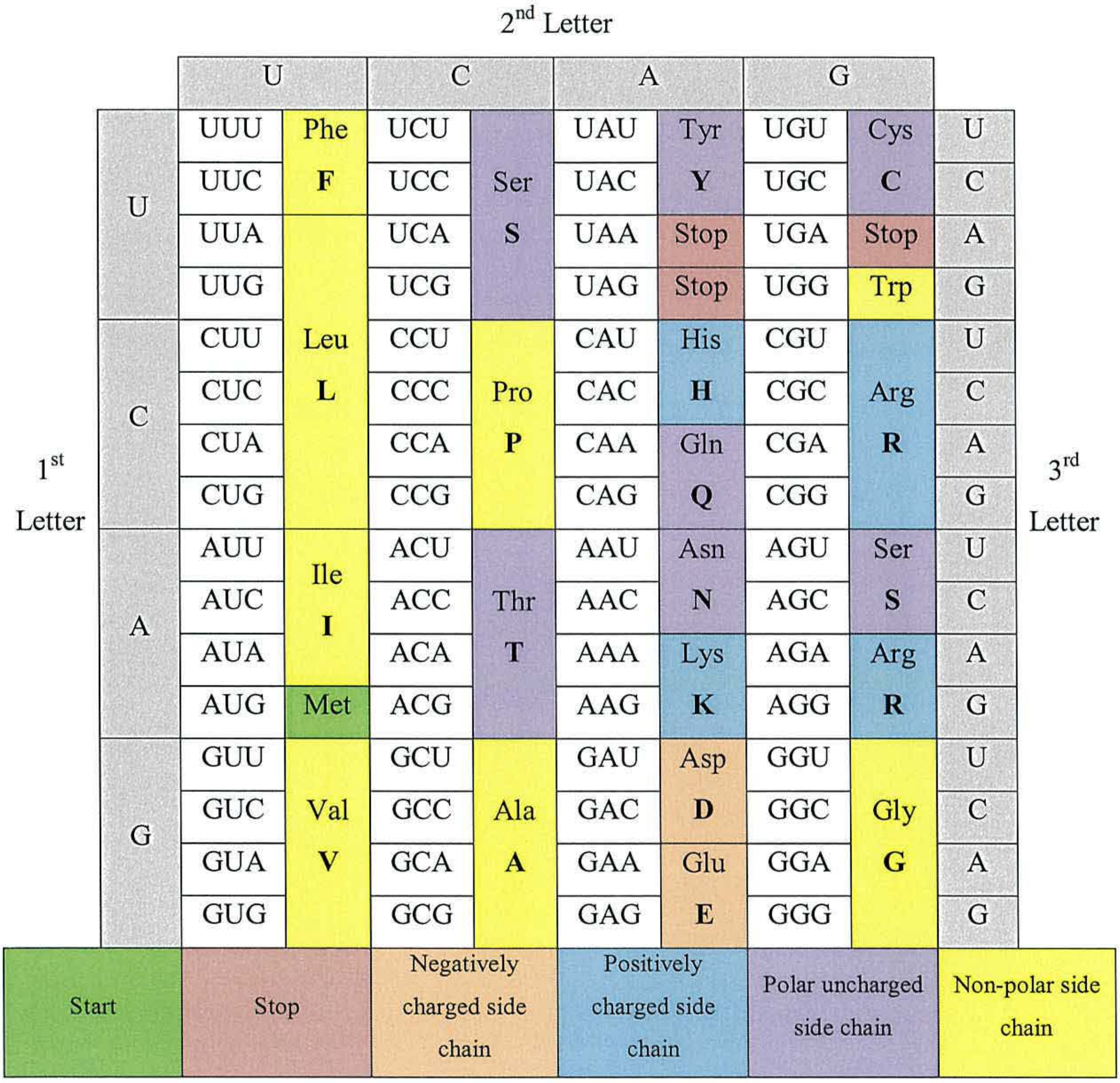

2nd Letter

1st Letter	U		C		A		G		3rd Letter
U	UUU	Phe	UCU		UAU	Tyr	UGU	Cys	U
	UUC	**F**	UCC	Ser	UAC	**Y**	UGC	**C**	C
	UUA		UCA	**S**	UAA	Stop	UGA	Stop	A
	UUG		UCG		UAG	Stop	UGG	Trp	G
C	CUU	Leu	CCU		CAU	His	CGU		U
	CUC	**L**	CCC	Pro	CAC	**H**	CGC	Arg	C
	CUA		CCA	**P**	CAA	Gln	CGA	**R**	A
	CUG		CCG		CAG	**Q**	CGG		G
A	AUU	Ile	ACU		AAU	Asn	AGU	Ser	U
	AUC	**I**	ACC	Thr	AAC	**N**	AGC	**S**	C
	AUA		ACA	**T**	AAA	Lys	AGA	Arg	A
	AUG	Met	ACG		AAG	**K**	AGG	**R**	G
G	GUU		GCU		GAU	Asp	GGU		U
	GUC	Val	GCC	Ala	GAC	**D**	GGC	Gly	C
	GUA	**V**	GCA	**A**	GAA	Glu	GGA	**G**	A
	GUG		GCG		GAG	**E**	GGG		G

Start	Stop	Negatively charged side chain	Positively charged side chain	Polar uncharged side chain	Non-polar side chain

Biosynthesis can be replicated *in vitro* to produce proteins of interest, this is discussed in section 2.1.1. Translation is initiated following a promoter sequence (AUG), subsequent AUG codons produce methionine amino acids until the ribosome reaches a stop codon, which ends protein synthesis. The sequence of DNA bases can therefore be altered to introduce new amino acids into a protein sequence, or change existing amino acids. The chemical structures of the 20 standard amino acids and their abbreviations are shown in *Figure 2.1.5.*

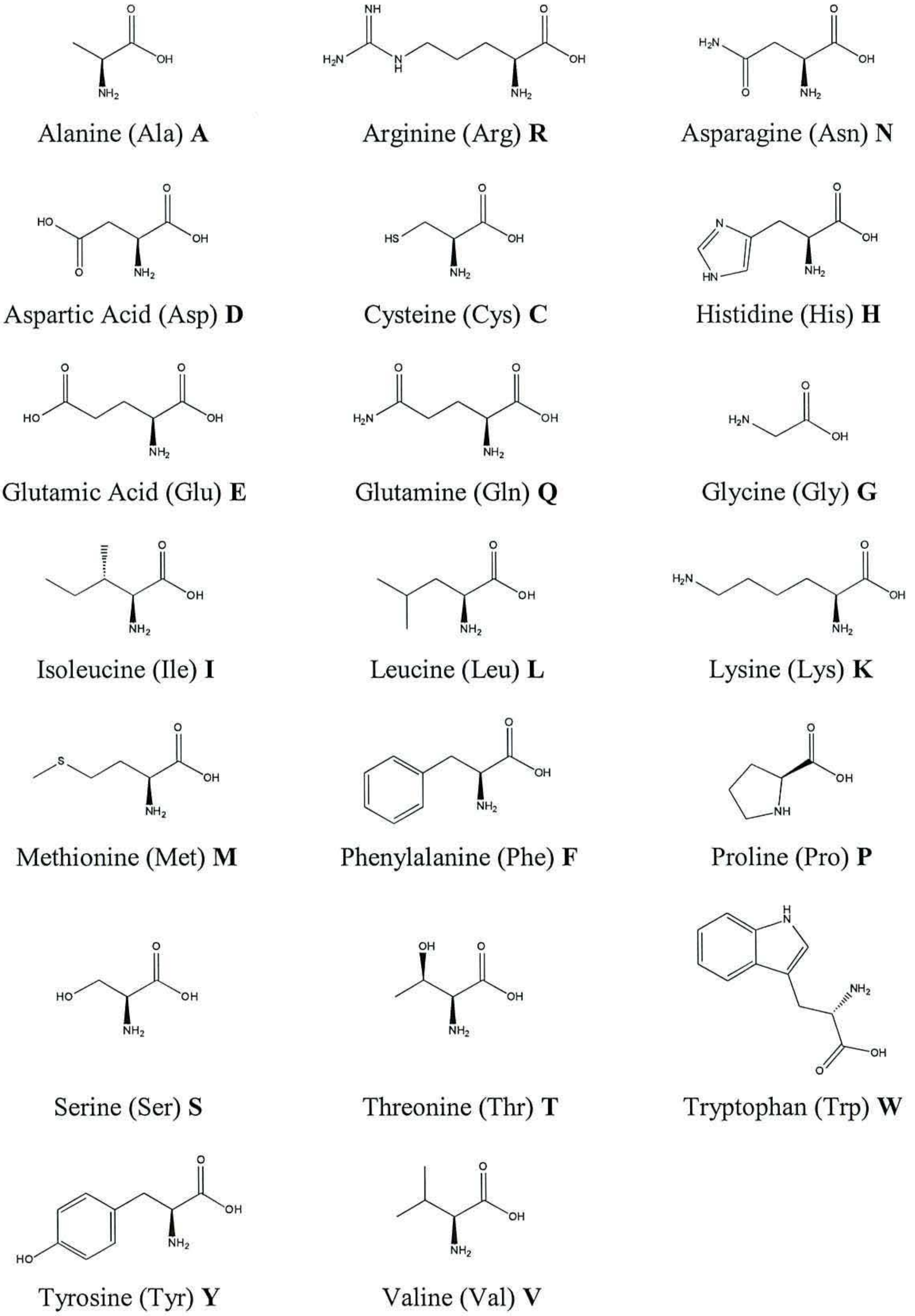

Alanine (Ala) **A**

Arginine (Arg) **R**

Asparagine (Asn) **N**

Aspartic Acid (Asp) **D**

Cysteine (Cys) **C**

Histidine (His) **H**

Glutamic Acid (Glu) **E**

Glutamine (Gln) **Q**

Glycine (Gly) **G**

Isoleucine (Ile) **I**

Leucine (Leu) **L**

Lysine (Lys) **K**

Methionine (Met) **M**

Phenylalanine (Phe) **F**

Proline (Pro) **P**

Serine (Ser) **S**

Threonine (Thr) **T**

Tryptophan (Trp) **W**

Tyrosine (Tyr) **Y**

Valine (Val) **V**

Figure 2.1.5 The chemical structures of the standard 20 amino acids

2.1.1 Recombinant DNA techniques

The manipulation of genetic material to biosynthesise proteins is facilitated using polymerase chain reactions (PCR).[221] This *in vitro* technique mimics the biosynthesis of proteins utilising replicated DNA sequences from specific genes from the genomic DNA of an organism, [221] this is further outlined in this section and illustrated in *Figure 2.1.6* and Figure *2.1.7.* DNA amplification (the amplification of a DNA sequence) uses the PCR to increase a few copies of a particular DNA strand or sequence to several million copies in a few hours. The process uses thermally stable DNA polymerase (DNAP), a DNA template, oligonucleotide sequences that bracket and compliment the sequence of DNA for amplification (primers), deoxynucleoside triphosphates (dNTPs) and divalent cations (commonly Mg^{2+}).[221] The reaction allows a target gene within the genomic DNA of an organism to be amplified many times over by denaturing the double stranded DNA at elevated temperatures then cooling the reaction to allow the primers to anneal to the template DNA. The thermally stable DNAP is then able to synthesise a complimentary strand of DNA to the template from the primer onwards using the available dNTPs. By thermally cycling the reaction mixture the process repeats and many copies of a target sequence can be generated in a very short time period. An illustration of the PCR method is shown[221] in *Figure 2.1.6.*

PCR is an extremely powerful technique as it allows target sequences such as genes from the DNA of any organism to be amplified to a high concentration, these genes can then be inserted into cloning vectors which allow the gene to be expressed as a protein. Based upon naturally occurring plasmids, vectors are circular double stranded DNA molecules which operate independently of chromosomal DNA, genes can be inserted into cloning vectors using restriction endonucleases and ligases.[221]

Restriction endonucleases are enzymes which cut specific DNA sequences and a variety of restriction sites are coded for in cloning vectors downstream of an inducible promoter sequence so that vectors can be cut open for genes to be inserted.[221] These restriction sites can be added into the target genes during PCR by incorporating the restriction sequence into the primers, the gene and vector can be cut using the respective restriction endonucleases and using a ligase the gene can be inserted into the vector. The modified vector containing the gene sequence is then amplified by growing selectively in a non-expression host in an antibiotic environment, ensuring only cells which contain the vector which contains antibiotic resistance will grow, yielding a concentrated solution of vectors containing the inserted gene. An illustration of the cloning process is shown in

Figure 2.1.7. In this work cloning is used to produce nitroreductases and modified nitroreductases which include a Cys-tag for immobilisation onto Au.

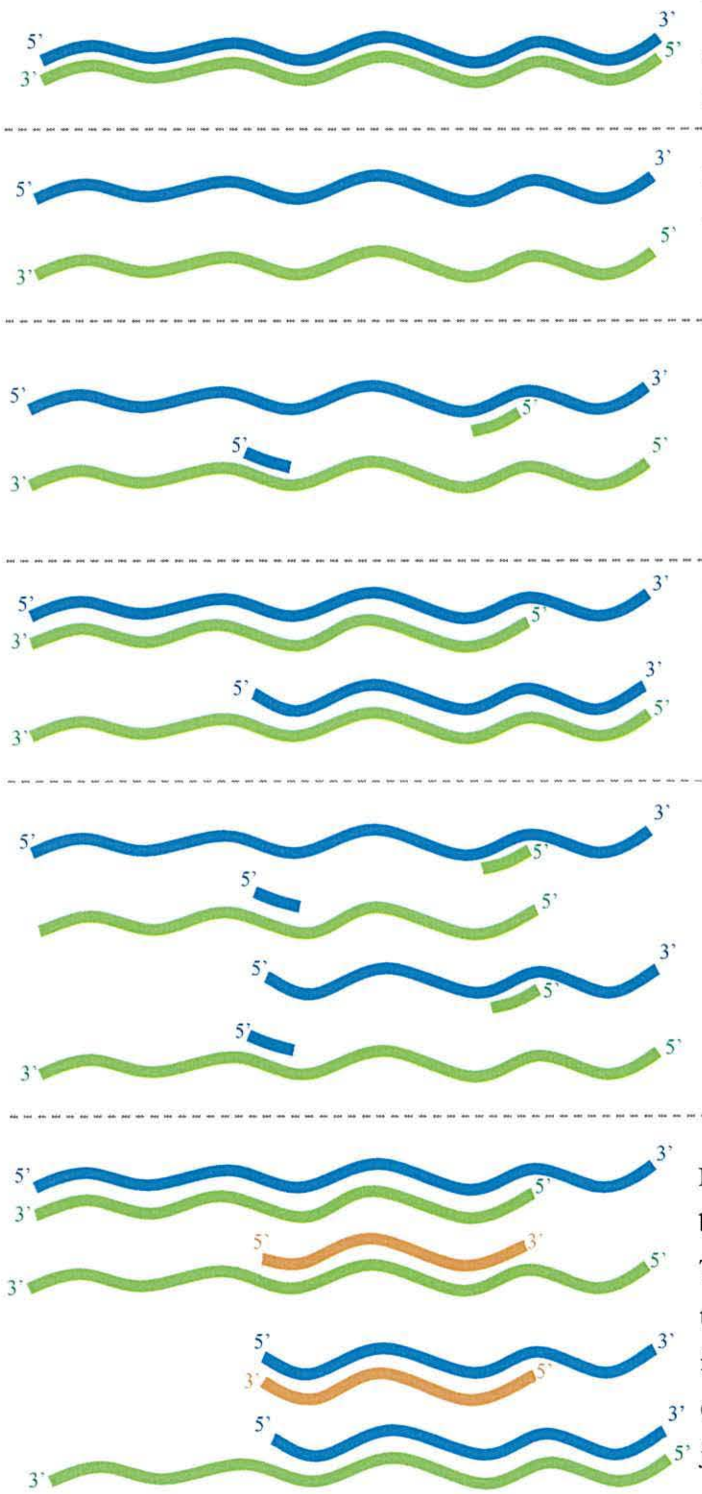

Template DNA is placed in a buffer solution with dNTPs, primers, DNAP and Mg^{2+}

Denaturation: Heating of the PCR to ~95°C causes denaturation of the double stranded template DNA

Annealing: Cooling of the PCR to a few degrees below the melting temperature of the primers allows them to bind to the specific sites they are complimentary to in the template DNA

Extension: DNAP extends the primers from the 3' using complimentary dNTPs to the template strand creating copies of the template DNA from each primer onwards.

The process is repeated and primers anneal upon cooling after denaturation

Elongation occurs and the region that is bracketed by primers is copied. Theoretically with each temperature cycle the sequence between the primers doubles in concentration yielding millions of copies of the desired DNA sequence in just a few hours

Figure 2.1.6. An illustration of a polymerase chain reaction (PCR) showing the amplification of a target DNA sequence by thermal cycling with a temperature stable DNA polymerase.[71, 221]

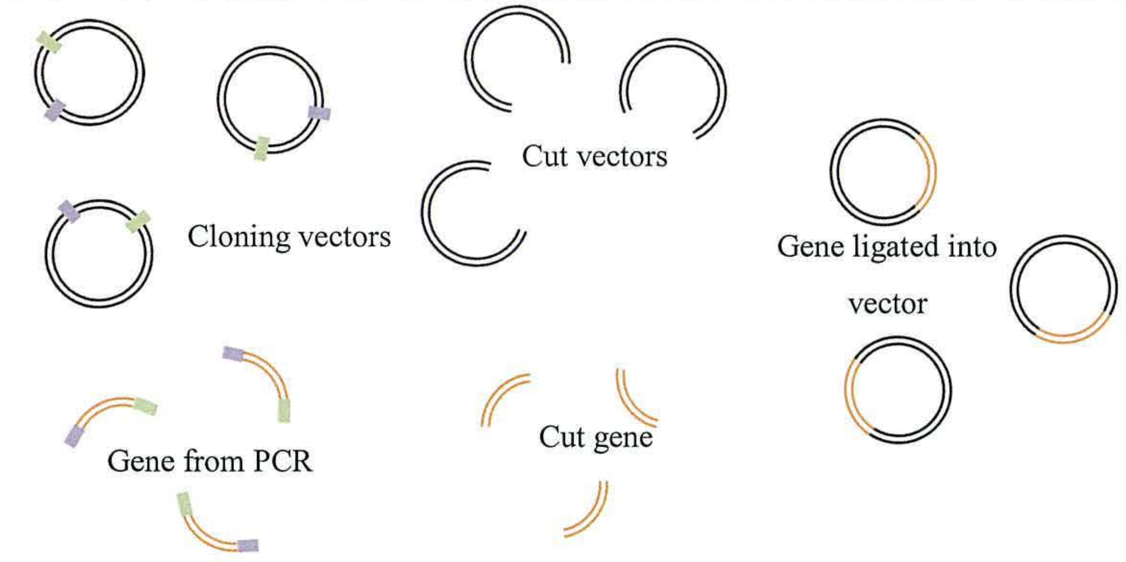

The vector contains a variety of restriction sites including X and Y. These sites are incorporated into the gene using the PCR primers

Restriction enzymes are used to cut the DNA at X and Y, leaving compatible ends between gene and vector

DNA ligase is used to bond the gene into the vector. The vector also provides antibiotic resistance to a specific antibiotic

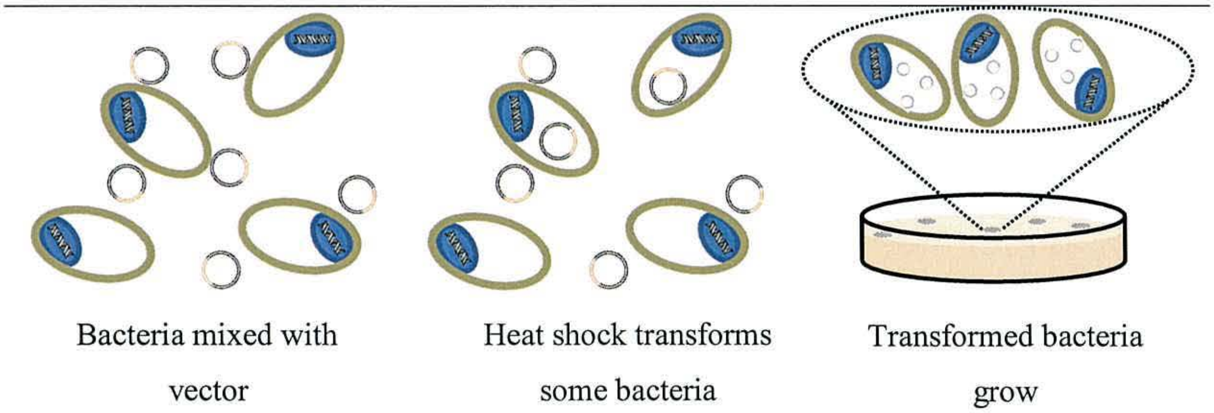

Vectors containing the gene are incubated on ice with a non-expressing bacterial host

The bacteria and vector solution is heated to 42 °C for 30 seconds, some of the vectors pass into the bacteria

The bacteria are grown in an antibiotic environment which the vector is resistant to. Only the bacteria with the vector grow

Figure 2.1.7 An illustration showing the cloning process. Once bacteria have been grown which contain the vector and gene the DNA can be isolated, purified and stored.

Figure 2.1.6 and *Figure 2.1.7* are illustrations of PCR and the cloning process, which are used in this research to produce nitroreductases and modified nitroreductases to assay their activity with the prodrug CB1954.

2.1.2 Protein expression

Recombinant vectors containing the gene insert can be transformed into expression hosts, unlike non-expressing hosts used to multiply the number of vectors without transcribing the gene, expression hosts possess all the biological tools necessary to synthesise the protein.[222] Proteins may be over-expressed by the action of a promoter sequence upstream of the gene which has a high affinity for RNA polymerase, causing the gene sequence to be produced in excess. The *lacUV5* promoter used in the pET expression vectors controls the T7 RNA polymerase site and only when isopropyl β-D-1-thiogalactopyranoside (IPTG, an analogue of allolactose) is present is expression activated.[223]

A purification sequence such as the His-tag system allows the proteins to be isolated from the cell free extract using immobilized metal-ion affinity-chromatography,[180] where the vector adds a sequence of 6 histidine residues to the end of the amino acid sequence so that the monomers bind to immobilised nickel. The nickel column is washed to remove all other molecules leaving only the immobilised over-expressed protein of interest, which is eluted using imidazole and then separated from the imidazole using a de-salting column.

2.1.3 Experimental methods for nitroreductase production

Unless otherwise stated the protocols and reactions for the recombinant DNA techniques used in the NTR synthesis followed the standard literature provided by the distributors for the DNA purification kits, restriction reactions, ligations, over expressions and protein purifications. From Promega were purchased; restriction enzymes (RE) and their respective buffers, T4 DNA ligase and respective buffer, from Novagen; pET-28a(+) vector, from GE Lifecare Health Sciences; HiTrap chelating column, PD-10 desalting column, from ProPure; Biuret Protein Assay Reagent, from LAB M; tryptone, yeast extract, LAB 12 Sensitivity Test Agar, from Fisher Scientific; pipette tips, bromophenol blue, from Sigma Aldrich; sodium dodecyl sulphate (SDS), KH_2PO_4, K_2HPO_4. Luria-Bertani (LB) broth was used as a growth media and comprised 10 gL^{-1} tryptone, 5 gL^{-1} yeast extract and 10 gL^{-1} sodium chloride. Agar plates were made using 40 gL^{-1} agar with dH_2O and for selective growth 50 μgml^{-1} kanamycin was added. Typically agarose gels were 1 % mass agarose to Tris/Borate/EDTA (TBE) buffer which comprised 45 mM tris, 45 mM boric acid and 1 mM EDTA.

PCR and cloning of NTRs

Primers were designed to include restriction sites compatible with the pET-28a(+) vector (Novagen, see the *Appendix*) to each end of the gene during PCR, ensuring the restriction site did not also occur naturally in the gene sequence.

Table 2.1.2. The primers for each of the genes. 1 and 3 are the forward and reverse primers respectively, incorporating only a restriction site. 2 is the corresponding forward primer with an additional sequence coding for 6 cysteine residues (highlighted in purple).

Gene	**Primer 5' – 3'**	**Restriction site**
yfkO	**1)** GGAGAGGATCCAATATGACAGAG CAATCC	*Bam*HI and *Hind*III
	2) GGAGAGGATCCTGTTGCTGTTGCTGTTGCAATATGACAGAGCAATCC	
	3) ACCGCAAAGCTTTTATTCGACCCATTTCAC	
nfrA1	**1)** AGGA GGATCCAGGATGAATAAAACGATTGAAA	*Bam*HI and *Sal*I
	2) AGGAGGATCCTGTTGCTGTTGCTGTTGCAGGATGAAAAAACGATTGAAA	
	3) GGGGAGTCGACTTACCTTTTGTTCAAA	
nfrA2	**1)** AGGATGGATCCCTAATGAATGAAGTATTGA	*Bam*HI and *Hind*III
	2) AGGATGGATCCTGTTGTTGTTGCTGTTGCCTAATGAATGAAGTATTGA	
	3) AGCCTAAAGCTTCTATTCGAGTTTAAATCC	
ydjA	**1)** CTGGAGGATCCCAAATGGATGCACTAGAA	*Bam*HI and *Hind*III
	2) CTGGAGGATCCTGTTGCTGTTGCTGTTGCCAAATGGATGCACTAGAA	
	3) TATCCCAAGCTTTCAGAAATAACGCACAAA	

Bacillus Licheniformis ATCC 14580 was grown overnight at 37 °C on nutrient agar to produce a series of opaque, flat, non-symmetrical colonies. Single separate colonies were selected and grown overnight on a test tube shaker in 5 ml Luria-Bertani (LB) broth, 1 ml aliquots of each were isolated and the genomic DNA extracted (Promega – Wizard Genomic DNA Purification Kit).[224] The genomic DNA of *Salmonella enterica subsp. enterica serovar Typhimurium str. LT2* was kindly supplied by Dr. Suhad Mohammad, Bangor University, Gwynedd, UK. PCR was used to amplify the respective genes using the following (dilutions made with ultra pure water (UPW)); 1 μl 10 % genomic DNA solution, 1.5 μl 10 % forward primer, 1.5 μl 10 % reverse primer, 1 μl DNA polymerase, 3 μl 25 mM $MgSO_4$, 5 μl 10X buffer, 5 μl 2 mM dNTPs, 32 μl UPW. PCR cycling conditions were 95 °C 5 min, 15 cycles of 94 °C 1 min, 68–58 °C 1 min, 72 °C 1 min, followed by 25 cycles of 94 °C 1 min, 58 °C 1 min, 72 °C 1 min with a final extension of 72 °C for 10 min. Ethidium bromide stained 1 % agarose gels (1 g Agarose, 100 ml TBE buffer, 2 μL ethidium bromide) were run at 100 mA in TBE buffer and visualised under UV light to confirm success of PCR.

The PCR products were purified (QIAquick PCR Purification Kit)[225] and corresponding restriction enzymes used to cut the gene and pET-28(+) vector, the restriction enzymes were deactivated and gene inserted into the vector. 1 μl T4 DNA ligation buffer, 0.7 μl UPW with 0.3 μl T4 DNA ligase added and the gene/vector solution incubated at approximately 16 °C overnight. This same process was utilised to insert the non-Cys-tag gene sequence into a modified pET-28(+) vector which contained a cysteine sequence downstream of the His-tag at the thrombin region of the vector sequence. There were therefore 3 types of vector constructed for each of the genes, non-Cys tag, Cys-tag from vector (Cys #1) and Cys-tag from primer (Cys #2).

After ligation a digestion was performed at the *Eco*RI site of the vector which sits between the two restriction sites used for gene insertion, using 1 μl *Eco*RI RE and 1 μl 10X Multicore buffer at 37 °C for 1 h, ensuring any self-ligating vectors are cut and therefore not transformed in hosts. 100 μl competent *DH5α* (non-expressing host) were added to the ligated solution of vector and insert and incubated on ice for 1 h, the solution was heat shocked at 42 °C for 4 minutes, returned to ice for 2 minutes then added to 500 μl LB and left stirring at 37 °C for 1 h.

Agar plates containing 50 μg ml^{-1} kanamycin (KM) (400 ml dH_2O, 16 g LAB 12 STA, 200 μl 100 μgml^{-1} KM) were spread with the transformed DH5α and left overnight at 37 °C. Colonies of DH5α were transferred to 5 ml LB with 50 μgml^{-1} KM and grown with shaking overnight. The produced plasmids were purified using 3 ml of each inoculate (Promega Wizard Plus SV Miniprep – DNA Purification System)[226] and to check the presence of the insert digested at 37 °C for 1 h (the reaction buffers, temperatures and times for all reactions were determined using the literature provided for Promega restriction enzymes)[227, 228] using the following solutions; 2 μl purified plasmid, 1 μl 10X Multicore buffer, 1 μl #1 RE, 1 μl #2 RE, 5 μl UPW along with a control containing no plasmid DNA. The solutions were run on a 1 % agarose gel, using 7 μl of digest with 1 μl loading dye. 2 μl of a successfully modified vector solution were added to 200 μl competent Rosetta, this was incubated on ice for 30 min, heat shocked at 42 °C for 50 sec, replaced to ice for 2 min, added to 400 μl LB and stirred at 37 °C for 45 min. This solution was then plated on 50 μgml^{-1} KM agar plates and grown overnight at 37 °C.

The induction process was scaled up from 5 ml growth solutions to 0.5 L growth solutions, with 5 ml over night cultures added to each vessel and 2 ml 100 mM IPTG (0.4 mM final concentration) used to induce over expression once the absorbance of the cultures reached 0.6 au at 600 nm. After a further 4 h growth the cells from the broth were harvested using centrifugation (7k rpm, 10 min, 4 °C), the cell pellets resuspended in 5 ml 20 mM imidazole buffer (IB) and sonicated thrice for 30 sec (with 30 sec cooling intervals) at 7 amplitude microns. The disrupted-cell solutions were then ultra-centrifuged (35k rpm, 45 minutes, 4 °C) and the CFEs loaded on to prepared nickel chelating columns (GE Healthcare Life Sciences – HiTrap), after washing, the proteins were eluted in 1 ml aliquots in 100 mM, 300 mM and 500 mM IB, and the most concentrated aliquots (2.5 ml total) desalted in an equilibrated PD-10 desalting column (GE Healthcare Life Sciences) and eluted in 0.1 M phosphate buffer comprised of K_2HPO_4 and KH_2PO_4. Samples of each purification were run on SDS-PAGE gels to confirm over-expression of the NTRs.

Standard method sodium dodecyl sulphate polyacrylamide gel electrophoresis (SDS-PAGE) was performed, creating the gels using 3.4 ml dH_2O, 4.0 ml 30 % acrylamide/bis solution (37.5:1), 2.5 ml 1.5 M tris-buffer pH 8.8, 100 μl 10 % SDS and 100 μl 10 % ammonium per sulphate (APS), just prior to setting between plates 15 μl N,N,N',N'-tetramethylethylenediamine (TEMED) was added. The stacking gel was created in the same way except 0.5 M tris-HCl buffer pH 6.8 was used, once polymerisation was complete the gels were submerged into the SDS-PAGE tank in SDS electrophoresis buffer of; dH_2O, 250 mM tris, 1.92 mM glycine and 0.1 % SDS. For total protein analysis of transformed hosts 1 ml aliquots of transformed *E. coli* Rosetta in LB were centrifuged at 13k rpm for 10 minutes and the supernatant discarded, the pellets were resuspended in 200 μl SDS loading buffer comprised of 1 ml dH_2O, 2.5 ml 0.5 M tris-HCl pH 6.8, 2 ml glycerol, 4 ml 10 % SDS, 0.5 ml 0.1 % bromophenol blue with 50 μl ml^{-1} β-mercaptoethanol. The samples were then heated to 95°C for 5 minutes and centrifuged for 2 minutes with 4 μl samples of the supernatant loaded into the gel wells alongside a reference protein ladder and put under 90V for approximately 1 hour. For the purified samples of NTR 2 μl of solution was mixed with the loading buffer before electrophoresis. The gels were then removed and placed into coomassie blue staining baths (1.25 g coomassie blue, 500 ml methanol, 100 ml acetic acid and 400 ml dH_2O) for 30 min followed by destaining with destaining solution (50 ml glacial acetic acid, 100 ml industrial methylated spirits and 350 ml dH_2O) typically overnight.

NTR assays

UV-vis spectroscopy was used to evaluate the activities of the NTRs with CB1954 measuring the absorbance of the reduced product where $\lambda_{max} = 420$ nm and a molar extinction coefficient $\varepsilon = 1200\ Lmol^{-1}cm^{-1}$.[72]

$$A = \varepsilon c l$$

Equation 2.2.01. Beer lambert law. A represents absorbance, ε the molar extinction coefficient, c the concentration and l the path length.[229]

The reactions were performed under different pH and temperatures to determine the optimal environmental conditions for the enzymes and the kinetic parameters calculated by increasing the concentration of prodrug and utilising SigmaPlot to solve for K_M and V_{max}. Enzymatic reactions such as those of NTRs with CB1954 follow Michaelis-Menten kinetics, where at high concentrations of substrate the reaction becomes zero order with respect to substrate and the decomposition of the enzymes-substrate complex becomes the rate limiting step.[71]

$$E + S \underset{k_{-1}}{\overset{k_1}{\rightleftharpoons}} ES \overset{k_2}{\longrightarrow} E + P$$

Equation 2.2.02. E is the enzyme, S the substrate, ES the enzyme substrate complex and P the product.[71]

The velocity of the reaction is therefore given by *Equation 2.2.03*[71]

$$v = \frac{d[P]}{dt} = k_2[ES]$$

Equation 2.2.03.[71]

The rate of production of *ES* is given by the difference between its generation and depletion.[71]

$$\frac{d[ES]}{dt} = k_1[E][S] - k_{-1}[ES] - k_2[ES]$$ *Equation 2.2.04.*[71]

When the substrate is in excess it can be approximated that $[ES]$ remains constant, known as the steady state assumption.[71]

$$\frac{d[ES]}{dt} = 0$$ *Equation 2.2.05.*[71]

Combining *Equation 2.2.04* with *Equation 2.2.05* we can simplify to *Equation 2.2.06*, where $[E]_T$ corresponds to the total enzyme concentration.[71]

$$[ES] = \frac{[E]_T[S]}{K_M + [S]}$$ *Equation 2.2.06.*[71]

Where K_M is defined as the Michaelis constant.[71]

$$K_M = \frac{k_{-1} + k_2}{k_1}$$ *Equation 2.2.07.*[71]

Equation 2.2.06 can be expressed by the experimentally measurable quantity v_0, the initial reaction velocity. The impact of rate influencing factors such as reversible reactions, enzyme inhibition and decreasing $[S]$ are limited by only measuring the velocity over the initial time period after the reaction is initiated.[71]

$$v_0 = \left(\frac{d[P]}{dt}\right) = k_2[ES] = \frac{k_2[E]_T[S]}{K_M + [S]}$$ *Equation 2.2.08.*[71]

At high substrate concentrations the enzyme becomes saturated and the reaction reaches maximum velocity, V_{max}[71]

$$V_{max} = k_2[E]_T$$ *Equation 2.2.09.*[71]

Combining *Equation 2.2.08* and *Equation 2.2.09* we obtain the Michaelis-Menten equation,[71] a basic expression which describes enzyme kinetics for simple enzymatic reactions which allows enzymes to be characterised experimentally by measuring v_0 against $[S]$[71]

$$v_0 = \frac{V_{max}[S]}{K_M + [S]}$$ *Equation 2.2.10 The Michaelis-Menten equation.*[71]

2.2 Gold coated magnetic nanoparticle synthesis

Unless otherwise stated in all instances all glassware prior to use was left for >24 h in *Aqua Regia* and thoroughly rinsed in deionised water and dried in an oven. Stirring unless otherwise stated was performed mechanically using a glass or PTFE shaft and either a glass or PTFE paddle and throughout all experimentation deionised filtered water (dH_2O) was used. Where magnetic decantation is described, it was performed using a commercially available 1.2 -1.4 T sintered neodymium magnet (e-magnets), the solution was typically within 1 cm of this surface for >48 hours to allow significant separation. The reagents were purchased from chemical distributors and were not modified or purified in anyway, from Sigma Aldrich; ferric chloride $FeCl_3.6H_2O$, ferrous chloride $FeCl_2.4H_2O$, ferrous sulphate $FeSO_4.7H_2O$, tetramethylammonium hydroxide (TMAOH) $(CH_3)_4NOH.5H_2O$, gold chloride $HAuCl_4.3H_2O$, polyethylenimine (PEI) branched ~25000 $gmol^{-1}$, hydroxylamine hydrochloride $NH_2OH.HCl$, potassium nitrate KNO_3, sodium borohydride $NaBH_4$, perchloric acid ($HClO_4$) 70 %, ammonium hydroxide (NH_4OH) 28 %, from Fisher Scientific; trisodium citrate $Na_3C_6H_5O_7.2H_2O$, hydrochloric acid (HCl) 36 %, nitric acid (HNO_3) 70 %, sodium hydroxide NaOH (Sigma Aldrich >99.99%).

Boiling citrate iron oxide nanoparticle @ Au synthesis

The initial boiling citrate synthesis was performed following a previously described procedure.[230] Fe_3O_4 was synthesised by dissolving 1.16 g $FeCl_3.6H_2O$ (4.25 mmol) and 0.43g $FeCl_2.4H_2O$ (2.13 mmol) into 62.5 ml deoxygenated deionised water, this solution was heated to 50 °C, maintained at this temperature whilst being mechanically stirred and purged with nitrogen. To this was added a deoxygenated solution of 30 ml 1M NH_4OH

containing 1.47g trisodium citrate (50 mM) at a rate of 4 ml/min, the clear orange solution darkened in colour until a clear dark brown/black colloid was obtained and stirring, purging and heating was maintained for a further 30 minutes. 1.2 ml of this solution was then added to 200 ml deoxygenated 0.5 mM trisodium citrate (0.0319 g), the solution was then vigorously stirred and bought to boiling then 10 ml 10 mM $HAuCl_4$ solution (0.039 g) was injected. The clear pale yellow solution darkened to brown through blue and purple becoming a clear deep ruby red after a few minutes characteristic of a gold colloid.[230]

A variation of this synthesis was followed as described;[215] Fe_3O_4 was first synthesised by dissolving 2.162 g $FeCl_3.6H_2O$ (8 mmol) and 0.795g $FeCl_2.4H_2O$ (4 mmol) into 10 ml purged 2 M HCl and added dropwise to 100 ml purged 0.7 M NH_4OH and stirred for 30 minutes. The black precipitate was magnetically isolated and stirred with 100 ml 2 M $HClO_4$ for a further 30 minutes and isolated by centrifuging for 10 minutes at 3k rpm and redsipersed with 100 ml dH_2O by probe sonication. 15 ml 5 mM $HAuCl_4$ solution (0.030 g) was bought to the boil in 120 ml dH_2O where 5 ml of the iron colloid was added followed by 5 ml 80 mM trisodium citrate (0.118 g) the solution became brown, blue, purple and then red within a few minutes.

Pre-seeding magnetite prior to Au deposition

The synthesis was performed as previously described;[231] 0.7g $FeSO_4.7H_2O$ (2.5 mmol) was dissolved in 80 ml deoxygenated dH_2O followed by the addition of 10 ml 2M KNO_3, 10 ml 1M NaOH and 10 ml 4 gL^{-1} PEI, the reaction solution was further purged for 10 minutes and then sealed and placed in a water bath at 95 °C without agitation for 2 hours. The black precipitate was then magnetically isolated and washed 3 times with dH_2O and redispersed in 80 ml dH_2O with probe sonication. Synthesis of Au seeds was performed as detailed by the authors[231] with 1 ml 1 % $HAuCl_4$ solution added to 90 ml dH_2O and vigorously stirred prior to the addition of 2 ml 38.8 mM trisodium citrate followed by 1 ml 20 mM fresh sodium borohydride in 38.8 mM trisodium citrate. The clear pale yellow solution became a deep purple through to pink and finally strawberry red and was further stirred for 15 minutes prior to storage at 5 °C in a dark bottle. 90 ml of this solution was then stirred with 2 ml of the probe sonicated 3.2 gL^{-1} PEI stabilized Fe_3O_4 cores for 2 hours which were then magnetically isolated and washed 3 times with dH_2O before being taken up in 90 ml dH_2O. Added to this was 10 ml 50 gL^{-1} PEI solution followed by heating to 60 °C for 1 hour, the seeded PEI stabilized cores were then magnetically isolated and washed 3 times before being redispersed *via* probe sonication in 20 ml dH_2O and added to 110 ml 0.01 M

NaOH (0.044 g). Under vigorous stirring 0.5 ml 1 % $HAuCl_4.3H_2O$ was added followed by 0.75 ml 0.2 M $NH_2OH.HCl$ and thereafter 4 subsequent additions of 0.5 ml 1 % $HAuCl_4$ solution followed by 0.25 ml 0.2 M $NH_2OH.HCl$. The particles were then magnetically separated and washed with dH_2O 3 times and redispersed in 20 ml dH_2O with probe sonication.

An alternative preparation of SPION@Au was developed during this study based on the above process but using approximately 10 nm magnetite cores initially. Fe_3O_4 cores were synthesised as described by Massart,[150] by dissolving 2.162 g $FeCl_3.6H_2O$ (8 mmol) and 0.795 g $FeCl_2.4H_2O$ (4 mmol) into 10 ml purged 0.5 M HCl, which was then added dropwise to a vigorously stirred and nitrogen protected 100 ml 1.5 M NaOH solution (6 g), the solution darkened through brown to black upon addition and the precipitate was collected magnetically and washed 3 times with dH_2O. 25 ml of the magnetite was then stirred with 10 gL^{-1} PEI in a 0.1 M NaOH solution for 2 hours and then magnetically isolated and washed 3 times in dH_2O, 0.5 ml of this colloid was then probe sonicated and stirred with 20 ml 3 nm gold seeds for 3 hours. The particles were magnetically isolated and washed 3 times with dH_2O and redispersed in 25 ml 1 mM trisodium citrate by probe sonication, initially 125 μl 1 % $HAuCl_4$ solution followed by 190 μl 0.2 M $NH_2OH.HCl$ was added under vigorous stirring and then with 10 minute intervals 4 iterations of 125 μl 1 % $HAuCl_4$ solution followed by 63 μl $NH_2OH.HCl$ were added, the particles were then magnetically isolated and washed 3 times with dH_2O and resuspended by probe sonication in 25 ml dH_2O. Variations of this synthesis included different PEI concentrations, different Au seed volumes, the presence of TMAOH upon seed reduction and the number and concentration of $HAuCl_4$ and $NH_2OH.HCl$ reductions.

1,2-diaminoethane functionalised iron oxide nanoparticles and Au seeding

Fe_3O_4 cores were synthesised as described by Massart,[150] by dissolving 2.162 g $FeCl_3.6H_2O$ (8 mmol) and 0.795 g $FeCl_2.4H_2O$ (4 mmol) into 10 ml purged 0.5 M HCl, which was then added dropwise to a vigorously stirred and nitrogen protected 100 ml 1.5 M NaOH solution (6 g), the solution darkened through brown to black upon addition and the precipitate was collected magnetically and washed 3 times with dH_2O. The flocculate was peptised in 0.8 M 1,2-diaminoethane then separated by centrifugation, redispersed in dH_2O and mixed with an Au seeding solution. Synthesis of the Au seeding solution was performed as detailed in the literature[232] with 1 ml 1 % $HAuCl_4$ solution added to 90 ml dH_2O and vigorously stirred prior to the addition of 2 ml 38.8 mM trisodium citrate followed by 1 ml 20 mM fresh sodium borohydride in 38.8 mM trisodium citrate. The clear pale yellow solution became a deep purple through to pink and finally strawberry red and was further stirred for 15 minutes prior to storage at 5 °C in a dark bottle.

Iterative hydroxylamine SPION@Au synthesis

The synthesis was followed as described elsewhere.[219] First Fe_3O_4 was synthesised by dissolving 2.162 g $FeCl_3.6H_2O$ (8 mmol) and 0.795 g $FeCl_2.4H_2O$ (4 mmol) into 10 ml purged 0.5 M HCl, which was then added dropwise to a vigorously stirred and nitrogen protected 100 ml 1.5 M NaOH solution (6 g), the solution darkened through brown to black upon addition and the precipitate was collected magnetically. This was washed in 100 ml 0.1M HNO_3 and isolated at 5000 rpm by centrifuging. The SPION were redispersed in 100 ml 0.01 M HNO_3 and heated to 90-95 °C whilst stirring continuously for 30 minutes, the black Fe_3O_4 becoming brown indicative of Fe_2O_3. The iron oxide was then isolated by centrifuging for 10 minutes at 5000 rpm, washed twice with dH_2O by repeating the procedure and then the flocculate peptised with 100 ml 0.1M TMAOH (1.812g). 7.5 ml 1.1 mM Fe_2O_3 was then probe sonicated with cooling intervals and stirred with 7.5 ml 0.1M trisodium citrate (0.221 g) for 10 minutes before adding 140 ml TMAOH giving a final concentration of 5 mM (0.1359 g). This is vigorously stirred with alternate additions of 1 % $HAuCl_4$ solution and 0.2 M $NH_2OH.HCl$ added dropwise with 10 minute intervals as described by the authors totalling 5 iterative gold chloride and hydroxylamine additions.

Particle characterization

Particles were characterised by transmission electron microscopy (TEM) at 80kV (Philips CM12), energy-dispersive X-ray spectroscopy (EDAX) (EDAX Genesis), powder X-ray diffraction (PXRD) Cu Kα emission (Philips PANalytical XPert PRO PW3040/60), UV-Vis spectrophotometry (Jasco V-550) and dynamic light scattering (DLS) HORIBA SZ-100Z system.

2.3 Nitroreductase immobilisation and electrochemistry

Cyclic voltammetry was used to assess the stripping profiles of the immobilized proteins on gold surfaces. Measurements were performed using an Autolab PGSTAT 30 computer-controlled electrochemical measurement system. The analysis was carried out with a three-electrode cell, using a saturated calomel reference electrode (SCE) and a platinum counter electrode. Prior to use, the cell was cleaned using a 50:50 mixture of concentrated

H_2SO_4:HNO_3 followed by rinsing in deionised water (nominal resistivity >18 M Ω cm at 25 °C), cleaning in a steam bath and drying in the oven. The working electrode was a gold coated glass slide, previously immersed in solutions of enzymes, which form SAMs on the Au surface. A seal was made between the working electrode and the electrolyte solution with O-rings defining a geometric area of 0.6 cm^2 an illustration and photograph of the experimental equipment and set-up is shown and discussed in Figure 5.1.1. Prior to the formation of the enzyme layer, the gold (111)-coated glass slides (Winkler GmbH, Germany) were flame annealed in a Bunsen burner until they attained red heat several times. After cooling in air for a short time, each slide was quenched in water. This procedure produces a flat gold surface with strong Au(111) characteristics. The gold surface was modified by immersing the slide in a 0.1 M pH 7.2 phosphate buffer and enzyme solution, typically at enzyme concentrations of approx. 5 mg/ml for a period of 48 h at 5 °C. After assembly, the modified electrode was rinsed with copious amounts of the buffer solution followed by 0.1 M NaOH. The electrochemical desorption was carried out between 0 V to -1.1 V vs. a saturated calomel electrode (SCE) at a rate of 50 mVs^{-1} in a solution of 0.1 M NaOH.

Chapter 3

NITROREDUCTASE EVALUATION

3.1 Introduction

Recombinant DNA techniques were used to insert NTR genes into pET-28(+) vectors. Agarose gel, gene sequencing, SDS-PAGE analyses and UV-visible spectroscopy were used to evaluate the enzymes. This chapter details these studies and their interpretation, identifying which enzymes are potentially suitable for application in DEPT. The disparity in activity often found when enzymes are isolated and genetically modified for experimental studies makes this a challenging and unpredictable area of research. Enzymes with a similar structure may have very different kinetic properties to a given substrate and likewise, modifying an enzymes amino acid sequence can profoundly change it's properties.[71] These challenges are detailed throughout the chapter and highlighted in section 3.1.1 below.

3.1.1 Preliminary investigation

A preliminary investigation to determine a procedure for generating and assaying NTRs for further study was undertaken with *ydgI* from *Bacillus Subtilis subsp. subtilis str. 168*, which revealed that inserting a sequence of six cysteine amino acids (Cys-tag) into an NTR monomer sequence significantly alters the resulting protein structure. In the study, *ydgI* was cloned using a pET-28a(+) vector (Novagen) which contains a His-tag sequence for affinity purification. His-tag's can be added to the N-terminus of a sequence and do not typically have a detrimental effect on an enzymes activity.[223] If they do, thrombin may be used to selectively cleave the purification tag from the protein if necessary. During the study the Cys-tag was also added to the N-terminus, the intention being to limit any structural change around the active site of *ydgI* and therefore limit any change to the NTR's activity. In the first instance, *ydgI* was cloned using pET-28a(+), purified using immobilized metal ion affinity chromatography[180] and shown to be active with the nitro group containing dinitroethylbenzene (DNEB).

The clone was repeated but with a Cys-tag added to the N-terminus of the sequence, upstream of the gene start position but downstream of the His-tag (Cys-tag #1). In this case, the enzyme was clearly present using SDS-PAGE analysis after induction, and the cell free extract of the expression host (Rossetta (DE3) pLysS Competent Cells) still showed activity to DNEB. However the enzyme would not bind to the nickel purification column and could therefore not be purified by immobilized metal ion affinity chromatography. As the only difference between the two proteins was the addition of the

Cys-tag, it can be assumed that this location of Cys-tag insertion prevents the His-tag accessing the nickel, thwarting purification.

The clone was repeated again but with a Cys-tag added further away from the His-tag, just after the start codon of the gene sequence (Cys-tag #2), the intention being to give the His-tag better access to the metal in the purification column. Analysing Cys-tag #2 with SDS-PAGE showed the enzyme was clearly present and crucially in this case could be purified from the cell free extract using immobilized metal ion affinity chromatography. However the enzyme subsequently showed significant loss in nitroreductase activity. Given the only difference between this protein and the first assayed was the addition of a Cys-tag just after the start codon of the gene it can be assumed that this location of Cys-tag insertion caused a change such that the enzyme loses activity to DNEB.

The results of this preliminary study indicate that while a Cys-tag can be inserted into the NTR sequence relatively easily, the outcome of this alteration cannot be easily predicted. The inability to purify a target protein or the potential loss of activity following modification creates a significant challenge in generating suitable enzymes for subsequent immobilisation. Screening of NTRs to determine potential candidacy for a CB1954 MNP-DEPT adds to our understanding of which structures are best suited to a CB1954 therapy, but how and where best to insert a Cys-tag will undoubtedly be specific to each NTR and in itself constitute an extremely thorough investigation.

So as to keep the focus of the NTR assays on the activity with CB1954, the Cys-tags were not added to every possible position between the N-terminus and the gene start codon. Instead they were added to just one or two locations for each enzyme as time allowed.

3.2 Plasmid digestion

Restriction endonucleases for *ydjA* and *ydjA-cys* were used to excise the genes from the vectors as shown in *Figure 3.2.1* and *Figure 3.2.2*. These figures show the gene was successfully inserted into the vector.

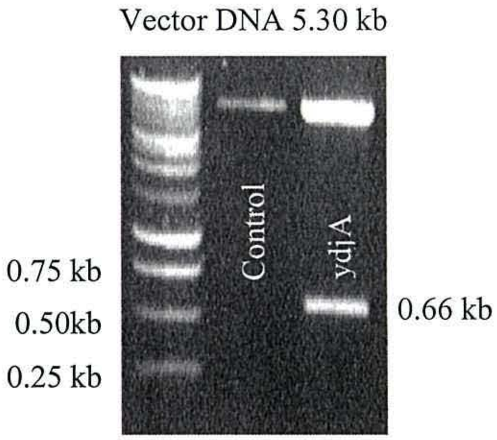

Figure 3.2.1. Agarose gel stained with ethidium bromide under exposure to UV light, showing the ydjA gene at 0.66 kb after excision from pET-28a(+) vector.

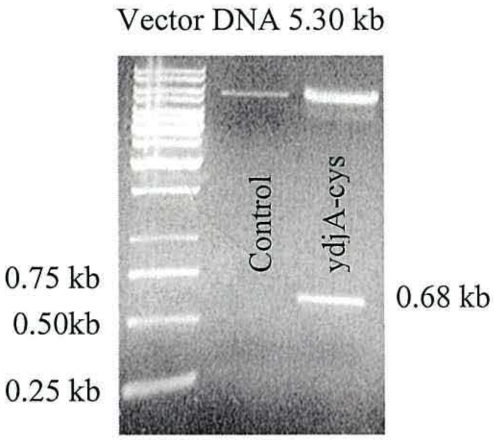

Figure 3.2.2. Agarose gel stained with ethidium bromide under exposure to UV light, showing the ydjA-cys gene at 0.68 kb after excision from pET-28a(+) vectors.

Restriction endonucleases for NTRs and cysteine modified NTRs from *B. Licheniformis* were used to excise the genes from the vectors as shown in *Figure 3.2.3*. The NTR gene sizes and protein weights for all the enzymes are shown in *Table 3.2.1* and the gene sequences attached to the *Appendix*.

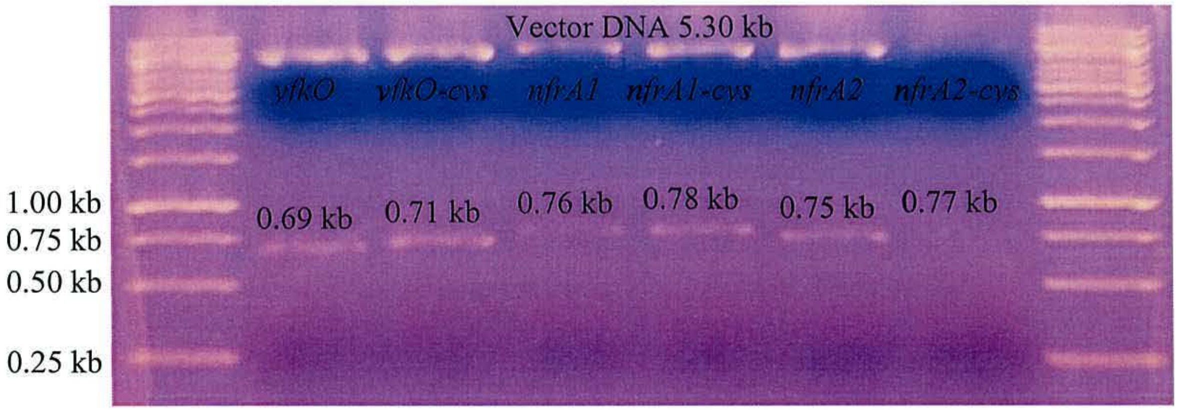

Figure 3.2.3. Agarose gel stained with ethidium bromide under exposure to UV light, showing the NTR genes after excision from pET-28a(+) vectors.

Table 3.2.1. The sizes of the genes and resulting proteins of the generated NTRs

NTR	Gene size	Monomer Mw (kDa)
ydjA	657 bp	23.68
ydjA-cys	675 bp	24.30
yfkO	693 bp	29.83
yfkO-cys	711 bp	30.45
nfrA1	759 bp	31.66
nfrA1-cys	777 bp	32.28
nfrA2	747 bp	30.75
nfrA2-cys	765 bp	31.37

3.3 SDS PAGE analysis

The NTRs were expressed and the cell free extract analysed by SDS-PAGE, *Figure 3.3.1* shows an example of this procedure with *ydjA*.

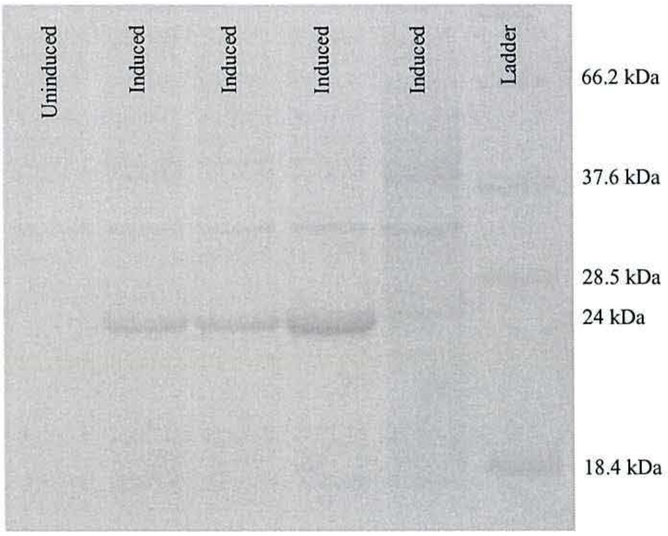

Figure 3.3.1. Cell free extract of host cells containing vectors with a ydjA gene. The samples induced with IPTG show bands at approximately 24 kDa indicating successful transformation and expression of the NTR.

At around 24 kDa, a distinct band is present in the samples where IPTG was introduced during growth, indicating successful transformation and expression of the NTR. This small scale analysis can be used to determine whether an NTR has successfully been cloned and expressed by the Rossetta host. If so the NTR can be purified using immobilized metal ion affinity chromatography. *Figure 3.3.2* shows the SDS PAGE gels and purification of *nfrA1*.

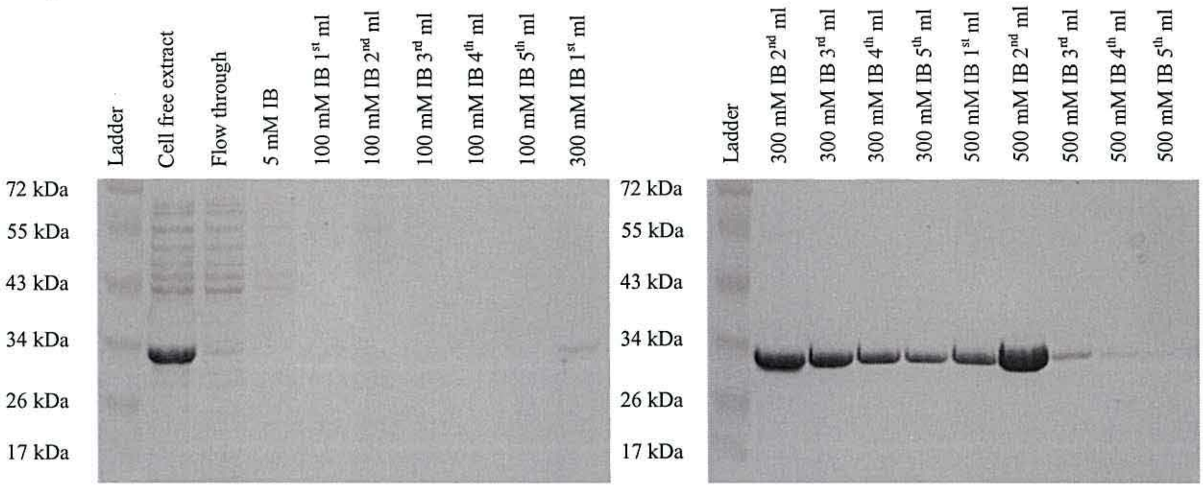

Figure 3.3.2. SDS PAGE gels showing the purification of nfrA1. The distinct bands visible at approximately 32 kDa indicate the presence of the NTR following over-expression and purification.

The *nfrA1* NTR monomer has a molecular weight of 31.66 kDa, the distinct band in the cell free extract indicates the successful over-expression of the enzyme during growth. The subsequent absence of this strong band in the column flow through indicates the His-tagged proteins bind to the nickel column while the majority of naturally occurring proteins from the *E. coli* host pass through.

Passing imidazole buffer (IB) through the column at concentrations of 5 mM and 100 mM (imidazole) displaces the naturally occurring proteins which have adsorbed to the nickel, while the more strongly bound *nfrA1* remains immobilised to the metal. After 5 ml 100 mM IB has passed through the column no further impurities are seen. At concentrations of 300 mM and 500 mM IB the *nfrA1* elutes, without impurity, indicating that pure *nfrA1* can be isolated after a minimum of 5 ml 100 mM IB is first used to wash the unwanted proteins from the column.

Three crucial properties for potential application in Au-MNP DEPT are the expression, purification and activity of an NTR. After cloning, expression and initial activity experiments with NAD(P)H and CB1954, the following table (*Table 3.3.1*) is generated of NTR candidates for Au-MNP DEPT from this study.

Table 3.3.1. Of the eleven NTRs initially screened for potential application in Au-MNP DEPT only the five highlighted in green express in Rossetta, can be purified and are active with NAD(P)H and CB1954.

NTR	**Expresses in Rossetta host?**	**Can be purified?**	**Active with NAD(P)H and CB1954?**
ydjA	Yes	Yes	No
ydjA-cys #1	Yes	No	-
ydjA-cys #2	Yes	Yes	No
yfkO	Yes	Yes	Yes
yfkO-cys #1	Not Determined	Not Determined	Not Determined
yfkO-cys #2	Yes	Yes	Yes
nfrA1	Yes	Yes	Yes
nfrA1-cys #1	Yes	No	-
nfrA1-cys #2	No	-	-
nfrA2	Yes	Yes	Yes
nfrA2-cys #1	Yes	No	-
nfrA2-cys #2	Yes	Yes	Yes

The concentration of IB needed to isolate the five candidate NTRs from the cell free extract for purification was determined using SDS PAGE. It was found that the NTRs should be first washed with 5 ml 100 mM IB and then isolated in 2.5 ml 500 mM IB, producing a highly concentrated and pure solution of NTR. *Figure 3.3.3* shows an SDS PAGE gel of the five purified NTRs against protein standards.

The gel shows bands at the expected weights for the protein monomers (*Table 3.2.1*) and the dimers for some of the NTRs, indicating that in these instances there was not complete denaturing of the dimers prior to SDS PAGE analysis, which may be due to histidine and cysteine residue interations dimers at high NTR concentrations.

It is quite typical to see the Cys-tagged NTRs express in lower concentrations than the His-tagged enzymes and may be due to the formation of disulphide bonds between the introduced cysteine residues within the protein structure, which can lead to the formation of inclusion bodies.[233]

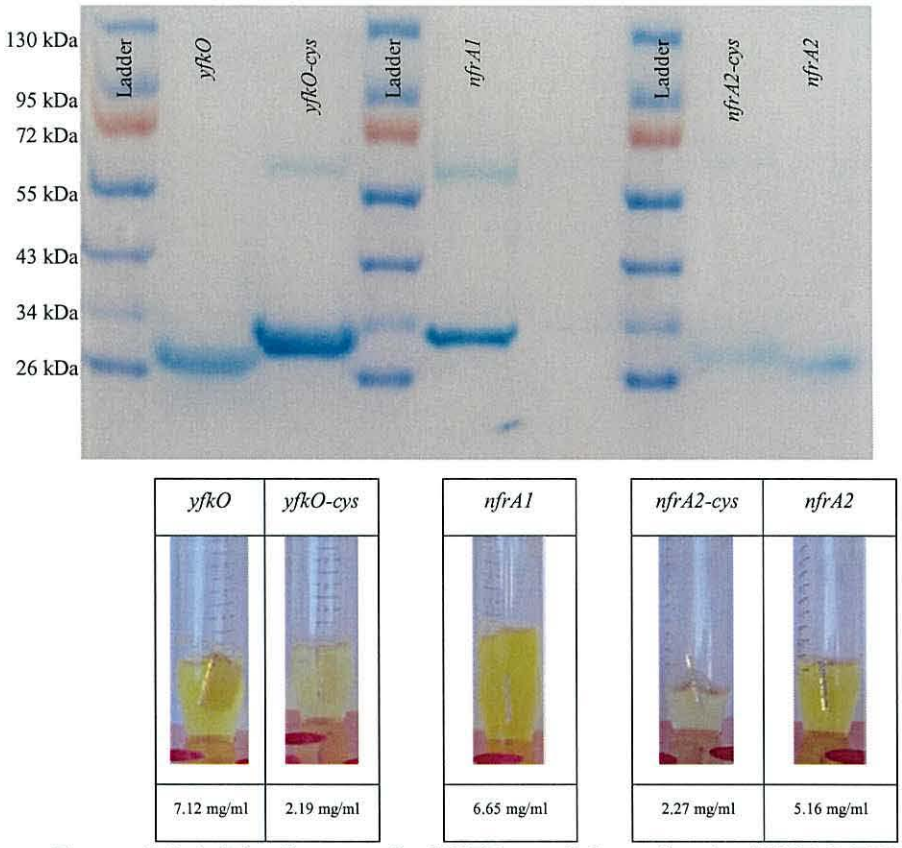

Figure 3.3.3. The five purified NTR candidates for Au-MNP DEPT.

3.4 Enzyme assay using ultraviolet-visible spectroscopy

UV-vis spectroscopy was used to measure the activities of the generated NTRs. Due to the limited solubility of CB1954 in aqueous solution, it was first dissolved in DMSO. However at concentrations above 5% DMSO it has been shown the solvent can inhibit the activity of NTRs with the prodrug.[82] To prevent the solvent inhibiting the enzyme reactions DMSO concentrations were always kept below 5%. Given the high molar extinction coefficient of NADH it was hoped that its oxidation could be measured by monitoring the reduction in absorbance at 340 nm. However due to the strong overlap in absorbance peaks of NADH and CB1954 this was not possible as shown in *Figure 3.4.1*.

The concentration of NADH and CB1954 are expected to decrease during the reaction, while the concentrations of the oxidised form of the cofactor, NAD+, and the reduced form of CB1954 are expected to increase. The reaction schemes are shown in the Introduction, in *Figure 1.2.1, Figure 1.3.1, Figure 1.3.3, Figure 1.3.4* and *Figure 1.3.5*. The UV-vis spectra of the reaction between *yfkO-cys*, NADH and CB1954 over 10 minutes is shown in *Figure 3.4.2*, with respective increases and decreases in absorbances at wavelengths corresponding to the different reaction species present. Reactions of *nfrA1* and *nfrA2* with cofactor and CB1954 are shown in *Figure 3.4.3* and *Figure 3.4.4*.

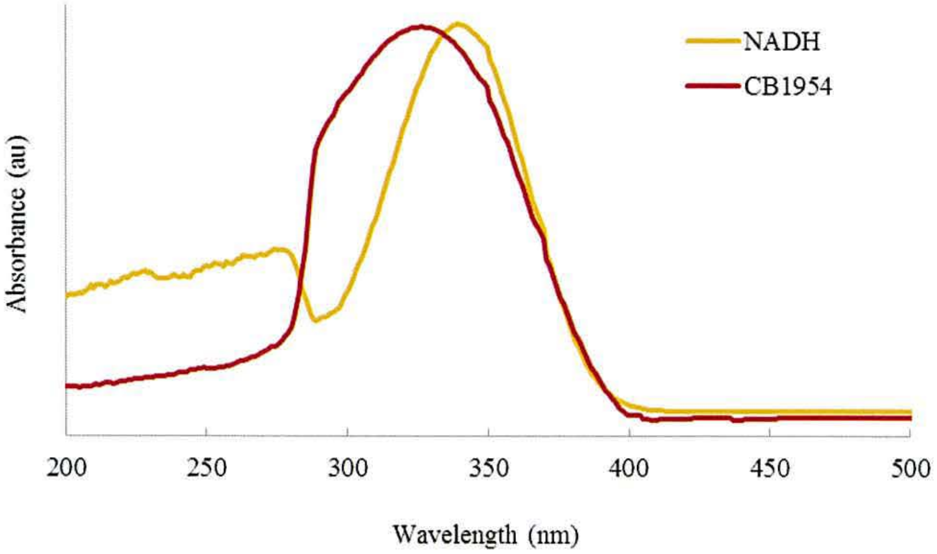

Figure 3.4.1. Overlaid UV-vis spectra of neat CB1954 (280 µM, ε = 1200 L $mol^{-1}cm^{-1}$*) and NADH (40 µM, ε = 6220 L* $mol^{-1}cm^{-1}$*) showing* λ_{max} *at 327 nm and 340 nm respectively and significant peak overlap.*

Peak *A* of *Figure 3.4.2* at approximately 260 nm is an absorbance region of the NTR, NAD+ and NADH. Both NADH and NAD+ have λ_{max} = 259 nm, meaning distinguishing the concentrations of the oxidised and reduced forms is not possible at this wavelength and cannot be easily correlated to the reduction of CB1954.

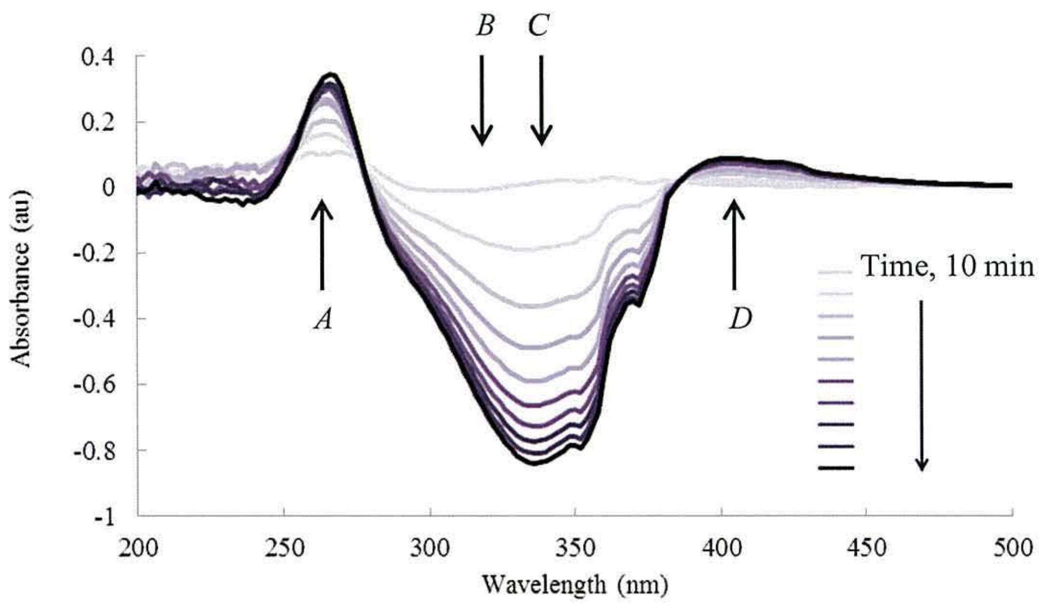

Figure 3.4.2. UV-vis spectra of yfkO-cys showing the reduction of CB1954 and oxidation of NADH. ***A*** *corresponds to NAD(H/+) λ_{max} = 259 nm and NTR absorbance ≈ 250nm to 290 nm.* ***B*** *depletion of CB1954 λ_{max} = 327 nm.* ***C*** *depletion of NADH λ_{max} = 340 nm.* ***D*** *generation of hydroxylamine derivative of CB1954 λ_{max} = 420 nm.*

As seen in *Figure 3.4.2* the peak at approximately 335 nm correlates to the $\lambda_{\max}$ of both CB1954 (*B*) and NADH (*C*) and although the isolated compounds have distinct maxima at 327 nm and 340 nm respectively, the individual concentrations can't be calculated quantitatively given the degree of peak overlap. The peak at $\lambda_{\max}$ = 420 nm corresponds to the 2- and 4- hydroxylamine derivatives of CB1954 and ε = 1200 L mol^{-1}cm^{-1}, which can be used to assay the NTRs and determine kinetic parameters by directly measuring the absorbance and therefore rate of product generation.[72]

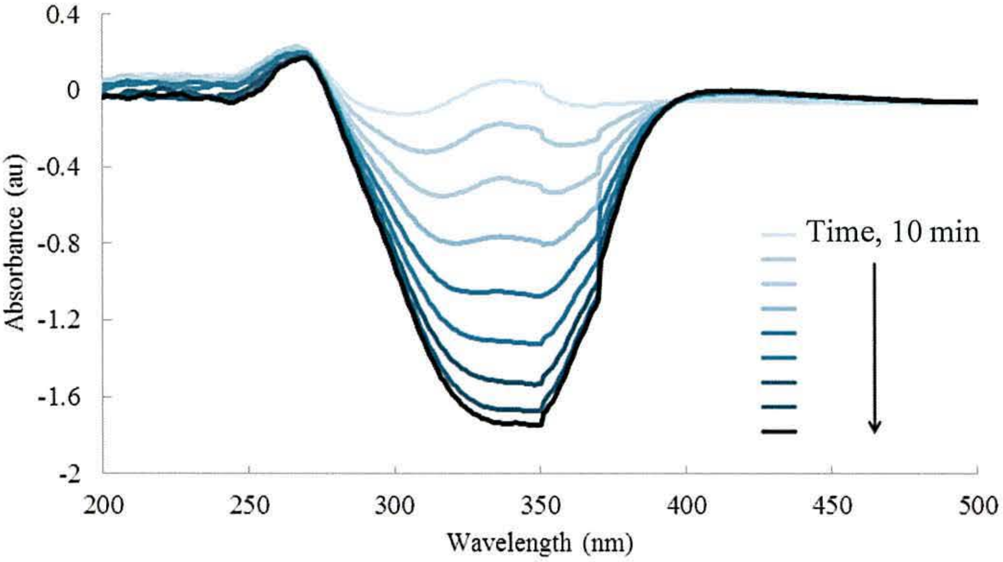

Figure 3.4.3. UV-vis spectra of nfrA1 sowing the reduction of CB1954 and oxidation of NADPH.

Monitoring the change in absorbance at 420 nm allows the generation of the hydroxylamine products to be measured directly *in situ*. Advantages of measuring the change in absorbance at this wavelength to characterise the NTRs includes the lack of interference from neighbouring absorbance peaks and the ability to accurately measure generation of the product over very short time periods.

To determine the suitability of each NTR for Au-MNP DEPT each enzyme was characterised with CB1954 by directly measuring the generation of both the 2- and 4-hydroxylamine derivatives, both of which are cytotoxic in a physiological environment, by measuring the change in absorbance at 420 nm *in situ.*[72, 82] These data are shown and discussed in sections *3.5*, *3.5* and *3.6*

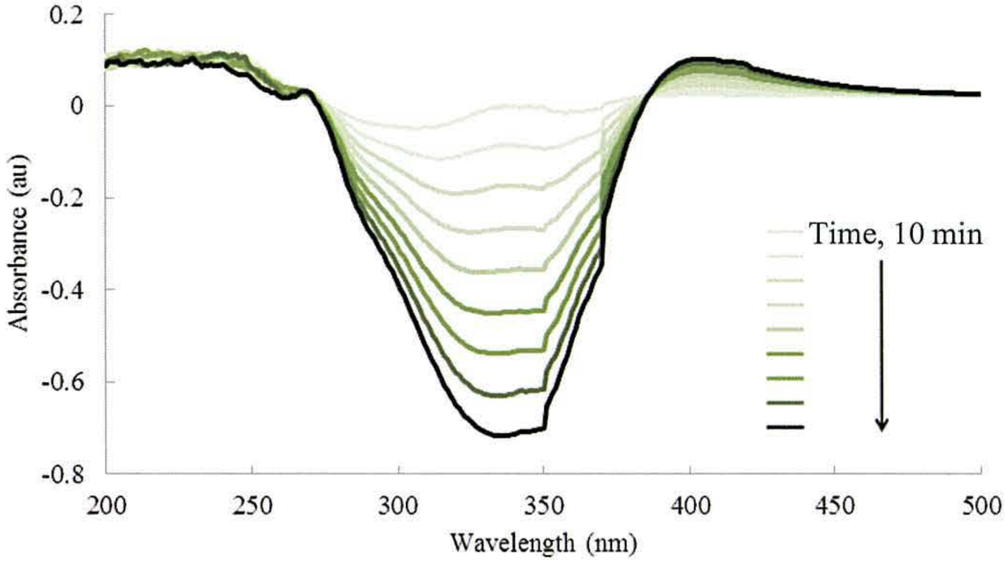

Figure 3.4.4. UV-vis spectra of nfrA2 showing the reduction of CB1954 and oxidation of NADPH.

3.5 Characterisation of *nfrA2* and *nfrA2-cys*

The capabilities of both *nfrA2* and *nfrA2-cys* to reduce CB1954 utilising NADH as a cofactor were analysed by monitoring the production of the hydroxylamine derivatives produced during reaction. Experiments showed the NTRs were active with both NADPH and NADH, so NADH was used for all UV-vis assays given its lower cost.

By increasing the concentrations of the enzymes whilst leaving the concentrations of the cofactor and prodrug constant, a linear relationship between the reaction rate and NTR concentration was observed. Each reaction was performed in triplicate and the average value calculated, standard deviations are represented by error bars.

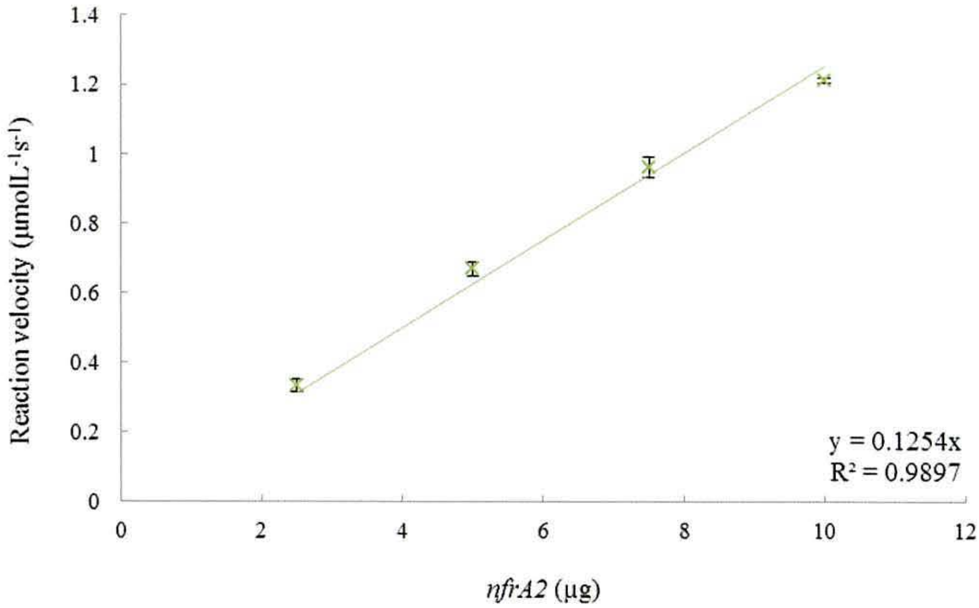

Figure 3.5.1. A graph showing the increasing rate of hydroxylamine derivative generation (λ_{max} = 420 nm, ε = 1200 L $mol^{-1}cm^{-1}$) with increasing concentration of nfrA2. These are initial rates taken during the first 30 seconds of reaction with 0.2 mM CB1954.

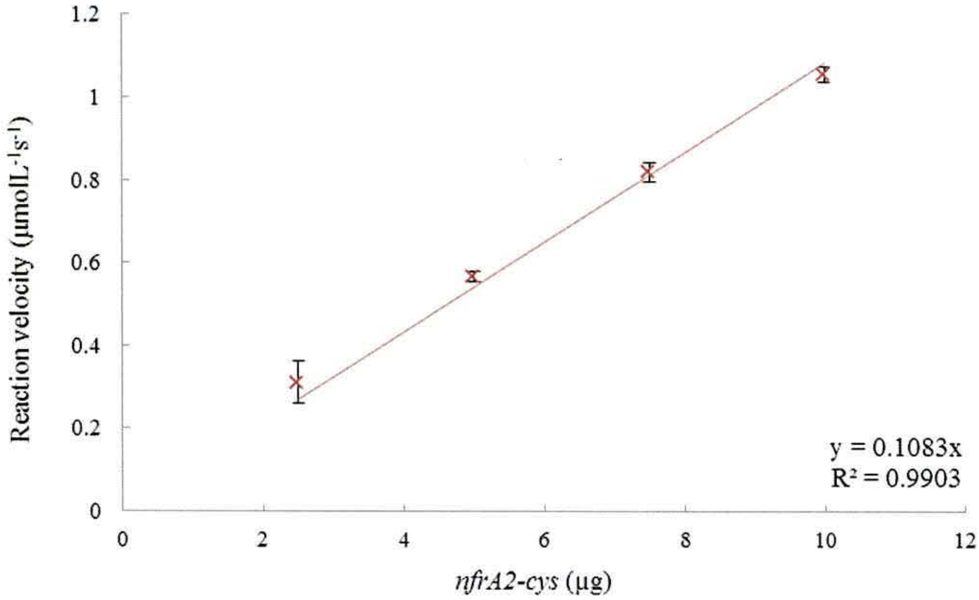

Figure 3.5.2. A graph showing the increasing rate of hydroxylamine derivative generation (λ_{max} = 420 nm, ε = 1200 L $mol^{-1}cm^{-1}$) with increasing concentration of nfrA2-cys. These are initial rates taken during the first 30 seconds of reaction with 0.2 mM CB1954.

The linear relationships show that as the concentration of NTRs is increased, the reaction proceeds at a faster rate.

3.5.1 K_m and V_{max} of *nfrA2* and *nfrA2-cys*

To calculate the K_m and V_{max} of the *nfrA2* and *nfrA2-cys* NTRs the enzyme activity was measured at increasing concentrations of CB1954. Each reaction was performed in triplicate and the average value calculated, standard deviations are represented by error bars.

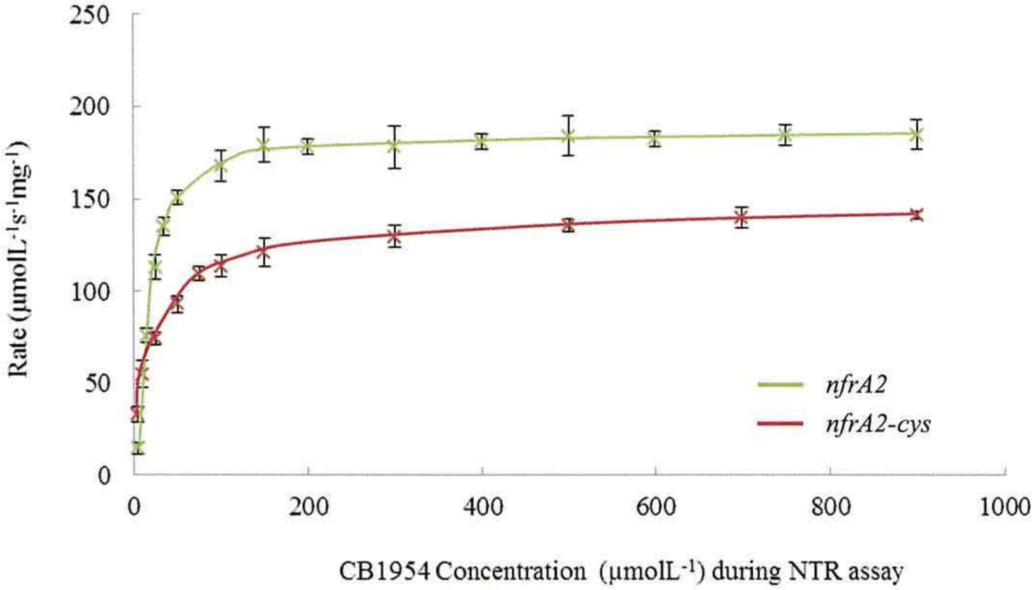

Figure 3.5.3. A graph showing the rate of hydroxylamine derivative generation (λ_{max} = 420 nm, ε = 1200 L $mol^{-1}cm^{-1}$) for the nfrA2 and nfrA2-cys NTRs with increasing CB1954 concentration.

Figure 3.5.3 shows the rate of reaction increases with increasing concentration of CB1954 until the reaction reaches V_{max}. Further details and discussion of the kinetic parameters of *nfrA2* and *nfrA2-cys* are discussed in section *3.8.*

3.5.2 Effect of pH on *nfrA2* and *nfrA2-cys* activity

To determine the optimum pH for *nfrA2* and *nfrA2-cys* the enzymes were assayed at 420 nm with the prodrug at various pHs in phosphate buffer. Each reaction was performed in triplicate and the average value calculated, standard deviations are represented by error bars.

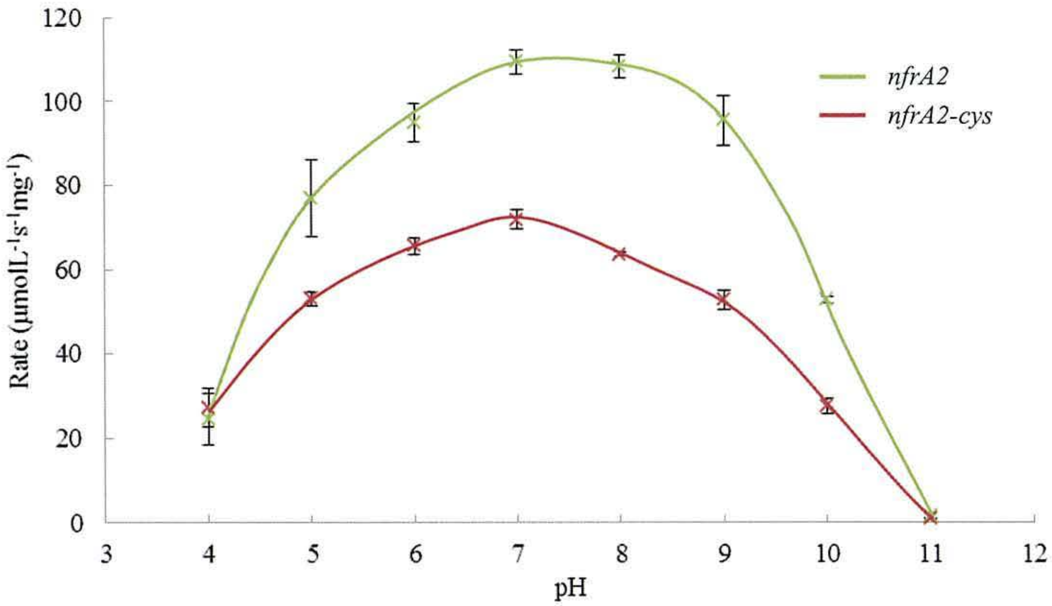

Figure 3.5.4. A graph showing the rate of hydroxylamine derivative generation (λ_{max} *= 420 nm,* ε *= 1200 L* $mol^{-1}cm^{-1}$*) of nfrA2 and nfrA2-cys with 0.2 mM CB1954 and 0.6 mM NADH at different pHs.*

There is a difference in profile between the two NTRs at pH 8, where the activity decreases significantly for *nfrA2-cys*. This indicates the non Cys-tag NTR is more stable in a basic environment than the cysteine modified NTR although both show high activity between pH 7 and pH 8.

3.5.3 Effect of temperature on *nfrA2* and *nfrA2-cys* activity

To determine the optimum temperature for *nfrA2* and *nfrA2-cys* the enzymes were assayed at 420 nm with the prodrug after incubation at a range of temperatures in phosphate buffer. Each reaction was performed in triplicate and the average value calculated, standard deviations are represented by error bars.

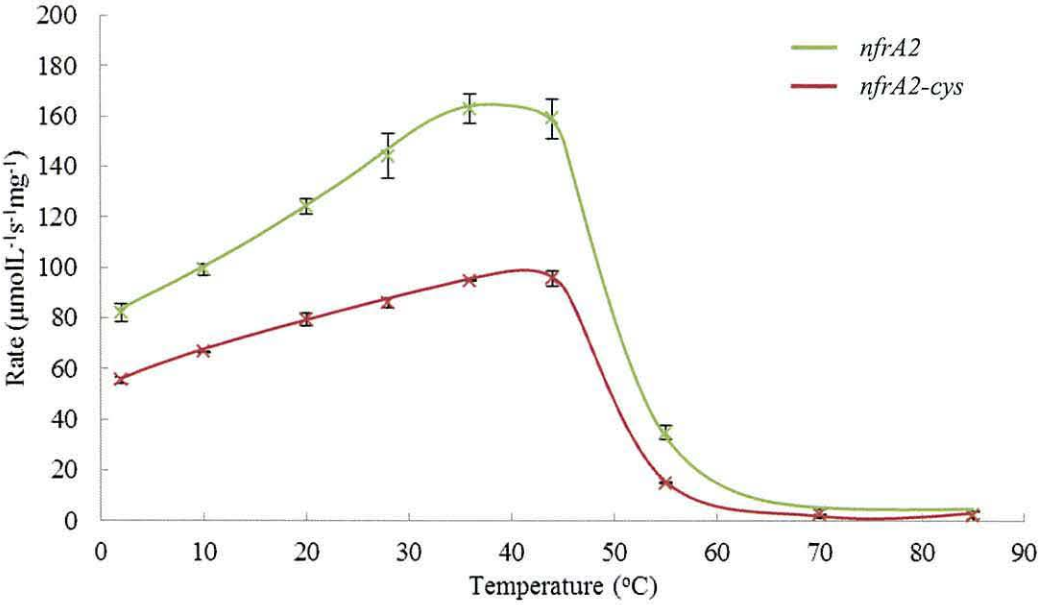

Figure 3.5.5. A graph showing the rate of hydroxylamine derivative generation (λ_{max} = 420 nm, ε = 1200 L $mol^{-1}cm^{-1}$) of nfrA2 and nfrA2-cys with 0.2 mM CB1954 and 0.6 mM NADH at different temperatures.

As the temperature is increased from 2 °C to 37 °C the reaction rate increases for both NTRs and above 50°C the structure becomes unstable, the enzymes thermally denature and lose activity to CB1954. A significant difference between the reaction profiles of the NTRs is the distinct optimum activity observed around 37 °C for *nfrA2*.

As the temperature increases during the reaction, the rate will increase as the enzyme and substrate encounter more frequently, until the temperature is high enough to disrupt the enzyme structure causing activity to drop significantly.[71] During the assay of *nfrA2-cys* the reaction rate increases incrementally with increasing temperature, while for *nfrA2* the enzyme is significantly more active around 37 °C. The introduction of the cysteine residues appears to have altered the NTR structure in such a way that the superior activity at this temperature is lost.

3.6 Characterisation of *nfrA1*

The capability of *nfrA1* to reduce CB1954 utilising NADPH as a cofactor was analysed by monitoring the production of the hydroxylamine derivatives produced during reaction. Experiments showed the NTR was selective for NADPH over NADH, so NADH was used for all enzyme assays.

By increasing the concentration of the enzyme whilst leaving the concentrations of the cofactor and prodrug constant, a linear relationship between reaction rate and NTR concentration was shown. Each reaction was performed in triplicate and the average value calculated, standard deviations are represented by error bars.

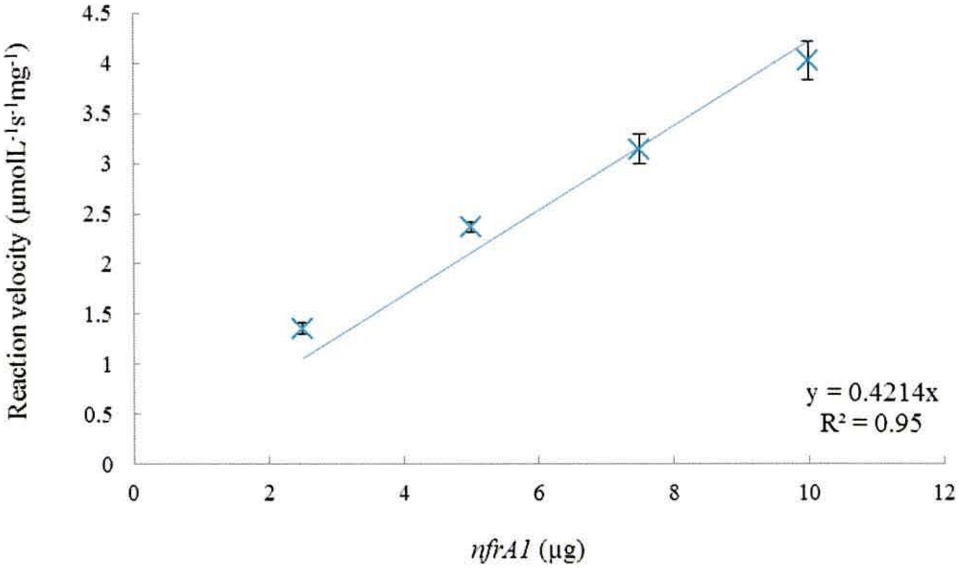

Figure 3.6.1. A graph showing the increasing rate of hydroxylamine derivative generation (λ_{max} = 420 nm, ε = 1200 L mol^{-1}cm^{-1}) with increasing concentration of nfrA1. These are initial rates taken during the first 30 seconds of reaction with 0.2 mM CB1954.

The linear relationship shows that as the concentration of NTR is increased, the reaction proceeds at a faster rate.

3.6.1 K_m and V_{max} of *nfrA1*

To calculate the K_m and V_{max} of the *nfrA1* NTR the enzyme activity was measured at increasing concentrations of CB1954. Each reaction was performed in triplicate and the average value calculated, standard deviations are represented by error bars.

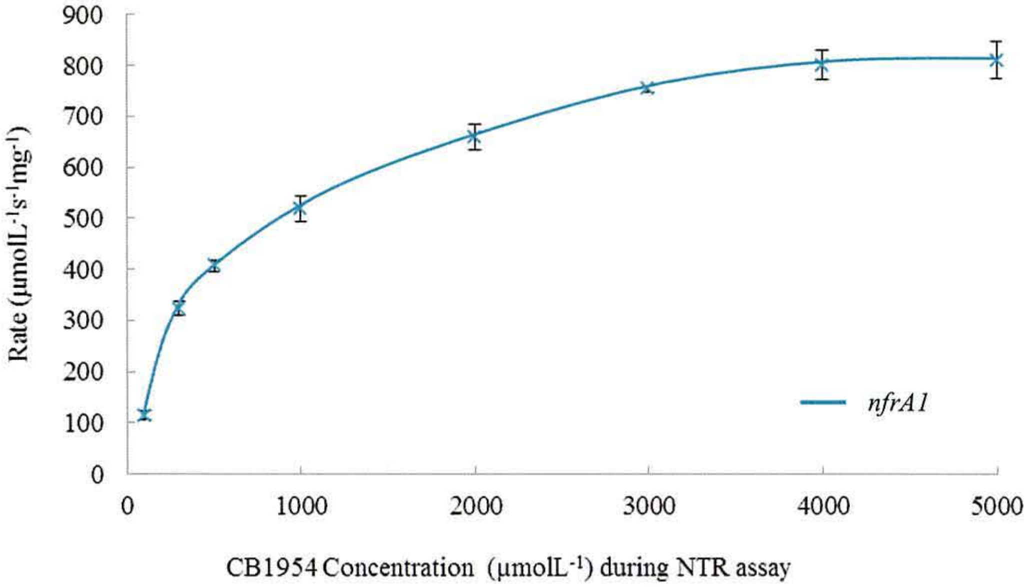

Figure 3.6.2. A graph showing the rate of hydroxylamine derivative generation (λ_{max} = 420 nm, ε = 1200 L mol^{-1}cm^{-1}) for nfrA1 with increasing CB1954 concentration.

Figure 3.6.2 shows the rate of reaction increases with increasing concentration of CB1954, further details and discussion of the kinetic parameters of *nfrA1* are discussed in section *3.8*.

3.6.2 Effect of pH on *nfrA1* activity

To determine the optimum pH for *nfrA1* the enzyme was assayed at 420 nm with the prodrug at various pHs in phosphate buffer. Each reaction was performed in triplicate and the average value calculated, standard deviations are represented by error bars.

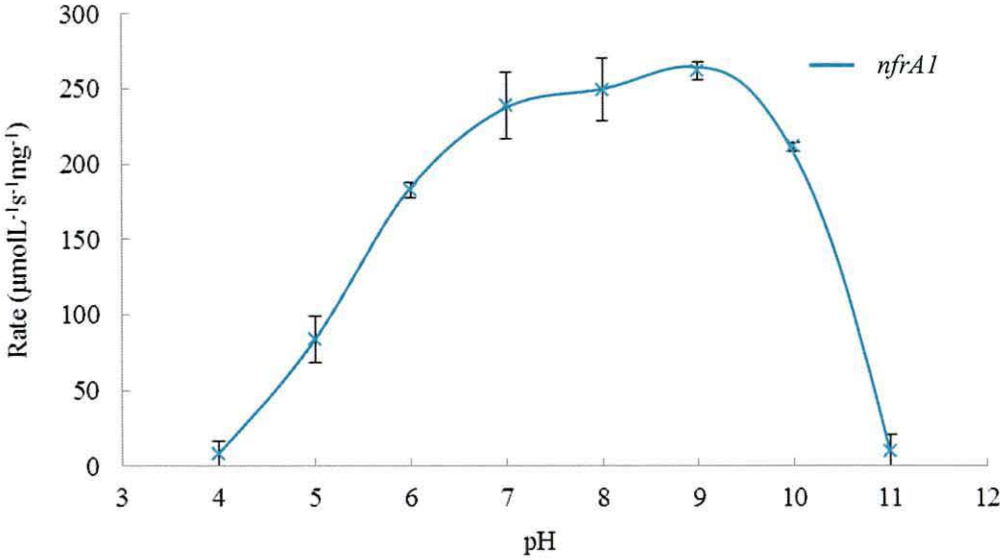

Figure 3.6.3. A graph showing the rate of hydroxylamine derivative generation (λ_{max} = 420 nm, ε = 1200 L $mol^{-1}cm^{-1}$) of nfrA1 with 0.2 mM CB1954 and 0.6 mM NADH at different pHs.

The profile for *nfrA1* shows activity in a broad range of pHs, retaining significant activity between pH 6 and 10, with an optimum between pH 7 and 9.

3.6.3 Effect of temperature on *nfrA1* activity

To determine the optimum temperature for *nfrA1* the enzyme was assayed with the prodrug after incubation at a range of temperatures in phosphate buffer. Each reaction was performed in triplicate and the average value calculated, standard deviations are represented by error bars.

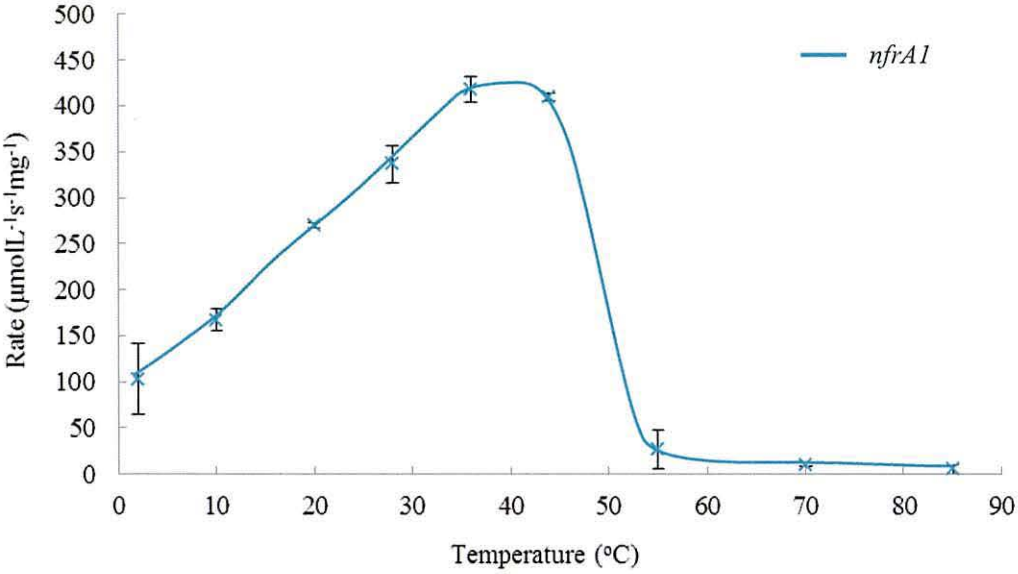

Figure 3.6.4. A graph showing the rate of hydroxylamine derivative generation (λ_{max} *= 420 nm,* ε *= 1200 L* $mol^{-1}cm^{-1}$*) of nfrA1 with 0.2 mM CB1954 and 0.6 mM NADH at different temperatures.*

The activity of *nfrA1* increases linearly until approximately 40 °C, the optimum temperature for the reaction and becomes inactive above 50 °C.

3.7 Characterisation of *yfkO* and *yfkO-cys*

The capabilities of both *yfkO* and *yfkO-cys* to reduce CB1954 utilising NADH as a cofactor were analysed by monitoring the production of the hydroxylamine derivatives produced during reaction. Experiments showed the NTRs were active with both NADH and NADPH, so NADH was used for all UV-vis assays given its lower cost.

By increasing the concentrations of the enzymes whilst leaving the concentrations of the cofactor and prodrug constant, a linear relationship between the reaction rate and NTR concentration was observed. Each reaction was performed in triplicate and the average value calculated, standard deviations are represented by error bars.

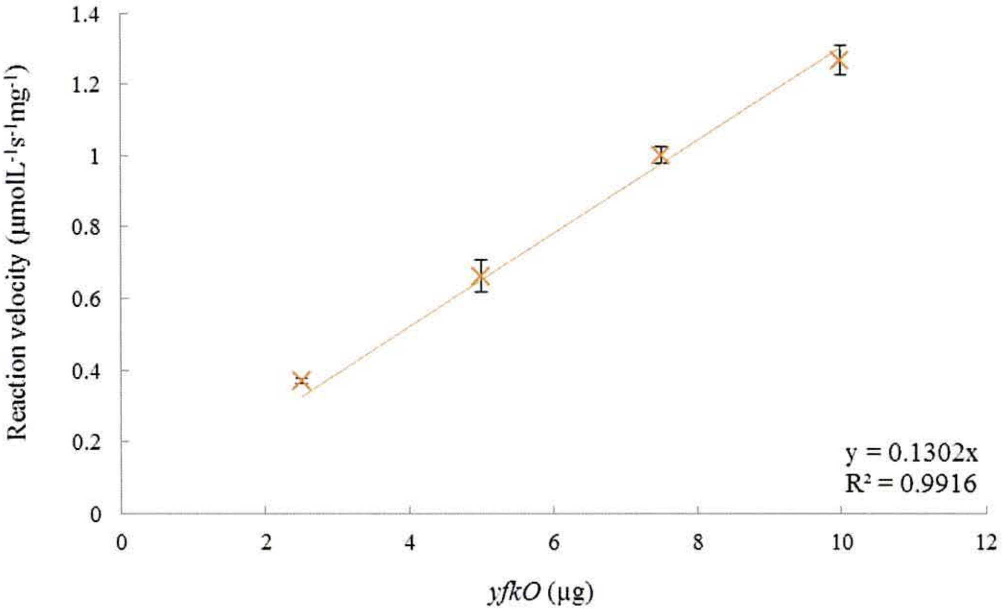

Figure 3.7.1. A graph showing the increasing rate of hydroxylamine derivative generation (λ_{max} = 420 nm, ε = 1200 L mol^{-1}cm^{-1}) with increasing concentration of yfkO. These are initial rates taken during the first 30 seconds of reaction with 0.2 mM CB1954.

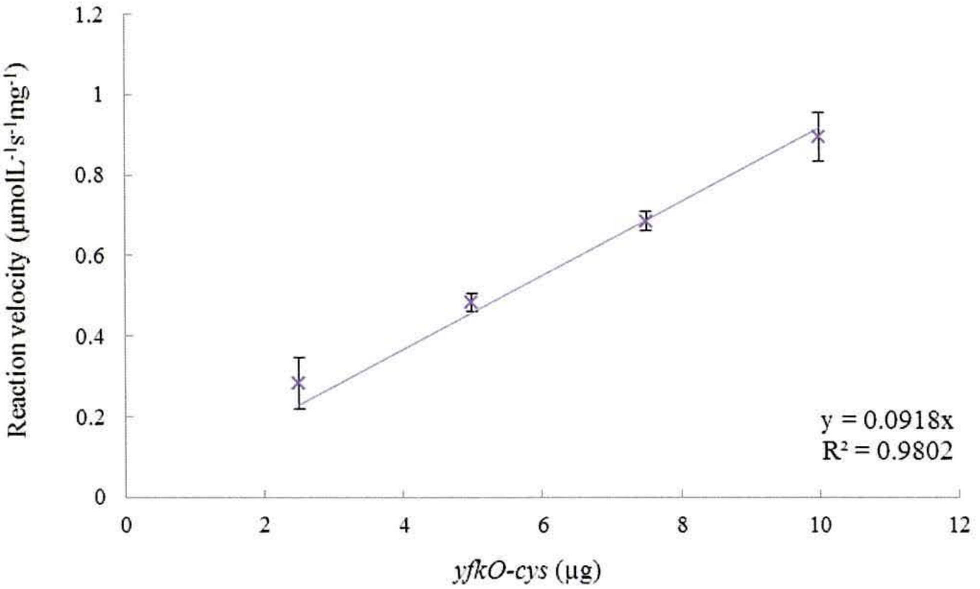

Figure 3.7.2. A graph showing the increasing rate of hydroxylamine derivative generation (λ_{max} = 420 nm, ε = 1200 L mol^{-1}cm^{-1}) with increasing concentration of yfkO-cys. These are initial rates taken during the first 30 seconds of reaction with 0.2 mM CB1954.

The linear relationship shows that as the concentration of NTR is increased, the reaction proceeds at a faster rate.

3.7.1 K_m and V_{max} of *yfkO* and *yfkO-cys*

To calculate the K_m and V_{max} of the *yfkO* and *yfkO-cys* NTRs the enzyme activity was measured at increasing concentrations of CB1954. Each reaction was performed in triplicate and the average value calculated, standard deviations are represented by error bars.

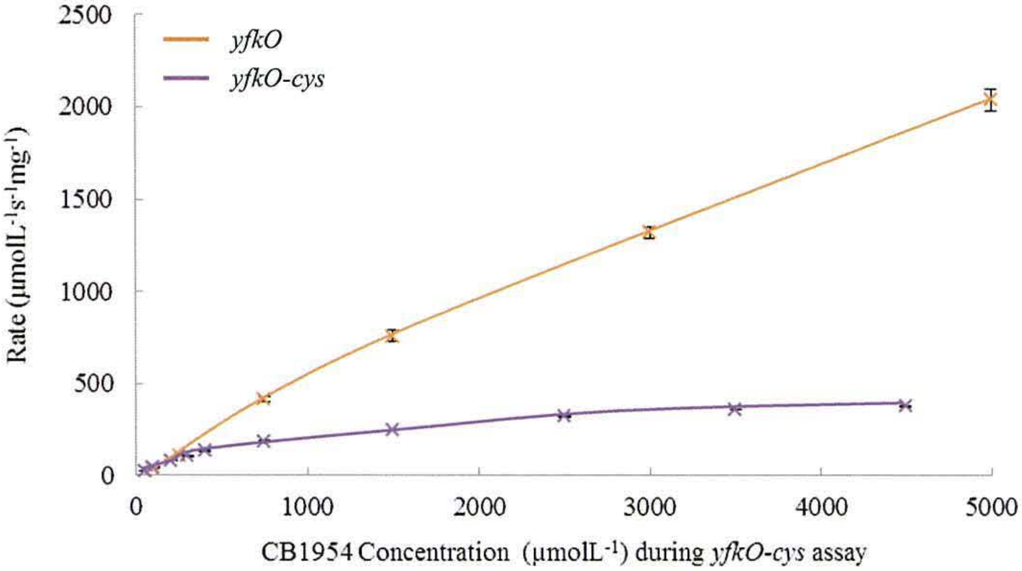

Figure 3.7.3. A graph showing the rate of hydroxylamine derivative generation (λ_{max} = 420 nm, ε = 1200 L $mol^{-1}cm^{-1}$) for the yfkO and yfkO-cys NTRs with increasing CB1954 concentration.

Figure 3.7.3 shows that the rate of reaction increases with increasing concentration of CB1954, further details and discussion of *yfkO* and *yfkO-cys* are discussed in section *3.8*.

3.7.2 Effect of pH on *yfkO* and *yfkO-cys* activity

To determine the optimum pH for *yfkO* and *yfkO-cys* the enzymes were assayed at 420 nm with the prodrug at various pHs in phosphate buffer. Each reaction was performed in triplicate and the average value calculated, standard deviations are represented by error bars.

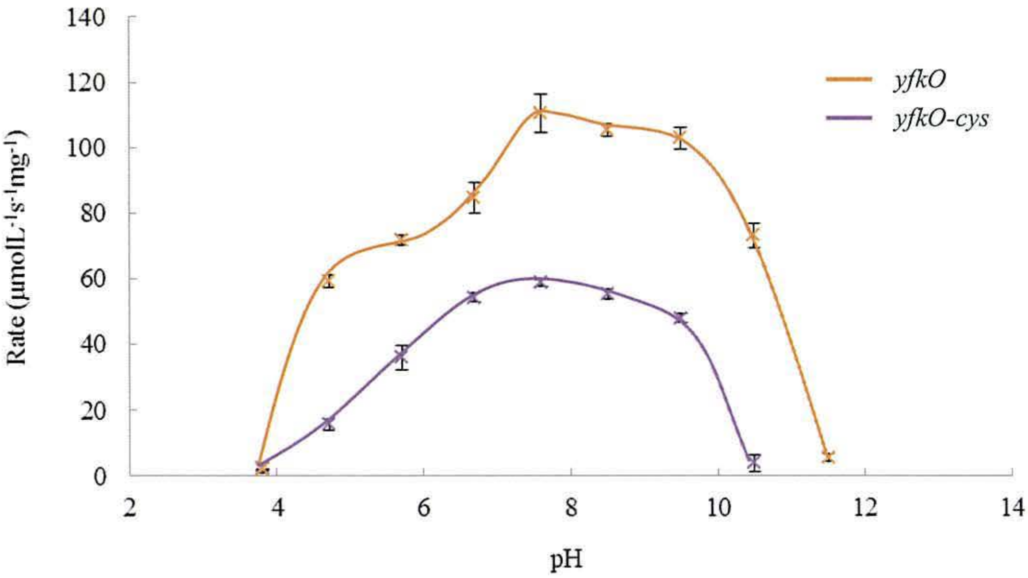

Figure 3.7.4. A graph showing the rate of hydroxylamine derivative generation (λ_{max} = 420 nm, ε = 1200 L $mol^{-1}cm^{-1}$) of yfkO and yfkO-cys with 0.2 mM CB1954 and 0.6 mM NADH at different pHs.

The NTRs both show significant activity between 7 and 9, with *yfkO* being significantly more stable outside the optimum pH range than *yfkO-cys*.

3.7.3 Effect of temperature on *yfkO* and *yfkO-cys* activity

To determine the optimum temperature for *yfkO* and *yfkO-cys* the enzymes were assayed at 420 nm with the prodrug after incubation at a range of temperatures in phosphate buffer. Each reaction was performed in triplicate and the average value calculated, standard deviations are represented by error bars.

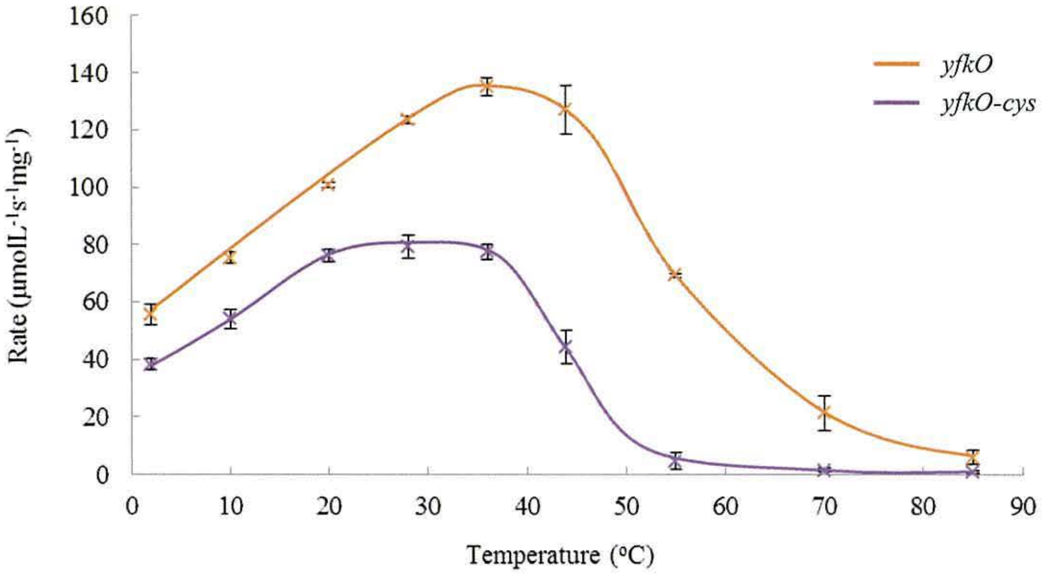

Figure 3.7.5. A graph showing the rate of hydroxylamine derivative generation (λ_{max} = 420 nm, ε = 1200 L $mol^{-1}cm^{-1}$) of yfkO and yfkO-cys with 0.2 mM CB1954 and 0.6 mM NADH at different temperatures.

The reaction rate increases for both NTRs until the optimum temperature between 30 °C and 40 °C is reached. Above this temperature the reaction rate decreases, although *yfkO* is significantly more stable at higher temperatures than *yfkO-cys*.

3.8 Comparison and discussion of nitroreductase kinetic properties

Each of the five NTR candidates reduced CB1954 to 2- and 4-hydroxylamine derivatives. Details of K_m, V_{max}, turnover numbers, specificity constants and optimum environmental conditions are summarised in in *Table 3.8.1.*

Table 3.8.1. Kinetic parameters and optimum conditions of the five NTRs nfrA2, nfrA2-cys, nfrA1, yfkO and yfkO-cys with CB1954. ND indicates 'not determined'.

NTR	**V_{max}** ($\mu molL^{-1}s^{-1}$)	**K_m** ($\mu molL^{-1}$)	**K_{cat}** (s^{-1})	**K_{cat}/K_m** ($M^{-1}s^{-1}$)	**Optimum pH**	**Optimum Temp.** (°C)
nfrA2	0.77 + 0.08	19.16 + 1.6	5.94	3.10×10^5	7.5	40
nfrA2-cys	0.56 + 0.07	20.29 + 1.6	4.39	2.16×10^5	7	40
nfrA1	0.92 + 0.09	685.9 + 43.3	29.1	4.24×10^4	7-9	40
yfkO	ND	>2359	ND	ND	7.5	35
yfkO-cys	4.62 + 0.46	1085.65 + 52.3	14.07	1.30×10^4	7.5	30

It is apparent in all the assays that genetic modification of the NTRs to include a sequence of 12 consecutive cysteine residues reduces enzyme activity towards CB1954. For *nfrA2* and *nfrA2-cys* these effects are relatively minimal, with similar kinetic parameters and similar stabilities in different environmental conditions. For *yfkO* and *yfkO-cys* the difference is more significant, the latter showing significantly lower activity towards the prodrug and is significantly less stable in different environmental conditions.

Figure 3.8.1 and *Figure 3.8.2* show overlays of the assays used to determine the K_m and V_{max} values for each of the NTRs, highlighting the different kinetic profiles of the different NTRs.

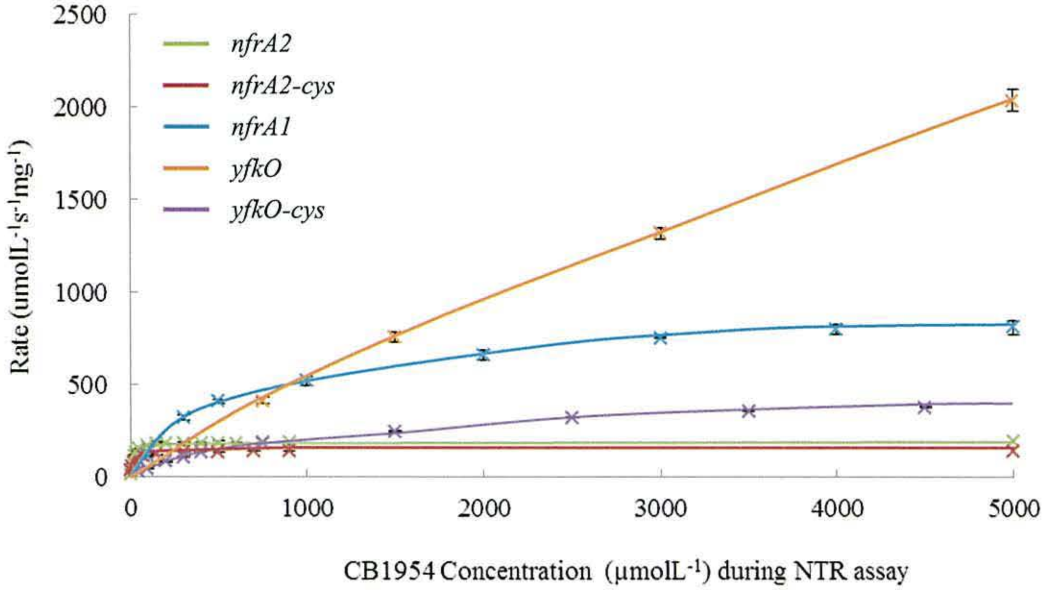

Figure 3.8.1. A graph showing the rate of hydroxylamine derivative generation (λ_{max} = 420 nm, ε = 1200 L $mol^{-1}cm^{-1}$)with increasing substrate concentration up to 5 mM CB1954 for the five candidate NTRs nfrA2, nfrA2-cys, nfrA1, yfkO and yfkO-cys

As is expected the reaction rates for the NTRs at different substrate concentrations varies significantly, with *yfkO* showing the fastest reaction rate at 5 mM CB1954 and *yfkO-cys* the fastest cysteine modified NTR. V_{max} could not be reached for *yfkO* given the limited solubility of CB1954, however the remaining NTRs were fully characterised.

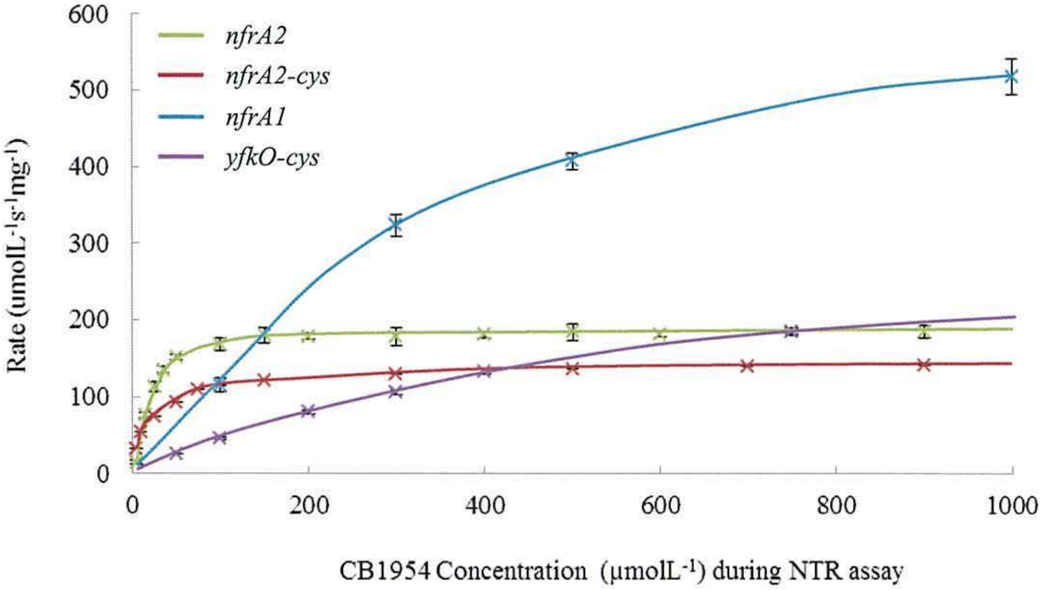

Figure 3.8.2. A graph showing the rate of hydroxylamine derivative generation (λ_{max} = 420 nm, ε = 1200 L $mol^{-1}cm^{-1}$) with increasing substrate concentration up to 1 mM CB1954 for the four candidate NTRs that were fully characterised, nfrA2, nfrA2-cys, nfrA1 and yfkO-cys.

Typically for a reaction that proceeds *via* a bi-bi ping-pong mechanism the specificity constant or catalytic efficiency K_{cat}/K_m is the most reliable indicator of activity as it is independent of the cofactor concentration.[73] Further to this the limited solubility of CB1954 under experimental conditions makes it difficult to measure activity beyond the initial reaction rate (>10 *x* [S] K_m) meaning estimates of independent global K_m and K_{cat} values can be extremely unreliable. As the concentration of prodrug needed for clinical applications are likely to be in the low μM range[44, 48] the specificity constant becomes an ideal measure of activity to compare the different enzymes.[74]

Table 3.8.2. A table compiling the kinetic parameters of NTRs with CB1954. Data is taken from literature references a,[72] b,[73] c,[74] d,[234] e,[86] f,[87] and m, this study

Organism		**NTR**		**K_m (μM)**	**K_{cat} (s^{-1})**	**K_{cat}/K_m ($M^{-1}s^{-1}$)**
Escherichia coli						
	a	*NfsB*	NADH	220	16	7.3E+04
	b	*NfsB*	NADH	900	6.2	6.9E+03
	c	*NfsB*	NADH	17200	140	8.1E+03
	a	*NfsB*	NADPH	46	2.9	6.3E+04
	d	*NfsB*	NADPH	860	6.0	7.0E+03
	b	*NfsB N71S/F124K*	NADH	170	7.5	4.4E+04
	b	*NfsB Y68G*	NADH	1830	20	1.1E+04
	b	*NfsB N71S*	NADH	189	7.0	3.7E+04
	c	*NfsB F124N*	NADH	3080	95	3.1E+04
	c	*NfsB T41L/N71S*	NADH	216	153	7.1E+05
	a	*NfsA*	NADH	3600	26	7.2E+03
	a	*NfsA*	NADPH	11000	62	5.6E+03
	a	*AzoR*	NADH	1400	0.15	1.1E+02
	a	*AzoR*	NADPH	6600	0.15	2.3E+01
	a	*NemA*	NADH	56	0.22	3.9E+03
	a	*NemA*	NADPH	55	0.05	8.7E+02
Bacillus licheniformis						
	d	*yfkO*	NADPH	30	1067	3.6E+07
	m	*yfkO*	NADH	>2359	ND	ND
	m	*yfkO-cys*	NADH	1086	14	1.3E+04
	m	*nfrA2*	NADH	19	5.9	3.1E+05
	m	*nfrA2-cys*	NADH	20	4.4	2.2E+05
	m	*nfrA1*	NADPH	686	29	4.2E+04
Staphylococcus saprophyticus						
	e	*Ssap-NtrB*	NADPH	1065	2.3	2.1E+03
Bacillus amyloliquefaciens						
	f	*ywrO*	NADPH	618	8.2	1.3E+04

The *E. coli* NTRs *MdaB, WrbA, KefF, YcdI, YdjA, YieF, YcaK* from reference *a*[72] and *Salmonella typhimurium ydjA* and *ydjA-cys* (*m*, this study) are inactive with CB1954.

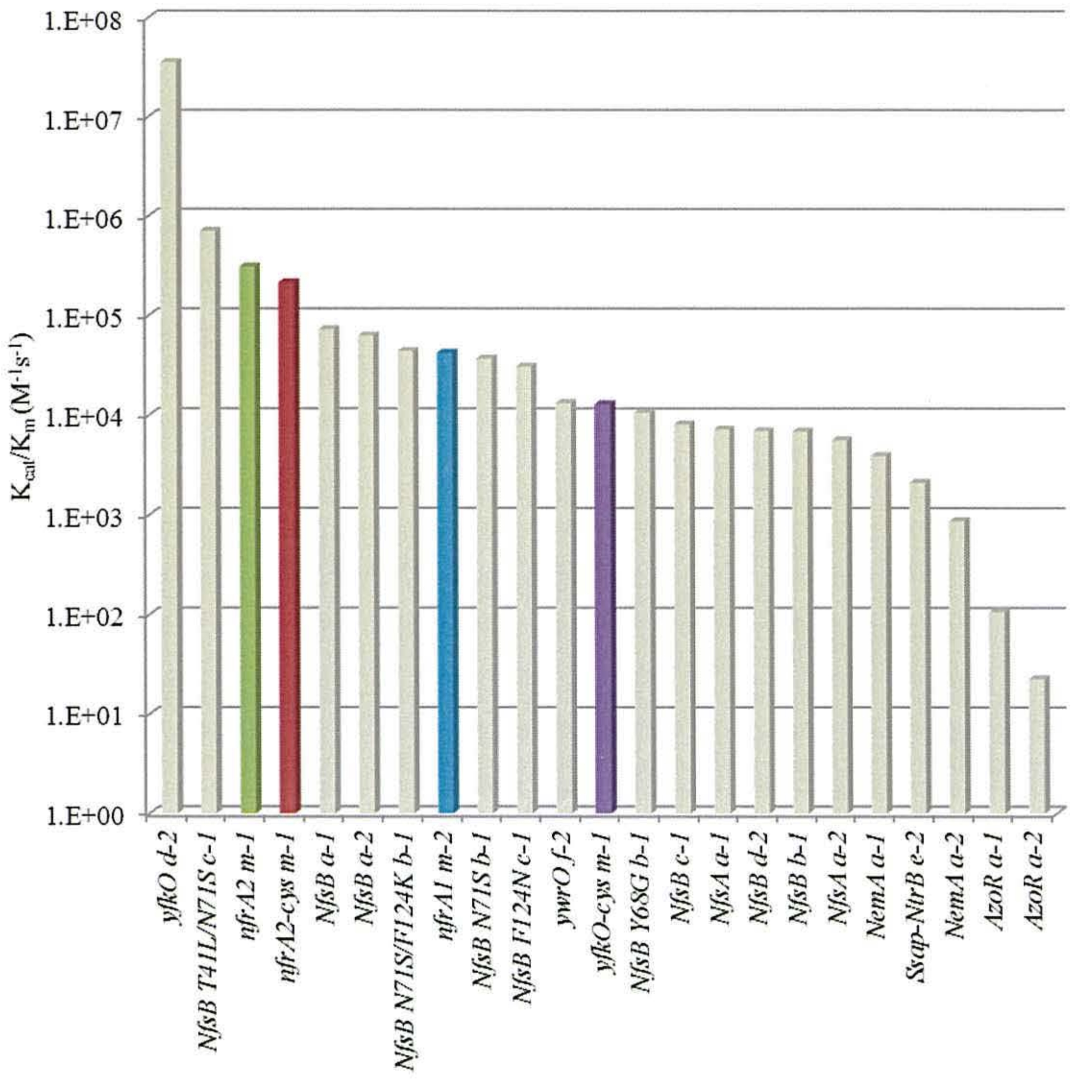

Figure 3.8.3. A graphical representation of the specificity constants listed in Table 3.8.2. The letters correspond to the references in Table 3.8.2 and the numbers represent the cofactor used in the study, 1 for NADH and 2 for NADPH. NTRs from this study are coloured green, nfrA2; red, nfrA2-cys; blue, nfrA1 and purple, yfkO-cys.

yfkO-cys and *nfrA1* compare well to other NTRs from the literature, with specificity constants of the order of the well-studied *E. coli NfsB* and some of its engineered analogues.[72-74] *nfrA2* and *nfrA2-cys* compare very favourably to other NTRs, with only one engineered *nfsB* NTR showing a higher specificity constant. This particular NTR was the result of intensive screening of engineered enzymes and combining the most effective mutations found from several studies. The only other NTR to show a higher specificity constant to *nfrA2* and *nfrA2-cys* is *yfkO* from *B. licheniformis*, which was also studied in this investigation.

Figure 3.7.3 indicates that V_{max} of *yfkO* would not be reached until concentrations of CB1954 were greater than the 5 mM used in this assay. However despite not being able to fully characterise the NTR, it would appear that the specificity constant would not be of the magnitude reported in the literature and I suspect not as high as *nfrA2* and *nfrA2-cys*.

The initial reaction rate should be taken when determining the kinetic parameters of an enzyme. However in the case of reference *d* the reaction was started and aliquots taken at six minute intervals.[234] It is not clear why this method was used, but assaying *yfkO* in this way may have led to the unusually large result obtained in the study by Emptage *et al.* and explain why the result is so different to this study, where the initial reaction rate was taken to be the generation of hydroxylamino derivatives produced during the first 30 seconds of reaction.

3.9 Concluding remarks

Measuring the activity of a series of NTRs with CB1954, *nfrA1*, *nfrA2(-cys)* and *yfkO(-cys)* were found to show potential application for Au-MNP DEPT. Given the specificity constants and activities of the NTRs in environments similar to those found in physiological conditions, the enzymes have excellent potential to be of use not just in Au-MNP DEPT but also to other NTR CB1954 therapies.

The structures of *nfrA1*, *yfkO* and *nfrA2* from *B. Licheniformis* have not yet been elucidated so the configuration around the active site of the enzymes remains unknown. However the results of extensive screening of single, double and triple *nfnB* mutants from *E. Coli* indicates that there is great potential, once the structural conformation is known, to genetically engineer the NTRs for improved activity with the prodrug.[73, 74] Given the already high specificity constants of *nfrA2* and *nfrA2-cys* and optimum activities at physiological pH's and temperatures these NTRs are of particular interest for DEPT.

The inactivity of *ydjA* from *Salmonella typhimurium* to CB1954 is also noteworthy as *ydjA* from *E. Coli* was predicted to be very active with a range of prodrugs given the wider, more flexible active site observed in X-ray studies of the protein. However the article by Prosser *et al.* which screened a range of NTRs from *E. Coli* found *ydjA* to be inactive with CB1954,[72] suggesting the general structure of *ydjA* is not suitable for DEPT, which is supported by this study.

Chapter 4

MAGNETIC NANOPARTICLES

4.1 Superparamagnetic nanoparticles

4.1.1 Introduction to superparamagnetic iron oxide nanoparticles

As is well reviewed in the literature, coprecipitation of iron ions in aqueous solution can yield superparamagnetic iron oxide nanoparticles of varying sizes and morphologies depending on the reagents used and reaction conditions, producing magnetic nanoparticles for potential application in biomedicine.[143, 152, 235] In a non-oxidising, basic environment, the reaction will proceed as *Equation 4.1.1* to produce magnetite.

$$2Fe^{3+} + Fe^{2+} + 8HO^{-} \rightarrow Fe_3O_4 + 4H_2O$$

Equation 4.1.1. Formation of magnetite from aqueous iron ions in a non-oxidising environment.

In an acidic environment magnetite can also transform to maghemite (γ-Fe_2O_3), shown in *Equation 4.1.2*.

$$Fe_3O_4 + 2HCl \rightarrow \gamma Fe_2O_3 + FeCl_2 + H_2O$$

Equation 4.1.2. Formation of maghemite (γ-Fe_2O_3) from magnetite.

Magnetite and maghemite are of the spinel group $A^{2+}B_2^{3+}O_4^{2-}$, the crystal structure is face centre cubic (fcc) with each oxide providing one octahedral site and two tetrahedral sites, in a normal spinel structure half of the octahedral sites are filled by B^{3+} cations and one eighth of the tetrahedral sites by A^{2+} cations. Magnetite is inverse spinel as both Fe^{2+} and Fe^{3+} are high spin, meaning Fe^{3+} is readily displaced by Fe^{2+} so both Fe^{2+} and Fe^{3+} are distributed among the octahedral sites. Oxidation of magnetite to maghemite occurs *via* diffusion of Fe^{2+} towards the surface, leaving some of the previously occupied octahedral sites vacant.[236] Accounting for the vacancies gives a unit cell of maghemite $(Fe_8^{3+})_{Td}(Fe_{40/3}^{3+}/\square_{8/3})_{Oh}O_{32}$ where $\square$ represents a site vacancy, compared to the magnetite structure $(Fe_8^{3+})_{Td}(Fe_8^{3+}/Fe_8^{2+})_{Oh}O_{32}$.[237]

In atmospheric conditions surface Fe^{2+} cations of magnetite oxidise to Fe^{3+} very rapidly, creating a surface layer effect of maghemite. Oxidation of the bulk material is kinetically hindered by the diffusion of Fe^{2+} cations through the crystal structure to the surface, so is heavily dependent on particle size; at particle diameters under 10 nm magnetite readily oxidises to maghemite throughout the nanocrystal given the small particle size.[238]

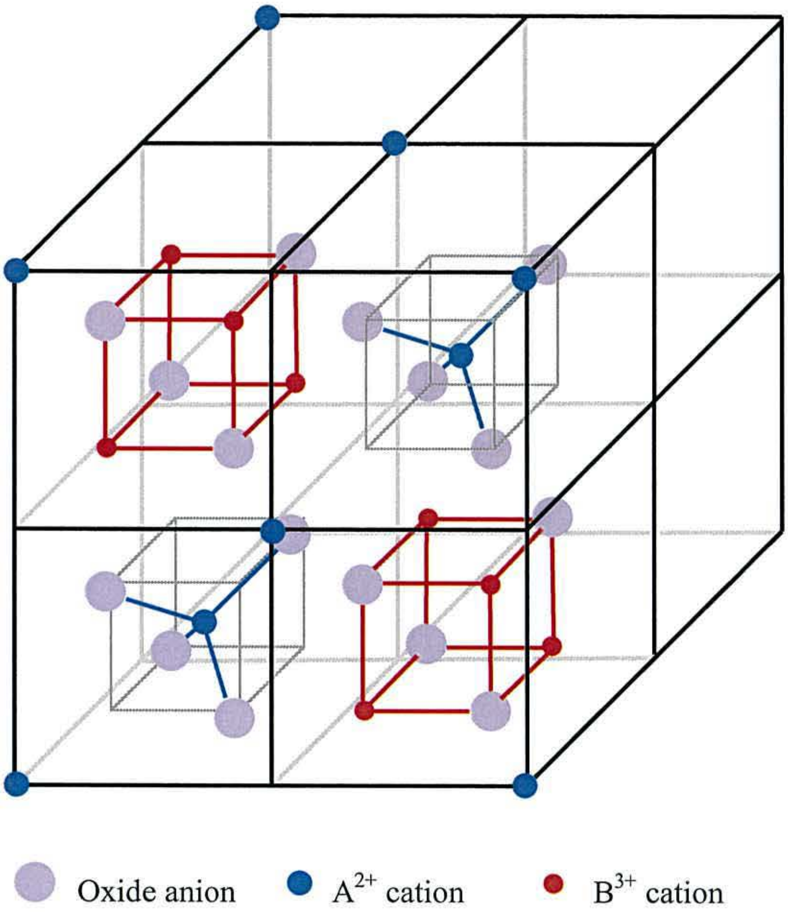

Figure 4.1.1. A partial illustration of the unit cell of a normal spinel structure. The full unit cell contains a further four sub-units in the back half of the illustration giving a total of 32 oxide anions, 16 B^{3+} cations and 8 A^{2+} cations.

Sub 10 nm iron oxide particles are called both magnetite and maghemite throughout the literature, but can more generally be referred to as superparamagnetic iron oxide nanoparticles (SPION) given the rapid oxidation of the former to the latter.[149] The coprecipitation method as described by Massart is arguably the simplest method to produce SPION, utilising iron chlorides in a 2:1 molar ratio of Fe^{3+}:Fe^{2+} and either sodium hydroxide or ammonium hydroxide as a base.[150] The black precipitate resulting from dropwise addition of the iron chlorides to the base can be easily isolated by magnetic decantation or centrifuging, washed with water and peptised by addition of either tetramethylammonium hydroxide (TMAOH) or perchloric acid. The isoelectric point of SPION is around pH 7, meaning the particles are only stable as a sol at a $pH < 5$ or $pH > 9$, hence the need to peptise the nanoparticles with either an acid or base, SPION produced using the Massart method are shown in *Figure 4.1.2*.

Figure 4.1.2. SPION produced from the Massart method.[150] *Left image, SPION in 1 M TMAOH and right image, SPION after stirring with 2 M perchloric acid, isolating by centrifuging and peptising with deionised water.*

4.1.2 Characterisation of synthesised superparamagnetic iron oxide nanoparticles

Transmission electron microscopy (TEM) was used to evaluate the SPION produced using the Massart method, the results of which are shown in *Figure 4.1.3*.

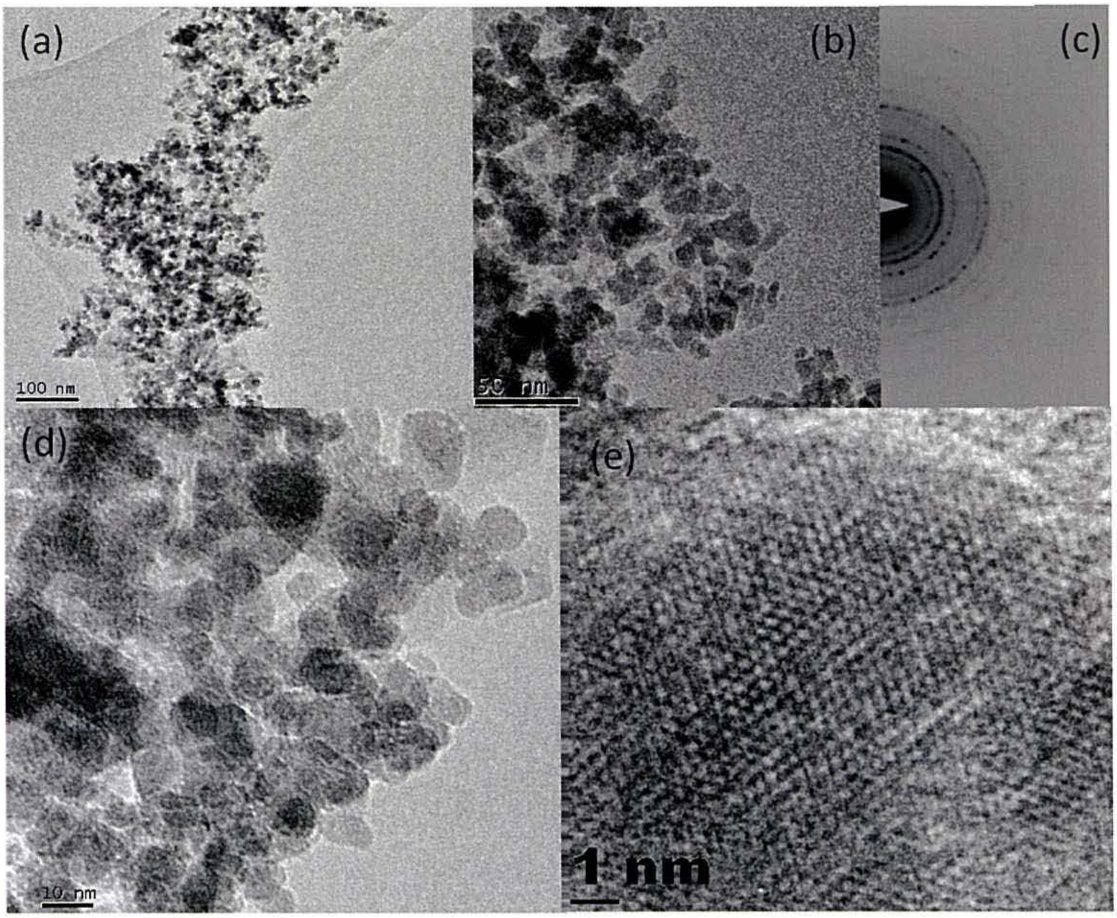

Figure 4.1.3. Results of TEM analysis of the SPION. (a), (b) and (d) are images of the particles at different magnifications. (c) selected area electron diffraction corresponding to spinel structure and (e) a high resolution image of a single particle highlighting its crystallinity

Powder x-ray diffraction (PXRD) was used to further assess the crystal structure of the particles and compare the SPION to magnetite/maghemite standards and the literature.[239] *Figure 4.1.5* through *Figure 4.1.8* show the XRD patterns with respective diffraction planes assigned. Detailed XRD spectra, along with peak assignments and the standard 2θ positions, relative peak intensities and corresponding diffraction planes for the inverse spinel structure of magnetite (JCPDS no. 19-0629) and defect spinel of maghemite (JCPDS no. 04-0755) are shown in the *Appendix*.

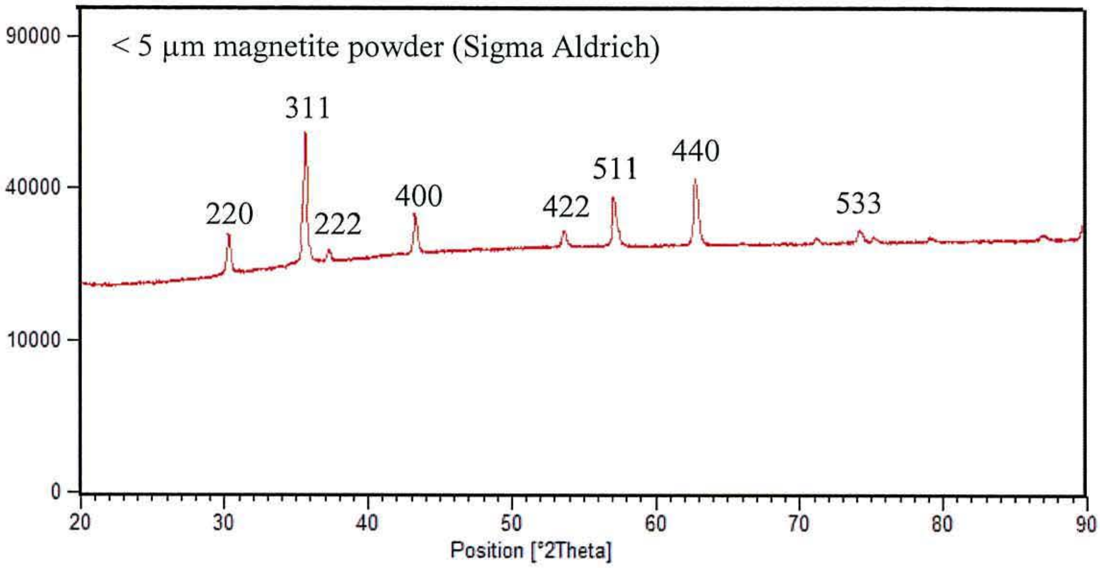

Figure 4.1.4. XRD pattern of < 5 µm magnetite powder as received from Sigma Aldrich. Full details shown in Table 01 and pattern 01 of the Appendix.

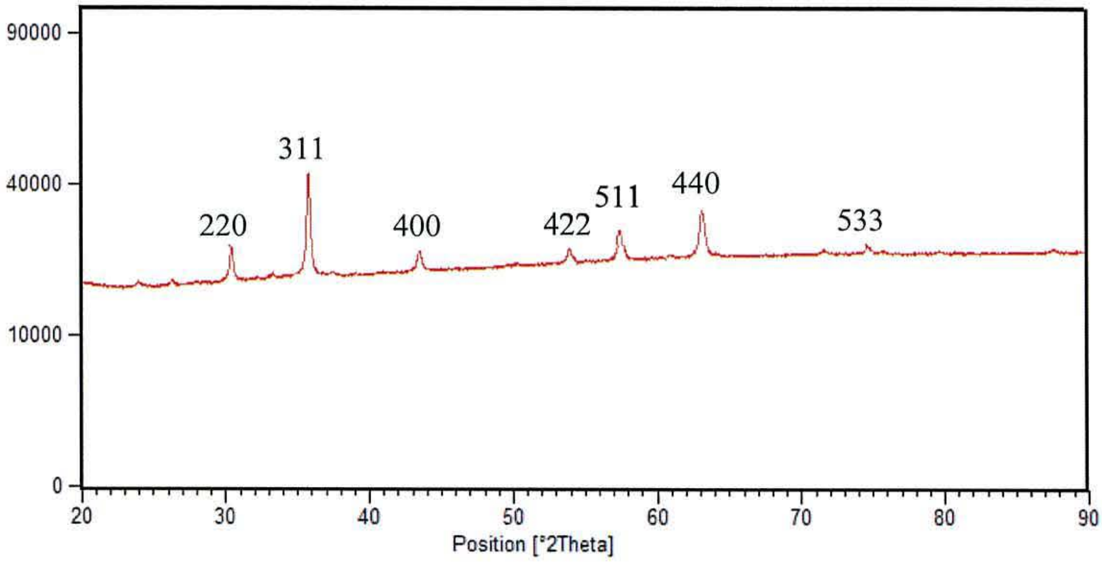

Figure 4.1.5. XRD pattern of 20 nm – 40 nm magnetite powder as received from Alfa Aesar. Full details shown in Table 02 and pattern 02 of the Appendix.

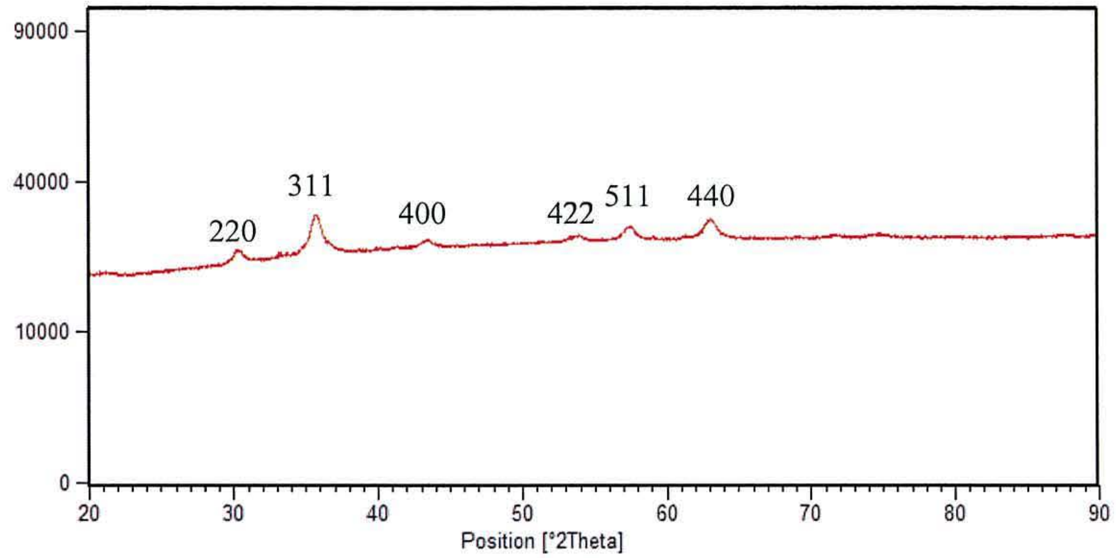

Figure 4.1.6. XRD pattern of 10 nm magnetite powder as received from Liquids Research Ltd. Full details shown in Table 03 and pattern 03 of the Appendix.

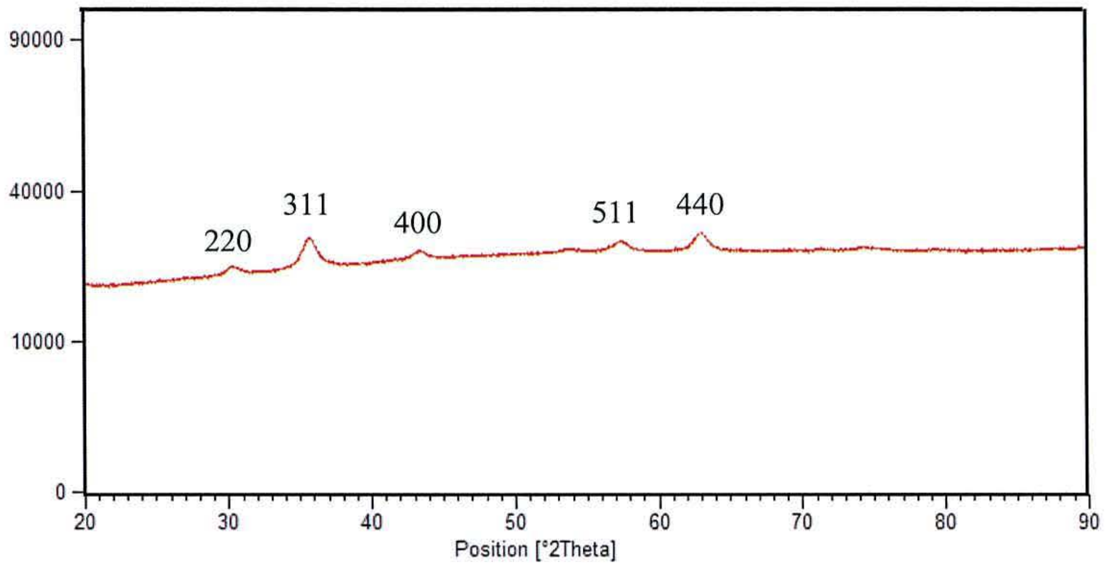

Figure 4.1.7. XRD pattern of as synthesised SPION. Full details shown in Table 04 and pattern 04 of the Appendix.

The XRD pattern for the SPION matches the JCPDS reference patterns for magnetite/maghemite. The key difference between *Figure 1.1.5* and *Figure 1.1.8* is the profiles of the peaks. The diffraction peaks of SPION are much broader and lower in intensity than those of the larger particles and most similar to the ≈ 10 nm sample obtained from Liquids Research Ltd. As the crystal size decreases from the larger crystals to those of nanoscale, the number of unit cells and diffraction planes within the crystal decreases, resulting in broader peaks for materials with smaller average crystal sizes.[240]

Peak broadening can be used to quantitatively assess average crystal size. However peak widths are influenced by a range of factors, including instrumental broadening, microstrain and crystal size and shape. Despite extensive calibration the average crystal sizes obtained *via* XRD measurements commonly differ significantly from those obtained from TEM, even when extensive care is taken to deconvolute the factors influencing peak profile.[239, 241, 242] This is in part due to the difficulties in obtaining true values for individual contributions to broadening, as well as accurately fitting peak profiles.

PANalytical X'Pert HighScore was used to evaluate the diffractograms, identify XRD peaks and fit the peak profiles against the experimental background, so that peak widths could be measured to give crystal and therefore particle size estimates. Applying this peak profiling to the iron oxide standards and then the as synthesised SPION yielded the following D_{XRD} values, which are within a ± 30% of the values expected and from TEM analysis. Full peak analysis is detailed in the *Appendix*.

Table 4.1.1. D_{XRD} measurements calculated from 311 peak widths using the Scherrer equation and K = 0.90.

Sample	**Peak position (2θ)**	**FWHM (2θ)**	**D_{XRD} (nm)**
20 nm – 40 nm powder	35.79	0.28	30
10 nm powder	35.73	0.96	9
SPION	35.67	1.08	8

TEM and XRD have been used to confirm the synthesised SPION are approximately 8 nm in size, roughly spherical in shape and crystalline. In solution SPION form a stable sol at pH < 5 or pH > 9 and display a superparamagnetic response in the presence and absence of a magnetic field, as shown in *Figure 4.1.9*.

Figure 4.1.8 A. SPION in the absence of a magnetic field

Figure 4.1.8 B. SPION in the presence of a magnetic field

Figure 4.1.8 C. SPION after removing from magnetic field and agitating

Using DLS the particles measured a z-average size of 63 nm in solution (see the *Appendix*). This diameter is substantially larger than the values obtained *via* TEM and XRD likely due to dilution of the sample in dH_2O. Without a stabilising surface ligand or suspending the particles in a highly charged environment they rapidly aggregate.

As expected the sol shows no distinct absorbance peak in the UV-visible region of the spectrum as seen in *Figure 4.2.0.*

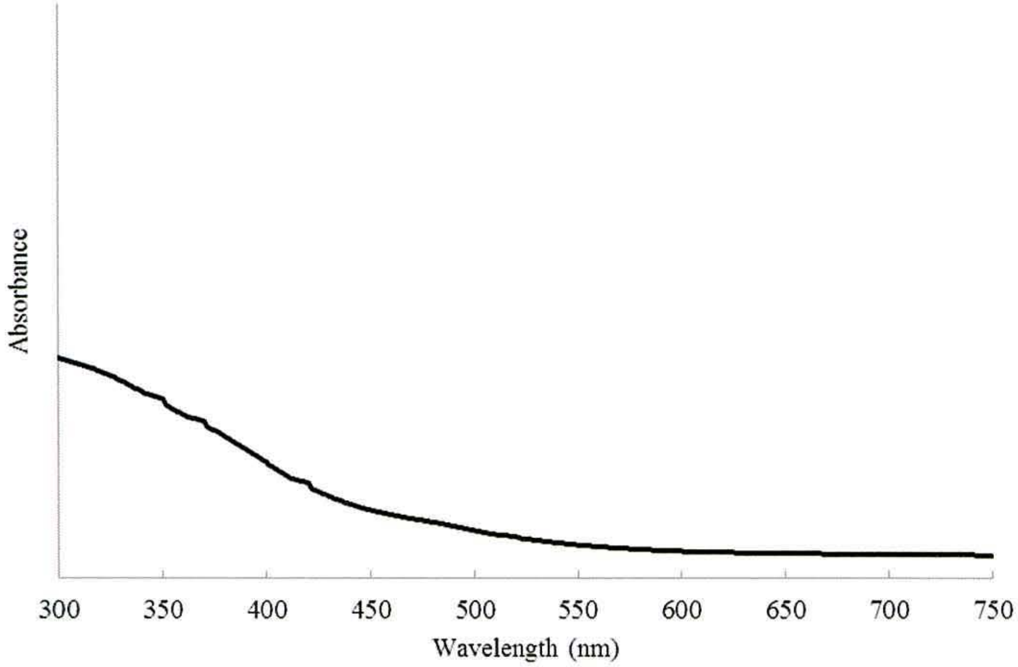

Figure 4.1.9. UV-vis spectrum of synthesised superparamagnetic iron oxide nanopaticles

4.2 Citrate reduction of Au onto iron oxide nanoparticles

Turkevich *et al.* developed a facile route to produce gold nanoparticles *via* reduction of Au^{3+} with citrate in aqueous solution.[243] This methodology was later refined by Frens[244] such that a gold colloid could be readily synthesised with average particle diameters of between 10 nm and 150 nm simply by altering the citrate:Au ratio.[244] A logical route to coating SPION with Au would be to perform a citrate reduction of Au^{3+} in a solution pre-populated with SPION. The experimental procedure employed by Lu *et al.* in their 2006 publication appears to follow such a route to yield magnetic nanoparticles with a surface coating of Au, as determined by SPR, EDAX and TEM.[230]

Analysis of the particles produced by Lu *et al.* suggested 3 possible populations of particle; bare SPION, particles of Au and Fe character and Au particles. Post reaction particles of two size populations were observed, one group < 10 nm (the expected size of bare SPION) and particles of approximately 20 nm which *via* TEM and EDAX appeared to be of Au character. EDAX suggested both Fe and Au were present in the mixed particle population, which would be expected whether or not SPION@Au were present, for example if the authors had inadvertently produced a separate Au colloid which was independent of the SPION. Lu *et al.* developed a magnetic filtration system to remove any non-magnetic entities and found that all particles post filtration possessed SPR (indicating an Au coating) and that the larger particles (of distinct Au character *via* TEM and EDAX) responded to a magnetic field such that a magnetic core/cores must be present, concluding both particle populations were SPION@Au.

The convenience of the SPION@Au preparation, being in aqueous solution and using only non-toxic reagents makes it an attractive method to employ, despite possible concerns of multiple particle types being produced. However attempted repetition of the reaction did not produce a stable magnetic sol. Two particle types were visibly present; a dark magnetic flocculate and a non-magnetic ruby red sol. The preliminary results are indicative of the reaction producing a classic gold colloid as detailed by Turkevich and Frens,[243, 244] and the SPION added to pre-seed the reaction solution, unstable without a tightly bound stabilising agent nor in a suitably high or low pH environment, flocculating.

A follow on study in 2008 by Pham *et al.*[218] utilised a very similar protocol to that of Lu *et al.*[230] which like this study also produced non-magnetic gold particles, however the authors also claim to have produced SPION@Au. Repeating the experiment as detailed by Pham *et al* did not yield a magnetic red colloid as described by the authors.

The preliminary observations of the Lu *et al.* and Pham *et al.* methods are that if SPION@Au are being produced during the citrate reduction reaction, they form a small fraction of the particle population. The ruby red particles which were stable as a sol did not respond to an external magnetic field of 1.28 T, suggesting the Au particles did not contain SPION cores.

4.3 Pre-seeding iron oxide particles with Au seeds

4.3.1 Seeding 50 nm iron oxide particles with gold nanoparticles

To avoid Au^{3+} nucleating during the reaction and growing to become gold particles without magnetic cores, small Au seeds can be first attached to SPION before further Au^{3+} reduction. This is an extension of the Brown *et al.* procedure of creating highly monodisperse gold colloids by reduction of Au^{3+} onto pre-existing Au particles.[232] By separating the nucleation and growth stages of particle generation, the authors were able to improve control of particle size and shape for Au colloids of larger particle size.

In 2009 Goon *et al.* published a procedure utilising this type of pre-seeding approach.[231] Fe_3O_4 particles were synthesised based on the Sugimoto method[245] and the magnetite cubes were functionalised with polyethyleneimine (PEI, Mw ≈ 25 000 $gmol^{-1}$, 0 to 4 gL^{-1}) and pre-synthesised 3 nm gold nanoparticles attached to the magnetite. Au^{3+} was then reduced onto the seeded magnetite particles to produce exclusively Au coated Fe_3O_4 nanoparticles. In this case the PEI acts to both stabilise the Fe_3O_4 and link Au seeds to the magnetite cores prior to surface coating. Preliminary characterisation of the particles obtained when repeating the Goon *et al.* method are shown in the following figures, full details of the XRD spectra are detailed in the *Appendix*.

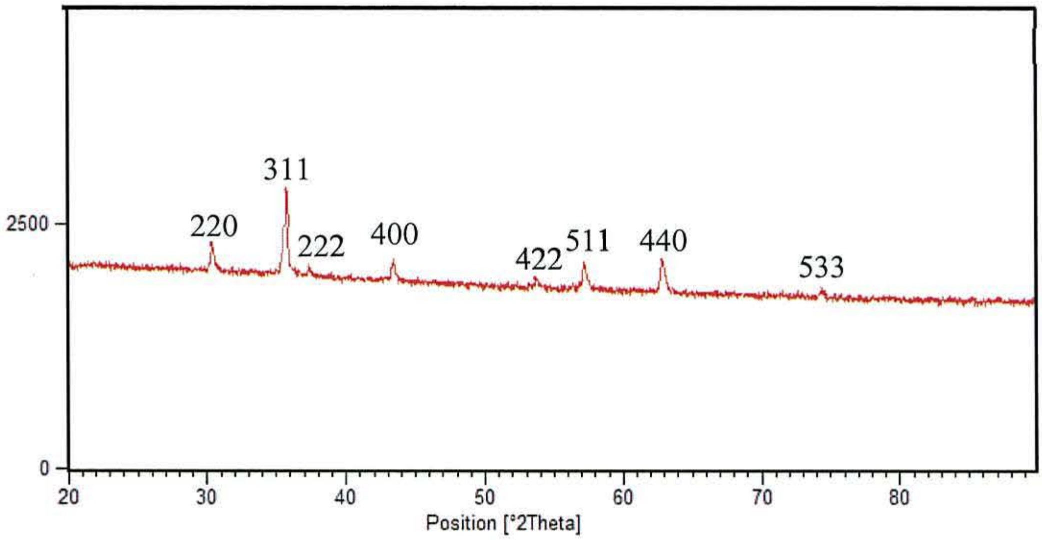

Figure 4.3.01. XRD pattern of Fe_3O_4 particles synthesised using the Goon et al. method.[231] *Full details shown in Table 05 and pattern 05 of the Appendix.*

The peaks of the diffraction pattern in *Figure 4.3.01* match those expected for magnetite, broadening associated with the 311 peak correspond to an average magnetite particle size of 45.37 nm, the size reported in the Goon *et al* article is approximately 50 nm (by TEM). Gold nanoparticles of approximately 3 nm were synthesised and stirred with the PEI functionalised magnetite for 2 hours, the Au seeded magnetite particles were then recovered magnetically.

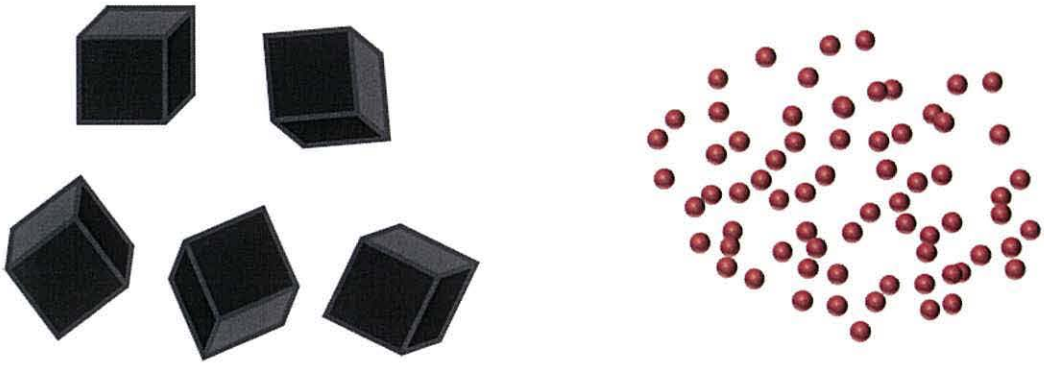

A. Illustration of PEI functionalised Fe_3O_4 *cubes*

B. Illustration of Au seeds

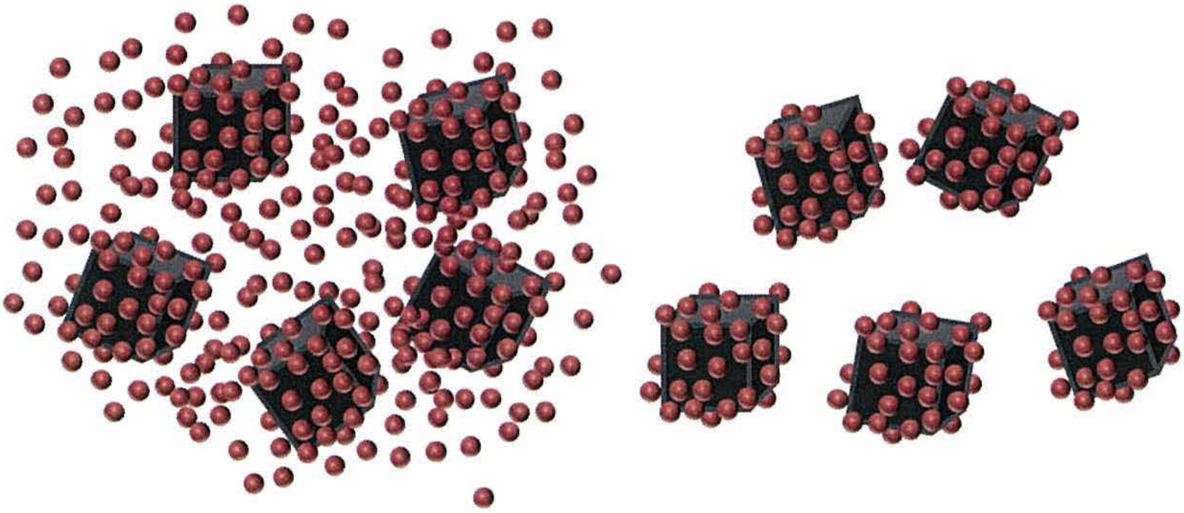

C. Illustration of PEI functionalised Fe_3O_4 *cubes being stirred with Au seeds*

D. Illustration of Au seeded Fe_3O_4 *after magnetic recovery from seeding solution*

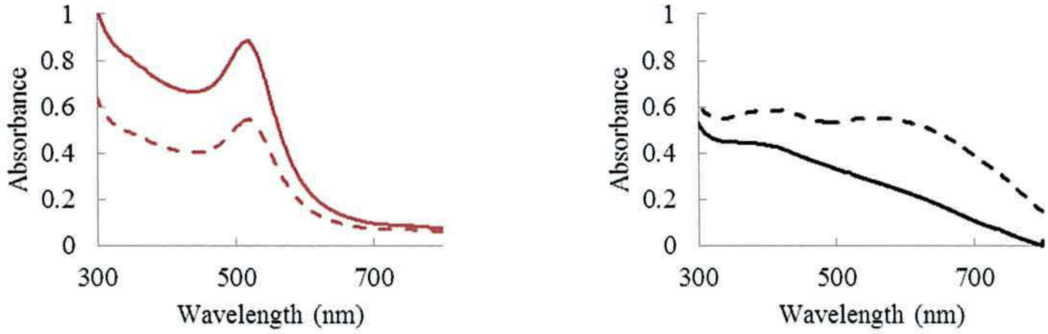

E. UV-vis spectra of Au seeds before stirring with magnetite (solid line) and after stirring with magnetite (dashed line).

F. UV-vis spectra of 50 nm magnetite before Au seeding (solid line) and after Au seeding (dashed line).

Figure 4.3.02. Graphical illustrations (A to D) and UV-spectra (E and F) detailing the Au seeding of PEI functionalised Fe_3O_4*.*

Figure 4.3.2 F shows the change in absorbance profile for the magnetite after seeding, with a broad peak around 600 nm which is absent for the un-seeded magnetite. This correlates well with the observations by Goon *et al.* and corresponds to the SPR of the Au seeds bound to the magnetite surface. SPR is extremely sensitive and by covalently bonding the Au seeds to magnetite the electron environment at the gold nanoparticle surface changes dramatically, causing this large shift in λ_{max}.

The concentration of a gold colloid can be determined experimentally by absorbance using *Equation 4.3.1* and *Equation 4.3.2*, as is well documented in the literature.[246-248] *Table 14* in the *Appendix* details the molar extinction coefficients for spherical citrate stabilised gold colloid standards of different sizes (Cytodiagnostics) giving solutions of k = 3.1927 and a = 11.077.[248]

$$A = \varepsilon c l$$

Equation 4.3.1. Beer lambert law. A represents absorbance, ε the molar extinction coefficient, c the concentration and l the path length.

$$ln\varepsilon = klnD + a$$

Equation 4.3.2. The linear relationship between particle diameter and molar extinction coefficient. ε represents the molar extinction coefficient and D the average particle diameter, k and a are constants.

As no TEM analysis was available to analyse the 3 nm seeds their loading onto the magnetite cores can only be calculated theoretically. The theoretical concentration of the Au colloid (assuming 100% reduction of Au^{3+} to 3 nm spheres) is 2.26 x 10^{17} particlesL^{-1}. From *Figure 4.3.02 E* the λ_{max} of the colloid is 520 nm, as expected for a citrate stabilised gold sol of this size and where A = 0.88544, D = 3 nm, c = 2.47 x 10^{17} particlesL^{-1}, which is in reasonable agreement with the theoretical value calculated measuring the absorbance at 520 nm. After stirring the Au seeds with PEI functionalised magnetite for 2 hours and magnetically recovering the Au-seeded magnetite the absorbance at 520 nm drops to A = 0.54603, corresponding to c = 1.52 x 10^{17} particlesL^{-1}, meaning 8.7 x 10^{15} Au seeds bound to the magnetite surface during stirring and were therefore subsequently magnetically removed. This represents a loading of approximately 640 Au seeds per magnetite core and given that excess gold particles remain in the seeding solution it suggests all available binding sites of the magnetite surface are occupied with seeds.

Reduction of Au^{3+} onto the Au seeded magnetite was performed by sequential addition of $HAuCl_4$ and NH_2OH, the intention being for the surface bound Au seeds to act as nucleation sites for the gold ions in solution, causing the seeds to swell in size and produce a complete surface covering of Au over the magnetite cores. *Figure 4.3.03* shows the UV-vis spectra of aliquots taken from the reaction vessel after each Au coating.

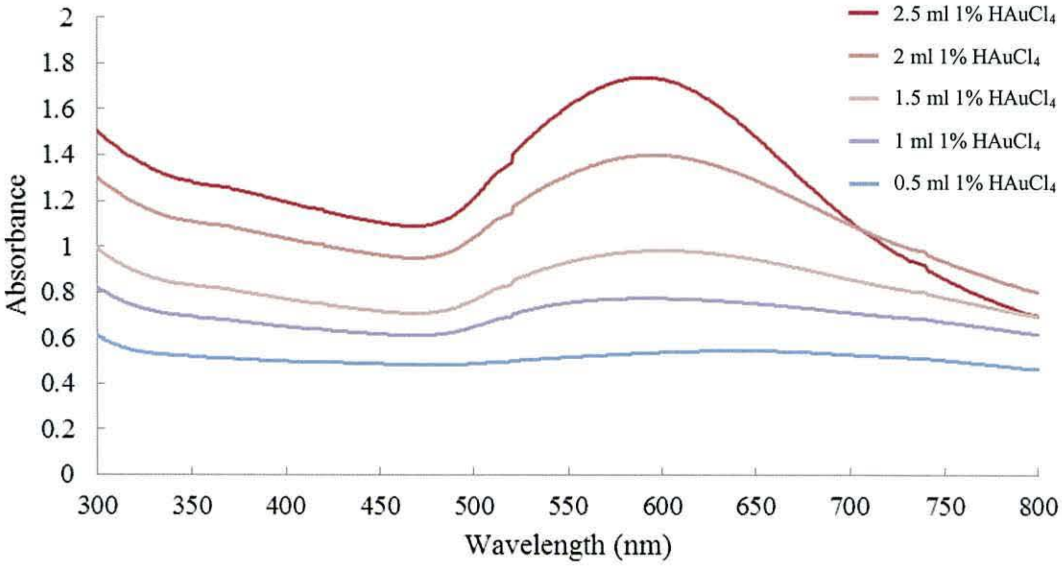

Figure 4.3.03. UV-vis spectra showing the absorbance profile of the Au coated magnetite after sequential addition of $HAuCl_4$ and NH_2OH as described by Goon et al.[231]

The UV-vis spectra of the Au coating process show a broad indistinct peak at around 650 nm blue shift and become more pronounced with each Au^{3+} addition, by the fifth addition there is a distinct peak with λ_{max} = 591 nm corresponding well to both the expected wavelength and the value reported by Goon *et al.* As the Au seeds grow and coalesce to form a layer over the Fe_3O_4 surface, the particle surface becomes increasingly similar to that of an Au nanoparticle.[231] Hence the gradual return of SPR. Au particles of larger sizes have higher λ_{max} as predicted by Mie theory and are observed experimentally (100 nm citrate stabilised Au colloid, Cytodiagnostics, λ_{max} = 572 nm).

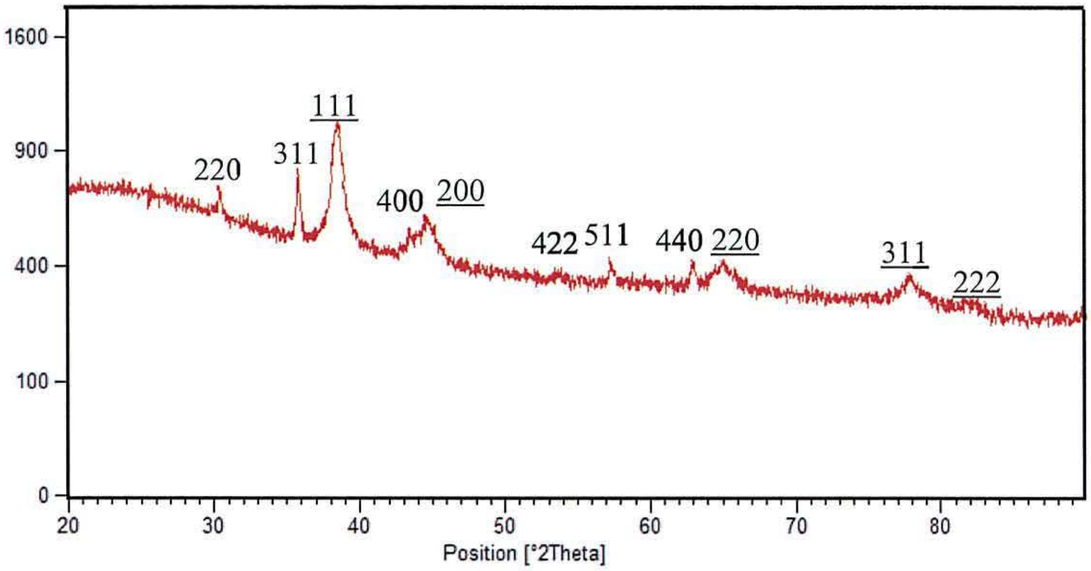

Figure 4.3.04. XRD pattern of Fe_3O_4 after pre-seeding with 3 nm Au and 5 iterative additions of $HAuCl_4$ and NH_2OH. Diffraction planes correspond to magnetite (unformatted numbers) and gold (underlined numbers). Full details shown in Table 06 and pattern 06 of the Appendix.

The XRD pattern shows the expected peaks for both magnetite and gold, for reference, XRD patterns of gold colloid standards are shown in the following figures. Detailed XRD patterns, along with peak assignments and the standard 2θ positions, relative peak intensities and corresponding diffraction planes for the fcc structure of gold (JCPDS no. 01-1172) are shown in the *Appendix*.

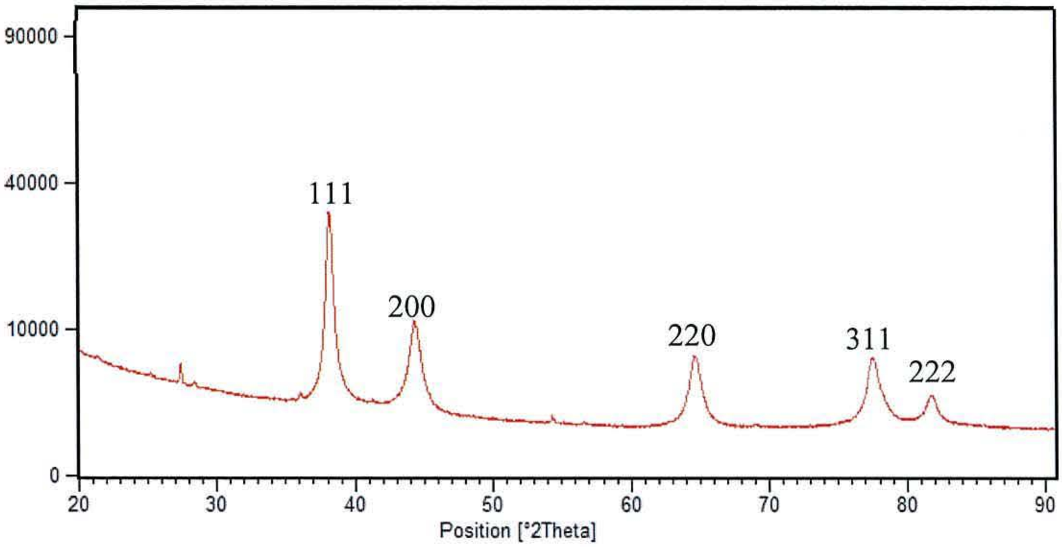

Figure 4.3.05. XRD pattern of 20 nm gold colloid as received from BioAssay Works. Full details shown in Table 07 and pattern 07 of the Appendix.

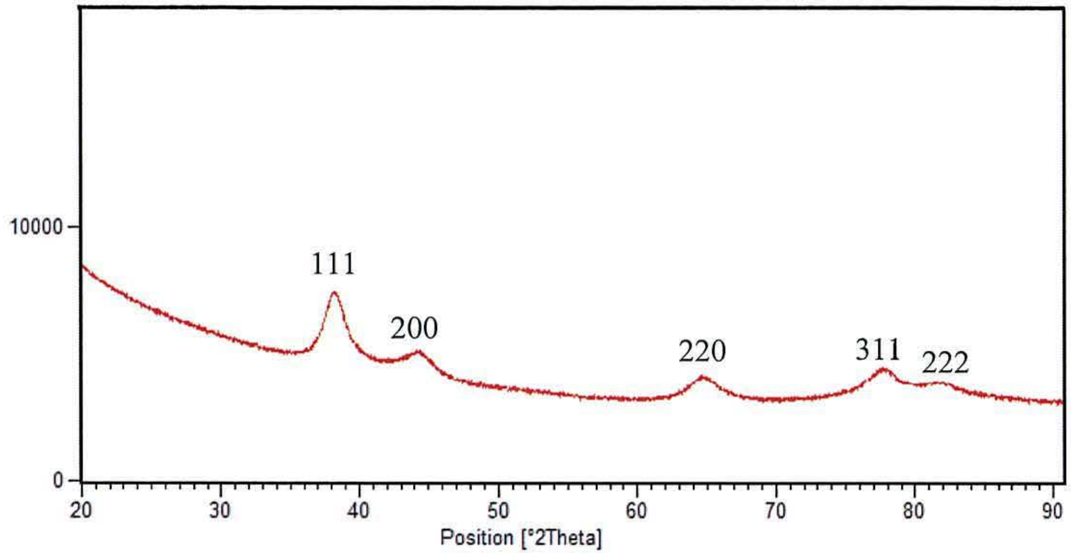

Figure 4.3.06. XRD pattern of 10 nm gold colloid as received from nanoComposix. Full details shown in Table 08 and pattern 08 of the Appendix.

Quantitative analysis of the coated Fe_3O_4@Au cannot be conducted using UV-vis and XRD alone. However the preliminary results support the findings of Goon *et al.* that magnetic Fe_3O_4 particles were synthesised and small Au seeds successfully attached to the surface, further reduction of Au^{3+} onto these particles resulted in a prominent SPR peak with XRD confirming the presence of nanocrystalline Au. The result is a stable magnetic sol which possesses the plasmonic properties of a gold colloid as shown in *Figure 4.3.03*.

The preliminary findings of this investigation suggest that pre-seeding of SPION with Au prior to further Au reduction is a potential strategy for the generation of SPION@Au. For application in MNP-DEPT the nanoparticles must be superparamagnetic, have an Au surface coating and importantly be of a biocompatible diameter, which is < 100 nm and ideally around 50 nm or smaller. The Goon *et al.* strategy is potentially a viable approach to generate these nanoparticles and by utilising smaller iron oxide particles than the ≈ 50 nm magnetite cores used by Goon *et al.* before Au coating it is hoped this can be achieved.

4.3.2 Seeding 10 nm iron oxide particles with gold nanoparticles

0.1 M TMAOH ($N(CH_3)_4^+ OH^-$) stabilised SPION as characterised in 4.1 were stirred with four different concentrations (1 gL^{-1}, 10 gL^{-1}, 50 gL^{-1} and 100 gL^{-1}) of polyethylenimine (PEI) (Sigma Aldrich, branched ~25000 $gmol^{-1}$) for 2 h, washed three times with dH_2O and redispersed in dH_2O. *Figure 4.3.07* shows a photograph of the obtained colloids.

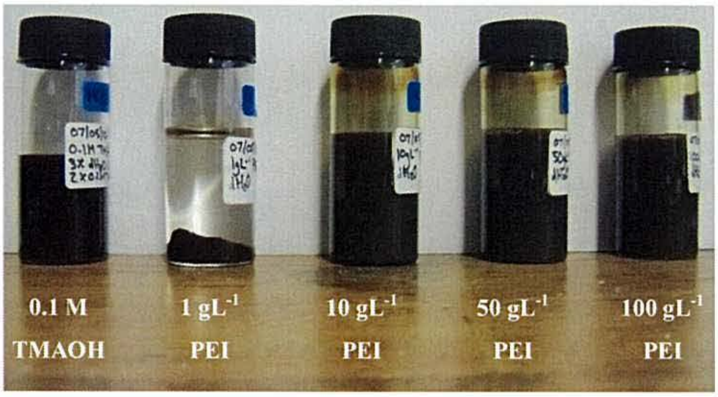

Figure 4.3.07. SPION after functionalising with respective concentrations of PEI, washing and redispersing in dH_2O

After functionalising SPION at concentrations of 10 gL^{-1} PEI and above, magnetic sols are formed which are stable in dH_2O for extended periods. After functionalising for 2 hours at the lower concentration of 1 gL^{-1} PEI the particles flocculate during washing stages, as the solution pH approaches 7.

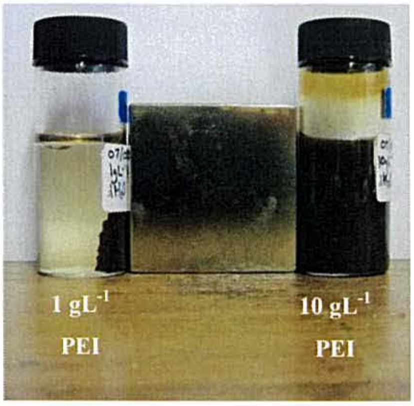

Figure 4.3.08. Image of magnetic response of PEI functionalised SPION

Attempts to seed PEI coated magnetite with 3 nm Au seeds consistently produced particle aggregations, the number of seeds necessary to produce an excess relative to the SPION was significantly higher than the theoretical value. It is possible that the branching, disordered nature of the PEI creates a mesh around the SPION core/cores such that individual SPION are not coated by a single uniform PEI layer, as observed when 50 nm Fe_3O_4 was functionalised. This could create a disordered SPION-PEI-Au seed structure, potentially leading to an extensive network of cross-linking and resulting in particle aggregation. To overcome this potential problem, simpler, shorter linking molecules were trialled instead of PEI.

4.3.3 Amine and amino acid functionalisation of iron oxide nanoparticles

Amino acids such as those shown in *Figure 4.3.09* are ideal candidates to stabilise SPION and bind Au seeds.

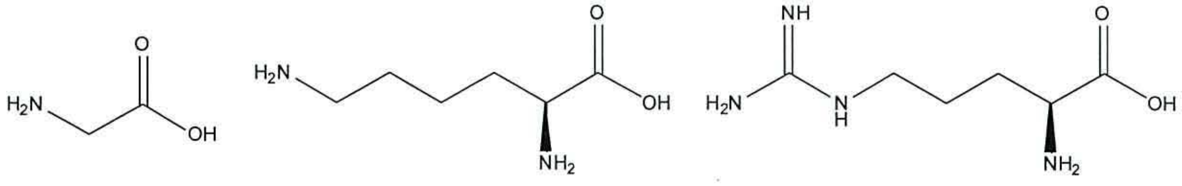

Glycine Lysine Arginine

Figure 4.3.09. Amino acids which can functionalise SPION.[249, 250]

Examples of amino acid stabilised SPION are not uncommon in the literature given the biocompatibility of the ligands and the ease with which the sols can be prepared.[249, 250] However Au nanoparticles are commonly stabilised with citrate, meaning ligand exchange from an Au/citrate solution and SPION/amino acid may occur. Amino acid stabilised SPION would therefore not be suitable for binding citrate stabilised Au seeds.

The use of diaminoalkanes allows direct linking of the Au seeds to the SPION without concern of ligand exchange. 1,2-diaminoethane was found to be excellent at peptising SPION and at bonding to Au seeds and is detailed in section 2.2.

A. SPION after washing and storing in dH_2O.[150] *B. SPION after peptising with 1,2-diaminoethane.* *C. As synthesised 3 nm Au seeds.*[232]

D. Au-loaded SPION in the absence of a magnetic field. *E. Au-seeded SPION in the presence of a magnetic field.*

Figure 4.3.10. Images showing the preparation and magnetic response of Au-seeded SPION using 1 2-diaminoethane as both a stabilising agent for SPION and Au linking agent.

Preliminary characterisation of the seeding and coating of SPION using 1 2-diaminoethane is shown in *Figure 4.3.11* and *Figure 4.3.12*, the full XRD pattern and peak assignments can be found in the *Appendix*.

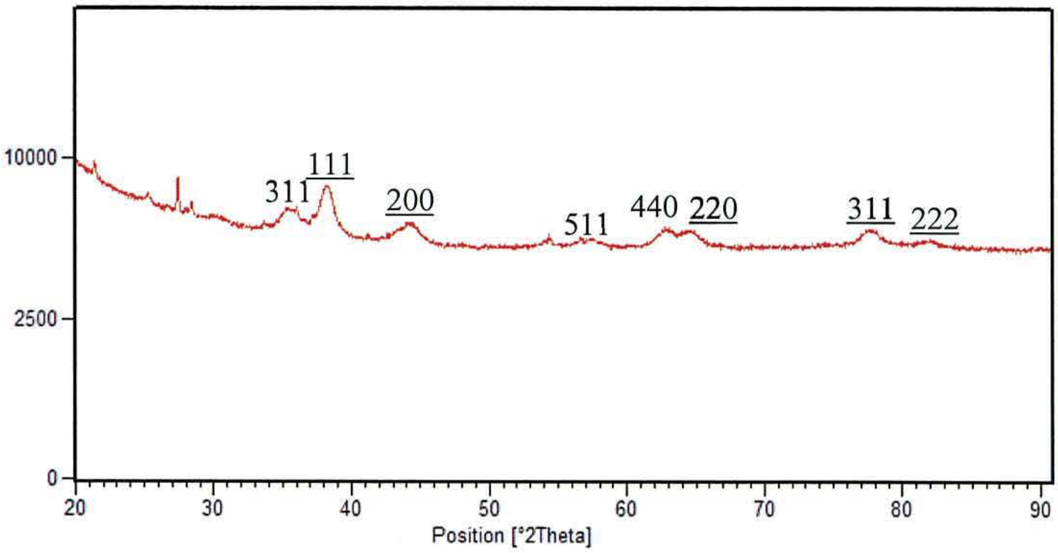

Figure 4.3.11. XRD pattern of Au-seeded SPION. Diffraction planes correspond to SPION (unformatted numbers) and gold (underlined numbers) Full details shown in Table 09 and pattern 09 of the Appendix.

The XRD pattern of the Au-seeded SPION shows the expected diffraction planes for both the SPION and Au, with the broad peaks corresponding to the small particle sizes. Attempts were made to reduce Au^{3+} onto Au-seeded SPION using $HAuCl_4$ and NH_2OH.

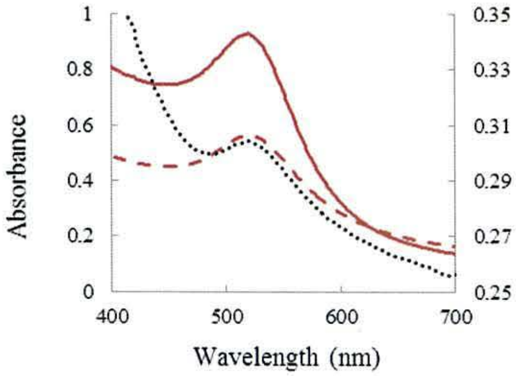

Figure 4.3.12 A. UV-vis spectra showing 3 nm Au seeds before seeding (red solid line, primary axis) after seeding (red dashed line, primary axis) and of the recovered Au-seeded SPION (black dotted line, secondary axis).

Figure 4.3.12 B. Photograph showing the sol after sequential, iterative addition of 300 μmol NH_2OH and 36.8 μmol $HAuCl_4$ to the Au-seeded SPION. The blue/grey colour indicates particle aggregation.

From *Figure 4.3.12 A* the concentration of the Au seeding solution drops after recovering the SPION from c = 2.60 x 10^{17} particlesL^{-1} to c = 1.57 x 10^{17} particlesL^{-1}, meaning 5.15 x 10^{15} particles bound to the SPION surface, corresponding to an average particle loading of 7.86 Au seeds per SPION core. In a solution of 5 mM sodium citrate and 1 mM TMAOH, 300 µmol NH_2OH and 36.8 µmol $HAuCl_4$ were added to the Au-seeded SPION. The resulting blue/grey suspension as displayed in *Figure 4.3.6 B* is the aggregate produced. Five iterations of $HAuCl_4$ is in theory sufficient to coarsen the immobilised Au-seeds, assuming spherical growth, equal in all directions, to 5.18 nm. Theoretically the SPION have an average surface area = 154 nm and eight spherical 5 nm Au particles have a footprint = 160 nm. Although the growth is not likely to be spherical or equal in all directions the experiment was designed to offer the approximate minimum amount of Au^{3+} needed to provide an outer surface coating of Au. If a stable sol can be produced in this way in theory the procedure can be refined to generate an Au coating of any thickness desirable.

$HAuCl_4$ is acidic so the pH of the reaction solution decreases with its addition, the aggregation of the particles is potentially due to the instability of SPION when suspended in a less basic environment. If the SPION cores begin to flocculate once the pH decreases and Au^{3+} is reducing onto the Au-seeded SPION surfaces, large agglomerations of particles can form causing irreversible aggregation. It is feasible that the Au-seeded SPION must be dispersed in a solution that is basic enough to allow addition of $HAuCl_4$ without bringing the solution pH below 9 until a complete Au shell is formed over the SPION surface.

4.4 Sequential hydroxylamine seeding to coat iron oxide particles with Au

$HAuCl_4$ and NH_2OH were added to SPION suspensions in a citrate solution, initially based on a replication of a synthetic method described by Lyon *et al.* The authors report a procedure where Au^{3+} is reduced directly onto SPION surfaces to create SPION@Au by alternative additions of $HAuCl_4$ and NH_2OH; after five iterations roughly spherical particles of approximately 60 nm are formed. These were characterised by TEM, EDAX, UV-vis and SQUID magnetometry.[219]

One of the pre-requisites the authors describe for direct surface reduction to occur is the oxidation of Fe_3O_4 to γ-Fe_2O_3, attempts to coat the former without first oxidising the particles apparently led to aggregation during early iterations of $HAuCl_4$. Due to time constraints this was not investigated in this study and was assumed to be the case. The oxidation is performed by heating Fe_3O_4 particles to 90°C – 100°C and stirring in a 0.01 M solution of HNO_3 for 30 minutes, the γ-Fe_2O_3 are then washed and TMAOH used to peptise.

Attempts to reproduce the SPION@Au particles using the Lyon *et al.* method repeatedly caused the sol to aggregate after only the first addition of $HAuCl_4$, similar to the aggregation observed when trying to reduce Au^{3+} onto the Au-seeded SPION. The pH of the reaction solution was found to decrease from > 10 to approximately 7 after the chloroauric acid was added, suggesting SPION flocculation may be the cause of aggregation. To keep the reaction pH > 9 during the early coating stages additional TMAOH was added to the solution. Control experiments indicate that a citrate functionalised gold colloid is stable up to concentrations of 5 mM TMAOH, as shown in *Figure 4.4.01.*

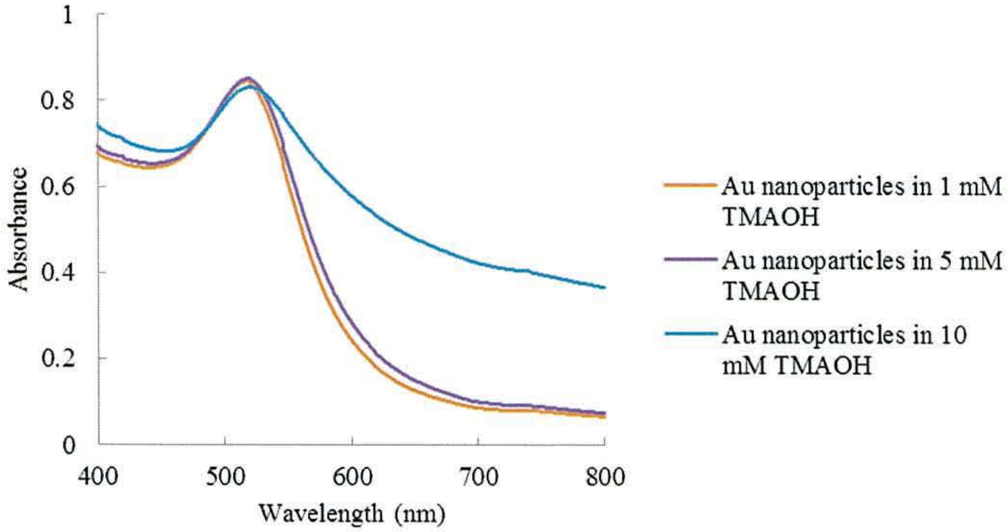

Figure 4.4.01. UV-vis spectra of Au nanoparticles in different concentrations of TMAOH.

At concentrations of 100 mM and 500 mM TMAOH aggregation of the Au colloid was instant, at 10 mM there was a distinct colour change from red to purple. However the colloid remained stable, while at concentrations of 5 mM and below there was no visual change to the Au nanoparticles. Repeating the SPION@Au synthesis as described by Lyon *et al.* in 5 mM TMAOH produced a stable sol with distinct SPR properties, as displayed in *Figure 4.5.2.* The distinct red colour of the produced sol indicates the reduction of Au^{3+} to nanoscale Au, however this gives no indication to the morphology of the produced particles so TEM was used to further investigate the particles.

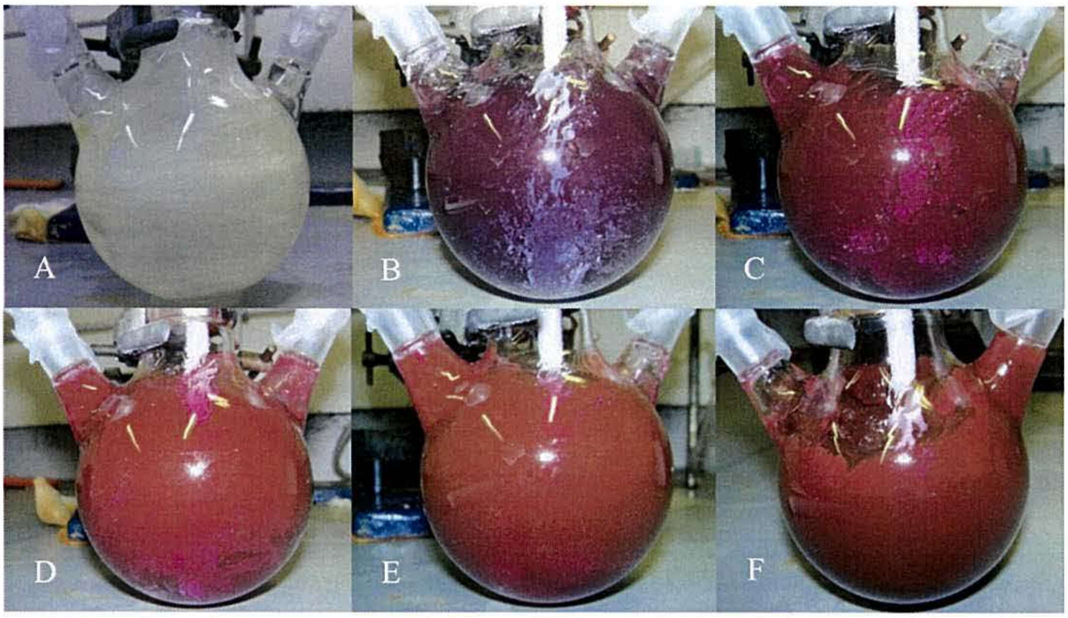

Figure 4.4.02. Photographs of the Au coating of SPION in 5mM citrate and 5 mM TMAOH. A is the bare SPION and B – F sequential additions of NH_2OH and $HAuCl_4$. The solutions are being vigorously stirred.

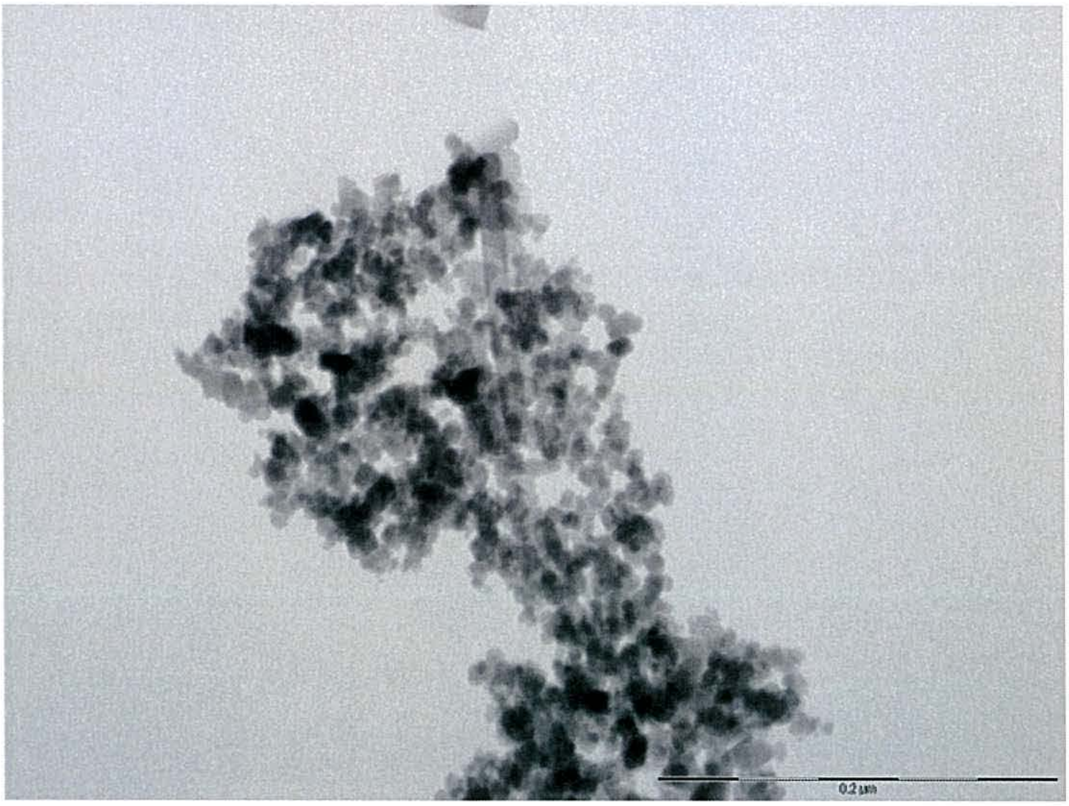

Figure 4.4.03. TEM image of the γ-Fe_2O_3, synthesised by heating Fe_3O_4 in a 0.01M solution of HNO_3 for 30 minutes. Scale bar is 200 nm.

TEM images of the bare SPION are similar to those in *Section 4.1.1*. However there is also anomalous tubular structures present, in *Figure 4.5.3* one can be seen near the centre of the image, representing a small proportion of the colloid. A report by Kang *et al.* in 1996 describes the synthesis of γ-Fe_2O_3 from Fe_3O_4, by heating Fe_3O_4 nanoparticles in an acidic environment for 30 minutes in air.[251] The authors describe needle-like γ-Fe_2O_3 forming within the solution of approximately 20 to 50 nm by 4 to 6 nm, these were separated by adjusting the pH back to 11 to peptise the smaller Fe_3O_4 and the larger needle-like structures were then easily magnetically separated. These tubular structures were not expected in the SPION solution and were not mentioned by Lyon *et al.* in their report.

After the first addition of NH_2OH and $HAuCl_4$ the solution changed colour from a light yellow to a blue/purple, a TEM image of these particles is shown in *Figure 4.5.4.*

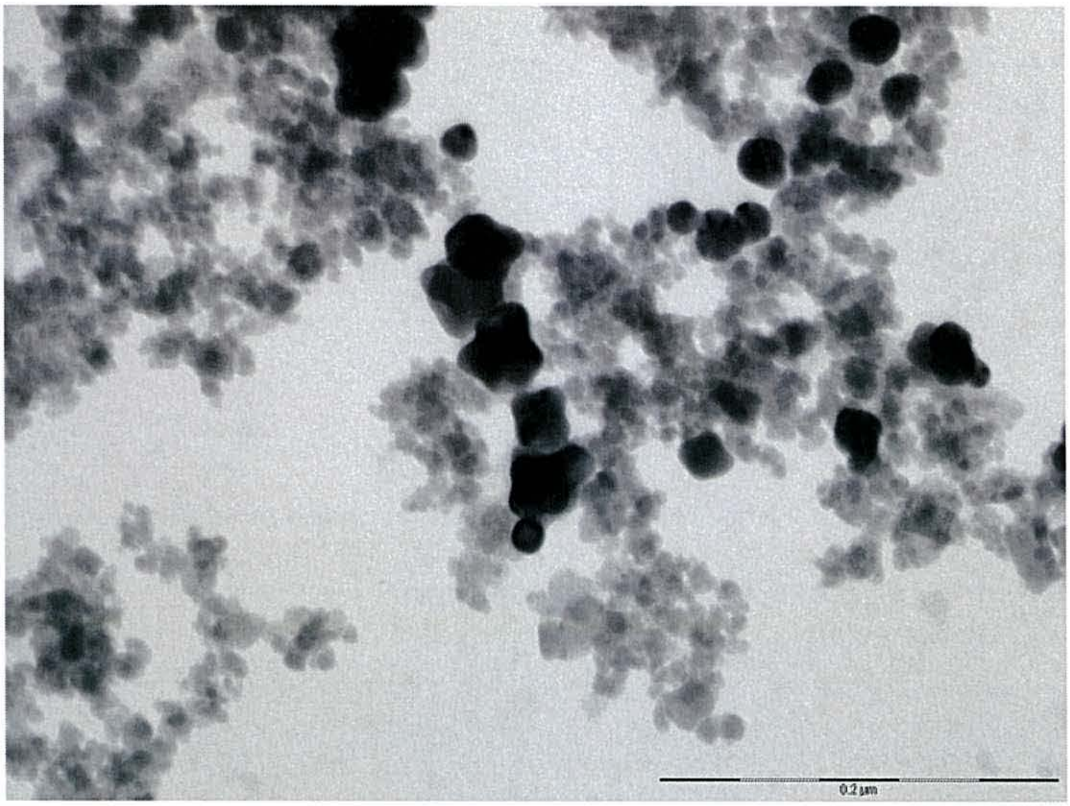

Figure 4.4.04. TEM image of the particles produced after 1 addition of NH_2OH and $HAuCl_4$. Scale bar is 200 nm

The TEM image appears to show two particle morphologies, smaller grey particles of approximately 10 nm in size and larger darker particles of sizes > 10 nm. The irregular shaped larger particles are likely to be Au, however the TEM image is significantly different to that shown in the Lyon *et al.* paper, with > 90% of the particles in the population appearing to be bare SPION. In the Lyon *et al.* article no bare SPION are visible in the images or mentioned in the text.

TEM images of the particles produced during the four subsequent iterations of NH_2OH and $HAuCl_4$ are shown in *Figure 4.5.5*. The same general observation can be made as reported by Lyon *et al.* that with each addition of chloroauric acid the Au particles become more morphologically uniform and spherical in shape. However, there are differences between the particles produced in this study and those reported by Lyon *et al.* the most significant being that the majority of the SPION remain bare and large needle like structures are present throughout.

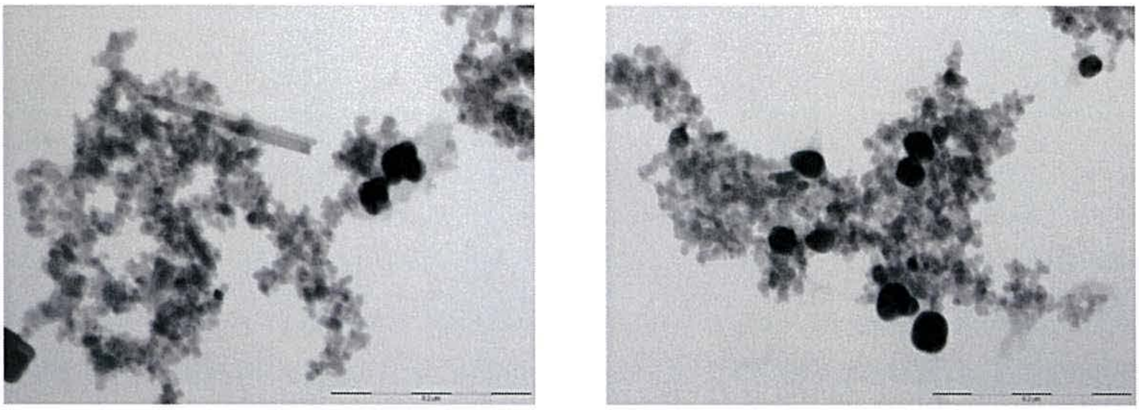

A. Particles after 2 iterations of NH_2OH and $HAuCl_4$

B. Particles after 3 iterations of NH_2OH and $HAuCl_4$

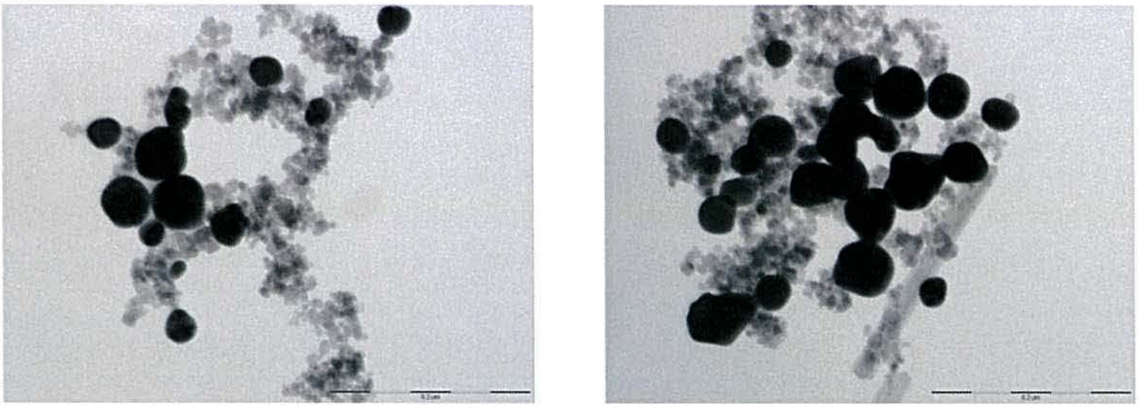

C. Particles after 4 iterations of NH_2OH and $HAuCl_4$

D. Particles after 5 iterations of NH_2OH and $HAuCl_4$

Figure 4.4.05. TEM images of the particles produced after 2 (A) 3 (B) 4 (C) and 5 (D) iterations of $HAuCl_4$ and NH_2OH. Scale bar is 200 nm

The images in *Figure 4.5.5* are representative of the particles formed in the reaction solution after the respective additions of NH_2OH and $HAuCl_4$ as described by Lyon *et al.*

The wide variety of particles observed was not expected. However did include some interesting features such as the particle hybrid shown in *Figure 4.5.6.*

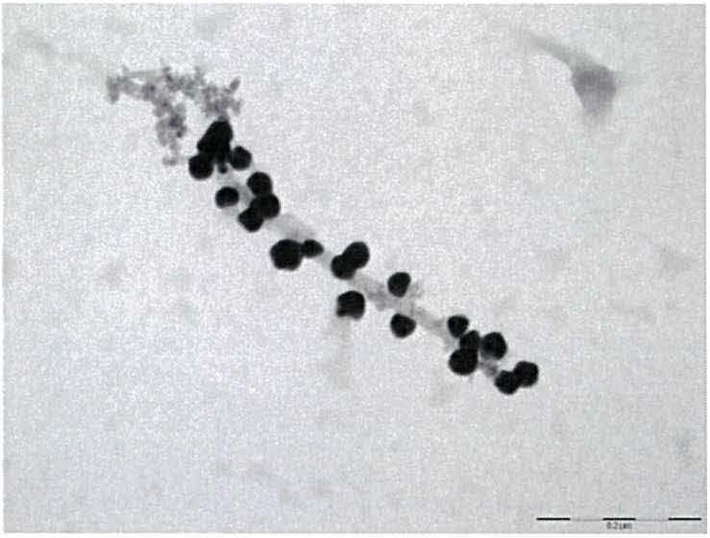

Figure 4.4.06. TEM image of a large γ-Fe_2O_3 needle with numerous Au particles bound to its surface. Scale bar is 200 nm

EDAX spectra taken during TEM of the particles after 5 iterations of $HAuCl_4$ and NH_2OH are shown in *Figure 4.5.7* and *Figure 4.5.8.*

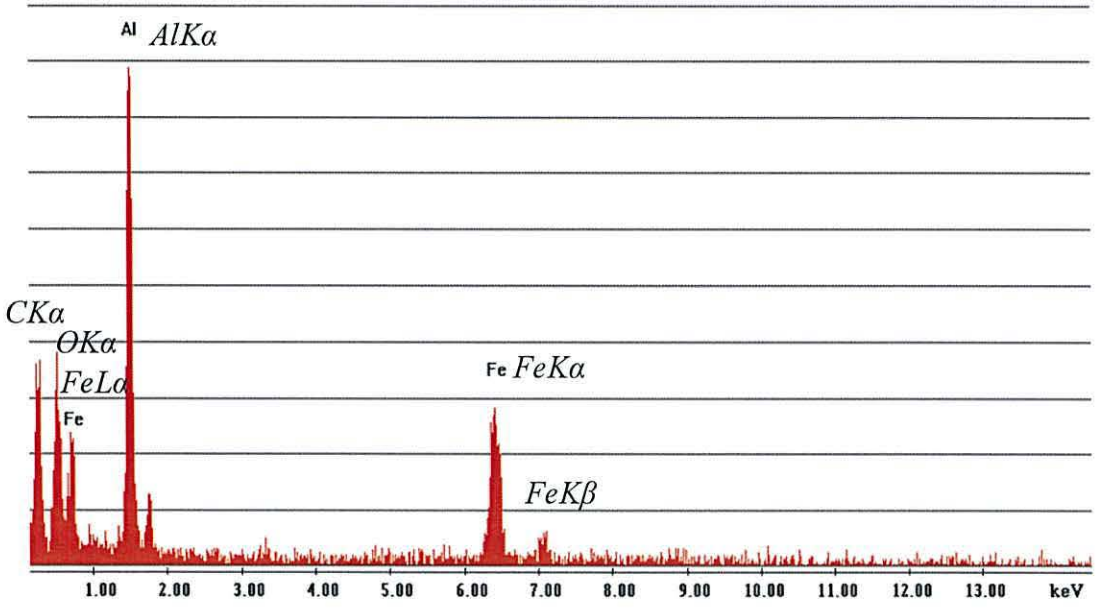

Figure 4.4.07. EDAX taken during TEM of an area containing mostly γ-Fe_2O_3 particles after five additions of NH_2OH and $HAuCl_4$ to SPION. The peaks from left to right correspond to CKα, OKα, FeLα, AlKα, FeKα and FeKβ

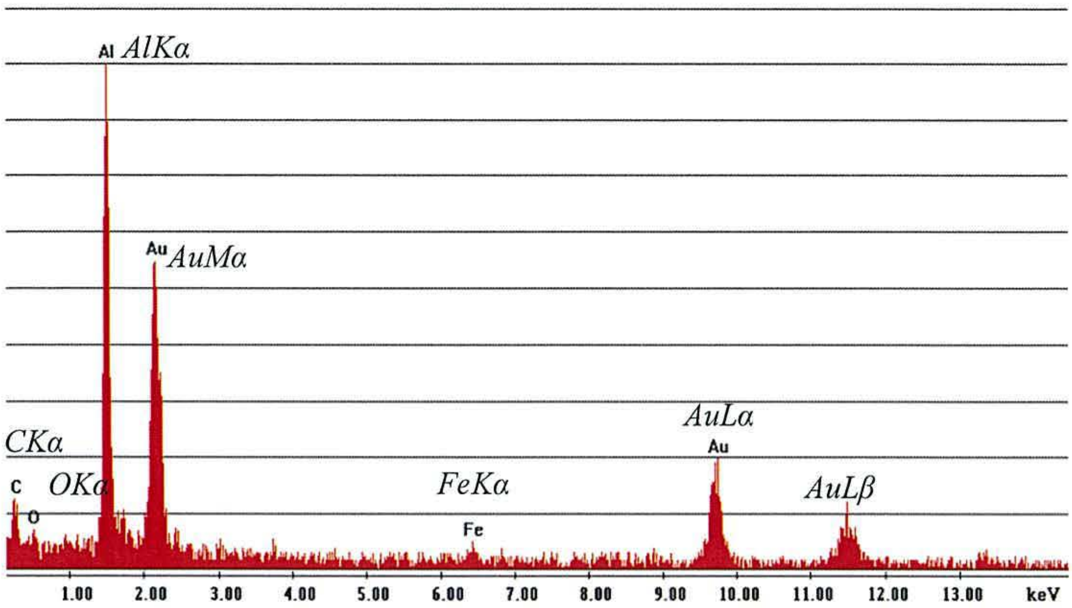

Figure 4.4.08. EDAX taken during TEM of an area containing mostly Au particles after five additions of NH_2OH and $HAuCl_4$ to SPION. The peaks from left to right correspond to CKα, OKα, AlKα, AuMα, FeKα AuLα and AuLβ

The XRD pattern of the particle mixture obtained using the Lyon *et al.* method is shown in *Figure 4.5.9.*

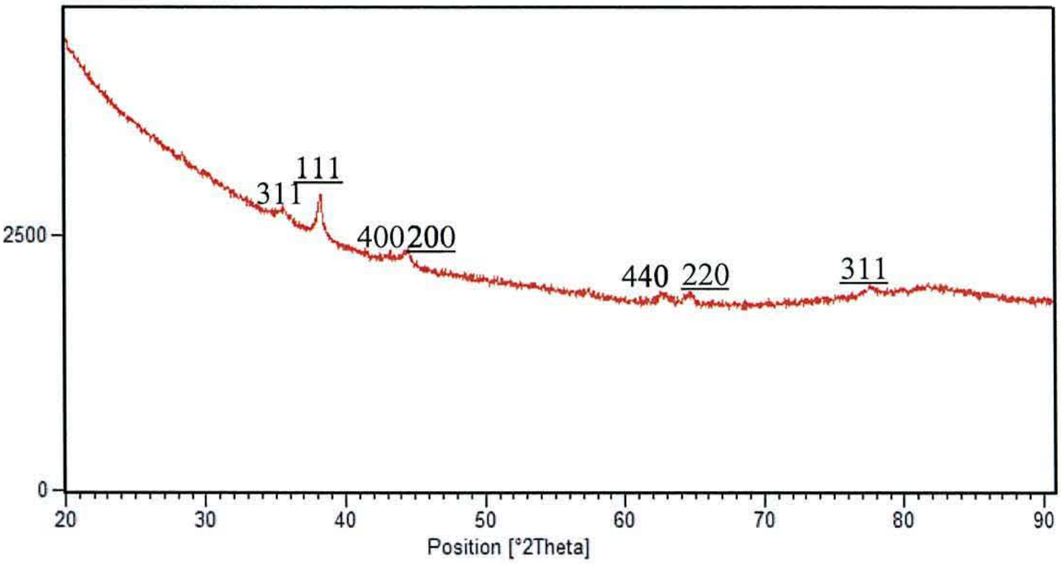

Figure 4.4.09. XRD pattern of the SPION@Au as synthesised using the Lyon et al method.[219] *Diffraction planes correspond to SPION (unformatted numbers) and gold (underlined numbers). Full details shown in table 10 and pattern 10 of the Appendix.*

As would be expected from the TEM images and EDAX spectra, the XRD pattern shows diffraction peaks for nanocrystalline Au and γ-Fe_2O_3/Fe_3O_4. UV-vis spectra of the particles between iterations is shown in *Figure 4.6.0.*

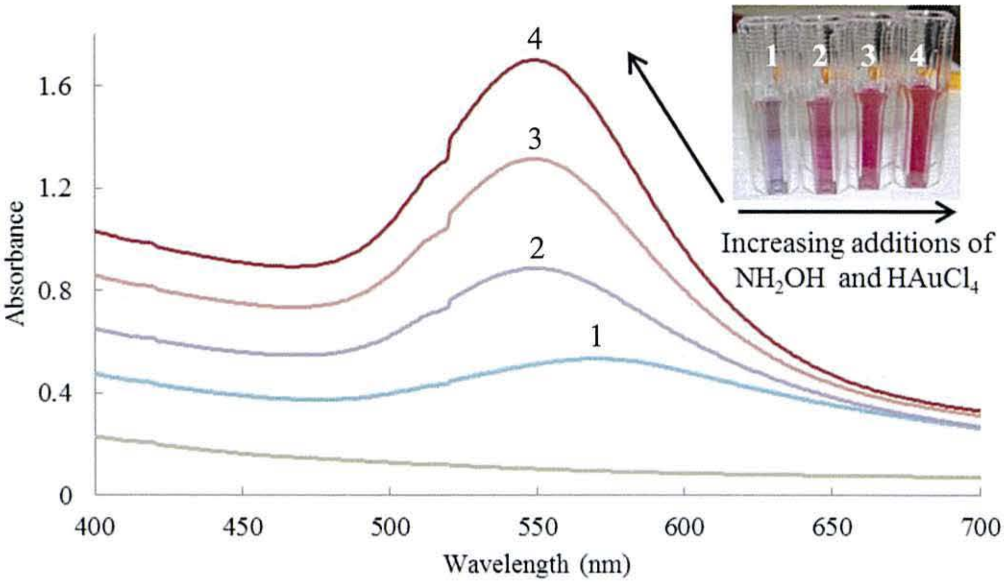

Figure 4.4.10. UV-vis spectra of γ-Fe_2O_3 during the Au coating process. The numbers correlate to the addition of $HAuCl_4$, the UV-vis absorbance profile and a photograph of the aliquot taken during reaction.

As expected, with increasing additions of $HAuCl_4$ the particles develop an absorbance peak which increases in intensity and blue shifts towards that observed for a citrate stabilised Au colloid of spherical particles. This corresponds well with observations made during TEM analysis, shown in *Figure 4.5.5.*

The particles produced by attempting to replicate the Lyon *et al.* method produce a stable colloid that possesses properties of both SPION and Au. However characterisation of the particles reveals a mixture of Au particles, SPION, γ-Fe_2O_3 needles and Au bound to γ-Fe_2O_3 needles. This particle mixture would not be suitable for application in DEPT and this procedure therefore needs to be refined to remove the bare γ-Fe_2O_3 needles, the Au bound to γ-Fe_2O_3 needles and confirm there are not any Au nanoparticles without a magnetic core.

4.5 Refining the iterative hydroxylamine seeding approach

Magnetic separation of the colloid produced from the Lyon *et al.* procedure revealed that all particles within the sol are magnetic and can be isolated into two colloids; Au coated particles and bare magnetic particles. Magnetic separation of the sols is shown in *Figure 4.5.01* and characterisation of the particles in *Figure 4.5.02*.

A. The colloid is placed against a 1.3 T magnet and the pH adjusted to 7

B. Particles migrate to the magnets surface, those furthest taking longer to travel

C. The Au@γ-Fe_2O_3 readily redisperse to form a stable sol which is easily isolated

D. The bare γ-Fe_2O_3 particles flocculate without the stabilising Au surface coating

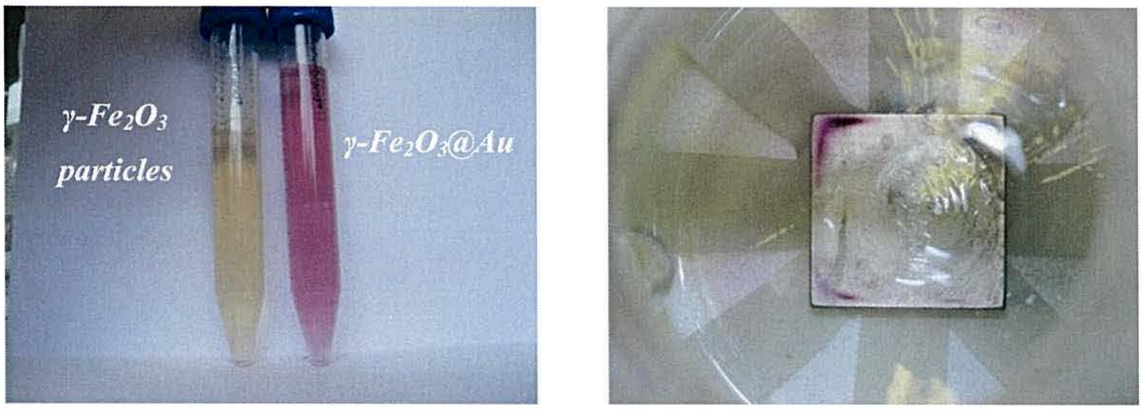

E. The γ-Fe_2O_3 particles peptise in 5mM TMAOH and the γ-Fe_2O_3@Au in dH_2O

F. Pure Au@γ-Fe_2O_3 can be repeatedly magnetically separated and redispersed. In this image, all have magnetically separated

Figure 4.5.01. Photographs detailing the magnetic purification of Au@γ-Fe_2O_3.

Figure 4.5.01 F shows the response of a pure Au@-γ-Fe_2O_3 in the presence of a magnetic field, the particles are pink in colour and all migrate to the magnets' surface.

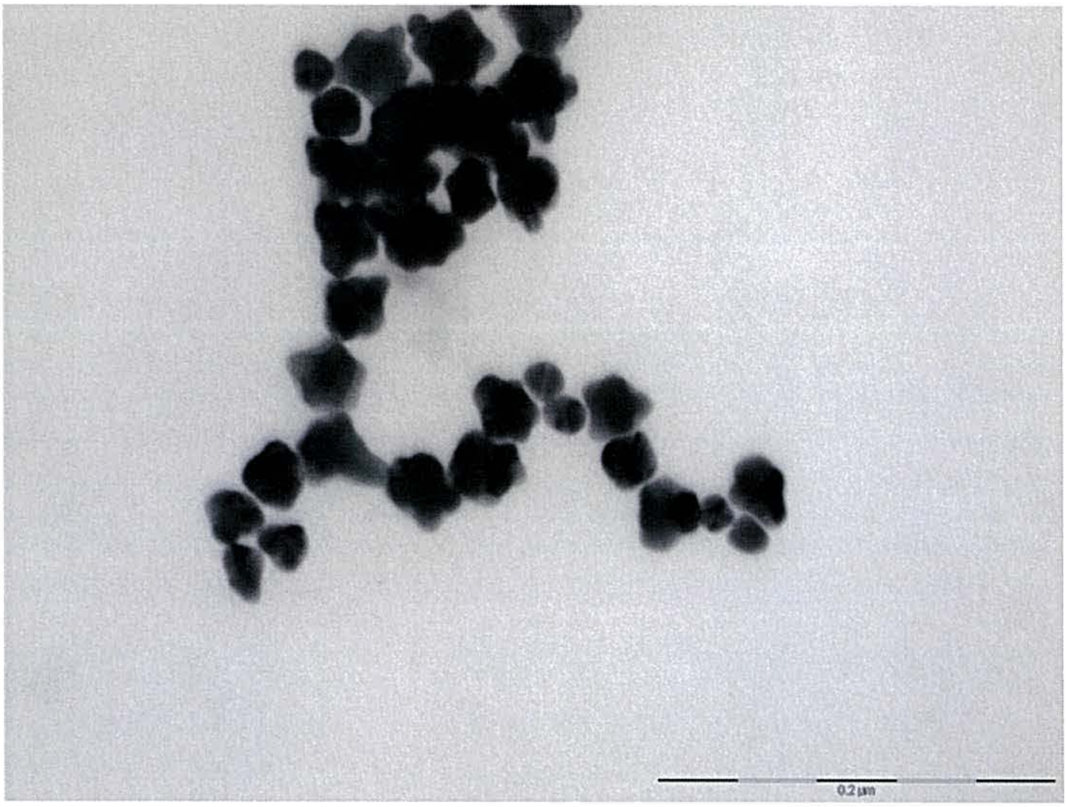

Figure 4.5.02. TEM image of isolated γ-Fe_2O_3@*Au from bare* γ-Fe_2O_3 *after 1* $HAuCl_4$ *addition. Scale bar 200 nm.*

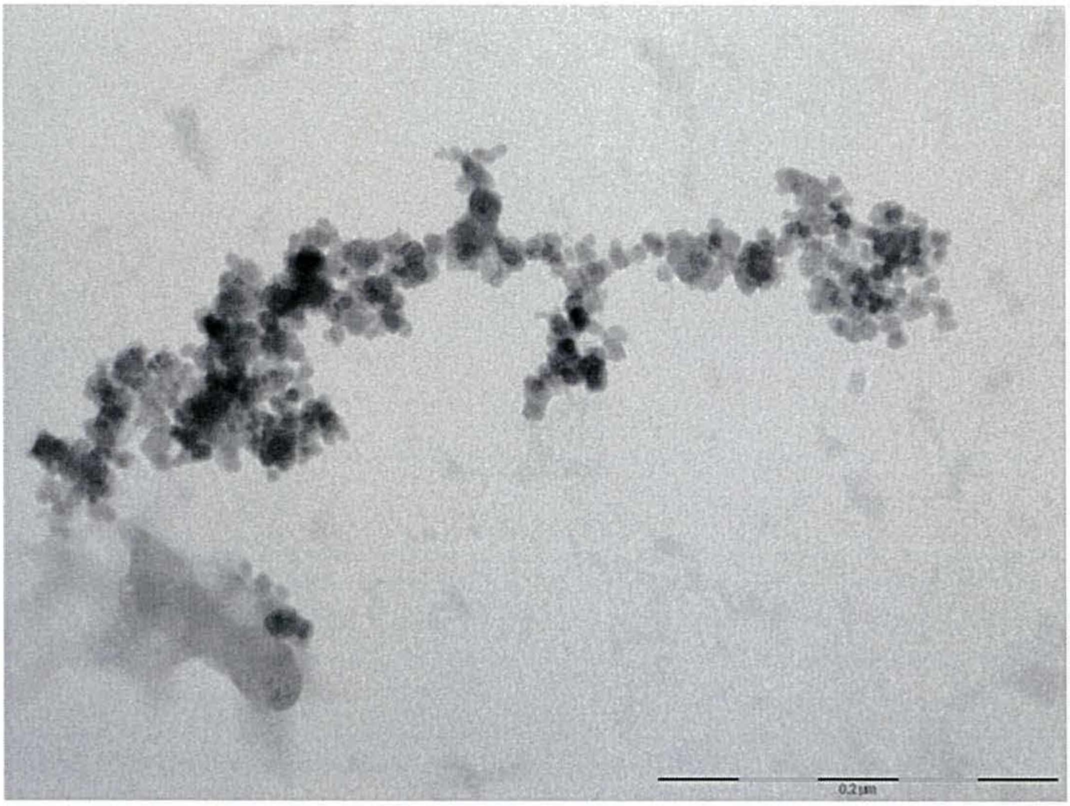

Figure 4.5.03. TEM image of bare γ-Fe_2O_3 *after magnetic separation from* γ-Fe_2O_3*@Au after 1* $HAuCl_4$ *addition. Scale bar 200 nm.*

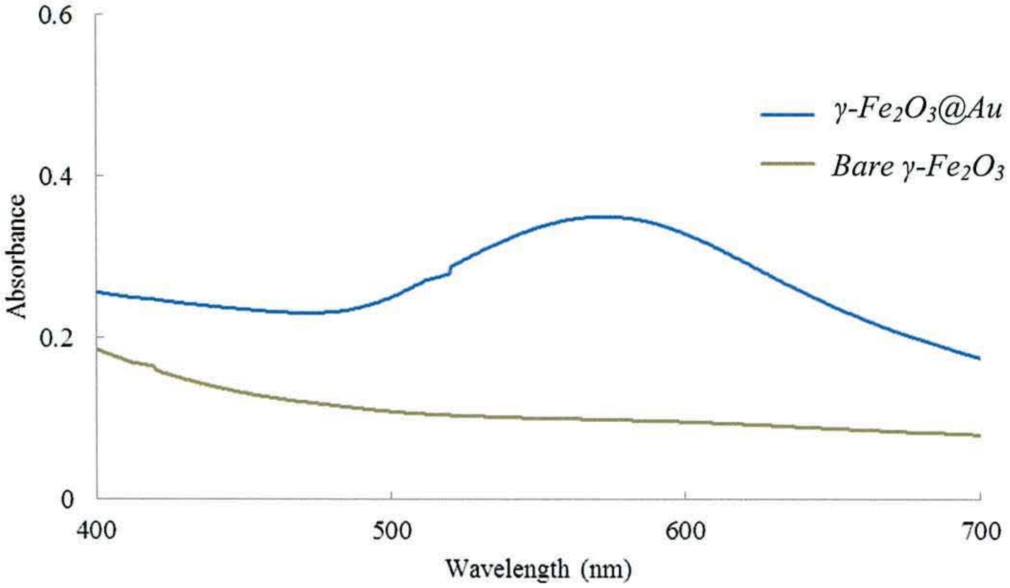

Figure 4.5.04. UV-vis spectra of isolated γ-Fe_2O_3*@Au and isolated bare* γ-Fe_2O_3 *after magnetic separation following 1* $HAuCl_4$ *addition.*

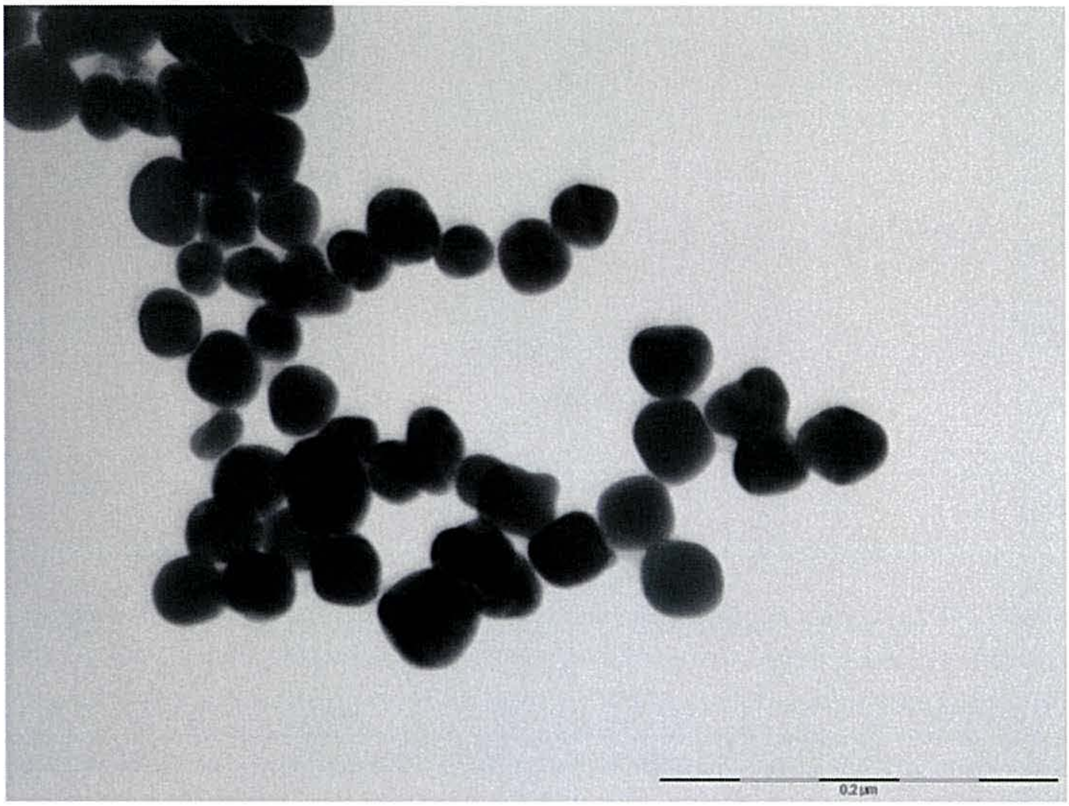

Figure 4.5.05. TEM image of isolated γ*-*Fe_2O_3*@Au from bare* γ*-*Fe_2O_3 *after 5* $HAuCl_4$ *additions. Scale bar 200 nm.*

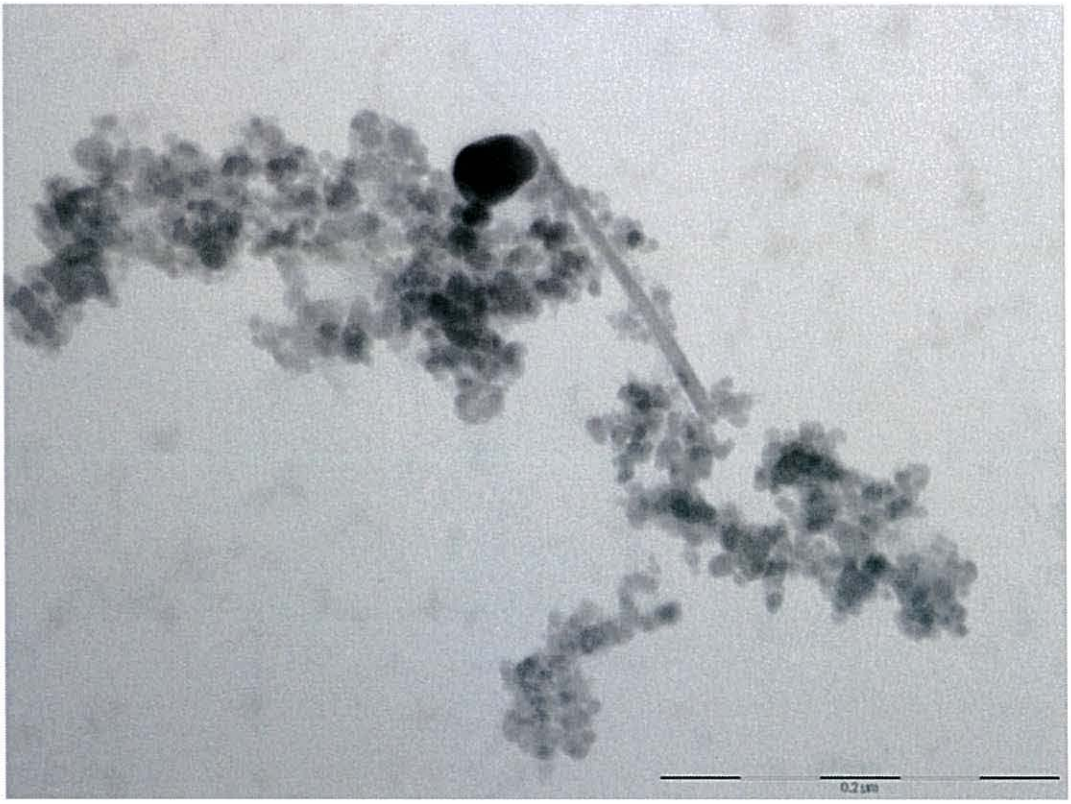

Figure 4.5.06. TEM image of bare γ*-*Fe_2O_3 *after magnetic separation from* γ*-*Fe_2O_3*@Au after 5* $HAuCl_4$ *additions. Scale bar 200 nm.*

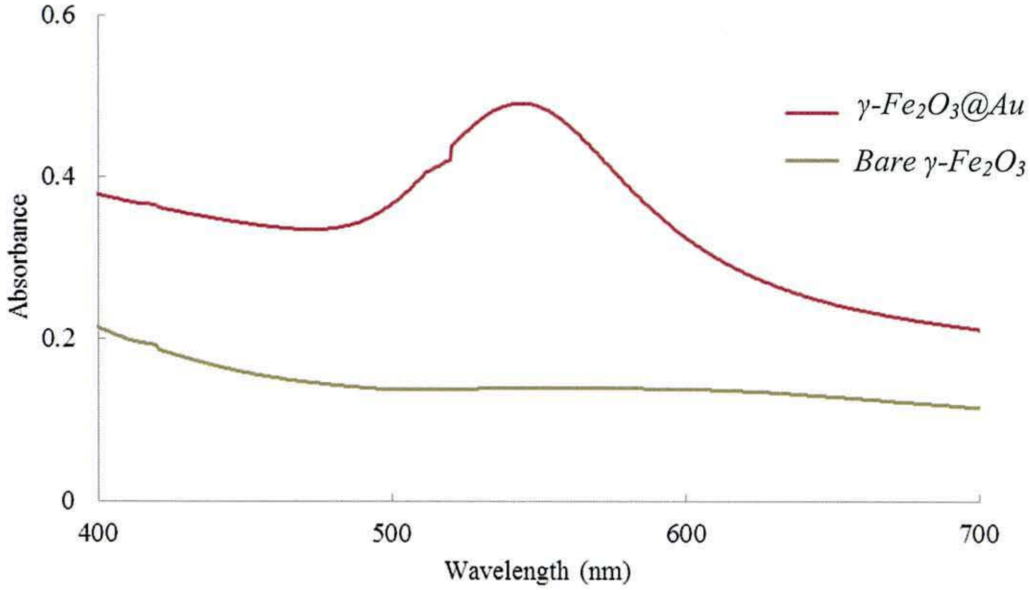

Figure 4.5.07. UV-vis spectra of isolated γ-Fe_2O_3@Au and isolated bare γ-Fe_2O_3 after magnetic separation following 5 $HAuCl_4$ additions.

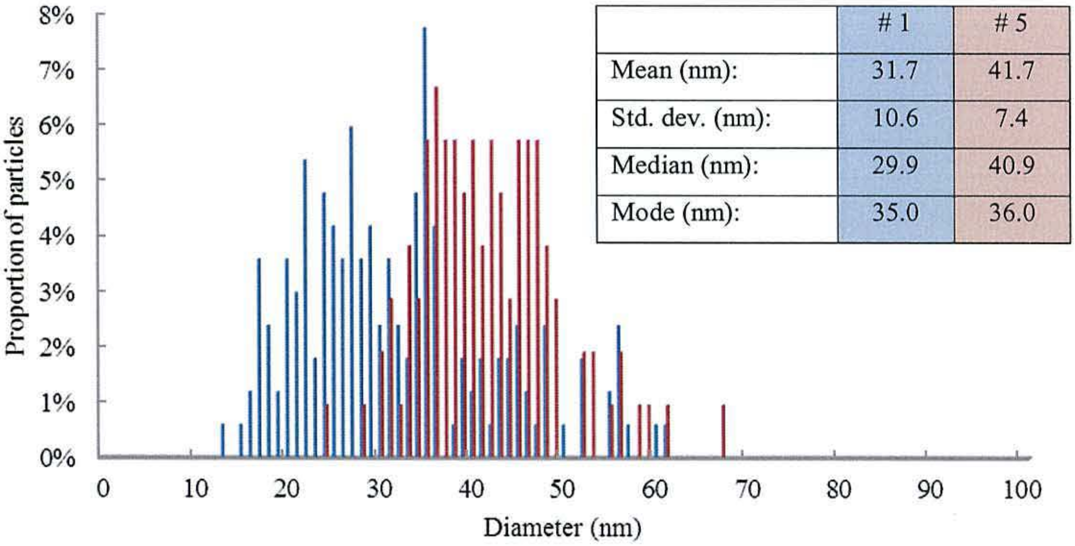

	# 1	# 5
Mean (nm):	31.7	41.7
Std. dev. (nm):	10.6	7.4
Median (nm):	29.9	40.9
Mode (nm):	35.0	36.0

Figure 4.5.08. Histogram showing the size distributions of the Au@γ-Fe_2O_3 after 1 addition of $HAuCl_4$ and NH_2OH (168 particles measured, blue) and 5 additions of $HAuCl_4$ and NH_2OH (105 particles measured, red)

XRD patterns of the isolated Au@γ-Fe_2O_3 after 1 and 5 additions of $HAuCl_4$ and NH_2OH are shown in *Figure 4.6.4* and *Figure 4.6.5* respectively, the full spectra and peak assignments can be found in the *Appendix*.

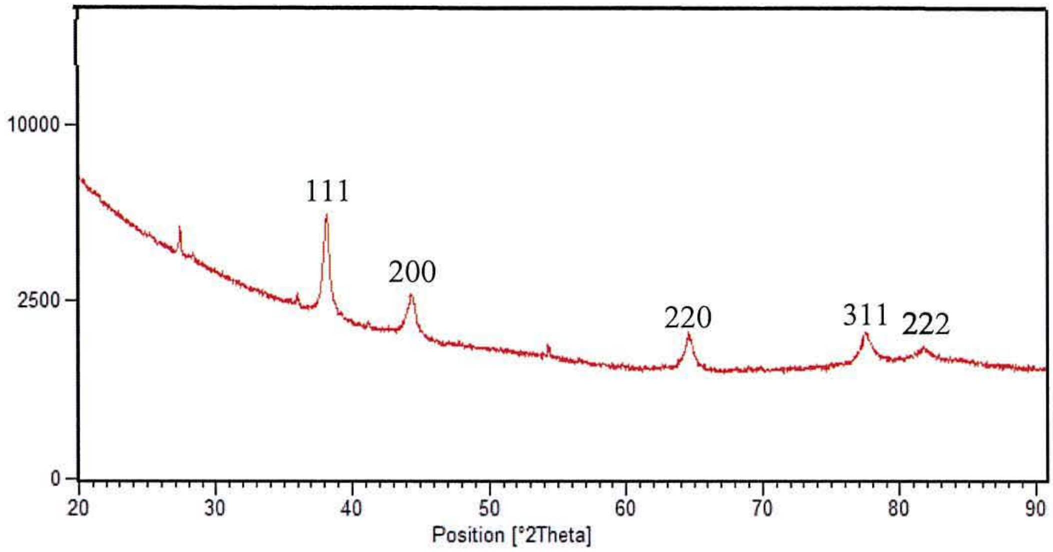

Figure 4.5.09. XRD pattern γ-Fe_2O_3@Au of after 1 addition of $HAuCl_4$ and NH_2OH. Full details shown in Table 11 and pattern 11 of the Appendix.

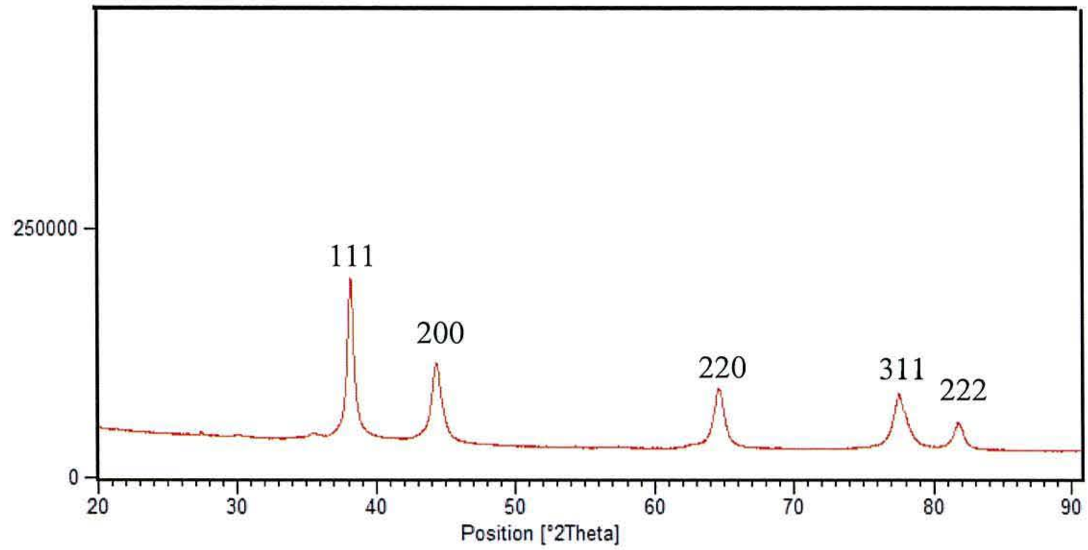

Figure 4.5.10. XRD pattern γ-Fe_2O_3@Au of after 5 additions of $HAuCl_4$ and NH_2OH. Full details shown in Table 12 and pattern 12 of the Appendix.

The XRD patterns for both particles show only the diffraction planes for Au, with similar peak broadening for the particles after 1 and 5 additions of $HAuCl_4$ indicating similar crystal sizes. The lack of significant diffraction peaks for maghemite suggest the particles are comprised of substantially more Au than γ-Fe_2O_3 after Au coating.

Lyon *et al.* report that addition of $HAuCl_4$ to Fe_3O_4 without first oxidising to γ-Fe_2O_3 causes aggregation during early additions of chloroauric acid. Jeong *et al.* found that despite magnetite oxidation, aggregation occurred during early additions of $HAuCl_4$ unless much lower concentrations of the gold precursor is added during the early coating stages, adding 1.27 x 10^{-8} mol $HAuCl_4$ compared to the 1.59 x 10^{-5} mol $HAuCl_4$ that Lyon *et al.* added at the first iteration.[253] Here oxidising Fe_3O_4 to γ-Fe_2O_3 by heating to 90°C – 100°C for 30 minutes led to the formation of maghemite needles among the nanoparticles, as reported elsewhere[251] but not by Lyon *et al.*

So as to remove the γ-Fe_2O_3 needles, produced by oxidising magnetite at high temperature in an acidic environment, the SPION synthesised in *Chapter 1.1* were used rather than the γ-Fe_2O_3 needle/nanoparticle mixture; this did not lead to aggregation during early coating stages as reported by Lyon *et al.* Characterisation of the SPION@Au is shown in the following figures.

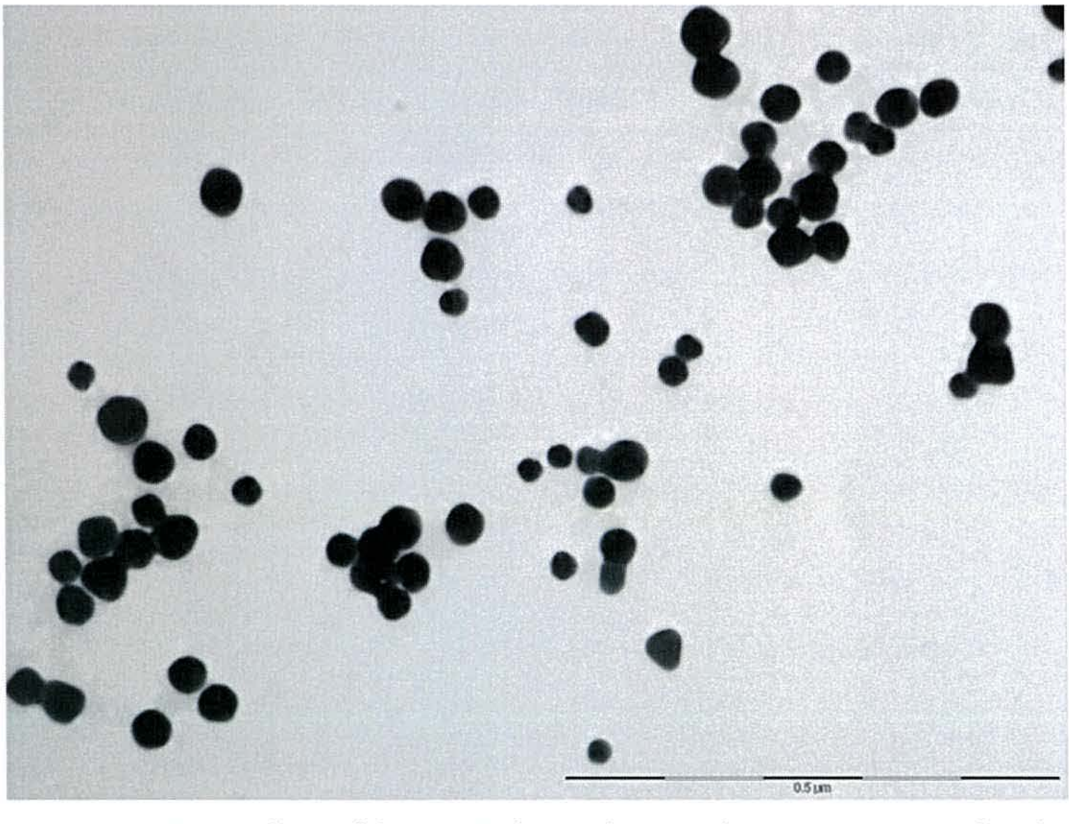

Figure 4.5.11. TEM analysis of the SPION@Au. The particles are approximately spherical with no anomalous morphologies such as needles. Scale bar is 500 nm.

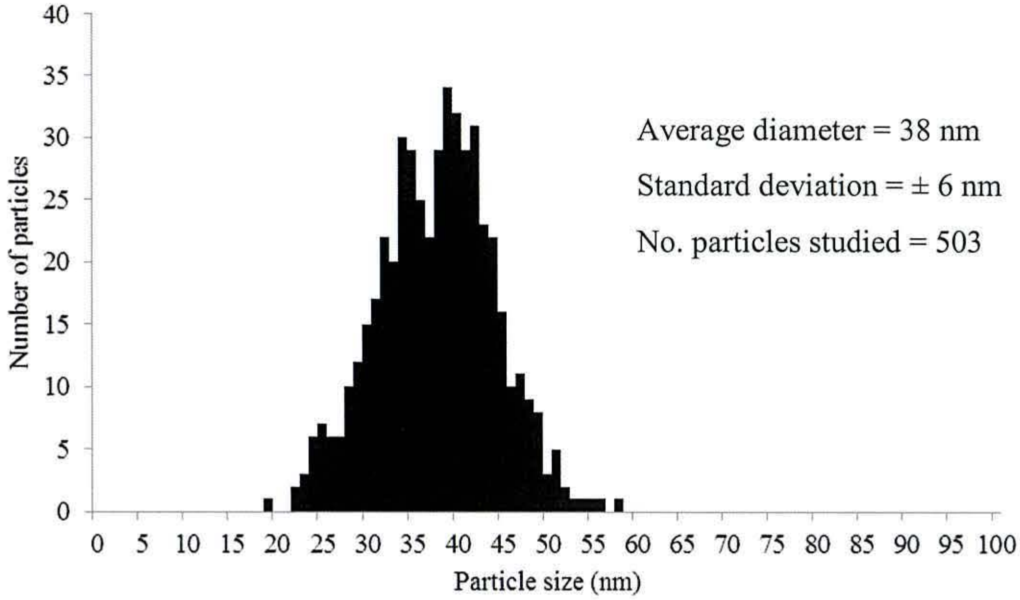

Figure 4.5.12. Size distribution of SPION@Au based on 503 particles showing an average diameter of 38 nm ± 6 nm.

As can be seen in *Figure 4.5.12* the particles are roughly spherical in shape with a Gaussian size distribution. Details of the size properties as determined by TEM are compiled in *Table 4.5.1* and compared to those obtained by Lyon *et al.* and Jeong *et al.* The particles produced in this study are smaller in size and possess a narrower size distribution than particles from both previous reports.

Table 4.5.1. A table showing the relative particle sizes from this study and studies by Lyon et al. and Jeong et al.

Synthesis	**Average size (nm)**	**Distribution (nm)**	**Relative standard deviation (%)**	**Median (nm)**	**Mode (nm)**
Lyon *et al.*	57	± 14	25	-	-
Jeong *et al.*	70	± 20	29	-	-
This study	38	± 6	16	38	39

EDAX taken during TEM do not contain peaks corresponding to iron as shown in *Figure 4.5.13*, the carbon peak is due to surface bound citrate and aluminium from the TEM grid, the remaining peaks correspond only to Au. UV-vis absorbance spectra were also taken of the SPION and SPION@Au in *Figure 4.5.14*, showing the SPR of the Au coated particles compared to the uncoated particles and XRD pattern of the SPION@Au shows only Au diffraction peaks.

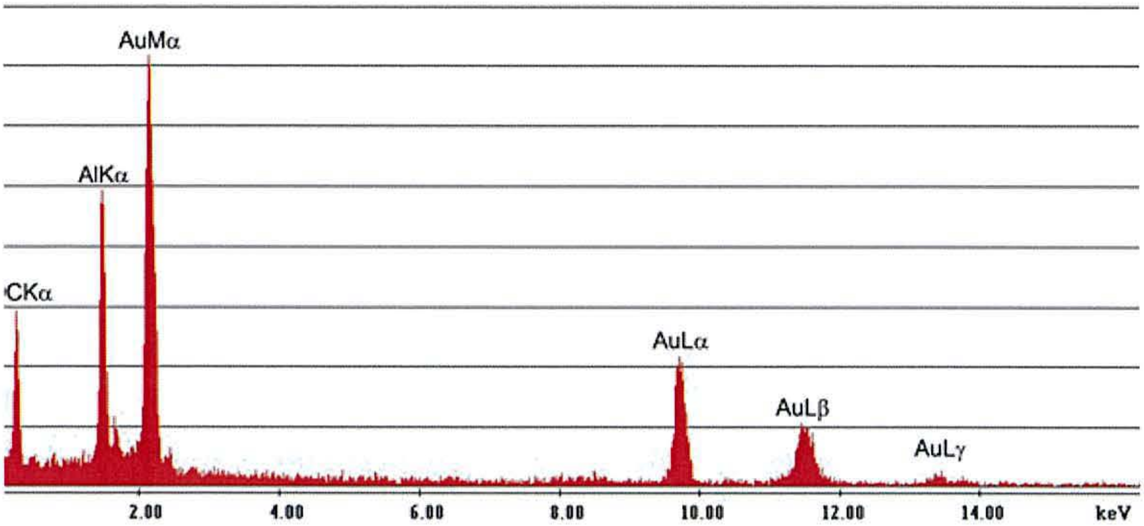

Figure 4.5.13. EDAX spectrum of the SPION@Au taken during TEM

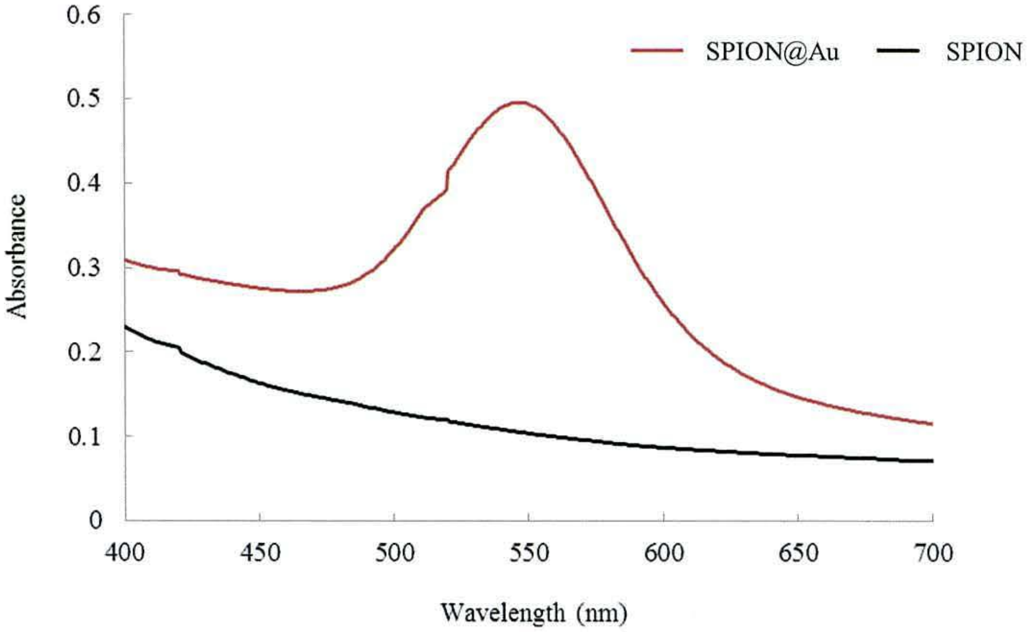

Figure 4.5.14. UV-vis spectra of SPION and SPION@Au

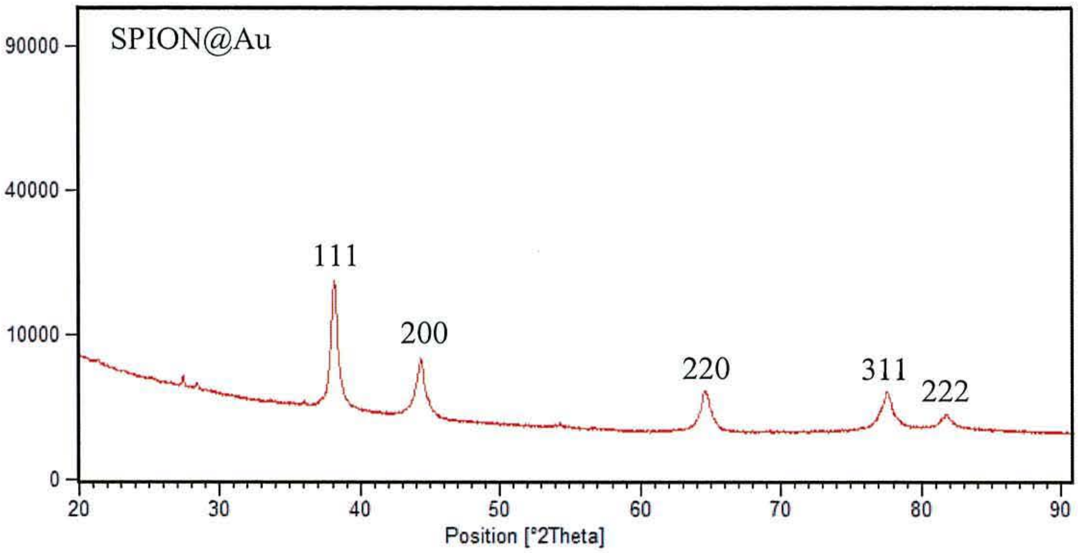

Figure 4.5.15. XRD pattern of SPION@Au showing the diffraction peaks expected for Au. Full details are shown in table 13 and pattern 13 of the Appendix.

4.6 Concluding remarks on magnetic nanoparticles

Attempts to produce SPION@Au utilising a citrate reduction reaction at elevated temperatures in the presence of pre-synthesised SPION as previously reported in the literature[218, 230] did not appear to produce particles which are suitable for MNP-DEPT as a substantial portion of the nanocrystalline Au produced did not respond to an external magnetic field. While the use of a pre-seeding approach to first attach smaller Au seeds to iron oxide cores produced Au coated particles which could be magnetically manipulated and rapidly separated from solution in the presence of a magnetic field, the particles would be too large for *in vivo* application.[231]

Direct reduction of $HAuCl_4$ onto SPION did not produce SPION@Au as reported in a previously published synthesis,[219] however modification of the process to separate the uncoated SPION from solution allowed SPION@Au of 38 nm ± 6 nm to be isolated. These particles were characterised by TEM, XRD, UV-vis and EDAX and possessed a magnetic response which allowed them to be readily separated from solution using 1.28 T magnets. There is no indication that bare SPION are present in the final colloid and the results of characterisation show only the expected properties of nano-gold. The particles are of an ideal size for *in vivo* application and would be suitable for experiments to investigate the viability of MNP-DEPT *in vitro*.

Chapter 5

ENZYME IMMOBILISATION

5.1 Electrochemical reduction of immobilised nitroreductases

5.1.1 The electrochemical cell

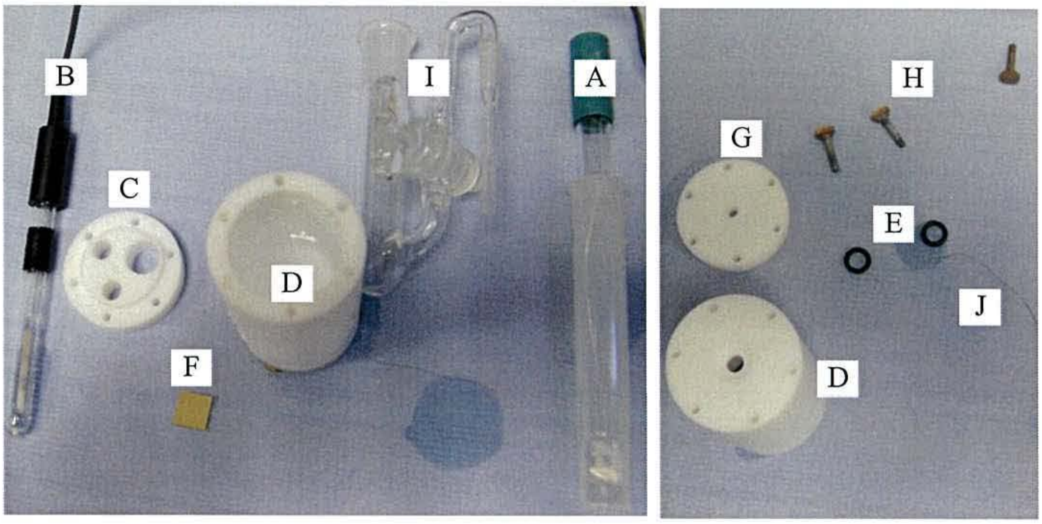

A. Pt counter electrode
B. Saturated calomel electrode (SCE)
C. PTFE cell lid
D. PTFE cell
E. Rubber o-rings
F. Au(111) gold coated glass slide
G. PTFE cell bottom
H. Brass screws
I. Salt bridge
J. Working electrode connection

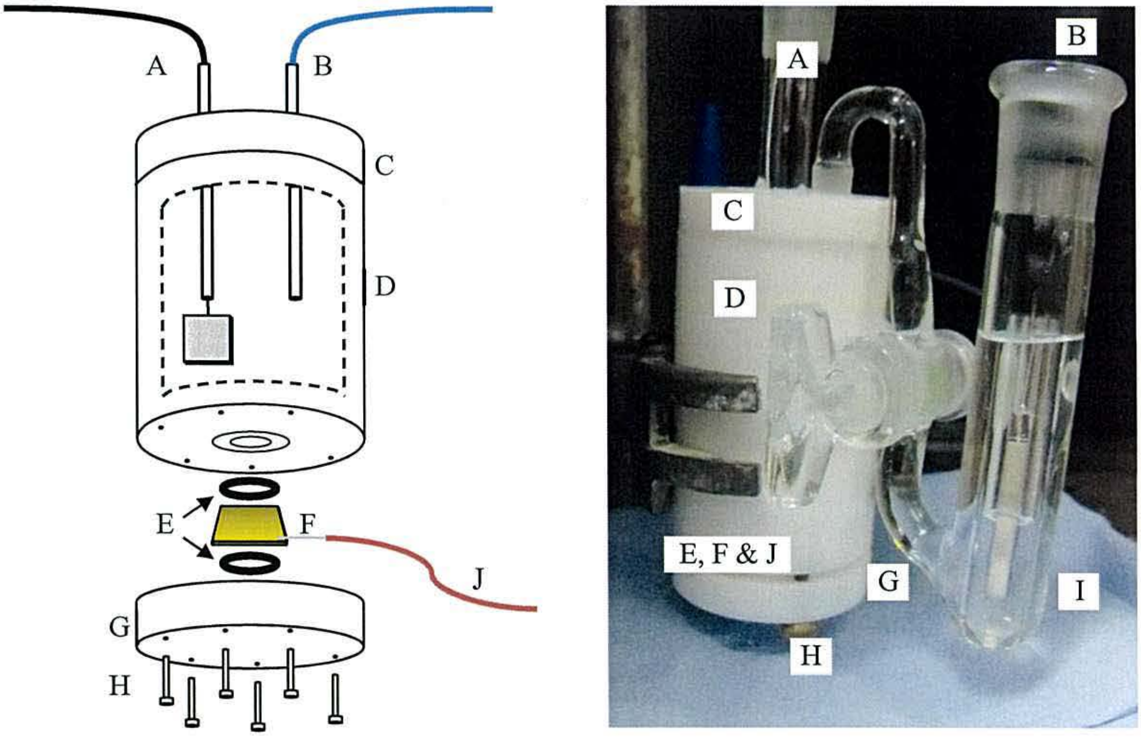

Illustration of electrochemical cell construction

Photograph of electrochemical cell during cyclic voltammetry

Figure 5.1.1. Images of the component parts and assembly of the electrochemical cell constructed for cyclic voltammetry of NTR functionalised Au(111) coated glass slides

5.1.2 Characterising Au-S bonding and nitroreductase immobilisation

Self-assembly of enzymes onto an Au surface occurs due to interactions between the functional groups of the amino acids in[187] the protein.[254187] The introduction of a consecutive series of cysteine amino acids into the NTRs provides a thermodynamically favourable bonding site between the Au surface and the proteins, cyclic voltammetry is used to profile the enzyme-Au bond. Au(111) coated glass slides (Winkler GmbH, Germany) were incubated with purified NTRs to allow the NTRs to self-assemble. The voltammograms showing electrochemical reduction of *yfkO-cys* after 24 hour incubation with Au(111) coated glass slides is shown in *Figure 5.1.2,* with reduction of a bare Au(111) coated glass slide shown for comparison.

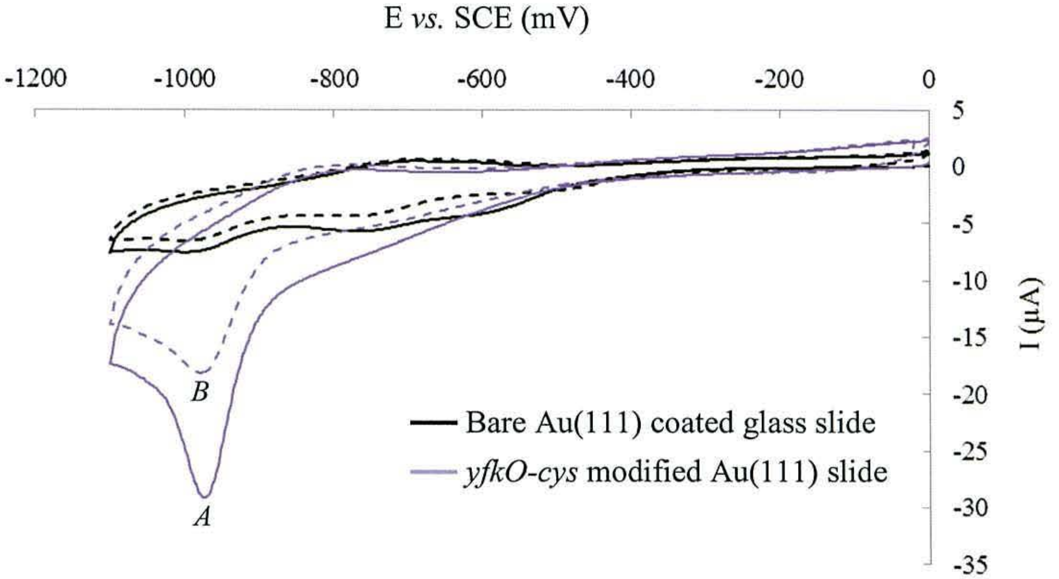

Figure 5.1.2. Voltammogram showing two consecutive reduction cycles of a bare Au(111) coated glass slide (1, black solid and 2 black dash) and two consecutive reduction cycles of an Au(111) coated glass slide after 24 hour incubation with yfkO-cys (1 purple solid A = -976.6 mV, -29.17 µA and 2 purple dash B = -979.0 mV, -18.19 µA. The potential is vs. SCE in an electrolyte of 0.1 M NaOH

The reduction cycles of the bare Au(111) coated glass slide shows the reduction of a gold surface under basic conditions between 0 and -1.1 V and the voltammograms obtained when the working electrode was incubated with *yfkO-cys* shows a distinct peak at *A* during the first reduction cycle (-976.6 mV, -29.17 µA), corresponding to the reduction of Au-S bonds between gold and the cysteines of *yfkO-cys.*[188] This is the potential previously shown for electrochemical reduction of Au-S bonds between a cysteine modified NTR and an Au(111) coated glass slide[199] and is typical for reductive desorption of thiols from Au(111) as is well reported in the literature.[255] During the second reduction cycle just minutes later, a similar peak is seen at *B* (-979.0 mV, -18.19 μA) indicating immediately after the desorption some of the cysteines re-bond to the Au surface. The notable difference between the two peaks is the lower current at B, indicating in the short time period between reduction cycles only a proportion of *yfkO-cys* reassemble at the gold surface *via* the Au-S bonds of the cysteines.

For application in MNP-DEPT the immobilisation of the NTR to the Au particle surface is important. The density of the monolayer, the orientation of the NTRs and the longevity of the Au-S bonds are properties central to the success of the therapy. To investigate the surface bonding further, *yfkO-cys* was incubated with Au(111) gold coated glass slides for 4 days before cyclic voltammetry. *Figure 5.1.3* shows the voltammogram with *C* (-974.1 mV, -29.68 μA) and D (-971.7 mV, -18.19 μA), the similar peak voltages and currents indicate there is no significant difference in the number or type of Au-S bonds between the electrode and NTR after the extended incubation period.

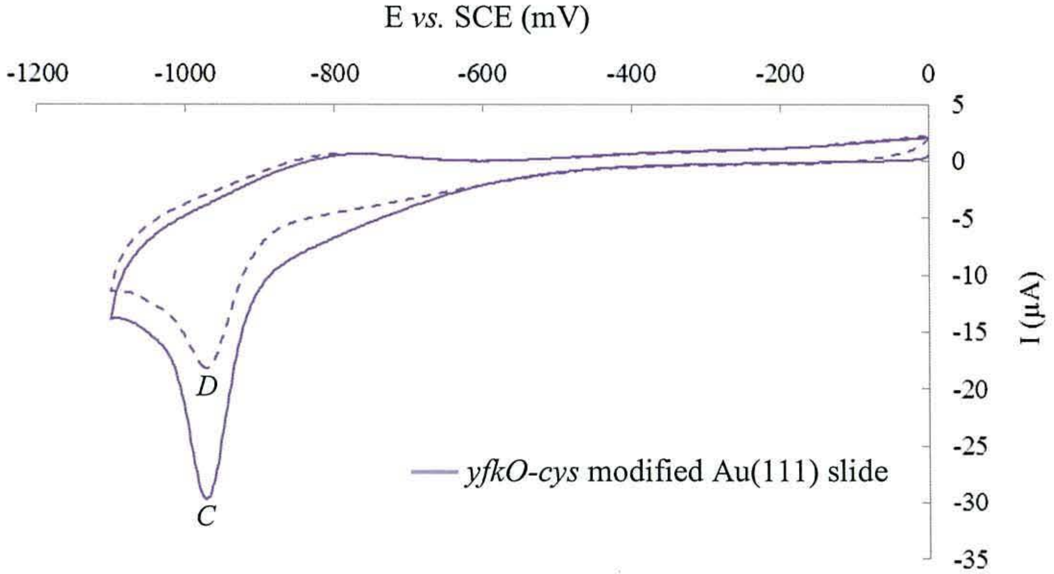

Figure 5.1.3. Voltammogram showing two consecutive reduction cycles of an Au(111) coated glass slide after 4 day incubation with yfkO-cys (1 purple solid C = -974.1 mV, -29.68 μA and 2 purple dash D = -971.7 mV, -18.19 μA). The potential is vs. SCE in an electrolyte of 0.1 M NaOH

Comparing *Figure 5.1.2* with *Figure 5.1.3* suggests that within a 24 hour period a surface layer of NTRs forms *via* Au-S linkages that saturates the Au surface, such that no further Au-S bonds form after 3 additional days of incubation, however it is not clear whether there is NTR surface exchange during this period. If an NTR dissociates from the Au surface during incubation there is an excess of NTRs in free solution to occupy the vacancy. For MNP-DEPT individual NTRs must remain immobilised to the Au surface after the colloid is washed from the incubation solution, so that only a monolayer of NTRs remain bound to the SPION@Au surface. To determine if *yfkO-cys* dissociates from the gold surface, an Au(111) coated glass slide was incubated for 4 days with the NTR then removed from the incubation solution, washed and immersed in dH_2O for 24 hours, the voltammogram is shown in *Figure 5.1.4*.

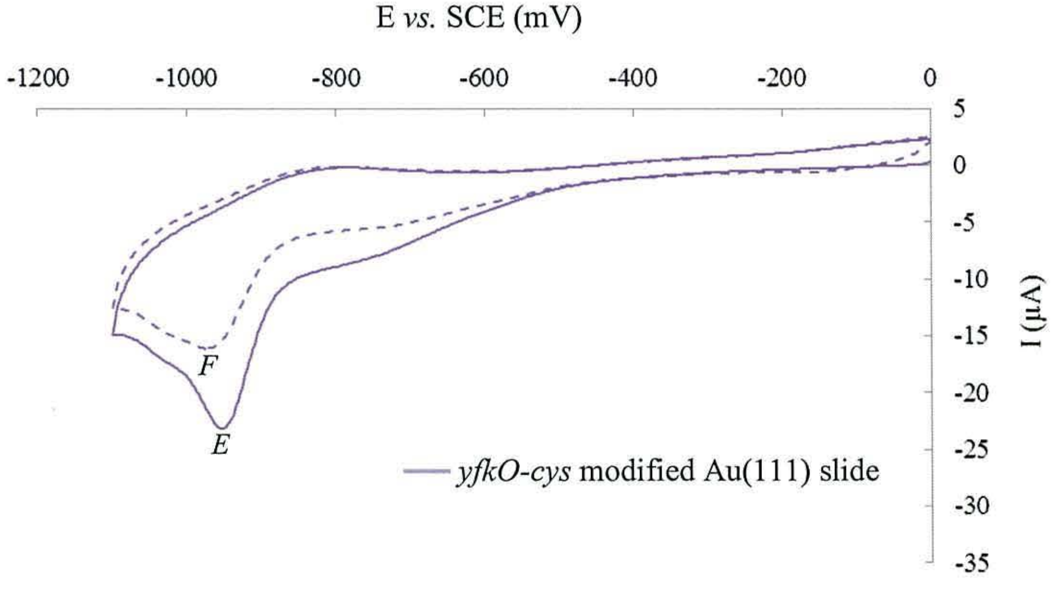

Figure 5.1.4. Voltammogram showing two consecutive reduction cycles of an Au(111) coated glass slide after 4 day incubation with yfkO-cys followed by removal, washing and 24 hour incubation in dH_2O (1 purple solid E = -954.6 mV, -23.18 µA and 2 purple dash F = -976.6 mV, -16.13 µA). The potential is vs. SCE in an electrolyte of 0.1 M NaOH

The reduction in current at *E* (-954.6 mV, -23.18 µA) compared to that observed at *C* in *Figure 5.1.3.* (-974.1 mV, -29.68 µA) indicates fewer Au-S bonds are being reduced at *E*. The 19.5 mV shift in potential also suggests the configuration of the Au-S bonds has changed. During incubation it would be expected the NTRs would adsorb to the Au surface with packing efficiency increasing over time, dependant on NTR concentration and temperature. If during the 24 hour period in dH_2O an NTR desorbs from the surface there isn't a readily available NTR in free solution to occupy the vacancy. This lower NTR density on the Au surface then allows the orientation and packing of the NTRs to change. An overlay of the first reduction cycles from the two experiments is shown in *Figure 5.1.5*.

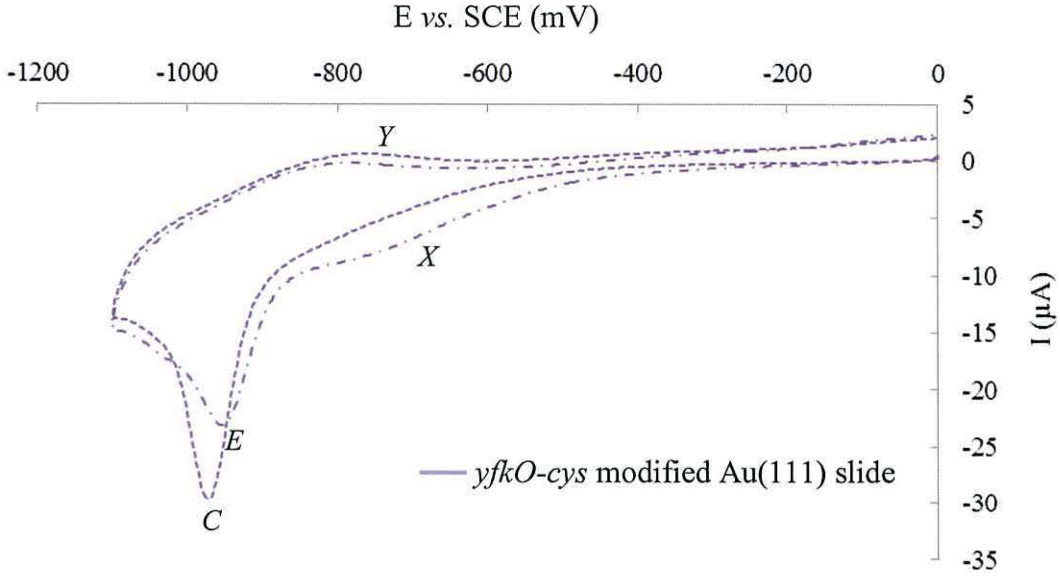

Figure 5.1.5. Voltammogram showing the first reduction cycles of an Au(111) coated glass slide after 4 day incubation with yfkO-cys (purple dotted C = -974.1 mV, -29.68 μA) and of an Au(111) coated glass slide after 4 day incubation with yfkO-cys followed by removal, washing and 24 hour incubation in dH_2O *(purple dash-dot E = -954.6 mV, -23.18 μA. The potential is vs. SCE in an electrolyte of 0.1 M NaOH*

The difference in potential and current of *E* compared to *C* suggests the number of Au-S bonds has both decreased and changed in nature.[191] These observations are supported by the shoulders labelled *X* and *Y*. As NTRs desorb from the Au surface the orientation of the remaining NTRs may change. As the NTR conformation changes different functional groups will adsorb to the surface, changing the shape of the immobilised NTR and influencing the Au-S bond and reduction potential.

The shoulder at *Y* is attributed to the rebinding of sulphur groups to Au and is present in each of the voltammograms. The cyclic voltammetry experiments are performed without stirring or agitation, so immediately after reduction, the NTRs, cysteines and sulphur groups remain in very close proximity to the Au surface such that they can rapidly re-associate. This produces the shoulders observed in the voltammograms and gives rise to the second reduction cycle which contains substantial Au-S character. The notable difference at *Y* suggests there is fewer NTRs readsorbing after the Au(111) coated glass slide is incubated for 24 hours in dH_2O, in-line with the differences observed between *C* and *E*.

5.2 Comparing Au-immobilisation of modified nitroreductases

5.2.1 Cyclic voltammetry of *yfkO* and *yfkO-cys*

To compare the immobilisation of the cysteine modified and non-cysteine modified NTRs samples of each were incubated with Au(111) coated glass slides, the results of the cyclic voltammetry experiments are shown in the following figures.

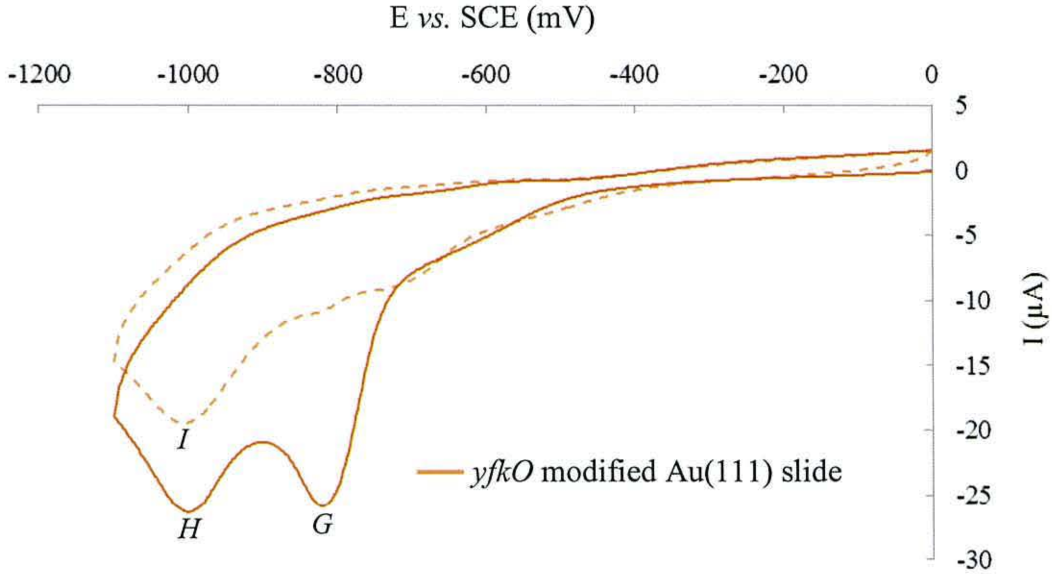

Figure 5.2.1. Voltammogram showing two consecutive reduction cycles of an Au(111) coated glass slide after 4 day incubation with yfkO (1 orange solid G = -822.8 mV, -25.86 μA; H = -1001.0 mV, -26.34 μA and 2 orange dash I = -1005.9 mV, -19.46 μA). The potential is vs. SCE in an electrolyte of 0.1 M NaOH

The first reduction cycle of *yfkO* shows two distinct peaks *G* = -822.8 mV, -25.86 μA and *H* = -1001.0 mV, -26.34 μA. Both peaks are in the region expected for Au-S bonds of cysteine[190] occur at a significantly different potential to that observed for the 12 Au-S bonds of *yfkO-cys*. They correspond to reduction of naturally occurring cysteine residues existing throughout the NTRs. The reduction potential of the majority of alkane thiols in a basic environment is – 1 V ± 0.25 V depending on the nature of the Au surface, the electrolyte and the alkane thiol environment.[188] Reductive desorption of alkane thiols between alkanes containing n carbons of n = 2 and n = 15, with different functional groups terminating the alkane thiols, have reduction potentials varying from -0.7 V to -1.1 V depending on the nature of the alkane.[256] The two desorption peaks present in the *yfkO* voltammogram therefore suggest there are two types of Au-S bonds are forming when the NTR adsorbs to the gold surface.

An overlay of the first reduction cycle of *yfkO* and *yfkO-cys* highlights the different bonding conformations of the two NTRs.

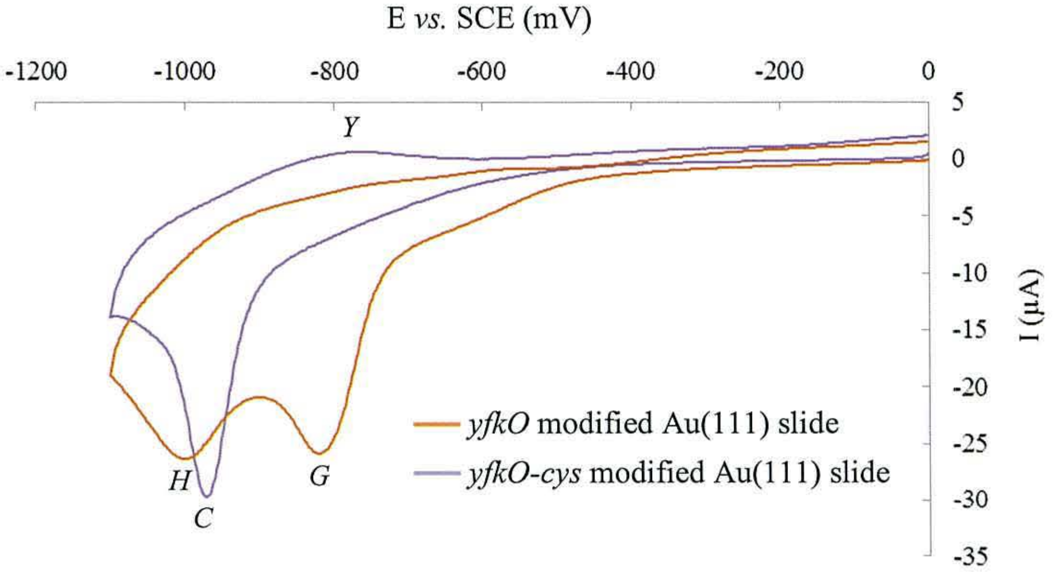

Figure 5.2.2. Voltammogram showing the first reduction cycles of an Au(111) coated glass slide after 4 day incubation with yfkO (orange solid G = -822.8 mV, -25.86 μA; H = -1001.0 mV, -26.34 μA) and yfkO-cys (purple solid C = -974.1 mV, -29.68 μA). The potential is vs. SCE in an electrolyte of 0.1 M NaOH

Both *yfkO* and *yfkO-cys* self-assemble at the Au surface in different orientations, with the latter bonding exclusively *via* just one type of Au-S bond at the potential expected for a sequence of 12 cysteines binding from an NTR to Au.[199] Without a preferential binding site *yfkO* adsorbs to the Au surface in a more disordered manner, leading to different bond energies between the Au and thiol of the naturally occurring cysteine.

5.2.2 Cyclic voltammetry of *nfrA1*

To compare the immobilisation of *nfrA1* to the other NTRs the enzyme was incubated with an Au(111) coated glass slide, the results of the cyclic voltammetry experiments are shown in *Figure 5.2.3*.

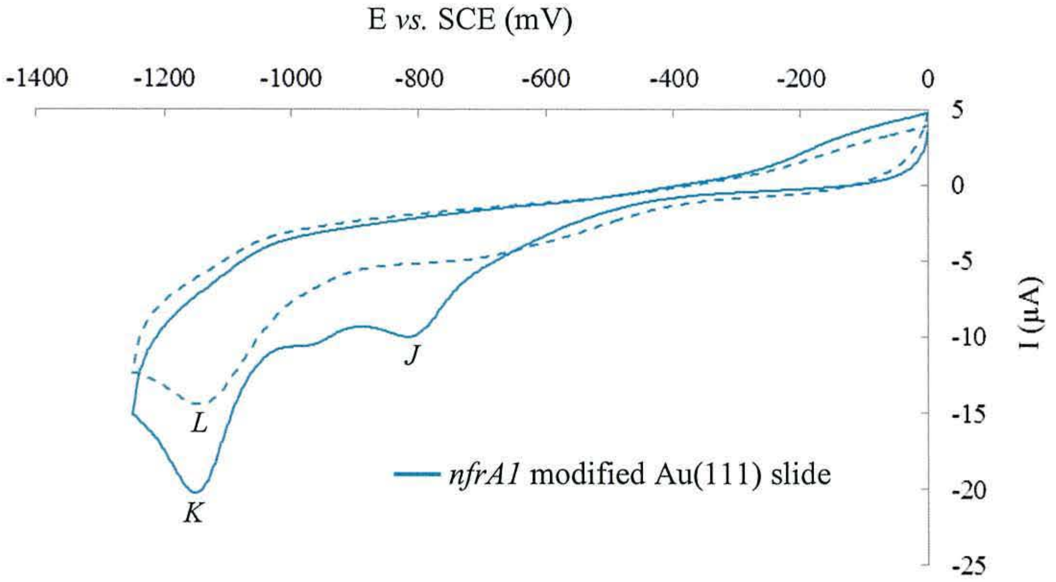

Figure 5.2.3. Voltammogram showing two consecutive reduction cycles of an Au(111) coated glass slide after 4 day incubation with nfrA1 (1 blue solid J = -817.9 mV, -10.03 µA; K = -1152.3 mV, -20.29 µA and 2 blue dash L = -1142.6 mV, -14.48 µA). The potential is vs. SCE in an electrolyte of 0.1 M NaOH

During the first reduction cycle the peaks at *J* and *K* indicate that Au-S bonds form between the NTR and the Au *via* the naturally occurring cysteine residues within the enzyme, producing two distinct bonding types as seen at *J* and *K* (*J* = -817.9 mV, -10.03 µA; *K* = -1152.3 mV, -20.29 µA)

Cyclic voltammetry of nfrA2 and nfrA2-cys

To compare the immobilisation of the cysteine modified and non-cysteine modified NTRs samples of each were incubated with Au(111) coated glass slides, the results of the cyclic voltammetry experiments are shown in the following figures.

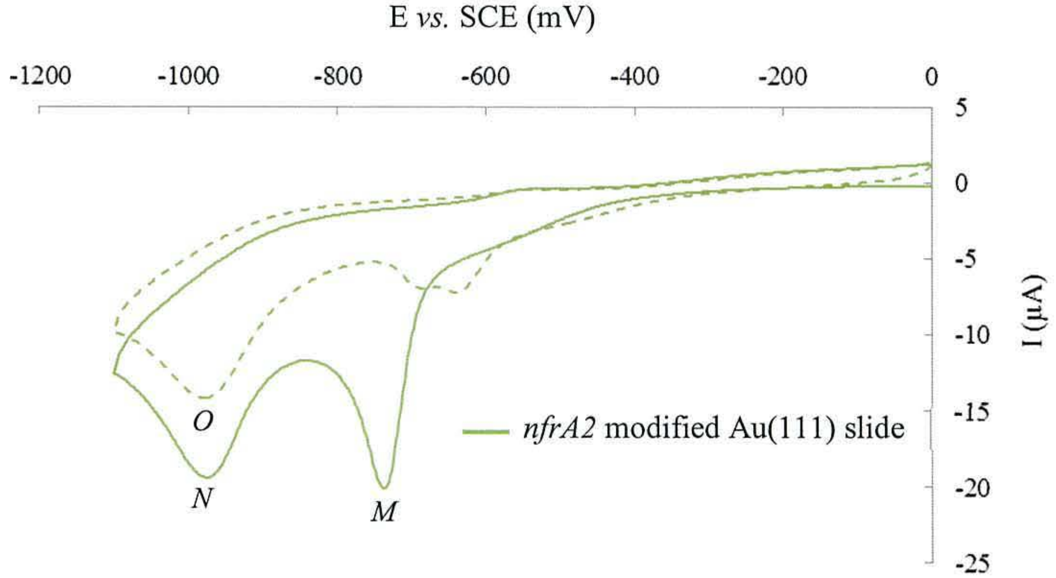

Figure 5.2.4. Voltammogram showing two consecutive reduction cycles of an Au(111) coated glass slide after 4 day incubation with nfrA2 (1 green solid M = -737.3 mV, -20.15 µA; N = -976.6 mV, -19.42 µA and 2 green dash O = -979.0 mV, -14.21 µA). The potential is vs. SCE in an electrolyte of 0.1 M NaOH

The two reduction peaks observed during the first reduction cycle at *M* and *N* (*M* = -737.3 mV, -20.15 µA; *N* = -976.6 mV, -19.42 µA) indicate naturally occurring cysteine groups bonding from the NTR to the Au surface. The second reduction cycle shows a shoulder between -600 mV and -700 mV and a peak at *O* (*O* = -979.0 mV, -14.21 µA). The shoulder corresponds to the thiol bond initially seen at *M* reforming in between cycles, the lower potential and current of the peak suggesting that during the short time period between reduction, the bond does not reform with the same configuration. The peak at *O* is similar in profile to that at *N* and is a common feature of the second reduction cycle for all the NTRs.

The reduction profile of *nfrA2-cys* (*Figure 5.2.5*) is remarkably similar to that of *nfrA2*, with two distinct peaks at *P* and *Q* during the first reduction cycle (*P* = -737.3 mV, -20.99 µA; *Q* = -957.0 mV, -20.83 µA). Similarly to *nfrA2* during the second reduction cycle there is a shoulder between -600 mV and -700 mV and a peak at *R* (*R* = -961.9 mV, -15.77 µA). The addition of a sequence of 12 cysteines into the NTR should provide a preferential binding site to Au. However the structure of the enzyme needs to be such that this sequence is accessible to the surface and not shielded internally within the protein structure. It appears for *nfrA2-cys* this is not the case. An overlay of the first reduction cycles of *nfrA2* and *nfrA2-cys* is shown in *Figure 5.2.6.*

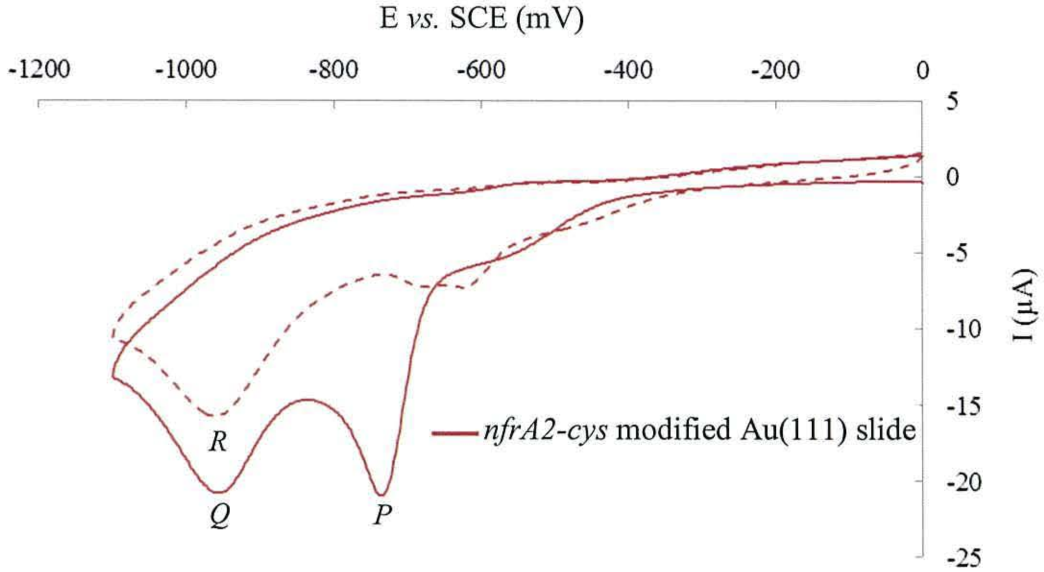

Figure 5.2.5. Voltammogram showing two consecutive reduction cycles of an Au(111) coated glass slide after 4 day incubation with nfrA2-cys (1 red solid P = -737.3 mV, -20.99 µA; Q = -957.0 mV, -20.83 µA and 2 red dash R = -961.9 mV, -15.77 µA). The potential is vs. SCE in an electrolyte of 0.1 M NaOH

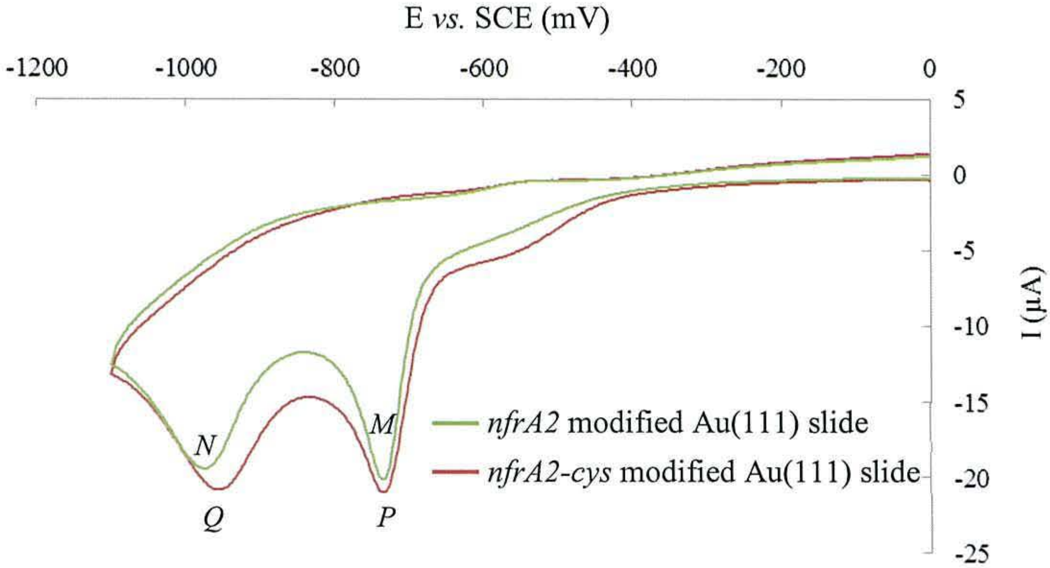

Figure 5.2.6. Voltammogram showing the first reduction cycles of an Au(111) coated glass slide after 4 day incubation with nfrA2 (M = -737.3 mV, -20.15 µA; N = -976.6 mV, -19.42 µA) and nfrA2-cys (red solid P = -737.3 mV, -20.99 µA; Q = -957.0 mV). The potential is vs. SCE in an electrolyte of 0.1 M NaOH

5.2.3 Concluding remarks on cyclic voltammetry

Each of the non-cysteine modified NTRs *yfkO*, *nfrA1* and *nfrA2* adsorb to Au(111) coated glass slides *via* naturally occurring cysteine residues existing throughout the NTR structures. The accessibility of cysteines from within the NTR to the Au surface varies between proteins and the orientation of the NTRs when immobilising to the surface is likely to be random. For each of the three NTRs this leads to multiple bonding conformations between protein and electrode, giving rise to the different reduction potentials of the Au-S bonds observed during cyclic voltammetry experiments.

Genetic modification of *nfrA2* to include a consecutive sequence of 6 cysteine residues into each monomer did not lead to a significant difference in the reduction profile of the immobilised NTR, suggesting the cysteine sequence is not able to access the Au surface from this location in the protein structure. However when a sequence of 6 cysteine residues is introduced into the *yfkO* sequence the reduction profile changes dramatically, *yfkO-cys* binds to the Au surface exclusively via one type of Au-S bond at the potential expected for a cysteine modified NTR.[199]

yfkO has therefore been genetically engineered to include a cysteine sequence which provides the enzyme with a preferential bonding site which does not include any of the naturally occurring amino acids from the enzyme structure, controlling the orientation of bonding and limiting any structural changes to the enzyme upon Au immobilisation.

5.3 *yfkO* and *yfkO-cys* immobilisation onto gold coated magnetic particles

Excess *yfkO* and *yfkO-cys* were incubated with samples of SPION@Au for 24 hours and the SPION@Au recovered by centrifugation. The supernatant was removed and the particles redispersed in dH_2O using an ultrasonic bath, the process was repeated and the resulting purified NTR@SPION@Au redispersed in dH_2O. The preparation is designed to ensure there is sufficient enzyme to saturate the SPION@Au surface and remove excess enzyme from free solution. Dynamic light scattering was used to characterise the NTR@SPION@Au. The results of this are shown in the following figures.

The hydrodynamic diameter of the SPION@Au is 58.2 nm, the size distribution of the particles, their morphology and surface bound citrate ions contribute to the larger hydrodynamic diameter compared to that observed of the dried particles obtained *via* TEM. The hydrodynamic diameter increases to 64.8 nm for *yfkO*@SPION@Au and to 67.5 nm for *yfkO-cys*@SPION@Au, the increased diameter indicating in both instances the

NTRs have immobilised onto the nanoparticle surface. From cyclic voltammetry experiments it is expected that *yfkO-cys* binds exclusively *via* the introduced sequence of cysteine residues while *yfkO* binds in a more random orientation. The difference between the two hydrodynamic diameters may therefore be caused by the more uniform immobilisation of *yfkO-cys* leading to a more ordered and larger solvation shell for *yfkO-cys*@SPION@Au.

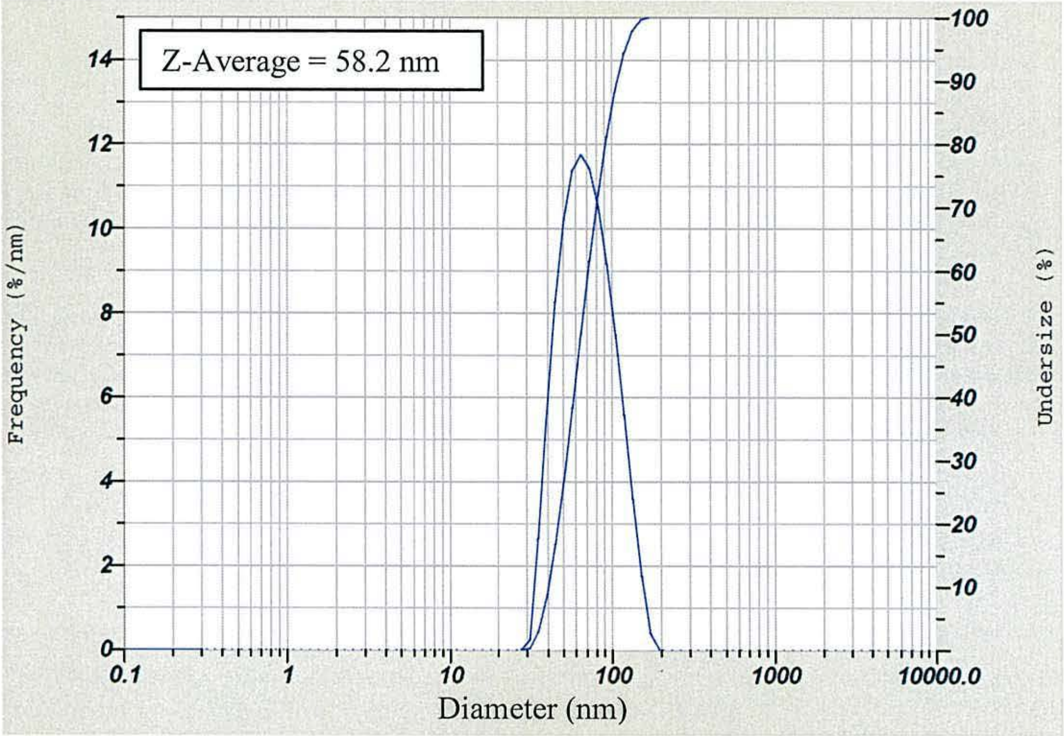

Figure 5.3.1. Dynamic light scattering measurement showing the average particle size of citrate stabilised SPION@Au in dH_2O

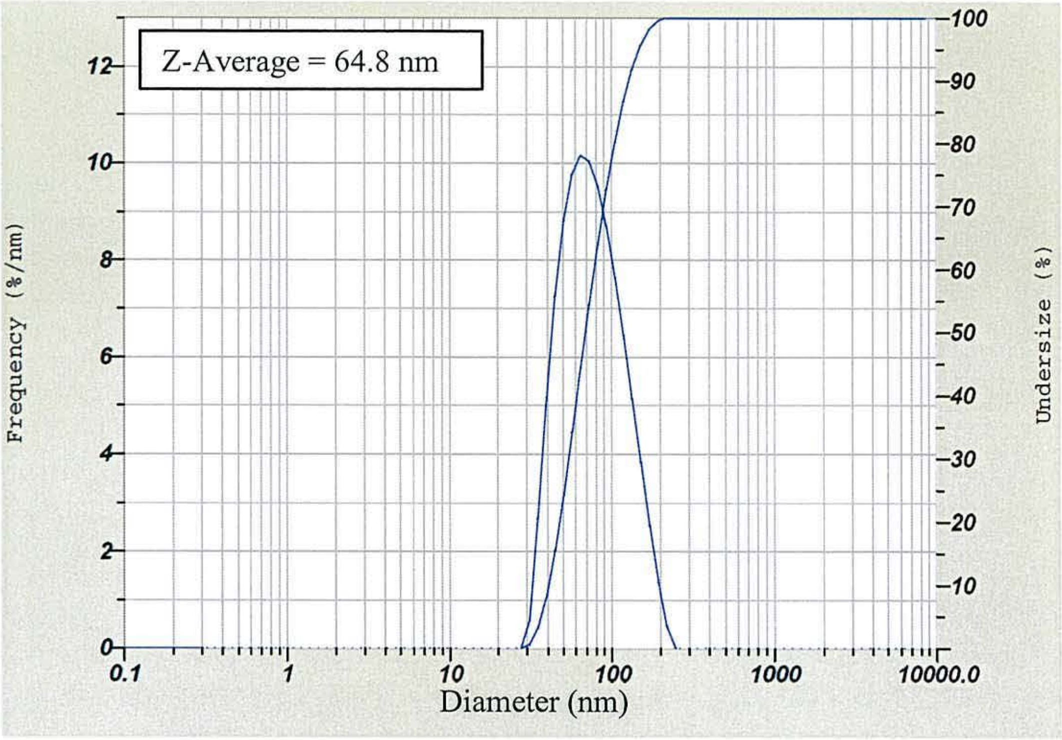

Figure 5.3.2. Dynamic light scattering measurement showing the average particle size of yfkO@SPION@Au in dH_2O

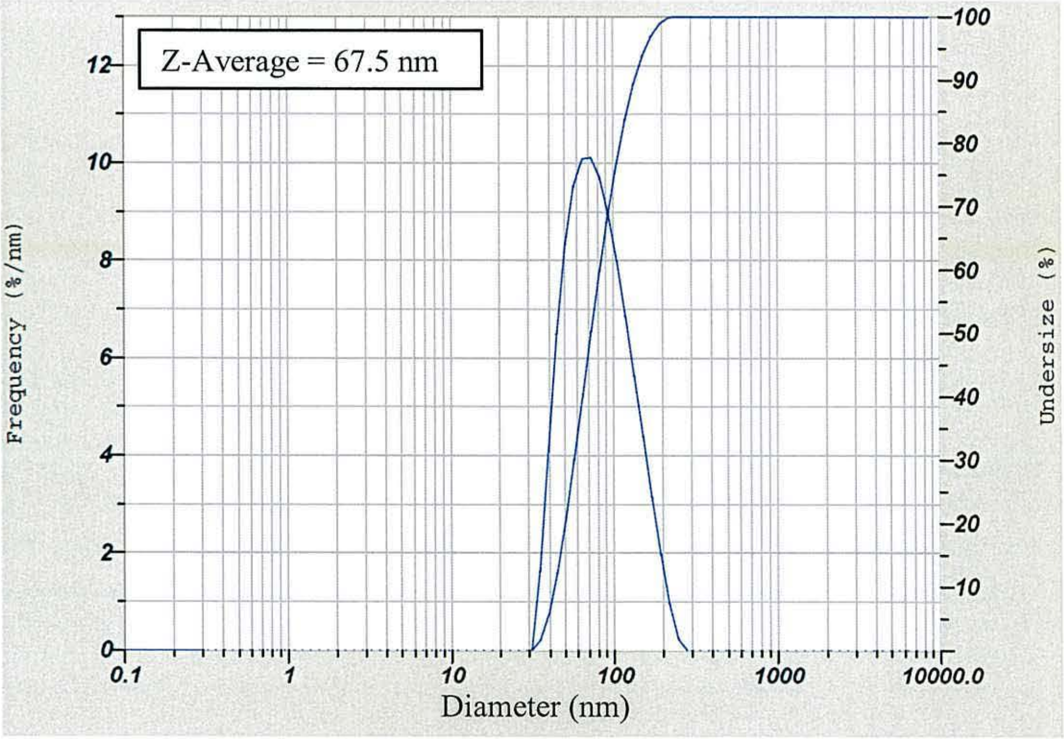

Figure 5.3.3. Dynamic light scattering measurement showing the average particle size of yfkO-cys@SPION@Au in dH_2O

5.4 Concluding remarks on enzyme immobilisation

Cyclic voltammetry reveals that each of the five candidate NTRs bond to an Au surface *via* Au-S bonds and that *yfkO-cys* does so exclusively *via* the introduced cysteine sequence. The bonding is such that naturally occurring cysteine residues throughout the enzyme are not involved in the immobilisation process meaning the enzyme binds with controlled orientation. DLS measurements show an increased hydrodynamic radius for *yfkO-cys*@SPION@Au compared to citrate@SPION@Au of 4.65 nm, the approximate size of an NTR,[80, 202] indicating the enzyme forms a monolayer over the nanoparticle surface *via* the introduced cysteine residues.

The immobilisation of enzymes onto nanoparticles typically improves the activity and stability of the enzymes.[257-259] However the nature of the immobilising bonds are critical to the effects to the enzymes kinetic properties.[260] It is envisaged that by introducing a preferential immobilising sequence outside of the native NTR structure any negative effects of immobilisation are limited as the accessibility to the active site is not hindered by random surface orientation. For a magnetically directed enzyme prodrug therapy (MNP-DEPT) it is important the enzyme orientation is controlled and a surface monolayer forms over the nanoparticles, utilising an introduced Cys-tag in combination with an Au surface coating to SPION provides a facile route to achieving this by exploiting thiol-Au self-assembly.

Chapter 6

CONCLUSION

6.1 Concluding remarks

The NTRs *yfkO*, *nfrA1* and *nfrA2* from *B. Licheniformis* and *ydjA* from *S. typhimurium* were cloned and assayed for their activity with the prodrug CB1954. The enzymes were genetically modified to include a preferential binding sequence to allow them to immobilise onto an Au surface and these analogues were also assayed with the prodrug in free solution. *yfkO*, *nfrA1* and *nfrA2* were shown to be active with CB1954 as were the cysteine modified analogues *yfkO-cys* and *nfrA2-cys*. *nfrA2* and *nfrA2-cys* were shown to be of particular interest for application in CB1954 NTR DEPT having higher specificity constants than many other NTRs identified as active with the prodrug, including the much studied *nfnB* from *E. coli.* Assaying and identifying new NTRs for application in DEPT is crucial to improve the efficacy of the treatment and the characterisation of these enzymes with CB1954 is an important step in improving our understanding of CB1954 nitroreduction and developing the therapy.

Attempts to reproduce literature that detail the synthesis of SPION@Au highlight the difficulties in creating the hybrid nanoparticles. However modifications to a procedure which directly reduces $HAuCl_4$ on to SPION allowed SPION@Au of a suitable size for *in vivo* application to be synthesised and isolated. The cysteine and non-cysteine modified NTRs self-assemble onto Au surfaces *via* thiol bonds and in the case of *yfkO-cys* exclusively *via* the introduced Cys-tag, controlling the orientation of the immobilised enzyme. This research is the first to employ such a strategy of exploiting the Au-S bond and incorporating an Au surface coating to magnetic nanoparticles in tandem with the introduction of a Cys-tag to NTRs so that a magnetically controllable DEPT can be developed.

6.2 Future directions

6.2.1 Developing nitroreductases for application in therapy

The structure activity relationship between NTRs and reduction of the 2- and 4-nitro groups of CB1954 should be fully understood if the treatment is to be optimised for use in DEPT. From the literature, research has been undertaken into the genetic modification of *nfnB* from *E. coli* incorporating single, double and triple mutants,[73, 74] computational methods have been utilised to understand the reaction mechanism[81] and some research has been done to identify NTRs across other bacterial species which may provide mechanistic insight or application for therapy.[72, 86, 87, 234]

The screening of potentially interesting NTRs for application in DEPT as has been described here is an important contribution to the previously reported research but is of most value if the absolute enzyme structure is elucidated. In the case of *yfkO*, *nfrA1* and *nfrA2* their activities with CB1954 under varying environmental conditions has been shown, yet their crystal structure remains unknown. However for *ydjA* the crystal structure revealed a wider, more flexible active site making the enzyme a promising candidate for DEPT as the NTR should theoretically be able to accommodate a wide variety of substrates,[202] yet as reported by Prosser *et al* and supported by this study, *ydjA* is not able to activate the prodrug.[72]

The future direction for the development of NTRs for DEPT should therefore be the consolidation and comparison of reduction rates of CB1954 with NTRs using a standardised method to determine kinetic parameters and applying this to all NTRs that have to date been assayed with CB1954 and shown activity. If the crystal structures of the NTRs can be elucidated a correlation between CB1954 reduction rate and the enzyme structure may be found so that an ideal NTR structure can be constructed for optimum efficacy in DEPT.

6.2.2 Immobilising nitroreductases onto magnetic nanoparticles for therapy

Figure 6.1.1 shows an illustration of a non-toxic prodrug being activated to a cytotoxic moiety *via* an enzyme functionalised nanoparticle. Immobilising nitroreductases onto magnetic particles may allow the enzymes to be manipulated magnetically, allowing them to be located to specific locations for targeted therapy by application of an external magnetic field.

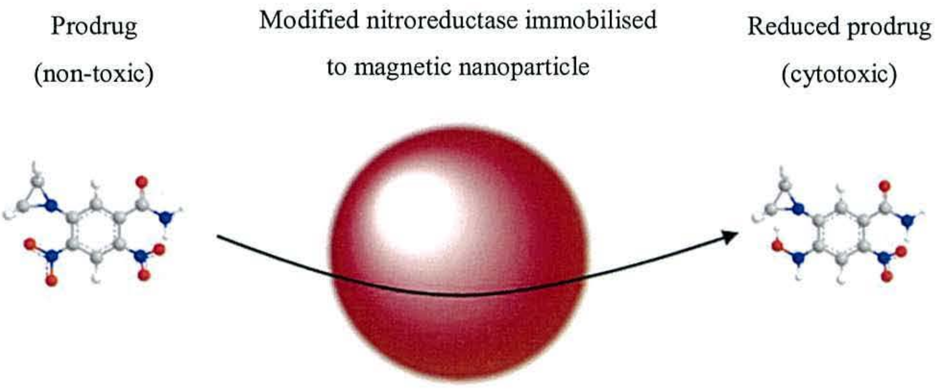

Figure 6.1.1. An illustration of the non-toxic prodrug CB1954 being activated to a cytotoxic hydroxylamine derivative following reduction by a nitroreductase. If the enzymes which catalyse this reaction can be immobilised onto magnetic nanoparticles, they may be magnetically located exclusively to disease sites by applying an external magnetic field.

The modification of the SPION@Au synthesis as reported by Lyon *et al.* led to the creation of particles of suitable diameter for *in vivo* application. Ideally the synthesis would not involve a purification step to separate uncoated SPION from SPION@Au. However there are distinct advantages to using such a simple coating process including the low cost, technical simplicity and non-toxicity of the reagents and solvents used during reaction. While the Au coating of the magnetic nanoparticles was achieved, the impact on the magnetic properties of the sol was not determined in this study and the Au loading of SPION will decrease the magnetic saturation of the particles. For application in DEPT the magnetic carriers should have a high magnetic saturation and it is likely that the Au coating thickness could be reduced to limit Au loading effects.

The addition of a Cys-tag to the NTR monomer sequence proved to be unpredictable, in some cases preventing enzyme purification and inhibiting activity while in other cases these effects were minimal. The varying nature of the Cys-tag insertion was also observed on immobilisation, with only one of the modified enzymes clearly binding *via* one type of Au-S bond. It is an important step in the development of MNP-DEPT to show that an NTR can be genetically modified to include a preferential binding site to Au and immobilised to SPION@Au. However the unpredictable nature of Cys-tag insertion such that an NTR may no longer purify, lose activity to the prodrug and may not preferentially bind *via* the Cys-tag suggests this immobilisation strategy could be optimised.

This study has shown that a Cys-tag may be inserted that does not significantly reduce enzyme activity to CB1954, such as the case with *nfrA2* and *nfrA2-cys* and that it is also possible to introduce a cysteine sequence to achieve controlled immobilisation such as the case with *yfkO* and *yfkO-cys*. It is therefore likely that for any given NTR structure there is an ideal Cys-tag location which provides controlled immobilisation while minimising negative effects to enzyme activity. To develop the immobilisation strategy for MNP-DEPT in the future priority should therefore be given to identifying an optimised NTR structure before identifying the optimum Cys-tag location for it. Assays of the immobilised NTR on the hybrid particles can then be undertaken to determine the viability of this therapy strategy.

REFERENCES

1. H. M. Atta, *Am. Surg.*, 1999, **65**, 1190-1192.
2. W. Moore, *Br. Med. J.*, 2011, **342**, 1598.
3. http://www.who.int/healthinfo/statistics/mortality/en/index.html, Accessed 2011.
4. C. La Vecchia, C. Bosetti, F. Lucchini, P. Bertuccio, E. Negri, P. Boyle and F. Levi, *Annals of Oncology*, 2010, **21**, 1323-1360.
5. M. Malvezzi, A. Arfe, P. Bertuccio, F. Levi, C. La Vecchia and E. Negri, *Annals of Oncology*, 2011, **22**, 947-956.
6. B. K. Edwards, M. L. Brown, P. A. Wingo, H. L. Howe, E. Ward, L. A. G. Ries, D. Schrag, P. M. Jamison, A. Jemal, X. C. Wu, C. Friedman, L. Harlan, J. Warren, R. N. Anderson and L. W. Pickle, *J. Natl. Cancer Inst.*, 2005, **97**, 1407-1427.
7. S. Eckhouse, G. Lewison and R. Sullivan, *Molecular Oncology*, 2008, **2**, 20-32.
8. P. Boyle, *Annals of Oncology*, 2008, **19**, 605-606.
9. M. J. Quinn, A. d'Onofrio, B. Moller, R. Black, C. Martinez-Garcia, H. Moller, M. Rahu, C. Robertson, L. J. Schouten, C. La Vecchia and P. Boyle, *Annals of Oncology*, 2003, **14**, 1148-1152.
10. L. Foulds, *Cancer Res.*, 1954, **14**, 327-339.
11. C. Lengauer, K. W. Kinzler and B. Vogelstein, *Nature*, 1998, **396**, 643-649.
12. B. Vogelstein and K. W. Kinzler, *Nat. Med.*, 2004, **10**, 789-799.
13. D. Hanahan and R. A. Weinberg, *Cell*, 2000, **100**, 57-70.
14. S. S. Hecht, *J. Natl. Cancer Inst.*, 1999, **91**, 1194-1210.
15. E. Cardis, M. Vrijheid, M. Blettner, E. Gilbert, M. Hakama, C. Hill, G. Howe, J. Kaldor, C. R. Muirhead, M. Schubauer-Berigan, T. Yoshimura and S. G. Int, *Br. Med. J.*, 2005, **331**, 77-80.
16. D. L. Mager, *Journal of Translational Medicine*, 2006, **4**, 14.
17. A. Storey, M. Thomas, A. Kalita, C. Harwood, D. Gardiol, F. Mantovani, J. Breuer, I. M. Leigh, G. Matlashewski and L. Banks, *Nature*, 1998, **393**, 229-234.
18. Y. Bendavid and A. Bernstein, *Cell*, 1991, **66**, 831-834.

19. M. Wainwright, *Rev. Med. Microbiol.*, 2002, **13**, 37-42.

20. K. Ohtsubo, M. Saito, T. Ishiko, M. Umeda, S. Sekita, K. Yoshihira, S. Natori, F. Sakabe, S. Udagawa and H. Kurata, *Jpn. J. Exp. Med.*, 1978, **48**, 257-264.

21. F. McCormick, *J. Surg. Oncol.*, 2011, **103**, 464-467.

22. V. Huff, *Nature Reviews Cancer*, 2011, **11**, 111-121.

23. D. J. Slamon, G. M. Clark, S. G. Wong, W. J. Levin, A. Ullrich and W. L. Mcguire, *Science*, 1987, **235**, 177-182.

24. A. Pardee and G. Stein, Book, *The biology and treatment of cancer: understanding cancer*, Wiley, 2008.

25. R. Weinberg, Book, *The Biology of Cancer*, Taylor & Francis, 2006.

26. http://www.nhs.uk/conditions/cancer, Accessed 2011.

27. C. Smith, *J. Clin. Pharmacol.*, 2005, **45**, 371-377.

28. H. L. Shi-ping Luh, *Journal of Zhejiang University Science B*, 2006, **7**, 118-128.

29. R. Langer, *Nature*, 1998, **392**, 5-10.

30. S. Muro, *J. Controlled Release*, 2012, **164**, 125-137.

31. F. Yamashita and M. Hashida, *Adv. Drug Deliv. Rev.*, 2013, **65**, 139-147.

32. S. Quasthoff and H. Hartung, *J. Neurol.*, 2002, **249**, 9-17.

33. R. Go and A. Adjei, *J. Clin. Oncol.*, 1999, **17**, 409-422.

34. G. Dubowchik and M. Walker, *Pharmacol. Ther.*, 1999, **83**, 67-123.

35. F. Kratz, I. A. Muller, C. Ryppa and A. Warnecke, *Chemmedchem*, 2008, **3**, 20-53.

36. O. Greco and G. Dachs, *J. Cell. Physiol.*, 2001, **187**, 22-36.

37. M. Rooseboom, J. N. M. Commandeur and N. P. E. Vermeulen, *Pharmacol. Rev.*, 2004, **56**, 53-102.

38. G. Philpott, W. Shearer, R. Bower and C. Parker, *Journal of Immunology*, 1973, **111**, 921-929.

39. S. K. Sharma and K. D. Bagshawe, Book, *Macromolecular Anticancer Therapeutics*, 2010, 393-406.

40. K. D. Bagshawe, S. K. Sharma, P. J. Burke, R. G. Melton and R. J. Knox, *Curr. Opin. Immunol.*, 1999, **11**, 579-583.

41. R. J. Francis, S. K. Sharma, C. Springer, A. J. Green, L. D. Hope-Stone, L. Sena, J. Martin, K. L. Adamson, A. Robbins, L. Gumbrell, D. O'Malley, E. Tsiompanou, H. Shahbakhti, S. Webley, D. Hochhauser, A. J. Hilson, D. Blakey and R. H. J. Begent, *Br. J. Cancer*, 2002, **87**, 600-607.

42. R. J. Knox, F. Friedlos and M. P. Boland, *Cancer Metastasis Rev.*, 1993, **12**, 195-212.
43. A. Mayer, R. J. Francis, S. K. Sharma, B. Tolner, C. J. Springer, J. Martin, G. M. Boxer, J. Bell, A. J. Green, J. A. Hartley, C. Cruickshank, J. Wren, K. A. Chester and R. H. J. Begent, *Clinical Cancer Research,* 2006, **12**, 6509-6516.
44. P. Patel, J. G. Young, V. Mautner, D. Ashdown, S. Bonney, R. G. Pineda, S. I. Collins, P. F. Searle, D. Hull, E. Peers, J. Chester, D. M. Wallace, A. Doherty, H. Leung, L. S. Young and N. D. James, *Molecular Therapy,* 2009, **17**, 1292-1299.
45. T. Connors, *Gene Ther.*, 1995, **2**, 702-709.
46. J. Harris, A. Gutierrez, H. Hurst, K. Sikora and N. Lemoine, *Gene Ther.,* 1994, **1**, 170-175.
47. G. Dachs, J. Tupper and G. Tozer, *Anticancer Drugs,* 2005, **16**, 349-359.
48. G. Chung-Faye, D. Palmer, D. Anderson, J. Clark, M. Downes, J. Baddeley, S. Hussain, P. Murray, P. Searle, L. Seymour, P. Harris, D. Ferry and D. Kerr, *Clinical Cancer Research,* 2001, **7**, 2662-2668.
49. G. Chung-Faye, M. Chen, N. Green, A. Burton, D. Anderson, V. Mautner, P. Searle and D. Kerr, *Gene Ther.,* 2001, **8**, 1547-1554.
50. M. Gnant, L. Noll, K. Irvine, M. Puhlmann, R. Terrill, H. Alexander and D. Bartlett, *J. Natl. Cancer Inst.,* 1999, **91**, 1744-1750.
51. R. J. Knox, F. Friedlos, M. Jarman and J. J. Roberts, *Biochem. Pharmacol.,* 1988, **37**, 4661-4669.
52. R. J. Knox, M. P. Boland, F. Friedlos, B. Coles, C. Southan and J. J. Roberts, *Biochem. Pharmacol.,* 1988, **37**, 4671-4677.
53. R. J. Knox, F. Friedlos, T. Marchbank and J. J. Roberts, *Biochem. Pharmacol.,* 1991, **42**, 1691-1697.
54. R. J. Knox, F. Friedlos, R. F. Sherwood, R. G. Melton and G. M. Anlezark, *Biochem. Pharmacol.,* 1992, **44**, 2297-2301.
55. G. M. Anlezark, R. G. Melton, R. F. Sherwood, B. Coles, F. Friedlos and R. J. Knox, *Biochem. Pharmacol.,* 1992, **44**, 2289-2295.
56. J. A. Bridgewater, C. J. Springer, R. J. Knox, N. P. Minton, N. P. Michael and M. K. Collins, *Eur. J. Cancer,* 1995, **31A**, 2362-2370.
57. N. A. Helsby, S. J. Wheeler, F. B. Pruijn, B. D. Palmer, S. J. Yang, W. A. Denny and W. R. Wilson, *Chem. Res. Toxicol.,* 2003, **16**, 469-478.

58. I. A. McNeish, N. K. Green, M. G. Gilligan, M. J. Ford, V. Mautner, L. S. Young, D. J. Kerr and P. F. Searle, *Gene Ther.*, 1998, **5**, 1061-1069.
59. A. Khan and W. Ross, *Chem. Biol. Interact.*, 1971, **4**, 11-19.
60. M. Boland, R. Knox and J. Roberts, *Biochem. Pharmacol.*, 1991, **41**, 867-875.
61. S. Weedon, N. Green, I. McNeish, M. Gilligan, V. Mautner, C. Wrighton, A. Mountain, L. Young, D. Kerr and P. Searle, *International Journal of Cancer,* 2000, **86**, 848-854.
62. D. Palmer, V. Mautner, D. Mirza, S. Oliff, W. Gerritsen, d. S. van, S. Hubscher, G. Reynolds, S. Bonney, R. Rajaratnam, D. Hull, M. Horne, J. Ellis, A. Mountain, S. Hill, P. Harris, P. Searle, L. Young, N. James and D. Kerr, *Journal of Clinical Oncology,* 2004, **22**, 1546-1552.
63. N. A. Helsby, D. M. Ferry, A. V. Patterson, S. M. Pullen and W. R. Wilson, *Br. J. Cancer,* 2004, **90**, 1084-1092.
64. J. A. Bridgewater, R. J. Knox, J. D. Pitts, M. K. Collins and C. J. Springer, *Hum. Gene Ther.,* 1997, **8**, 709-717.
65. A. H. Djeha, A. Hulme, M. T. Dexter, A. Mountain, L. S. Young, P. F. Searle, D. J. Kerr and C. J. Wrighton, *Cancer Gene Ther.,* 2000, **7**, 721-731.
66. W. Wilson, S. Pullen, A. Hogg, N. Helsby, K. Hicks and W. Denny, *Cancer Res.,* 2002, **62**, 1425-1432.
67. B. D. Palmer, W. R. Wilson, S. Cliffe and W. A. Denny, *J. Med. Chem.,* 1992, **35**, 3214-3222.
68. G. Anlezark, R. Melton, R. Sherwood, W. Wilson, W. Denny, B. Palmer, R. Knox, F. Friedlos and A. Williams, *Biochem. Pharmacol.,* 1995, **50**, 609-618.
69. F. Friedlos, W. Denny, B. Palmer and C. Springer, *J. Med. Chem.,* 1997, **40**, 1270-1275.
70. G. J. Atwell, S. Yang, F. B. Pruijn, S. M. Pullen, A. Hogg, A. V. Patterson, W. R. Wilson and W. A. Denny, *J. Med. Chem.,* 2007, **50**, 1197-1212.
71. D. V. Voet J. G., Book, *Biochemistry*, John Wiley and Sons, Inc, 2004.
72. G. A. Prosser, J. N. Copp, S. P. Syddall, E. M. Williams, J. B. Smaill, W. R. Wilson, A. V. Patterson and D. F. Ackerley, *Biochem. Pharmacol.,* 2010, **79**, 678-687.
73. P. R. Race, A. L. Lovering, S. A. White, J. I. Grove, P. F. Searle, C. W. Wrighton and E. I. Hyde, *J. Mol. Biol.,* 2007, **368**, 481-492.

74. D. Jarrom, M. Jaberipour, C. P. Guise, S. Daff, S. A. White, P. F. Searle and E. I. Hyde, *Biochemistry (N. Y.),* 2009, **48**, 7665-7672.

75. M. Dolores Roldan, E. Perez-Reinado, F. Castillo and C. Moreno-Vivian, *FEMS Microbiol. Rev.*, 2008, **32**, 474-500.

76. T. Haack, L. Erdinger and G. Boche, *Mutat. Res. -Genet. Toxicol. Environ. Mutag.*, 2001, **491**, 183-193.

77. K. Durchschein, M. Hall and K. Faber, *Green Chem.*, 2013, **15**, 1764-1772.

78. P. R. Race, A. L. Lovering, R. M. Green, A. Ossor, S. A. White, P. F. Searle, C. J. Wrighton and E. I. Hyde, *J. Biol. Chem.*, 2005, **280**, 13256-13264.

79. C. A. Haynes, R. L. Koder, A. F. Miller and D. W. Rodgers, *J. Biol. Chem.*, 2002, **277**, 11513-11520.

80. G. Parkinson, J. Skelly and S. Neidle, *J. Med. Chem.*, 2000, **43**, 3624-3631.

81. A. Christofferson and J. Wilkie, *Biochem. Soc. Trans.*, 2009, **37**, 413-418.

82. S. O. Vass, D. Jarrom, W. R. Wilson, E. I. Hyde and P. F. Searle, *Br. J. Cancer,* 2009, **100**, 1903-1911.

83. T. Kobori, H. Sasaki, W. C. Lee, S. Zenno, K. Saigo, M. E. P. Murphy and M. Tanokura, *J. Biol. Chem.*, 2001, **276**, 2816-2823.

84. J. I. Grove, A. L. Lovering, C. Guise, P. R. Race, C. J. Wrighton, S. A. White, E. I. Hyde and P. F. Searle, *Cancer Res.*, 2003, **63**, 5532-5537.

85. D. I. Svergun, M. V. Petoukhov, M. H. J. Koch and S. Konig, *J. Biol. Chem.*, 2000, **275**, 297-302.

86. A. Celik and G. Yetis, *Bioorg. Med. Chem.*, 2012, **20**, 3540-3550.

87. G. Anlezark, T. Vaughan, E. Fashola-Stone, N. Michael, H. Murdoch, M. Sims, S. Stubbs, S. Wigleys and N. Minton, *Microbiology-Sgm,* 2002, **148**, 297-306.

88. L. F. Tietze and B. Krewer, *Chemical Biology & Drug Design,* 2009, **74**, 205-211.

89. G. Xu and H. McLeod, *Clinical Cancer Research,* 2001, **7**, 3314-3324.

90. B. Huber, E. Austin, C. Richards, S. Davis and S. Good, *Proc. Natl. Acad. Sci. U. S. A.*, 1994, **91**, 8302-8306.

91. N. R. Jabir, S. Tabrez, G. M. Ashraf, S. Shakil, G. A. Damanhouri and M. A. Kamal, *International Journal of Nanomedicine,* 2012, **7**, 4391-4408.

92. X. Dong, X. Qiu, Q. Liu and J. Jia, *Tumor Biol.*, 2013, **34**, 3273-3278.

93. S. K. Arora, A. L. Porter, J. Youtie and P. Shapira, *Scientometrics,* 2013, **95**, 351-370.

94. M. C. Daniel and D. Astruc, *Chem. Rev.*, 2004, **104**, 293-346.

95. F. E. Wagner, S. Haslbeck, L. Stievano, S. Calogero, Q. A. Pankhurst and P. Martinek, *Nature,* 2000, **407**, 691-692.

96. M. Faraday, 1857, **147**, 145-181.

97. S. Panigrahi, S. Basu, S. Praharaj, S. Pande, S. Jana, A. Pal, S. K. Ghosh and T. Pal, *Journal of Physical Chemistry C,* 2007, **111**, 4596-4605.

98. P. K. Sudeep and T. Emrick, *Polymer Reviews,* 2007, **47**, 155-163.

99. C. Y. Jiang and V. V. Tsukruk, *Adv Mater,* 2006, **18**, 829-840.

100. X. L. Luo, A. Morrin, A. J. Killard and M. R. Smyth, *Electroanalysis,* 2006, **18**, 319-326.

101. K. K. Jain, *Clinica Chimica Acta,* 2005, **358**, 37-54.

102. A. J. Mieszawska, W. J. M. Mulder, Z. A. Fayad and D. P. Cormode, *Molecular Pharmaceutics,* 2013, **10**, 831-847.

103. P. K. Jain, X. Huang, I. H. El-Sayed and M. A. El-Sayad, *Plasmonics,* 2007, **2**, 107-118.

104. J. L. West and N. J. Halas, *Annu. Rev. Biomed. Eng.,* 2003, **5**, 285-292.

105. S. Rana, A. Bajaj, R. Mout and V. M. Rotello, *Adv. Drug Deliv. Rev.,* 2012, **64**, 200-216.

106. S. Santra, D. Dutta, G. A. Walter and B. M. Moudgil, *Technology in Cancer Research & Treatment,* 2005, **4**, 593-602.

107. N. G. Portney and M. Ozkan, *Analytical and Bioanalytical Chemistry,* 2006, **384**, 620-630.

108. A. G. Cuenca, H. B. Jiang, S. N. Hochwald, M. Delano, W. G. Cance and S. R. Grobmyer, *Cancer,* 2006, **107**, 459-466.

109. X. M. Qian and S. M. Nie, *Chem. Soc. Rev.,* 2008, **37**, 912-920.

110. L. R. Hirsch, R. J. Stafford, J. A. Bankson, S. R. Sershen, B. Rivera, R. E. Price, J. D. Hazle, N. J. Halas and J. L. West, *Proc. Natl. Acad. Sci. U. S. A.,* 2003, **100**, 13549-13554.

111. R. Sharma and C. J. Chen, *Journal of Nanoparticle Research,* 2009, **11**, 671-689.

112. S. Link and M. A. El-Sayed, *International Reviews in Physical Chemistry,* 2000, **19**, 409-453.

113. D. F. Emerich and C. G. Thanos, *Biomol. Eng.,* 2006, **23**, 171-184.

114. Z. P. Xu, Q. H. Zeng, G. Q. Lu and A. B. Yu, *Chemical Engineering Science,* 2006, **61**, 1027-1040.

115. C. Burda, X. B. Chen, R. Narayanan and M. A. El-Sayed, *Chem. Rev.*, 2005, **105**, 1025-1102.

116. S. K. Ghosh and T. Pal, *Chem. Rev.*, 2007, **107**, 4797-4862.

117. E. Katz and I. Willner, *Angewandte Chemie-International Edition,* 2004, **43**, 6042-6108.

118. P. Mulvaney, *Langmuir,* 1996, **12**, 788-800.

119. S. Underwood and P. Mulvaney, *Langmuir,* 1994, **10**, 3427-3430.

120. A. C. Templeton, J. J. Pietron, R. W. Murray and P. Mulvaney, *J Phys Chem B,* 2000, **104**, 564-570.

121. D. Pissuwan, S. M. Valenzuela and M. B. Cortie, *Trends Biotechnol.*, 2006, **24**, 62-67.

122. E. Katz and I. Willner, *Angewandte Chemie-International Edition,* 2004, **43**, 6042-6108.

123. E. C. Dreaden, A. M. Alkilany, X. Huang, C. J. Murphy and M. A. El-Sayed, *Chem. Soc. Rev.*, 2012, **41**, 2740-2779.

124. B. D. Chithrani and W. C. W. Chan, *Nano Letters,* 2007, **7**, 1542-1550.

125. R. Shukla, V. Bansal, M. Chaudhary, A. Basu, R. R. Bhonde and M. Sastry, *Langmuir,* 2005, **21**, 10644-10654.

126. B. D. Chithrani, A. A. Ghazani and W. C. W. Chan, *Nano Letters,* 2006, **6**, 662-668.

127. A. E. Nel, L. Maedler, D. Velegol, T. Xia, E. M. V. Hoek, P. Somasundaran, F. Klaessig, V. Castranova and M. Thompson, *Nature Materials,* 2009, **8**, 543-557.

128. A. Verma, O. Uzun, Y. H. Hu, Y. Hu, H. S. Han, N. Watson, S. L. Chen, D. J. Irvine and F. Stellacci, *Nature Materials,* 2008, **7**, 588-595.

129. T. B. Huff, M. N. Hansen, Y. Zhao, J. Cheng and A. Wei, *Langmuir,* 2007, **23**, 1596-1599.

130. J. Lovric, H. S. Bazzi, Y. Cuie, G. R. A. Fortin, F. M. Winnik and D. Maysinger, *Journal of Molecular Medicine-Jmm,* 2005, **83**, 377-385.

131. C. M. Goodman, C. D. McCusker, T. Yilmaz and V. M. Rotello, *Bioconjug. Chem.*, 2004, **15**, 897-900.

132. Y. Chen, Y. Hung, I. Liau and G. S. Huang, *Nanoscale Research Letters,* 2009, **4**, 858-864.

133. E. E. Connor, J. Mwamuka, A. Gole, C. J. Murphy and M. D. Wyatt, *Small,* 2005, **1**, 325-327.

134. A. M. Alkilany and C. J. Murphy, *Journal of Nanoparticle Research,* 2010, **12**, 2313-2333.

135. R. K. Gilchrist, R. Medal, W. D. Shorey, R. C. Hanselman, J. C. Parrott and C. B. Taylor, *Ann. Surg.,* 1957, **146**, 596-606.

136. K. Maier-Hauff, F. Ulrich, D. Nestler, H. Niehoff, P. Wust, B. Thiesen, H. Orawa, V. Budach and A. Jordan, *J. Neurooncol.,* 2011, **103**, 317-324.

137. I. L. Medintz, H. T. Uyeda, E. R. Goldman and H. Mattoussi, *Nature Materials,* 2005, **4**, 435-446.

138. X. H. Gao, Y. Y. Cui, R. M. Levenson, L. W. K. Chung and S. M. Nie, *Nat. Biotechnol.,* 2004, **22**, 969-976.

139. Q. A. Pankhurst, J. Connolly, S. K. Jones and J. Dobson, *Journal of Physics D-Applied Physics,* 2003, **36**, R167-R181.

140. A. H. Morrish, Book, *The Physical Principles of Magnetism*, Wiley-IEEE Press, 2001.

141. D. Jiles, Book, *Introduction to Magnetism and Magnetic Materials*, Chapman & Hall, 1991.

142. M. Colombo, S. Carregal-Romero, M. F. Casula, L. Gutierrez, M. P. Morales, I. B. Boehm, J. T. Heverhagen, D. Prosperi and W. J. Parak, *Chem. Soc. Rev.,* 2012, **41**, 4306-4334.

143. S. Laurent, D. Forge, M. Port, A. Roch, C. Robic, L. V. Elst and R. N. Muller, *Chem. Rev.,* 2008, **108**, 2064-2110.

144. L. Yan, C. ZhongWen and G. Ning, *Chinese Science Bulletin,* 2012, **57**, 3972-3978.

145. A. G. Roca, R. Costo, A. F. Rebolledo, S. Veintemillas-Verdaguer, P. Tartaj, T. Gonzalez-Carreno, M. P. Morales and C. J. Serna, *Journal of Physics D-Applied Physics,* 2009, **42**, 224002-224002.

146. A. Sandhu, H. Handa and M. Abe, *Nanotechnology,* 2010, **21**, 442001-442001.

147. J. E. Rosen, L. Chan, D. Shieh and F. X. Gu, *Nanomedicine-Nanotechnology Biology and Medicine,* 2012, **8**, 275-290.

148. E. Pollert, P. Veverka, M. Veverka, O. Kaman, K. Zaveta, S. Vasseur, R. Epherre, G. Goglio and E. Duguet, *Progress in Solid State Chemistry,* 2009, **37**, 1-14.

149. A. S. Teja and P. Y. Koh, *Progress in Crystal Growth and Characterization of Materials,* 2009, **55**, 22-45.

150. R. Massart, *IEEE Trans. Magn.,* 1981, **17**, 1247-1248.

151. D. Portet, B. Denizot, E. Rump, J. Lejeune and P. Jallet, *J. Colloid Interface Sci.*, 2001, **238**, 37-42.

152. A. K. Gupta and M. Gupta, *Biomaterials*, 2005, **26**, 1565-1573.

153. C. Tassa, S. Y. Shaw and R. Weissleder, *Acc. Chem. Res.*, 2011, **44**, 842-852.

154. S. L. Easo and P. V. Mohanan, *Carbohydr. Polym.*, 2013, **92**, 726-732.

155. E. Okon, D. Pouliquen, P. Okon, Z. V. Kovaleva, T. P. Stepanova, S. G. Lavit, B. N. Kudryavtsev and P. Jallet, *Laboratory Investigation*, 1994, **71**, 895-903.

156. A. S. Karakoti, S. Das, S. Thevuthasan and S. Seal, *Angewandte Chemie-International Edition*, 2011, **50**, 1980-1994.

157. J. S. Tsuji, A. D. Maynard, P. C. Howard, J. T. James, C. W. Lam, D. B. Warheit and A. B. Santamaria, *Toxicological Sciences*, 2006, **89**, 42-50.

158. G. Bayramoglu and M. Y. Arica, *J. Hazard. Mater.*, 2008, **156**, 148-155.

159. T. Kuroiwa, Y. Noguchi, M. Nakajima, S. Sato, S. Mukataka and S. Ichikawa, *Process Biochemistry*, 2008, **43**, 62-69.

160. A. K. Johnson, A. M. Zawadzka, L. A. Deobald, R. L. Crawford and A. J. Paszczynski, *Journal of Nanoparticle Research*, 2008, **10**, 1009-1025.

161. N. A. Kalkan, S. Aksoy, E. A. Aksoy and N. Hasirci, *J Appl Polym Sci*, 2012, **123**, 707-716.

162. R. Konwarh, N. Karak, S. K. Rai and A. K. Mukherjee, *Nanotechnology*, 2009, **20**, 225107.

163. M. Namdeo and S. K. Bajpai, *Journal of Molecular Catalysis B-Enzymatic*, 2009, **59**, 134-139.

164. S. A. Ansari, Q. Husain, S. Qayyum and A. Azam, *Food and Chemical Toxicology*, 2011, **49**, 2107-2115.

165. R. K. Dutta, P. K. Sharma and A. C. Pandey, *Journal of Nanoparticle Research*, 2010, **12**, 1211-1219.

166. J. Huang, C. Liu, H. Xiao, J. Wang, D. Jiang and E. Gu, *International Journal of Nanomedicine*, 2007, **2**, 775-784.

167. N. Miletic, V. Abetz, K. Ebert and K. Loos, *Macromolecular Rapid Communications*, 2010, **31**, 71-74.

168. H. F. Jia, G. Y. Zhu and P. Wang, *Biotechnol. Bioeng.*, 2003, **84**, 406-414.

169. D. F. M. Neri, V. M. Balcao, M. G. Carneiro-da-Cunha, L. B. Carvalho Jr. and J. A. Teixeira, *Catalysis Communications*, 2008, **9**, 2334-2339.

170. K. A. Mahmoud, K. B. Male, S. Hrapovic and J. H. T. Luong, *Acs Applied Materials & Interfaces,* 2009, **1**, 1383-1386.

171. R. S. Prakasham, G. S. Devi, K. R. Laxmi and C. S. Rao, *Journal of Physical Chemistry C,* 2007, **111**, 3842-3847.

172. K. E. Sapsford, W. R. Algar, L. Berti, K. B. Gemmill, B. J. Casey, E. Oh, M. H. Stewart and I. L. Medintz, *Chem. Rev.,* 2013, **113**, 1904-2074.

173. A. Xu, Y. Ma and H. Coelfen, *Journal of Materials Chemistry,* 2007, **17**, 415-449.

174. C. K. Thai, H. X. Dai, M. S. R. Sastry, M. Sarikaya, D. T. Schwartz and F. Baneyx, *Biotechnol. Bioeng.,* 2004, **87**, 129-137.

175. B. D. Reiss, C. B. Mao, D. J. Solis, K. S. Ryan, T. Thomson and A. M. Belcher, *Nano Letters,* 2004, **4**, 1127-1132.

176. S. R. Whaley, D. S. English, E. L. Hu, P. F. Barbara and A. M. Belcher, *Nature,* 2000, **405**, 665-668.

177. M. T. Zin, H. Ma, M. Sarikaya and A. K. Y. Jen, *Small,* 2005, **1**, 698-702.

178. P. Pandey, S. P. Singh, S. K. Arya, V. Gupta, M. Datta, S. Singh and B. D. Malhotra, *Langmuir,* 2007, **23**, 3333-3337.

179. E. Hochuli, W. Bannwarth, H. Dobeli, R. Gentz and D. Stuber, *Bio-Technology,* 1988, **6**, 1321-1325.

180. J. Porath, *Protein Expr. Purif.,* 1992, **3**, 263-281.

181. K. B. Lee, S. Park and C. A. Mirkin, *Angewandte Chemie-International Edition,* 2004, **43**, 3048-3050.

182. I. S. Lee, N. Lee, J. Park, B. H. Kim, Y. Yi, T. Kim, T. K. Kim, I. H. Lee, S. R. Paik and T. Hyeon, *J. Am. Chem. Soc.,* 2006, **128**, 10658-10659.

183. A. Munoz and M. Costa, *Toxicol. Appl. Pharmacol.,* 2012, **260**, 1-16.

184. O. Cohavi, D. Reichmann, R. Abramovich, A. B. Tesler, G. Bellapadrona, D. B. Kokh, R. C. Wade, A. Vaskevich, I. Rubinstein and G. Schreiber, *Chemistry-a European Journal,* 2011, **17**, 1327-1336.

185. J. M. Kogot, H. J. England, G. F. Strouse and T. M. Logan, *J. Am. Chem. Soc.,* 2008, **130**, 16156-16162.

186. E. Boisselier and D. Astruc, *Chem. Soc. Rev.,* 2009, **38**, 1759-1782.

187. A. Ulman, *Chem. Rev.,* 1996, **96**, 1533-1554.

188. J. C. Love, L. A. Estroff, J. K. Kriebel, R. G. Nuzzo and G. M. Whitesides, *Chem. Rev.,* 2005, **105**, 1103-1169.

189. Z. Y. Zhong, S. Patskovskyy, P. Bouvrette, J. H. T. Luong and A. Gedanken, *J Phys Chem B,* 2004, **108**, 4046-4052.

190. K. Arihara, T. Ariga, N. Takashima, K. Arihara, T. Okajima, F. Kitamura, K. Tokuda and T. Ohsaka, *Physical Chemistry Chemical Physics,* 2003, **5**, 3758-3761.

191. G. Hager and A. G. Brolo, *J Electroanal Chem,* 2003, **550**, 291-301.

192. Y. Zhao, F. Zhou, H. Zhou and H. Su, *Physical Chemistry Chemical Physics,* 2013, **15**, 1690-1698.

193. P. Tengvall, I. Lundstrom and B. Liedberg, *Biomaterials,* 1998, **19**, 407-422.

194. F. X. Zhang, L. Han, L. B. Israel, J. G. Daras, M. M. Maye, N. K. Ly and C. J. Zhong, *Analyst,* 2002, **127**, 462-465.

195. Z. Shen, G. A. Stryker, R. L. Mernaugh, L. Yu, H. P. Yan and X. Q. Zeng, *Anal. Chem.,* 2005, **77**, 797-805.

196. K. S. Carmon, R. E. Baltus and L. A. Luck, *Biochemistry (N. Y.),* 2004, **43**, 14249-14256.

197. W. Huang, J. Q. Wang, D. Bhattacharyya and L. G. Bachas, *Anal. Chem.,* 1997, **69**, 4601-4607.

198. J. M. Lee, H. K. Park, Y. Jung, J. K. Kim, S. O. Jung and B. H. Chung, *Anal. Chem.,* 2007, **79**, 2680-2687.

199. C. D. Gwenin, M. Kalaji, P. A. Williams and R. M. Jones, *Biosens. Bioelectron.,* 2007, **22**, 2869-2875.

200. M. Dolores Roldan, E. Perez-Reinado, F. Castillo and C. Moreno-Vivian, *FEMS Microbiol. Rev.,* 2008, **32**, 474-500.

201. C. D. Gwenin, M. Kalaji, P. A. Williams and C. M. Kay, *Biodegradation,* 2011, **22**, 463-474.

202. J. Choi, J. Lee, K. Nishi, Y. Kim, C. Jung and J. Kim, *J. Mol. Biol.,* 2008, **377**, 258-267.

203. A. K. Gupta and M. Gupta, *Biomaterials,* 2005, **26**, 3995-4021.

204. Phuong Ha-Lien Tran, Thao Truong-Dinh Tran, Toi Van Vo and B. Lee, *Arch. Pharm. Res.,* 2012, **35**, 2045-2061.

205. L. H. Reddy, J. L. Arias, J. Nicolas and P. Couvreur, *Chem. Rev.,* 2012, **112**, 5818-5878.

206. A. H. Lu, E. L. Salabas and F. Schuth, *Angewandte Chemie-International Edition,* 2007, **46**, 1222-1244.

207. C. Corot, P. Robert, J. M. Idee and M. Port, *Adv. Drug Deliv. Rev.*, 2006, **58**, 1471-1504.

208. Z. C. Xu, Y. L. Hou and S. H. Sun, *J. Am. Chem. Soc.*, 2007, **129**, 8698-8708.

209. J. Lin, W. L. Zhou, A. Kumbhar, J. Wiemann, J. Y. Fang, E. E. Carpenter and C. J. O'Connor, *Journal of Solid State Chemistry,* 2001, **159**, 26-31.

210. T. Kinoshita, S. Seino, K. Okitsu, T. Nakayama, T. Nakagawa and T. A. Yamamoto, *J. Alloys Compounds,* 2003, **359**, 46-50.

211. F. X. Chen, G. Q. Xu and T. S. A. Hor, *Mater Lett,* 2003, **57**, 3282-3286.

212. A. R. Tao, S. Habas and P. Yang, *Small,* 2008, **4**, 310-325.

213. L. Wang, H. Park, S. I. Lim, M. J. Schadt, D. Mott, J. Luo, X. Wang and C. Zhong, *Journal of Materials Chemistry,* 2008, **18**, 2629-2635.

214. L. Y. Wang, J. Luo, Q. Fan, M. Suzuki, I. S. Suzuki, M. H. Engelhard, Y. H. Lin, N. Kim, J. Q. Wang and C. J. Zhong, *J Phys Chem B,* 2005, **109**, 21593-21601.

215. C. K. Lo, D. Xiao and M. M. F. Choi, *Journal of Materials Chemistry,* 2007, **17**, 2418-2427.

216. M. Gonzales and K. M. Krishnan, *J Magn Magn Mater,* 2007, **311**, 59-62.

217. M. Casavola, R. Buonsanti, G. Caputo and P. D. Cozzoli, *European Journal of Inorganic Chemistry,* 2008, **6**, 837-854.

218. T. T. H. Pham, C. Cao and J. Sim, *J Magn Magn Mater,* 2008, **320**, 2049-2055.

219. J. L. Lyon, D. A. Fleming, M. B. Stone, P. Schiffer and M. E. Williams, *Nano Letters,* 2004, **4**, 719-723.

220. J. Watson and F. Crick, *Nature,* 1953, **171**, 737-738.

221. K. Mullis, F. Ferre and R. Gibb, Book, *The Polymerase Chain Reaction*, 1994.

222. H. P. Sorensen and K. K. Mortensen, *J. Biotechnol.*, 2005, **115**, 113-128.

223. Novagen, pET Systems Manual, 11th Edition, 2006.

224. Promega, Wizard® Genomic DNA Purification Kit, 2010.

225. QIAquick, QIAquick PCR Purification Kit Protocol, 2001.

226. Promega, Wizard® Plus SV Minipreps DNA Purification System, 2010.

227. Promega, Applications and Reaction Conditions for Restriction Enzymes, 2011.

228. Promega, Restriction Enzyme Reference Information, 2011.

229. R. W. Ricci, M. A. Ditzler and L. P. Nestor, *J. Chem. Educ.,* 1994, **71**, 983-985.

230. Q. H. Lu, K. L. Yao, D. Xi, Z. L. Liu, X. P. Luo and Q. Ning, *J Magn Magn Mater,* 2006, **301**, 44-49.

231. I. Y. Goon, L. M. H. Lai, M. Lim, P. Munroe, J. J. Gooding and R. Amal, *Chemistry of Materials,* 2009, **21**, 673-681.

232. K. R. Brown, D. G. Walter and M. J. Natan, *Chemistry of Materials,* 2000, **12**, 306-313.

233. F. Baneyx and M. Mujacic, *Nat. Biotechnol.,* 2004, **22**, 1399-1408.

234. C. D. Emptage, R. J. Knox, M. J. Danson and D. W. Hough, *Biochem. Pharmacol.,* 2009, **77**, 21-29.

235. Q. A. Pankhurst, N. K. T. Thanh, S. K. Jones and J. Dobson, *Journal of Physics D-Applied Physics,* 2009, **42**, 224001-224001.

236. J. P. Jolivet and E. Tronc, *J. Colloid Interface Sci.,* 1988, **125**, 688-701.

237. R. L. Rebodos and P. J. Vikesland, *Langmuir,* 2010, **26**, 16745-16753.

238. B. Gilbert, J. E. Katz, J. D. Denlinger, Y. Yin, R. Falcone and G. A. Waychunas, *Journal of Physical Chemistry C,* 2010, **114**, 21994-22001.

239. A. Corrias, G. Mountjoy, D. Loche, V. Puntes, A. Falqui, M. Zanella, W. J. Parak and M. F. Casula, *Journal of Physical Chemistry C,* 2009, **113**, 18667-18675.

240. J. I. Langford and A. J. C. Wilson, *Journal of Applied Crystallography,* 1978, **11**, 102-113.

241. P. J. Vikesland, A. M. Heathcock, R. L. Rebodos and K. E. Makus, *Environ. Sci. Technol.,* 2007, **41**, 5277-5283.

242. H. Borchert, E. Shevehenko, A. Robert, I. Mekis, A. Kornowski, G. Grubel and H. Weller, *Langmuir,* 2005, **21**, 1931-1936.

243. J. Turkevich, P. C. Stevenson and J. Hillier, 1951, **11**, 55-75.

244. G. Frens, *Nature-Physical Science,* 1973, **241**, 20-22.

245. T. Sugimoto and E. Matijevic, *J. Colloid Interface Sci.,* 1980, **74**, 227-243.

246. X. Liu, M. Atwater, J. Wang and Q. Huo, *Colloids and Surfaces B-Biointerfaces,* 2007, **58**, 3-7.

247. P. Jain, K. Lee, I. El-Sayed and M. El-Sayed, *J Phys Chem B,* 2006, **110**, 7238-7248.

248. G. A. Rance, D. H. Marsh and A. N. Khlobystov, *Chemical Physics Letters,* 2008, **460**, 230-236.

249. S. L. Tie, Y. Q. Lin, H. C. Lee, Y. S. Bae and C. H. Lee, *Colloids and Surfaces A-Physicochemical and Engineering Aspects,* 2006, **273**, 75-83.

250. Z. Durmus, H. Kavas, M. S. Toprak, A. Baykal, T. G. Altincekic, A. Aslan, A. Bozkurt and S. Cosgun, *J. Alloys Compounds,* 2009, **484**, 371-376.

251. Y. S. Kang, S. Risbud, J. F. Rabolt and P. Stroeve, *Chemistry of Materials,* 1996, **8**, 2209-2218.

252. L. Wang, J. Luo, M. Maye, Q. Fan, R. Qiang, M. Engelhard, C. Wang, Y. Lin and C. Zhong, *Journal of Materials Chemistry,* 2005, **15**, 1821-1832.

253. J. Jeong, T. H. Ha and B. H. Chung, *Anal. Chim. Acta,* 2006, **569**, 203-209.

254. M. Iosin, F. Toderas, P. L. Baldeck and S. Astilean, *J. Mol. Struct.,* 2009, **924-26**, 196-200.

255. E. Pensa, C. Vericat, D. Grumelli, R. C. Salvarezza, S. H. Park, G. S. Longo, I. Szleifer and M. D. Leo, *Physical Chemistry Chemical Physics,* 2012, **14**, 12355-12367.

256. S. Imabayashi, D. Hobara, T. Kakiuchi and W. Knoll, *Langmuir,* 1997, **13**, 4502-4504.

257. A. Gole, C. Dash, V. Ramakrishnan, S. Sainkar, A. Mandale, M. Rao and M. Sastry, *Langmuir,* 2001, **17**, 1674-1679.

258. A. Gole, C. Dash, C. Soman, S. Sainkar, M. Rao and M. Sastry, *Bioconjug. Chem.,* 2001, **12**, 684-690.

259. M. Lv, E. Zhu, Y. Su, Q. Li, W. Li, Y. Zhao and Q. Huang, *Prep. Biochem. Biotechnol.,* 2009, **39**, 429-438.

260. H. Hinterwirth, W. Lindner and M. Laemmerhofer, *Anal. Chim. Acta,* 2012, **733**, 90-97.

APPENDIX

pET-28a-c(+) vector

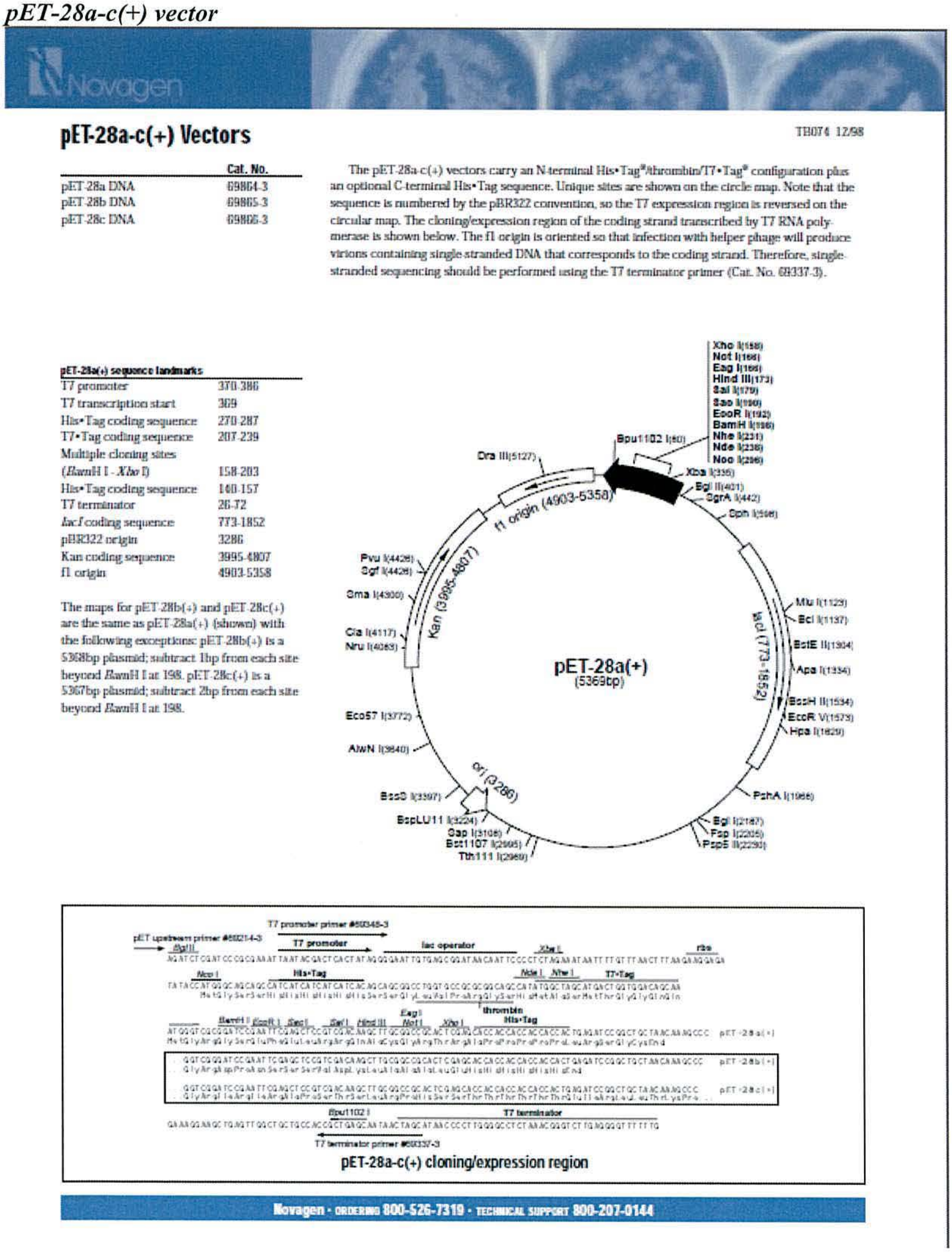

Novagen

pET-28a-c(+) Vectors

TB074 12/98

	Cat. No.
pET-28a DNA	69864-3
pET-28b DNA	69865-3
pET-28c DNA	69866-3

The pET-28a-c(+) vectors carry an N-terminal His•Tag®/thrombin/T7•Tag® configuration plus an optional C-terminal His•Tag sequence. Unique sites are shown on the circle map. Note that the sequence is numbered by the pBR322 convention, so the T7 expression region is reversed on the circular map. The cloning/expression region of the coding strand transcribed by T7 RNA polymerase is shown below. The f1 origin is oriented so that infection with helper phage will produce virions containing single-stranded DNA that corresponds to the coding strand. Therefore, single-stranded sequencing should be performed using the T7 terminator primer (Cat. No. 69337-3).

pET-28a(+) sequence landmarks	
T7 promoter	370-386
T7 transcription start	369
His•Tag coding sequence	270-287
T7•Tag coding sequence	207-239
Multiple cloning sites	
(*Bam*H I - *Xho* I)	158-203
His•Tag coding sequence	140-157
T7 terminator	26-72
lacI coding sequence	773-1852
pBR322 origin	3286
Kan coding sequence	3995-4807
f1 origin	4903-5358

The maps for pET-28b(+) and pET-28c(+) are the same as pET-28a(+) (shown) with the following exceptions: pET-28b(+) is a 5368bp plasmid; subtract 1bp from each site beyond *Bam*H I at 198. pET-28c(+) is a 5367bp plasmid; subtract 2bp from each site beyond *Bam*H I at 198.

pET-28a-c(+) cloning/expression region

Novagen · ORDERING **800-526-7319** · TECHNICAL SUPPORT **800-207-0144**

Nitroreductase Evaluation

The yfkO gene along with sequencing results of yfkO and yfkO-cys

pEt-28a(+) sequencing in black Start codon His-tag

```
TAATTTTGTTTAACTTTAAGAAGGAGATATACCATGGGCAGCAGCCATCATCATCATCATCACA
TAATTTTGTTTAACTTTAAGAAGGAGATATACCATGGGCAGCAGCCATCATCATCATCATCACA
TAATTTTGTTTAACTTTAAGAAGGAGATATACCATGGGCAGCAGCCATCATCATCATCATCACA
```

yfkO **is in orange and** ***yfkO-cys*** **is in purple**

```
GCAGCGGCCTGGTGCCGCGCGGCAGCCATATGGCTAGCATGACTGGTGGACAGCAAATGGGTCG
GCAGCGGCCTGGTGCCGCGCGGCAGCCATATGGCTAGCATGACTGGTGGACAGCAAATGGGTCG
GCAGCGGCCTGGTGCCGCGCGGCAGCCATATGGCTAGCATGACTGGTGGACAGCAAATGGGTCG
```

BamHI **site Cys-tag** ***yfkO*** **gene is underlined**

```
CGGATCCTGTTGCTGTTGCTGTTGCAATATGACAGAGCAATCCAAGAAGCAAGAGATTCTTGAC
CGGATCC                  AATATGACAGAGCAATCCAAGAAGCAAGAGATTCTTGAC
CGGATCCTGTTGCTGTTGCTGTTGCAATATGACAGAGCAATCCAAGAAGCAAGAGATTCTTGAC
```

```
GCATTCCAATTTAGACATGCGACAAAAGAATTTGATCCGGACAGAAAGATATCAGATGAGGATT
GCATTCCAATTTAGACATGCGACAAAAGAATTTGATCCGGACAGAAAGATATCAGATGAGGATT
GCATTCCAATTTAGACATGCGACAAAAGAATTTGATCCGGACAGAAAGATATCAGATGAGGATT
```

```
TTCAGTTCATTTTAGAAGCGGGCAGACTGTCGCCAAGCTCGGTCGGCCTCGAACCGTGGCAATT
TTCAGTTCATTTTAGAAGCGGGCAGACTGTCGCCAAGCTCGGTCGGCCTCGAACCGTGGCAATT
TTCAGTTCATTTTAGAAGCGGGCAGACTGTCGCCAAGCTCGGTCGGCCTCGAACCGTGGCAATT
```

```
TGTCGTCGTCCAAAATAAAGAGCTGCGTGAAAAACTGCGTCAAGTCTCATGGGGTGCACAGGGG
TGTCGTCGTCCAAAATAAAGAGCTGCGTGAAAAACTGCGTCAAGTCTCATGGGGTGCACAGGGG
TGTCGTCGTCCAAAATAAAGAGCTGCGTGAAAAACTGCGTCAAGTCTCATGGGGTGCACAGGGG
```

```
CAGCTTCCGACAGCCAGCCATTTCGTTTTGCTGCTCGGACGCACGGCTAAGGAAATGCGACGTG
CAGCTTCCGACAGCCAGCCATTTCGTTTTGCTGCTCGGACGCACGGCTAAGGAAATGCGACGTG
CAGCTTCCGACAGCCAGCCATTTCGTTTTGCTGCTCGGACGCACGGCTAAGGAAATGCGACGTG
```

```
ATTCCGGCTATGTTGCAGATCAATTAAAGCATGTGAAAAAAATGCCGGAGGACATCATTGAAAA
ATTCCGGCTATGTTGCAGATCAATTAAAGCATGTGAAAAAAATGCCGGAGGACATCATTGAAAA
ATTCCGGCTATGTTGCAGATCAATTAAAGCATGTGAAAAAAATGCCGGAGGACATCATTGAAAA
```

TATGCTGAAAGAAGACGGCGTTCTGGAAAGTTTCCAAGACGGCGATTTTCATTTGTACGAAAGC

TATGCTGAAAGAAGACGGCGTTCTGGAAAGTTTCCAAGACGGCGATTTTCATTTGTACGAAAGC

TATGCTGAAAGAAGACGGCGTTCTGGAAAGTTTCCAAGACGGCGATTTTCATTTGTACGAAAGC

GACAGGGCGATGTTTGACTGGGTATCAAAGCAAACGTACATCGCGCTCGCCAACATGATGACGG

GACAGGGCGATGTTTGACTGGGTATCAAAGCAAACGTACATCGCGCTCGCCAACATGATGACGG

GACAGGGCGATGTTTGACTGGGTATCAAAGCAAACGTACATCGCGCTCGCCAACATGATGACGG

CTGCCGCTTTGATCGGCATTGACTCCTGCCCGATTGAAGGCTTTAACTACGACAAAGTCCACGA

CTGCCGCTTTGATCGGCATTGACTCCTGCCCGATTGAAGGCTTTAACTACGACAAAGTCCACGA

CTGCCGCTTTGATCGGCATTGACTCCTGCCCGATTGAAGGCTTTAACTACGACAAAGTCCACGA

CATCCTTGAAAAAGAAGGGGTGTTGGAGGATGGCCGCTTTGACATCTCGGTCATGGCCGCTTTC

CATCCTTGAAAAAGAAGGGGTGTTGGAGGATGGCCGCTTTGACATCTCGGTCATGGCCGCTTTC

CATCCTTGAAAAAGAAGGGGTGTTGGAGGATGGCCGCTTTGACATCTCGGTCATGGCCGCTTTC

GGATACCGTGTGAAAGAGCCGCGTCCGAAGACGAGACGGGCGCTTGATCAAATCGTGAAATGGG

GGATACCGTGTGAAAGAGCCGCGTCCGAAGACGAGACGGGCGCTTGATCAAATCGTGAAATGGG

GGATACCGTGTGAAAGAGCCGCGTCCGAAGACGAGACGGGCGCTTGATCAAATCGTGAAATGGG

Stop codon and *HindIII* site and back to pET-28a(+) sequence

TCGAATAAAAGCTTGCGGCCGCACTCGAGCACCACCACCACCACCACTGAGATCCGGCTGCTAA

TCGAATAAAAGCTTGCGGCCGCACTCGAGCACCACCACCACCACCACTGAGATCCGGCTGCTAA

TCGAATAAAAGCTTGCGGCCGCACTCGAGCACCACCACCACCACCACTGAGATCCGGCTGCTAA

The nfrA1 gene along with the sequencing results of nfrA1

Start codon His-tag pET-28a(+) sequencing in black

ACCATGGGCAGCAGCCATCATCATCATCATCACAGCAGCGGCCTGGTGCCGCGCGGCAGCCATA
ACCATGGGCAGCAGCCATCATCATCATCATCACAGCAGCGGCCTGGTGCCGCGCGGCAGCCATA

***nfrA1* is in blue *BamHI* site *nfrA1* gene is underlined**

TGGCTAGCATGACTGGTGGACAGCAAATGGGTCGCGGATCCAGGATGAATAAAACGATTGAAAC
TGGCTAGCATGACTGGTGGACAGCAAATGGGTCGCGGATCCAGGATGAATAAAACGATTGAAAC

TATTTTAAATCACCGTTCGATCAGGTCTTTTACAGATCGGCTCCTGACCGAAGAAGAGGTTCGC
TATTTTAAATCACCGTTCGATCAGGTCTTTTACAGATCGGCTCCTGACCGAAGAAGAGGTTCGC

CTGCTTGTGGAGAGCGCTCAAAGCGCATCGACGTCAAGCTATATTCAAGCATATTCAATCATCG
CTGCTTGTGGAGAGCGCTCAAAGCGCATCGACGTCAAGCTATATTCAAGCATATTCAATCATCG

GTGTCACCGATCCGGACAAGAAGCGCAAGCTTGCGGAATTGGCCGGGAACCAGCCATATGTTGA
GTGTCACCGATCCGGACAAGAAGCGCAAGCTTGCGGAATTGGCCGGGAACCAGCCATATGTTGA

AAAAAACGGCCATCTGTTTGTATTTTGCGCAGATCTTTACAGGCATGACAAAATCGCTCGGAAA
AAAAAACGGCCATCTGTTTGTATTTTGCGCAGATCTTTACAGGCATGACAAAATCGCTCGGAAA

AAGGGTGTAGATATTACAGCTTCTCTTGAAGGGACGGAAACCTTTATGGTCAGCGTCATCGATG
AAGGGTGTAGATATTACAGCTTCTCTTGAAGGGACGGAAACCTTTATGGTCAGCGTCATCGATG

CAGCGCTTGCCGCTCAAAATATGTCAATAGCGGCCGAATCAATGGGCCTCGGCATCTGCTATAT
CAGCGCTTGCCGCTCAAAATATGTCAATAGCGGCCGAATCAATGGGCCTCGGCATCTGCTATAT

CGGTGGGATTCGCAACAATTTGAACGAAGTCTCCGAGCTTCTTGAAACACCTGAATACGTTCTT
CGGTGGGATTCGCAACAATTTGAACGAAGTCTCCGAGCTTCTTGAAACACCTGAATACGTTCTT

CCGCTGTTCGGGCTTGTCGTCGGCCAGCCGGCCAACCCTTCGGCCAAAAAACCGCGTCTGCCGC
CCGCTGTTCGGGCTTGTCGTCGGCCAGCCGGCCAACCCTTCGGCCAAAAAACCGCGTCTGCCGC

TTGATCACATTTATCATGAAAATGTCTATCAAGCGGATGATGCCGAGTTTGAAAAGCATTTGTC
TTGATCACATTTATCATGAAAATGTCTATCAAGCGGATGATGCCGAGTTTGAAAAGCATTTGTC

CGCATATGACGAAACGATTTCAAACTATTATCAAAAGCGGACGGACGGCAAACGGTCTGACAAA

CGCATATGACGAAACGATTTCAAACTATTATCAAAAGCGGACGGACGGCAAACGGTCTGACAAA

TGGACAGACCAGATCACCGGCAGCCTCAAAAAGCCGCCGCGTGCGTATATGAATGAATTCGTTA

TGGACAGACCAGATCACCGGCAGCCTCAAAAAGCCGCCGCGTGCGTATATGAATGAATTCGTTA

Stop codon and *SalI* site and back to pET-28a(+) sequence

AAGGAAAAGGTTTGAACAAAAGGTAAGTCGACAAGCTTGCGGCCGCACTCGAGCACCACCACCA

AAGGAAAAGGTTTGAACAAAAGGTAAGTCGACAAGCTTGCGGCCGCACTCGAGCACCACCACCA

CCACCACTGAGATCCGGCTGCTAACAAAGCCCGGTCGGGATC

CCACCACTGAGATCCGGCTGCTAACAAAGCCCGAAAGGAGC

The nfrA2 gene along with sequencing results of nfrA2 and nfrA2-cys

pET-28a(+) sequencing in black **Start codon** **His-tag**

```
AATTTTGTTTAACTTTAAGAAGGAGATATACCATGGGCAGCAGCCATCATCATCATCATCACAG
AATTTTGTTTAACTTTAAGAAGGAGATATACCATGGGCAGCAGCCATCATCATCATCATCACAG
AATTTTGTTTAACTTTAAGAAGGAGATATACCATGGGCAGCAGCCATCATCATCATCATCACAG
```

nfrA2 **is in green and** ***nfrA2-cys*** **is in red**

```
CAGCGGCCTGGTGCCGCGCGGCAGCCATATGGCTAGCATGACTGGTGGACAGCAAATGGGTCGC
CAGCGGCCTGGTGCCGCGCGGCAGCCATATGGCTAGCATGACTGGTGGACAGCAAATGGGTCGC
CAGCGGCCTGGTGCCGCGCGGCAGCCATATGGCTAGCATGACTGGTGGACAGCAAATGGGTCGC
```

BamHI **site** **Cys-tag** ***nfrA2*** **gene is underlined**

```
GGATCCTGTTGTTGTTGCTGTTGCCTAATGAATGAAGTATTGAAAACATTGAAAGACCATAGAT
GGATCC                  CTAATGAATGAAGTATTGAAAACATTGAAAGACCATAGAT
GGATCCTGTTGTTGTTGCTGTTGCCTAATGAATGAAGTATTGAAAACATTGAAAGACCATAGAT
```

```
CAATCCGCAGCTATACAGATGAGCCCGTGAGCCCTGAACAGCTGGACGACATTATTCAAGCCGT
CAATCCGCAGCTATACAGATGAGCCCGTGAGCCCTGAACAGCTGGACGACATTATTCAAGCCGT
CAATCCGCAGCTATACAGATGAGCCCGTGAGCCCTGAACAGCTGGACGACATTATTCAAGCCGT
```

```
TCAAGCCGCGCCGAATTCCATTAACGGCCAGCAGGTCACCGTGATTACGGTTCAGGATGAGGAA
TCAAGCCGCGCCGAATTCCATTAACGGCCAGCAGGTCACCGTGATTACGGTTCAGGATGAGGAA
TCAAGCCGCGCCGAATTCCATTAACGGCCAGCAGGTCACCGTGATTACGGTTCAGGATGAGGAA
```

```
CGGAAAAAGAAAATTGCCGAACTGGCCGGCGGACAGGTCTGGATCGAGCAGGCCCCTGTTTTCC
CGGAAAAAGAAAATTGCCGAACTGGCCGGCGGACAGGTCTGGATCGAGCAGGCCCCTGTTTTCC
CGGAAAAAGAAAATTGCCGAACTGGCCGGCGGACAGGTCTGGATCGAGCAGGCCCCTGTTTTCC
```

```
TTTTGTTCTGCGCGGACTTCAACCGTGCGAAAATCGCCCTTGAGAAAAACGGCGAAACGCTTGC
TTTTGTTCTGCGCGGACTTCAACCGTGCGAAAATCGCCCTTGAGAAAAACGGCGAAACGCTTGC
TTTTGTTCTGCGCGGACTTCAACCGTGCGAAAATCGCCCTTGAGAAAAACGGCGAAACGCTTGC
```

```
GATCACAGACGGAATGGAATCCGTGCTTGTCGGAGCTGTCGACGCAGGCATCGCCCTCGGGACG
GATCACAGACGGAATGGAATCCGTGCTTGTCGGAGCTGTCGACGCAGGCATCGCCCTCGGGACG
GATCACAGACGGAATGGAATCCGTGCTTGTCGGAGCTGTCGACGCAGGCATCGCCCTCGGGACG
```

GCCACAGCAGCCGCTGAATCGATGGGACTTGGCACTGTGCCGATCGGCGCGGTCCGCGGCCGTG
GCCACAGCAGCCGCTGAATCGATGGGACTTGGCACTGTGCCGATCGGCGCGGTCCGCGGCCGTG
GCCACAGCAGCCGCTGAATCGATGGGACTTGGCACTGTGCCGATCGGCGCGGTCCGCGGCCGTG

CAGAAGAGTTGATCAAACTGCTCAATATTCCTGAATACGTCTTCCCTGTCGCAGGACTTGTCGT
CAGAAGAGTTGATCAAACTGCTCAATATTCCTGAATACGTCTTCCCTGTCGCAGGACTTGTCGT
CAGAAGAGTTGATCAAACTGCTCAATATTCCTGAATACGTCTTCCCTGTCGCAGGACTTGTCGT

CGGCCATCCGGCGGACCGCTCCGCCAAAAAGCCGCGCCTCCCGGAACAAGCGGTAAGGCACAGC
CGGCCATCCGGCGGACCGCTCCGCCAAAAAGCCGCGCCTCCCGGAACAAGCGGTAAGGCACAGC
CGGCCATCCGGCGGACCGCTCCGCCAAAAAGCCGCGCCTCCCGGAACAAGCGGTAAGGCACAGC

GAAACGTATCAACCGGATTTAAAACCGCTGATCGACGCGTACGATGAAGAAATATCCGAATACA
GAAACGTATCAACCGGATTTAAAACCGCTGATCGACGCGTACGATGAAGAAATATCCGAATACA
GAAACGTATCAACCGGATTTAAAACCGCTGATCGACGCGTACGATGAAGAAATATCCGAATACA

TGACAAAACGGACTAACGGACAGGAAACAAGAAACTGGTCTCAGGGCATATCCGCTTATTACAA
TGACAAAACGGACTAACGGACAGGAAACAAGAAACTGGTCTCAGGGCATATCCGCTTATTACAA
TGACAAAACGGACTAACGGACAGGAAACAAGAAACTGGTCTCAGGGCATATCCGCTTATTACAA

Stop codon

TAAAGTGTACTATCCTCACATCCGTGAAATGCTTGAGAAACAAGGATTTAAACTCGAATAGAAG
TAAAGTGTACTATCCTCACATCCGTGAAATGCTTGAGAAACAAGGATTTAAACTCGAATAGAAG
TAAAGTGTACTATCCTCACATCCGTGAAATGCTTGAGAAACAAGGATTTAAACTCGAATAGAAG

***HindIII* site and back to pET-28a(+) sequence**

CTTGCGGCCGCACTCGAGCACCACCACCACCACCACTGAGATCCGGCTGCTAA
CTTGCGGCCGCACTCGAGCACCACCACCACCACCACTGAGATCCGGCTGCTAA
CTTGCGGCCGCACTCGAGCACCACCACCACCACCACTGAGATCCGGCTGCTAA

XRD patterns

JCPDS no. 19-0629, showing the standard 2θ, relative intensities and corresponding diffraction planes for magnetite, which has an inverse spinel structure.

Position [°2θ]	**d-spacing [Å]**	**Rel. Int. [%]**	***hkl***
18.269	4.852	8	1 1 1
30.095	2.967	30	2 2 0
35.422	2.532	100	3 1 1
37.052	2.4243	8	2 2 2
43.052	2.0993	20	4 0 0
53.391	1.7146	10	4 2 2
56.942	1.6158	30	5 1 1
62.515	1.4845	40	4 4 0
65.743	1.4192	2	5 3 1
70.924	1.3277	4	6 2 0
73.948	1.2807	10	5 3 3
74.960	1.2659	4	6 2 2
78.929	1.2119	2	4 4 4
86.617	1.1221	4	6 4 2
89.610	1.0930	12	7 3 1

JCPDS no. 04-0755, showing the standard 2θ, relative intensities and corresponding diffraction planes for maghemite, which has a defect spinel structure.

Position [°2θ]	**Rel. Int. [%]**	***hkl***
18.392	5	1 1 1
21.238	1	2 0 0
23.836	5	2 1 0
26.110	2	2 1 1
30.272	34	2 2 0
32.172	19	3 0 0
33.928	1	3 1 0
35.597	100	3 1 1
37.280	1	2 2 2
38.783	6	3 2 0
43.472	24	4 0 0
53.886	12	4 2 2
57.166	33	5 1 1
59.597	<1	5 2 0
60.457	10	5 2 1
62.726	53	4 4 0
65.185	1	5 3 0
71.401	7	6 2 0
74.677	11	5 3 3
75.372	3	6 2 2

Table 01. XRD pattern of < 5 μm magnetite powder as received from Sigma Aldrich (01)

Position [°2θ]	**Height [cts]**	**FWHM [°2θ]**	**d-spacing [Å]**	**Rel. Int. [%]**	**hkl**
18.5100	902.10	0.2985	4.78956	2.85	1 1 1
30.3099	7397.89	0.2652	2.94648	23.38	2 2 0
35.6615	31643.93	0.2545	2.51562	100.00	3 1 1
37.2930	2122.03	0.2166	2.40923	6.71	2 2 2
43.2942	8529.40	0.2404	2.08816	26.95	4 0 0
53.6531	3494.95	0.3205	1.70688	11.04	4 2 2
57.1764	12123.71	0.2649	1.60978	38.31	5 1 1
62.7591	17886.19	0.2528	1.47934	56.52	4 4 0
71.1501	1376.81	0.2483	1.32406	4.35	6 2 0
74.1874	3080.51	0.3035	1.27719	9.73	5 3 3
75.1902	1237.06	0.2960	1.26262	3.91	6 2 2
79.1475	456.48	1.4731	1.20913	1.44	4 4 4
86.9150	1410.10	0.2965	1.11992	4.46	6 4 2
89.8138	4606.84	0.3101	1.09114	14.56	7 3 1

Table 02. XRD pattern of 20 nm – 40 nm magnetite powder as received from Alfa Aesar (02)

Position [°2θ]	**Height [cts]**	**FWHM [°2θ]**	**d-spacing [Å]**	**Rel. Int. [%]**	**hkl**
23.9572	584.28	0.5465	3.71145	2.77	2 1 0
26.2727	733.08	0.3799	3.38936	3.47	2 1 1
30.4061	6099.67	0.2686	2.93738	28.88	2 2 0
33.2805	765.06	0.1583	2.68996	3.62	3 0 0
35.7870	21120.74	0.2779	2.50709	100.00	3 1 1
43.4662	3458.74	0.3720	2.08030	16.38	4 0 0
53.9114	2236.95	0.4162	1.69931	10.59	4 2 2
57.4454	6351.87	0.3488	1.60288	30.07	5 1 1
63.0773	9970.01	0.3439	1.47264	47.20	4 4 0
71.5959	525.56	0.7492	1.31691	2.49	6 2 0
74.6099	1225.63	0.6450	1.27100	5.80	5 3 3
87.4931	559.40	0.8760	1.11400	2.65	6 4 2
90.3914	2381.15	0.2834	1.08567	11.27	7 3 1

Table 03. XRD pattern of 10 nm magnetite powder as received from Liquids Research Ltd (03)

Position [°2θ]	**Height [cts]**	**FWHM [°2θ]**	**d-spacing [Å]**	**Rel. Int. [%]**	**hkl**
30.3358	1894.38	0.7547	2.94402	26.81	2 2 0
35.7287	7064.80	0.9510	2.51104	100.00	3 1 1
43.3968	1380.54	0.6990	2.08346	19.54	4 0 0
53.6642	917.22	1.1315	1.70655	12.98	4 2 2
57.3851	2414.23	0.7649	1.60442	34.17	5 1 1
63.0091	3118.21	1.3189	1.47407	44.14	4 4 0

Table 04. XRD pattern of as synthesised SPION (04)

Position [°2θ]	**Height [cts]**	**FWHM [°2θ]**	**d-spacing [Å]**	**Rel. Int. [%]**	**hkl**
30.2480	584.08	3.4086	2.95237	10.83	2 2 0
35.6652	5393.89	1.0843	2.51537	100.00	3 1 1
43.3410	1330.23	0.9098	2.08602	24.66	4 0 0
53.7227	422.45	0.6711	1.70483	7.83	4 2 2
57.3197	1862.29	0.8487	1.60610	34.53	5 1 1
62.9279	3240.41	1.0509	1.47578	60.08	4 4 0

Table 05. XRD pattern of Fe_3O_4 *as synthesised using the Goon et al method (05)*

Position [°2θ]	Height [cts]	FWHM [°2θ]	d-spacing [Å]	Rel. Int. [%]	hkl
18.6594	90.33	0.8029	4.75548	5.25	1 1 1
30.4438	517.06	0.1506	2.93626	30.04	2 2 0
35.7896	1721.04	0.1840	2.50899	100.00	3 1 1
37.4211	136.43	0.2007	2.40326	7.93	2 2 2
43.4498	352.93	0.3011	2.08276	20.51	4 0 0
53.8039	193.07	0.2676	1.70386	11.22	4 2 2
57.3233	394.35	0.1673	1.60734	22.91	5 1 1
62.9121	538.93	0.3011	1.47733	31.31	4 4 0
74.3988	94.45	0.4896	1.27408	5.49	5 3 3

Table 06. XRD pattern of Fe_3O_4 *after Au seeding and reduction of* Au^{3+} *onto the particle surface, as synthesised using the Goon et al method (06)*

Position [°2θ]	Height [cts]	FWHM [°2θ]	d-spacing [Å]	Rel. Int. [%]	hkl
30.3880	41.94	1.0103	2.93908	8.62	2 2 0
35.7878	275.80	0.1985	2.50703	56.68	3 1 1
38.5279	486.56	0.8858	2.33480	100.00	1 1 1
44.6121	121.20	1.3028	2.02949	24.91	2 0 0
53.7040	18.91	0.4909	1.70538	3.89	4 2 2
57.3258	54.20	0.4087	1.60594	11.14	5 1 1
62.9377	91.92	0.1996	1.47557	18.89	4 4 0
65.0314	57.33	1.9241	1.43303	11.78	2 2 0
77.7721	37.75	2.6586	1.22703	7.76	3 1 1

JCPDS no. 01-1172, showing the standard 2θ, relative intensities and corresponding diffraction planes for gold.

Position [°2θ]	**d-spacing [Å]**	**Rel. Int. [%]**	***hkl***
38.269	2.350	100.0	1 1 1
44.600	2.030	53.0	2 0 0
64.678	1.440	33.0	2 2 0
77.549	1.230	40.0	3 1 1
82.352	1.170	9.0	2 2 2
98.085	1.020	3.0	4 0 0

Table 07. XRD pattern of 20 nm gold colloid as received from BioAssay Works (07)

Position [°2θ]	**Height [cts]**	**FWHM [°2θ]**	**d-spacing [Å]**	**Rel. Int. [%]**	**hkl**
38.1712	25619.53	0.5297	2.35580	100.00	1 1 1
44.3419	7512.89	0.8111	2.04122	29.32	2 0 0
64.6125	4654.36	0.7911	1.44131	18.17	2 2 0
77.5594	4551.74	0.7974	1.22987	17.77	3 1 1
81.7197	1410.36	0.7053	1.17745	5.51	2 2 2

Table 08. XRD pattern of 10 nm gold colloid as received from nanoComposix (08)

Position [°2θ]	**Height [cts]**	**FWHM [°2θ]**	**d-spacing [Å]**	**Rel. Int. [%]**	**hkl**
38.2318	2695.09	1.1904	2.35220	100.00	1 1 1
44.2346	324.98	2.6776	2.04592	12.06	2 0 0
64.6874	444.50	1.0819	1.43982	16.49	2 2 0
77.6093	439.08	1.1731	1.22920	16.29	3 1 1

Table 09. XRD pattern of Au-seeded SPION (09)

Position [°2θ]	Height [cts]	FWHM [°2θ]	d-spacing [Å]	Rel. Int. [%]	hkl
35.6225	463.12	2.2936	2.51828	20.90	*3 1 1*
35.8373	340.28	2.6115	2.50368	15.36	*3 1 1*
38.1944	2215.96	0.9152	2.35442	100.00	1 1 1
44.1779	816.46	1.5091	2.04842	36.84	2 0 0
54.1397	233.96	1.4614	1.69268	10.56	4 2 2
57.1373	270.10	2.3505	1.61079	12.19	5 1 1
62.8160	674.16	1.4752	1.47814	30.42	4 4 0
64.6235	614.39	1.5735	1.44109	27.73	2 2 0
77.5690	653.46	1.7954	1.22974	29.49	3 1 1
81.4911	218.15	3.4918	1.18017	9.84	2 2 2

Table 10. Au@γ-Fe$_2$O$_3$ as produced using the Lyon et al method (10)

Position [°2θ]	Height [cts]	FWHM [°2θ]	d-spacing [Å]	Rel. Int. [%]	hkl
35.5597	155.72	0.8570	2.52259	23.13	3 1 1
38.1802	673.29	0.3983	2.35526	100.00	1 1 1
44.3875	190.68	0.6017	2.03923	28.32	2 0 0
64.6042	94.18	0.6439	1.44147	13.99	2 2 0
77.5679	134.23	0.2497	1.22975	19.94	3 1 1
81.5560	43.21	0.7878	1.17940	6.42	2 2 2

Table 11. Au@γ-Fe_2O_3 after 1 addition of $HAuCl_4$ and NH_2OH followed by magnetic separation (11)

Position [°2θ]	**Height [cts]**	**FWHM [°2θ]**	**d-spacing [Å]**	**Rel. Int. [%]**	**hkl**
36.0211	393.32	0.0963	2.49133	13.89	3 1 1
38.1351	2832.44	0.4824	2.35794	100.00	1 1 1
44.3271	828.13	0.8566	2.04187	29.24	2 0 0
64.5864	547.63	0.8621	1.44183	19.33	2 2 0
77.5504	580.26	0.8239	1.22999	20.49	3 1 1
81.8015	239.41	4.0000	1.17648	8.45	2 2 2

Table 12. Au@γ-Fe_2O_3 after 5 additions of $HAuCl_4$ and NH_2OH followed by magnetic separation (12)

Position [°2θ]	**Height [cts]**	**FWHM [°2θ]**	**d-spacing [Å]**	**Rel. Int. [%]**	**hkl**
38.1633	135528.00	0.3760	2.35626	100.00	1 1 1
44.3354	41433.08	0.6124	2.04151	30.57	2 0 0
64.5999	25452.76	0.6496	1.44156	18.78	2 2 0
77.5457	22633.06	0.7733	1.23005	16.70	3 1 1
81.7336	8212.60	0.5439	1.17728	6.06	2 2 2

Table 13. XRD pattern of SPION@Au (13)

Position [°2θ]	**Height [cts]**	**FWHM [°2θ]**	**d-spacing [Å]**	**Rel. Int. [%]**	**hkl**
38.1398	14034.19	0.4369	2.35766	100.00	1 1 1
44.3200	3986.53	0.6727	2.04218	28.41	2 0 0
64.5891	2225.86	0.6594	1.44177	15.86	2 2 0
77.5328	1925.60	0.7355	1.23022	13.72	3 1 1
81.6971	634.02	0.5908	1.17772	4.52	2 2 2

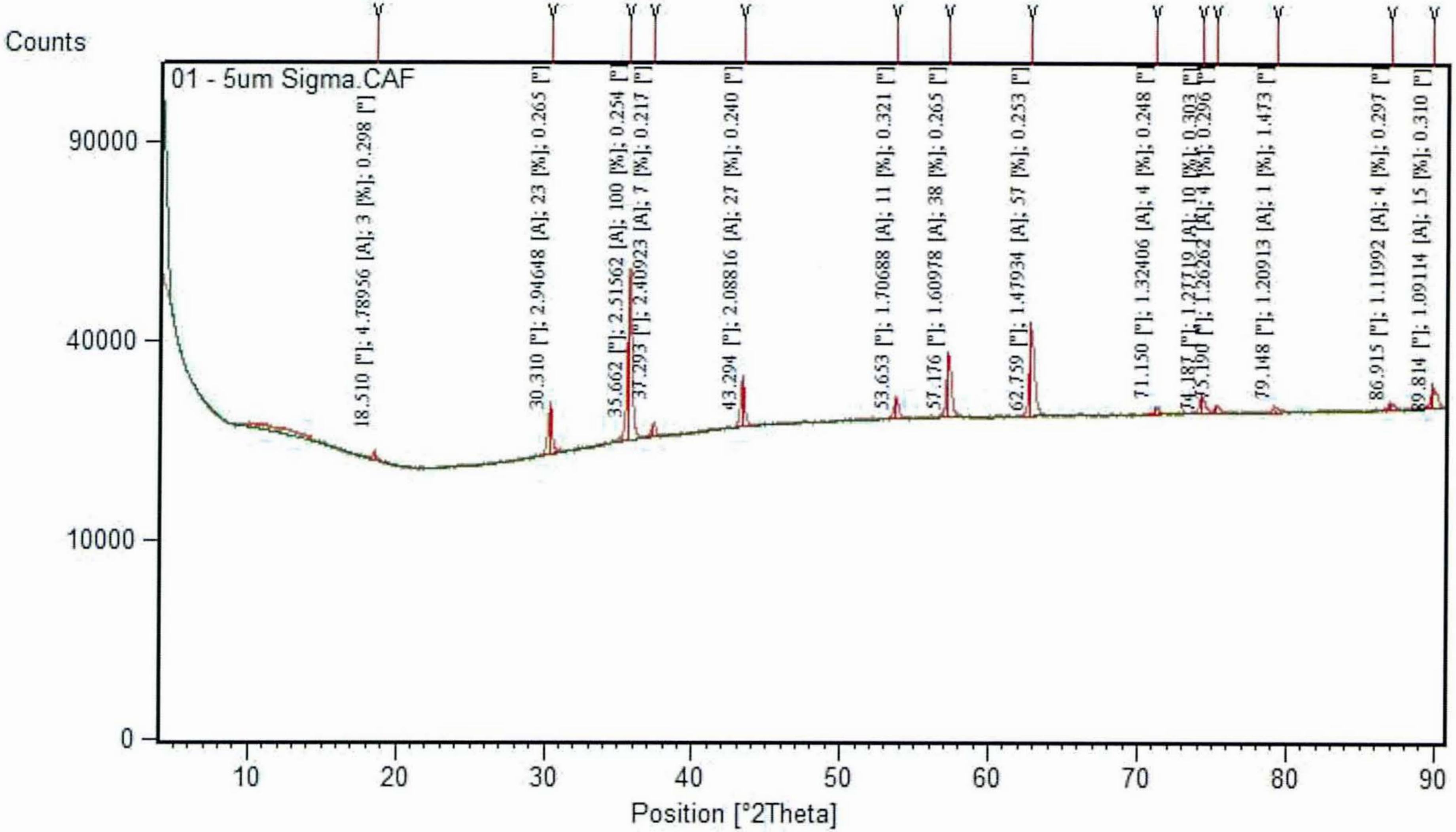
Counts
01 - 5um Sigma.CAF
90000
40000
10000
0
10
20
30
40
50
60
70
80
90
Position [°2Theta]
18.510 [°]; 4.78956 [A]; 3 [%]; 0.298 [°]
30.310 [°]; 2.94648 [A]; 23 [%]; 0.265 [°]
35.662 [°]; 2.51562 [A]; 100 [%]; 0.254 [°]
37.293 [°]; 2.40923 [A]; 7 [%]; 0.217 [°]
43.294 [°]; 2.08816 [A]; 27 [%]; 0.240 [°]
53.653 [°]; 1.70688 [A]; 11 [%]; 0.321 [°]
57.176 [°]; 1.60978 [A]; 38 [%]; 0.265 [°]
62.759 [°]; 1.47934 [A]; 57 [%]; 0.253 [°]
71.150 [°]; 1.32406 [A]; 4 [%]; 0.248 [°]
74.187 [°]; 1.27719 [A]; 10 [%]; 0.303 [°]
75.190 [°]; 1.26262 [A]; 4 [%]; 0.296 [°]
79.148 [°]; 1.20913 [A]; 1 [%]; 1.473 [°]
86.915 [°]; 1.11992 [A]; 4 [%]; 0.297 [°]
89.814 [°]; 1.09114 [A]; 15 [%]; 0.310 [°]

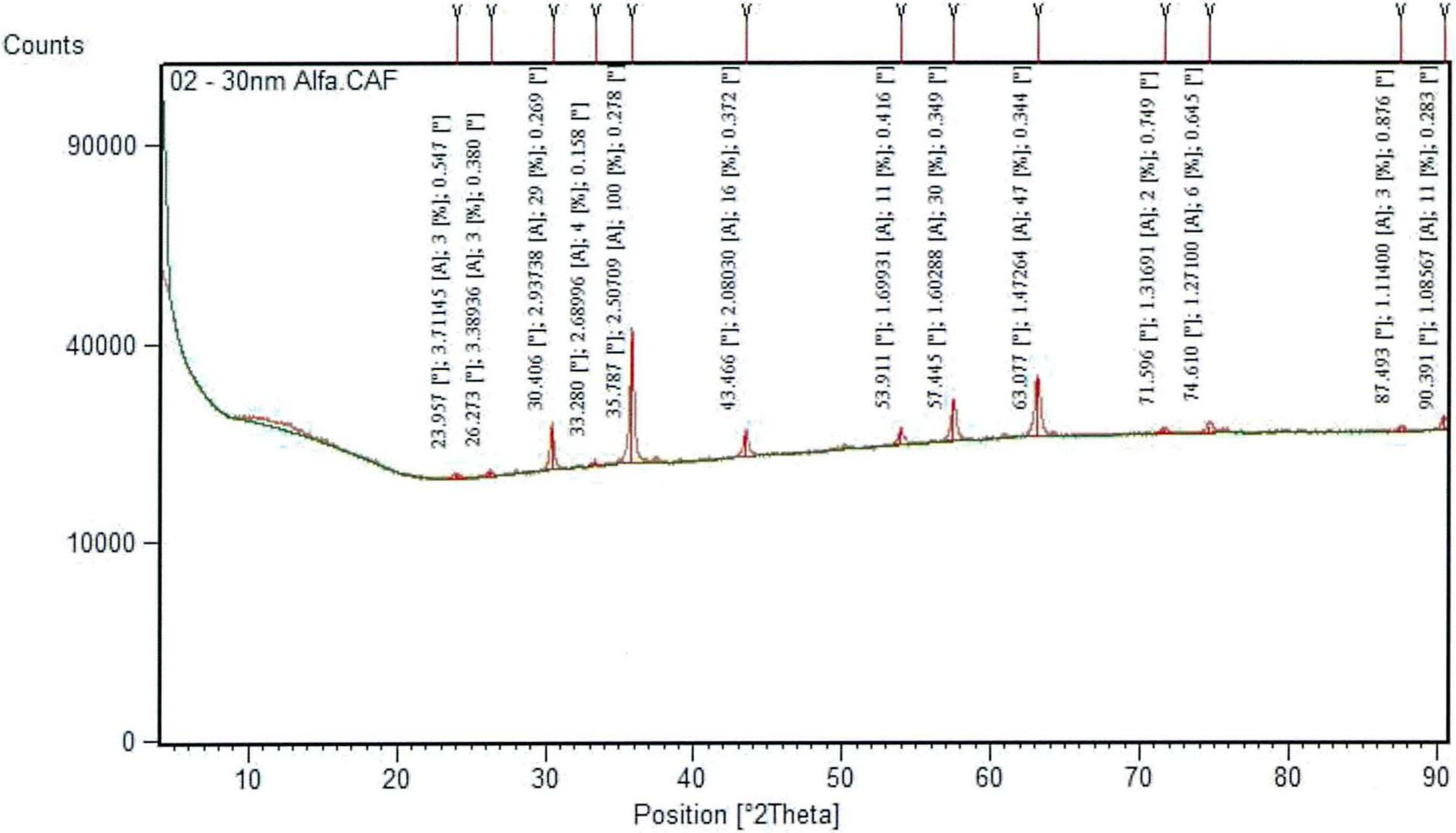
Counts
02 - 30nm Alfa.CAF
90000
40000
10000
0
10
20
30
40
50
60
70
80
90
Position [°2Theta]
23.957 [°]; 3.71145 [A]; 3 [%]; 0.547 [°]
26.273 [°]; 3.38936 [A]; 3 [%]; 0.380 [°]
30.406 [°]; 2.93738 [A]; 29 [%]; 0.269 [°]
33.280 [°]; 2.68996 [A]; 4 [%]; 0.158 [°]
35.787 [°]; 2.50709 [A]; 100 [%]; 0.278 [°]
43.466 [°]; 2.08030 [A]; 16 [%]; 0.372 [°]
53.911 [°]; 1.69931 [A]; 11 [%]; 0.416 [°]
57.445 [°]; 1.60288 [A]; 30 [%]; 0.349 [°]
63.077 [°]; 1.47264 [A]; 47 [%]; 0.344 [°]
71.596 [°]; 1.31691 [A]; 2 [%]; 0.749 [°]
74.610 [°]; 1.27100 [A]; 6 [%]; 0.645 [°]
87.493 [°]; 1.11400 [A]; 3 [%]; 0.876 [°]
90.391 [°]; 1.08567 [A]; 11 [%]; 0.283 [°]

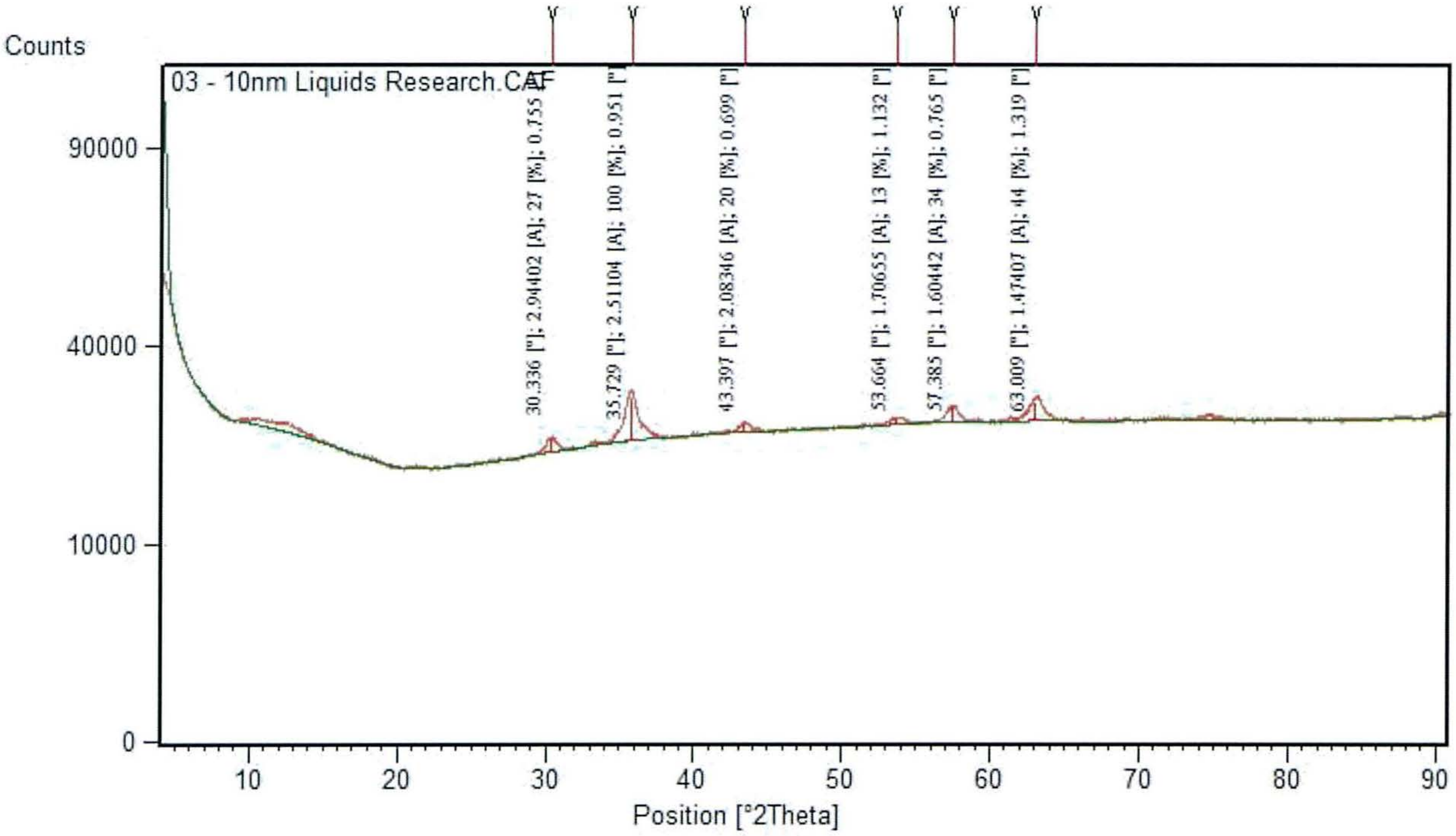
Counts
03 - 10nm Liquids Research.CAF
30.336 [°]; 2.94402 [A]; 27 [%]; 0.755 [°]
35.729 [°]; 2.51104 [A]; 100 [%]; 0.951 [°]
43.397 [°]; 2.08346 [A]; 20 [%]; 0.699 [°]
53.664 [°]; 1.70655 [A]; 13 [%]; 1.132 [°]
57.385 [°]; 1.60442 [A]; 34 [%]; 0.765 [°]
63.009 [°]; 1.47407 [A]; 44 [%]; 1.319 [°]
90000
40000
10000
0
10
20
30
40
50
60
70
80
90
Position [°2Theta]

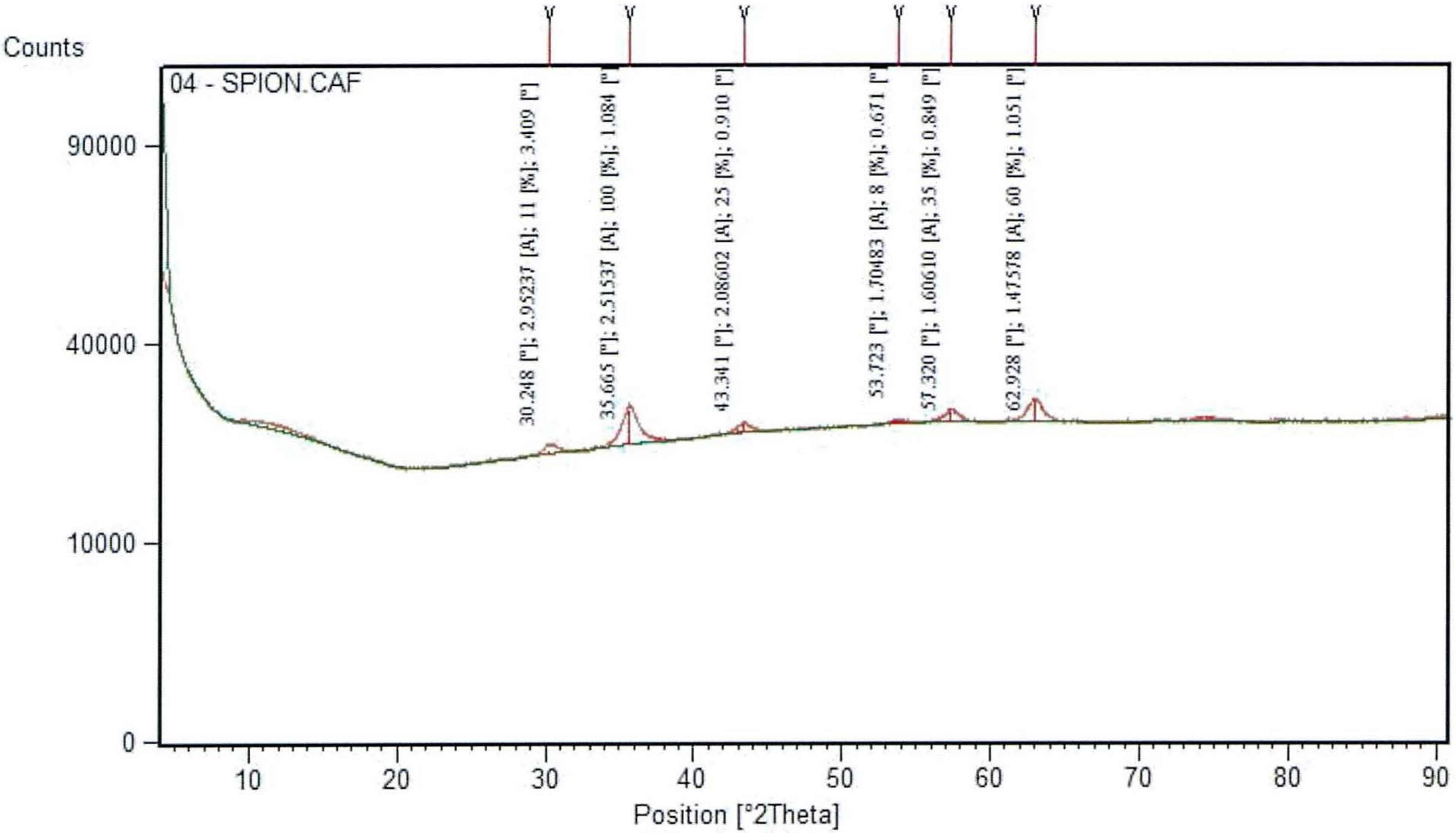
Counts
04 - SPION.CAF
90000
40000
10000
0
10
20
30
40
50
60
70
80
90
Position [°2Theta]
30.248 [°]; 2.95237 [A]; 11 [%]; 3.409 [°]
35.665 [°]; 2.51537 [A]; 100 [%]; 1.084 [°]
43.341 [°]; 2.08602 [A]; 25 [%]; 0.910 [°]
53.723 [°]; 1.70483 [A]; 8 [%]; 0.671 [°]
57.320 [°]; 1.60610 [A]; 35 [%]; 0.849 [°]
62.928 [°]; 1.47578 [A]; 60 [%]; 1.051 [°]

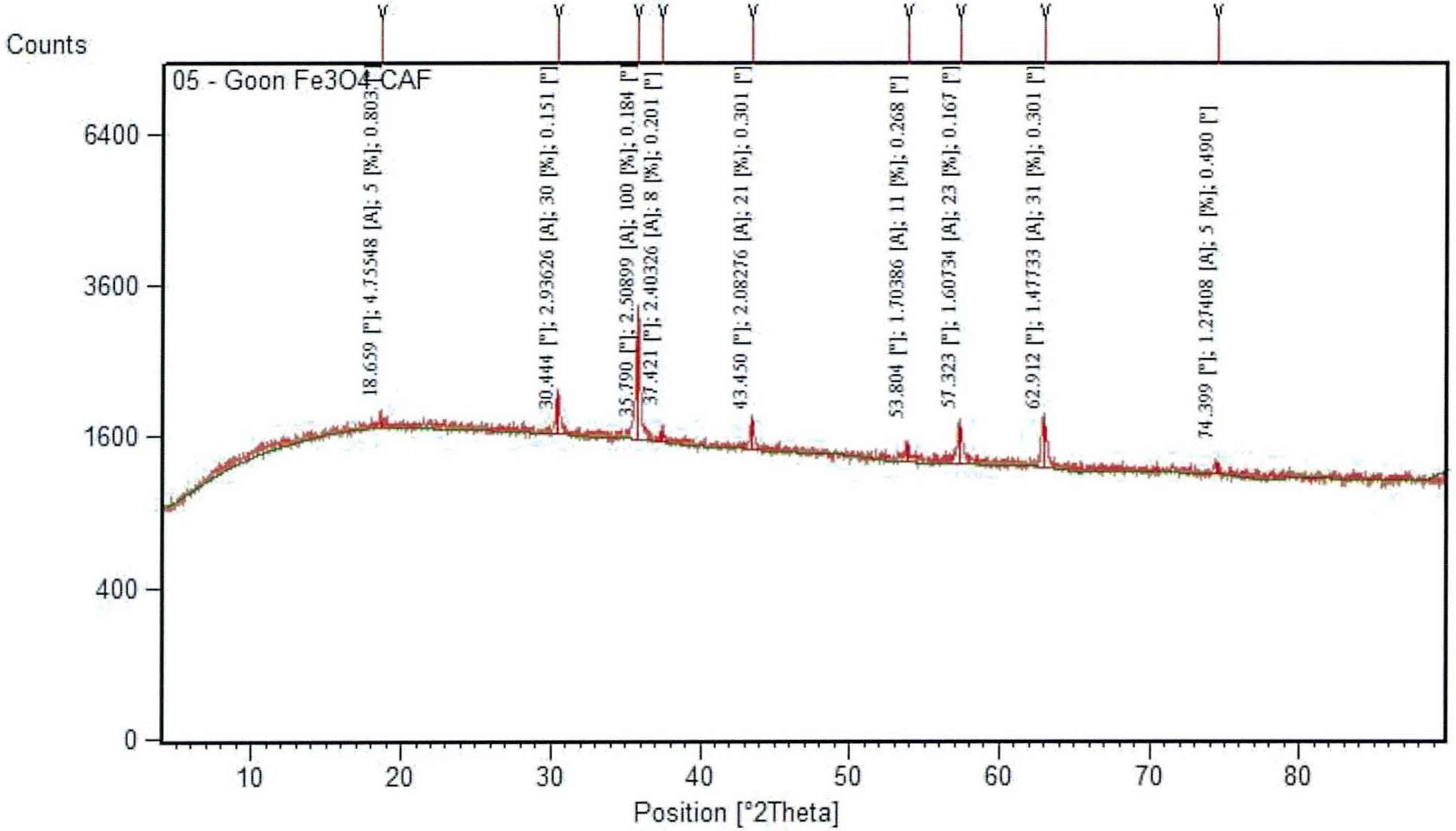
Counts
05 - Goon Fe3O4-CAF
6400
3600
1600
400
0
10
20
30
40
50
60
70
80
Position [°2Theta]
18.659 [°]; 4.75548 [A]; 5 [%]; 0.803
30.444 [°]; 2.93626 [A]; 30 [%]; 0.151 [°]
35.790 [°]; 2.50899 [A]; 100 [%]; 0.184 [°]
37.421 [°]; 2.40326 [A]; 8 [%]; 0.201 [°]
43.450 [°]; 2.08276 [A]; 21 [%]; 0.301 [°]
53.804 [°]; 1.70386 [A]; 11 [%]; 0.268 [°]
57.323 [°]; 1.60734 [A]; 23 [%]; 0.167 [°]
62.912 [°]; 1.47733 [A]; 31 [%]; 0.301 [°]
74.399 [°]; 1.27408 [A]; 5 [%]; 0.490 [°]

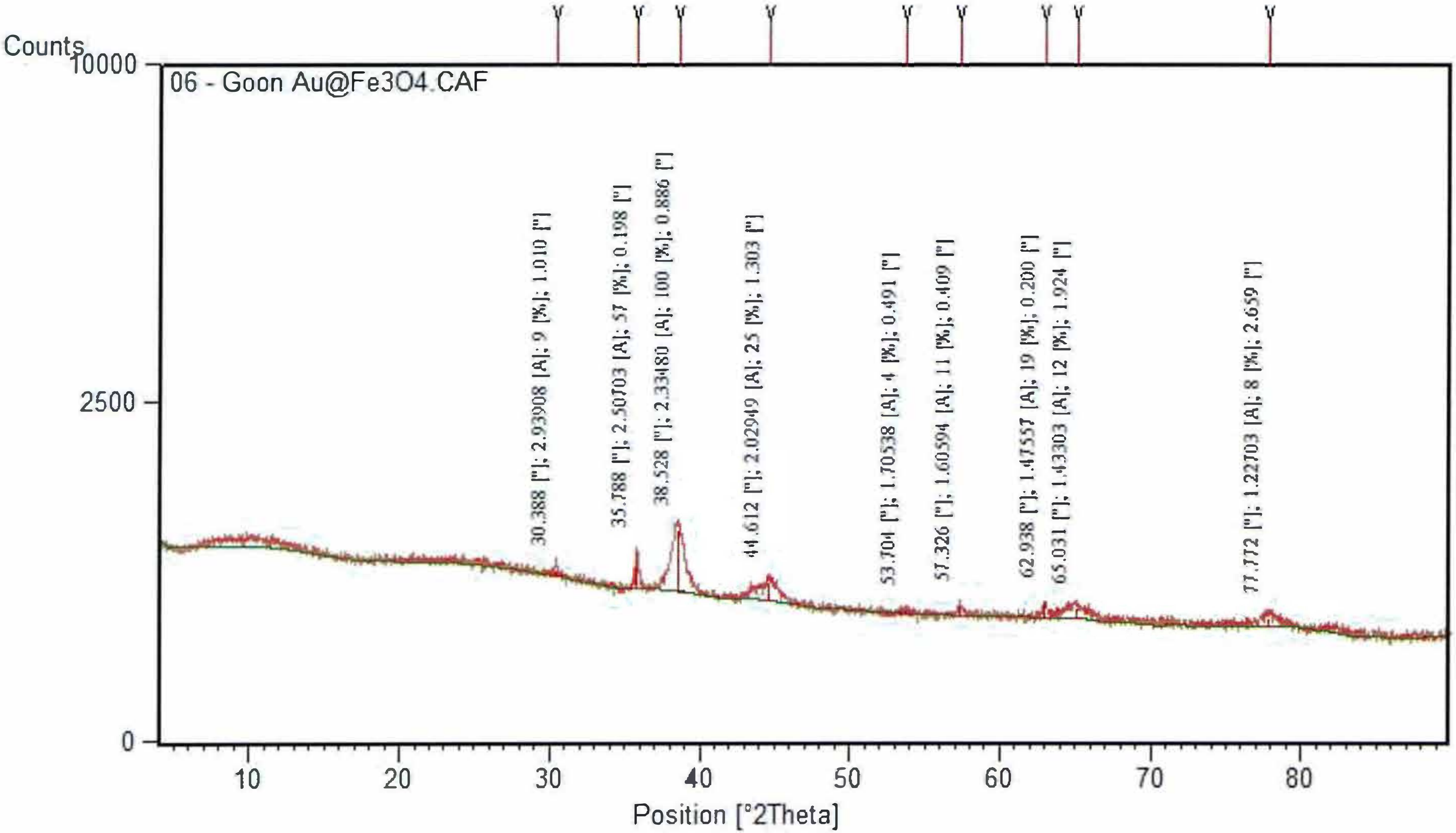
Counts
10000
2500
0
06 - Goon Au@Fe3O4.CAF
30.388 [°]; 2.93908 [Å]; 9 [%]; 1.010 [°]
35.788 [°]; 2.50703 [Å]; 57 [%]; 0.198 [°]
38.528 [°]; 2.33480 [Å]; 100 [%]; 0.886 [°]
44.612 [°]; 2.02949 [Å]; 25 [%]; 1.303 [°]
53.704 [°]; 1.70538 [Å]; 4 [%]; 0.491 [°]
57.326 [°]; 1.60594 [Å]; 11 [%]; 0.409 [°]
62.938 [°]; 1.47557 [Å]; 19 [%]; 0.200 [°]
65.031 [°]; 1.43303 [Å]; 12 [%]; 1.924 [°]
77.772 [°]; 1.22703 [Å]; 8 [%]; 2.659 [°]
10
20
30
40
50
60
70
80
Position [°2Theta]

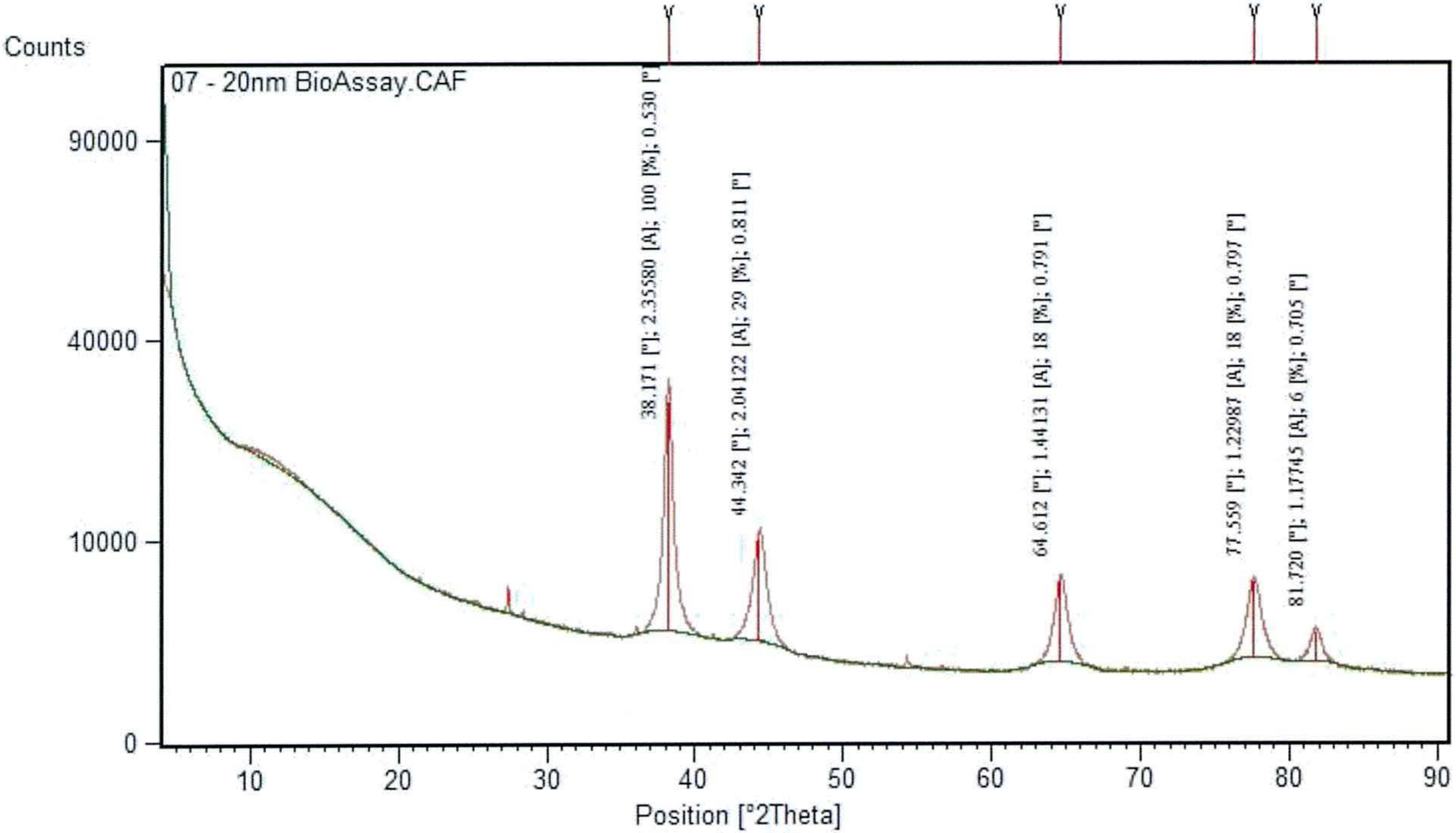
Counts
07 - 20nm BioAssay.CAF
90000
40000
10000
0
38.171 [°]; 2.35580 [A]; 100 [%]; 0.530 [°]
44.342 [°]; 2.04122 [A]; 29 [%]; 0.811 [°]
64.612 [°]; 1.44131 [A]; 18 [%]; 0.791 [°]
77.559 [°]; 1.22987 [A]; 18 [%]; 0.797 [°]
81.720 [°]; 1.17745 [A]; 6 [%]; 0.705 [°]
10
20
30
40
50
60
70
80
90
Position [°2Theta]

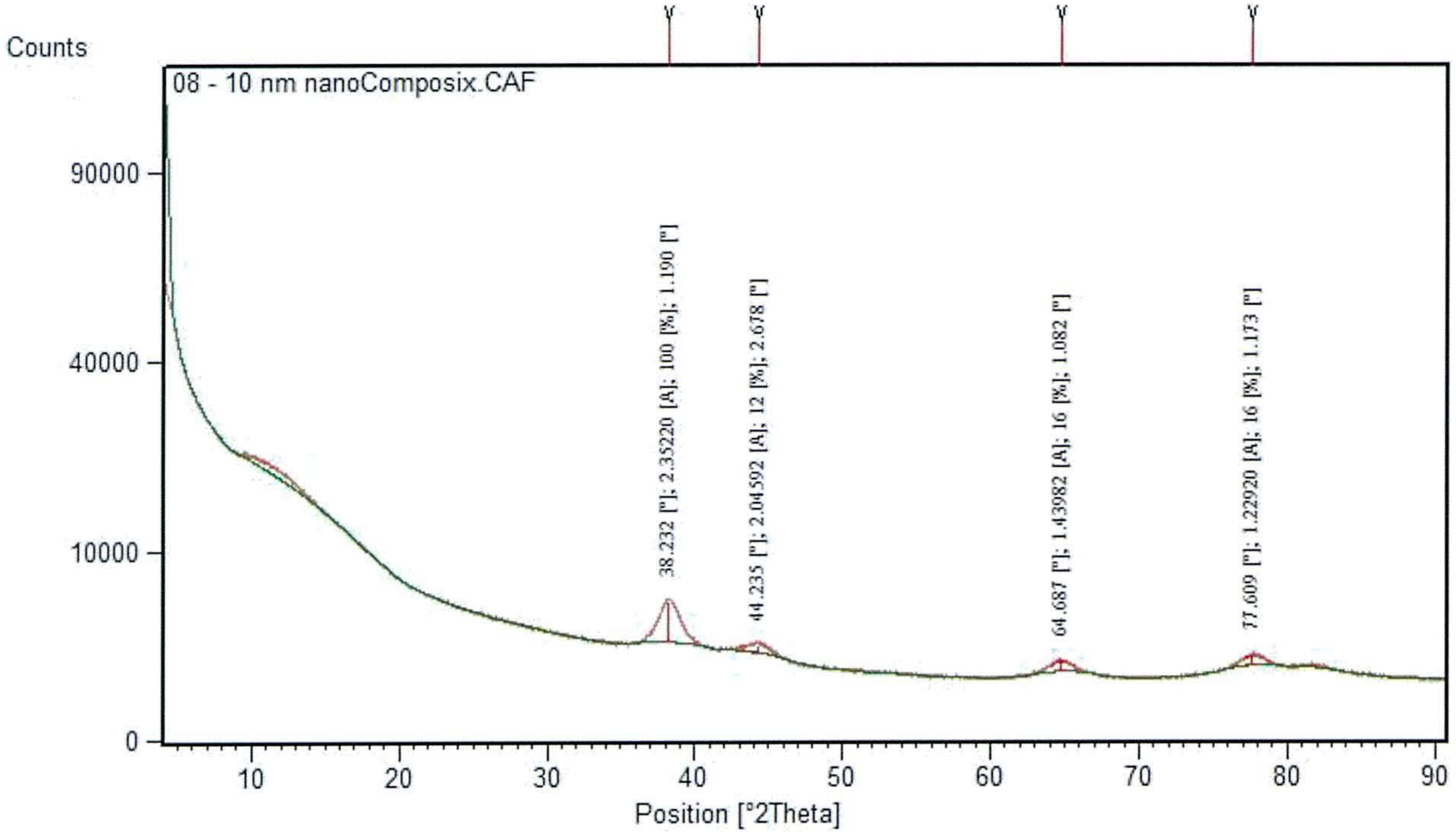
Counts
08 - 10 nm nanoComposix.CAF
90000
40000
10000
0
38.232 [°]; 2.35220 [A]; 100 [%]; 1.190 [°]
44.235 [°]; 2.04592 [A]; 12 [%]; 2.678 [°]
64.687 [°]; 1.43982 [A]; 16 [%]; 1.082 [°]
77.609 [°]; 1.22920 [A]; 16 [%]; 1.173 [°]
10
20
30
40
50
60
70
80
90
Position [°2Theta]

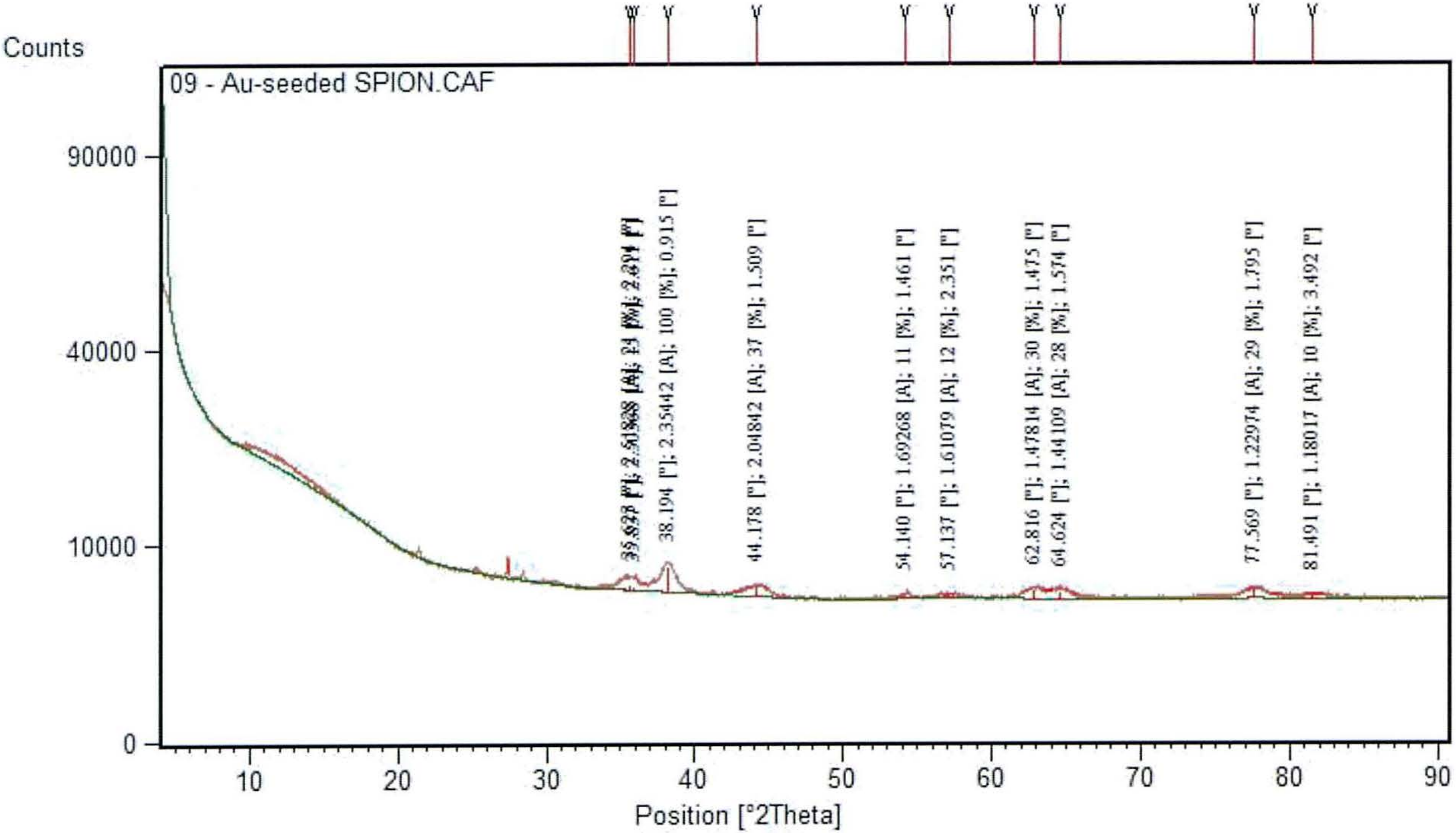
Counts
09 - Au-seeded SPION.CAF
90000
40000
10000
0
10
20
30
40
50
60
70
80
90
Position [°2Theta]
38.194 [°]; 2.35442 [A]; 100 [%]; 0.915 [°]
44.178 [°]; 2.04842 [A]; 37 [%]; 1.509 [°]
54.140 [°]; 1.69268 [A]; 11 [%]; 1.461 [°]
57.137 [°]; 1.61079 [A]; 12 [%]; 2.351 [°]
62.816 [°]; 1.47814 [A]; 30 [%]; 1.475 [°]
64.624 [°]; 1.44109 [A]; 28 [%]; 1.574 [°]
77.569 [°]; 1.22974 [A]; 29 [%]; 1.795 [°]
81.491 [°]; 1.18017 [A]; 10 [%]; 3.492 [°]

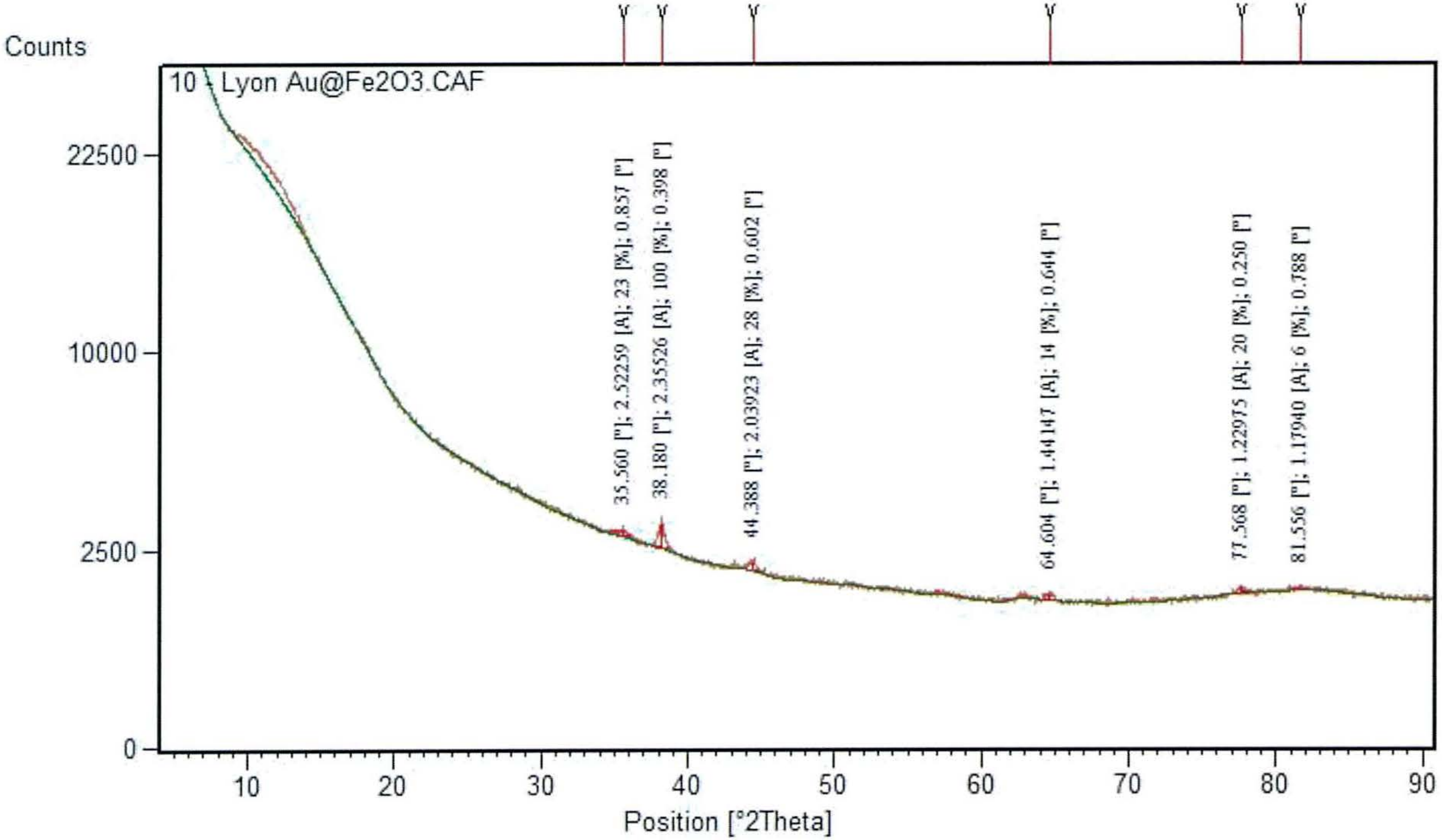
Counts
10 - Lyon Au@Fe2O3.CAF
22500
10000
2500
0
35.560 [°]; 2.52259 [A]; 23 [%]; 0.857 [°]
38.180 [°]; 2.35526 [A]; 100 [%]; 0.398 [°]
44.388 [°]; 2.03923 [A]; 28 [%]; 0.602 [°]
64.604 [°]; 1.44147 [A]; 14 [%]; 0.644 [°]
77.568 [°]; 1.22975 [A]; 20 [%]; 0.250 [°]
81.556 [°]; 1.17940 [A]; 6 [%]; 0.788 [°]
10
20
30
40
50
60
70
80
90
Position [°2Theta]

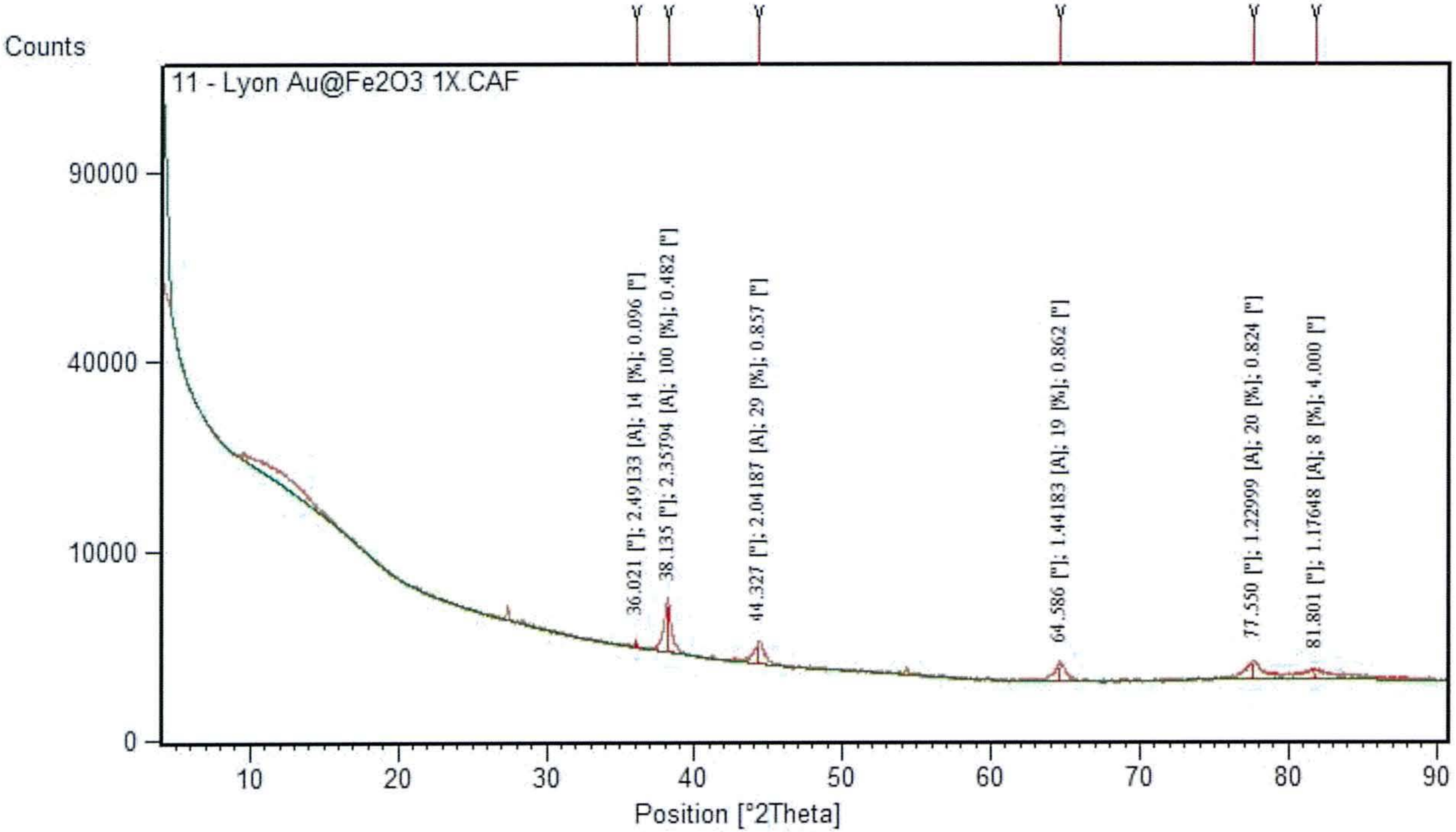
Counts
11 - Lyon Au@Fe2O3 1X.CAF
90000
40000
10000
0
36.021 [°]; 2.49133 [A]; 14 [%]; 0.096 [°]
38.135 [°]; 2.35794 [A]; 100 [%]; 0.482 [°]
44.327 [°]; 2.04187 [A]; 29 [%]; 0.857 [°]
64.586 [°]; 1.44183 [A]; 19 [%]; 0.862 [°]
77.550 [°]; 1.22999 [A]; 20 [%]; 0.824 [°]
81.801 [°]; 1.17648 [A]; 8 [%]; 4.000 [°]
10
20
30
40
50
60
70
80
90
Position [°2Theta]

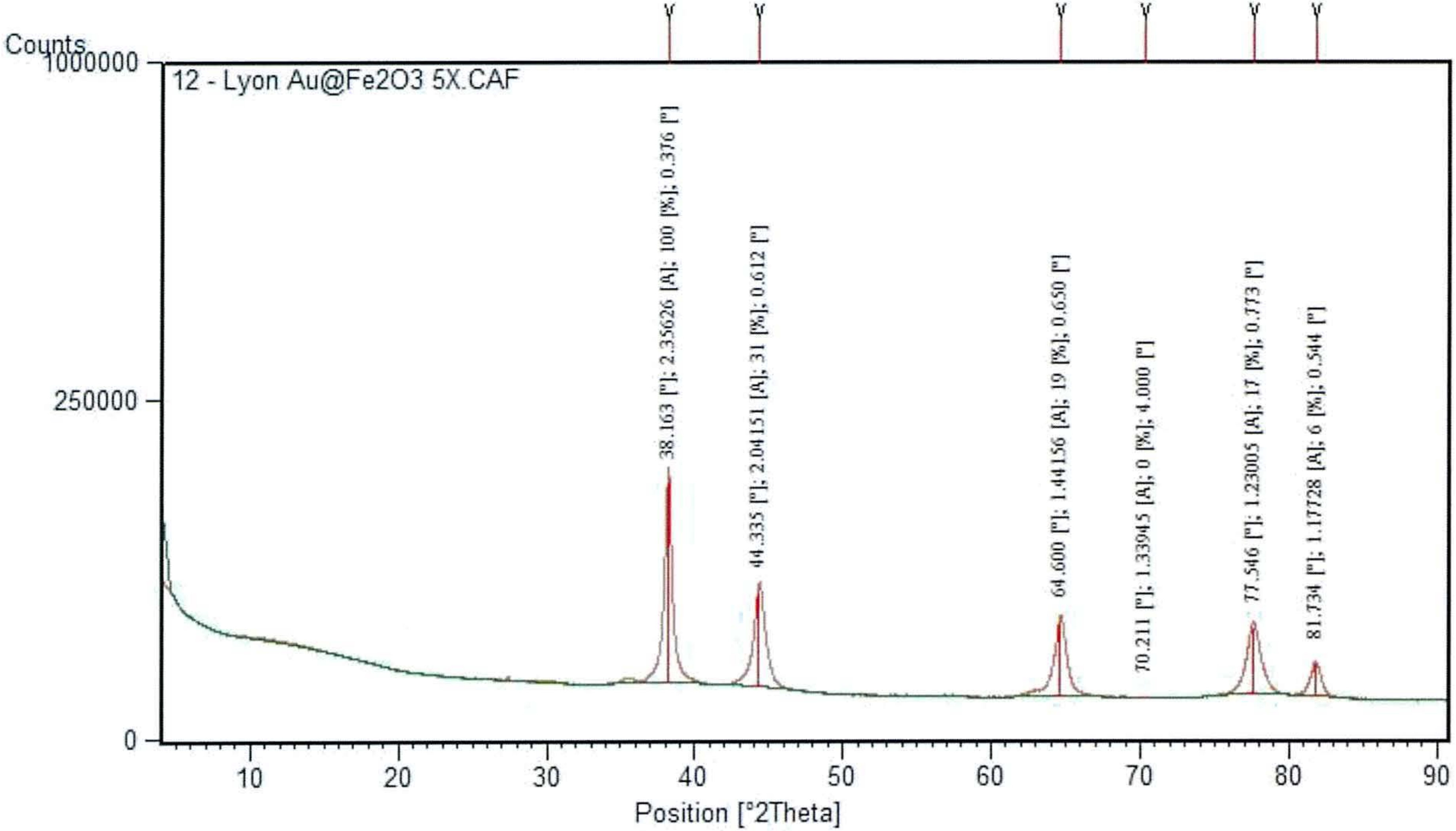
Counts
1000000
250000
0
12 - Lyon Au@Fe2O3 5X.CAF
38.163 [°]; 2.35626 [Å]; 100 [%]; 0.376 [°]
44.335 [°]; 2.04151 [Å]; 31 [%]; 0.612 [°]
64.600 [°]; 1.44156 [Å]; 19 [%]; 0.650 [°]
70.211 [°]; 1.33945 [Å]; 0 [%]; 4.000 [°]
77.546 [°]; 1.23005 [Å]; 17 [%]; 0.773 [°]
81.734 [°]; 1.17728 [Å]; 6 [%]; 0.544 [°]
10
20
30
40
50
60
70
80
90
Position [°2Theta]

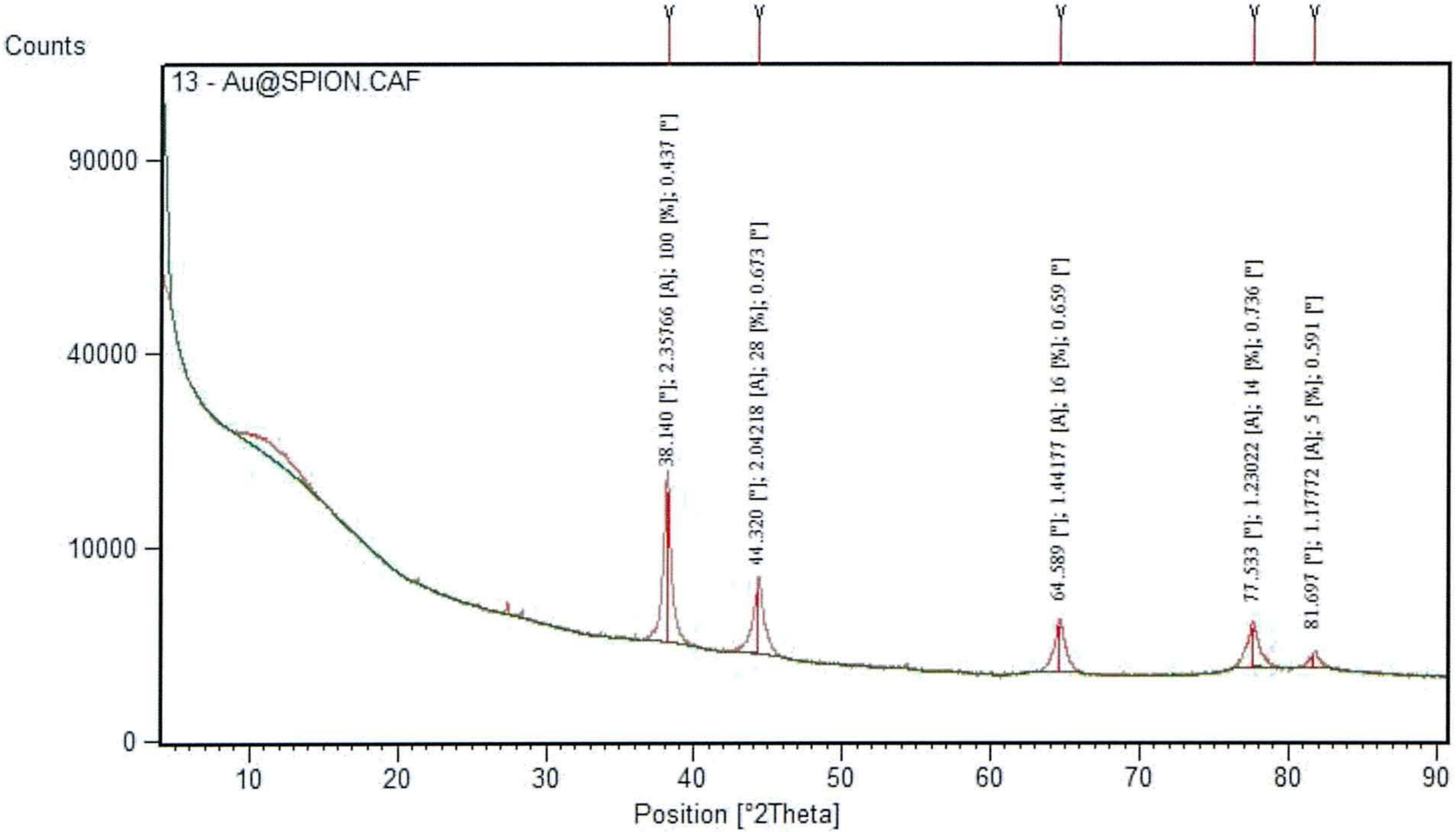
Counts
13 - Au@SPION.CAF
90000
40000
10000
0
38.140 [°]; 2.35766 [A]; 100 [%]; 0.437 [°]
44.320 [°]; 2.04218 [A]; 28 [%]; 0.673 [°]
64.589 [°]; 1.44177 [A]; 16 [%]; 0.659 [°]
77.533 [°]; 1.23022 [A]; 14 [%]; 0.736 [°]
81.697 [°]; 1.17772 [A]; 5 [%]; 0.591 [°]
10
20
30
40
50
60
70
80
90
Position [°2Theta]

DLS analysis of SPION from Section 4.1 following dilution with dH_2O

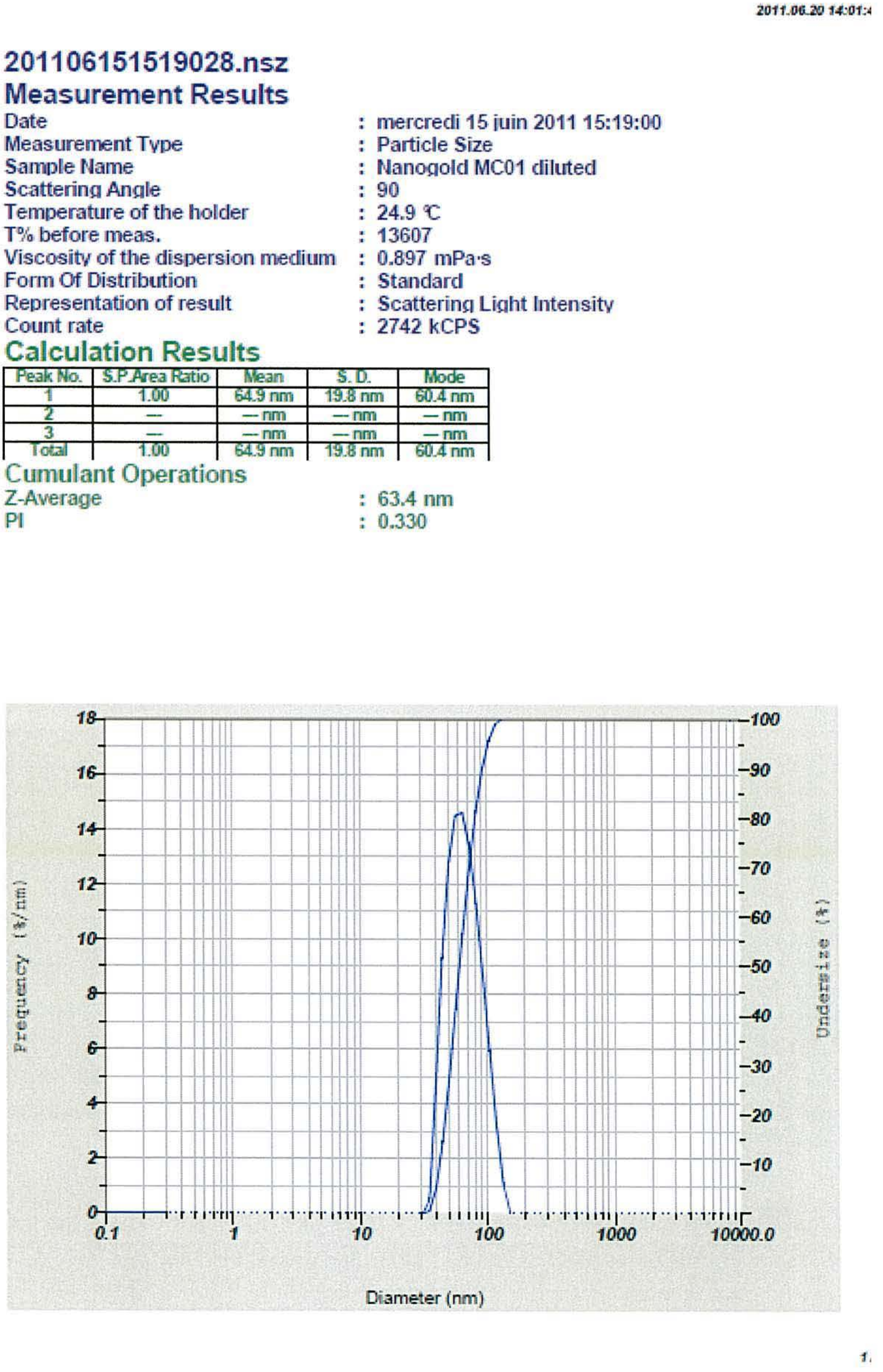

2011.06.20 14:01:

201106151519028.nsz

Measurement Results

Date : mercredi 15 juin 2011 15:19:00
Measurement Type : Particle Size
Sample Name : Nanogold MC01 diluted
Scattering Angle : 90
Temperature of the holder : 24.9 ℃
T% before meas. : 13607
Viscosity of the dispersion medium : 0.897 mPa·s
Form Of Distribution : Standard
Representation of result : Scattering Light Intensity
Count rate : 2742 kCPS

Calculation Results

Peak No.	S.P.Area Ratio	Mean	S. D.	Mode
1	1.00	64.9 nm	19.8 nm	60.4 nm
2	—	— nm	— nm	— nm
3	—	— nm	— nm	— nm
Total	1.00	64.9 nm	19.8 nm	60.4 nm

Cumulant Operations

Z-Average : 63.4 nm
PI : 0.330

1.

Table 14. A table showing the molar extinction coefficients of spherical citrate stabilised gold colloid standards of varying sizes (Cytodiagnostics).

Diameter	**Nanoparticles/ml**	**Peak SPR Wavelength**	**Molar Ext ($M^{-1}cm^{-1}$)**
5 nm	5.47×10^{13}	515-520 nm	1.10×10^{7}
10 nm	5.98×10^{12}	515-520 nm	1.01×10^{8}
20 nm	6.54×10^{11}	524 nm	9.21×10^{8}
30 nm	1.79×10^{11}	526 nm	3.36×10^{9}
40 nm	7.15×10^{10}	530 nm	8.42×10^{9}
50 nm	3.51×10^{10}	535 nm	1.72×10^{10}
60 nm	1.96×10^{10}	540 nm	3.07×10^{10}
80 nm	7.82×10^{9}	553 nm	7.70×10^{10}
100 nm	3.84×10^{9}	572 nm	1.57×10^{11}